10-31-2018

Remote Estimation of Surface Water pCO_2 in the Gulf of Mexico

Shuangling Chen
University of South Florida, shuangling1988@gmail.com

Remote Estimation of Surface Water pCO_2 in the Gulf of Mexico

by

Shuangling Chen

A dissertation submitted in partial fulfillment
of the requirements for the degree of
Doctor of Philosophy
College of Marine Science
University of South Florida

Major Professor: Chuanmin Hu, Ph.D.
Robert H. Byrne, Ph.D.
Lisa L. Robbins, Ph.D.
Mark E. Luther, Ph.D.
David F. Naar, Ph.D.

Date of Approval:
September 24, 2018

Keywords: surface pCO_2, sea surface salinity, remote sensing, dominant controls

DEDICATION

This dissertation is dedicated to my parents Yufen and Wen. Thank you for your cheerful encouragement and selfless love. Thanks also to my uncle Hequn and my siblings Yunxia and Jianbei for their concerns and spiritual support.

ACKNOWLEDGEMENTS

This dissertation would not have been possible without the guidance of Dr. Chuanmin Hu. Thank you for mentoring and supporting me throughout this work. I am very grateful for your enthusiasm, persistence, and dedication to scientific research. Thank you also to my committee members, Dr. Byrne, Dr. Robbins, Dr. Luther, and Dr. Naar for their help and support throughout this dissertation work.

Many individuals and groups were instrumental towards completion of this dissertation. In particular, I would like to thank my coauthors (especially Wei-Jun Cai, Rik Wanninkhof, and Bo Yang), as well as friends and colleagues within the Optical Oceanography Lab (especially Jen Cannizzaro, David English, Brian Barnes, Brock Murch, Mengqiu Wang, and Shaojie Sun) and the College of Marine Science.

This research was made possible, in part, by a grant from the U.S. Geological Survey (USGS). Endowed fellowships from the College of Marine Science, University of South Florida (Gulf Oceanographic Charitable Trust Fellowship, Tampa Bay Parrot Head Fellowship, and George Lorton Fellowship) also provided immeasurable support for this research. Of particular importance was access to the large datasets collected and shared by many groups over the past decades. I wish to emphasis the great efforts and contributions of NOAA and several colleges and institutes (Columbia University, Texas A and M University, University of Delaware, University of South Florida, Florida Fish and Wildlife Conservation Commission) for their data (both ship-based and buoy data time series), and to thank all the researchers who collected and contributed

data used in this research – their efforts are much appreciated. Also I want to thank NASA for providing the MODIS satellite data, without which, this research would not have been possible.

TABLE OF CONTENTS

LIST OF TABLES iii

LIST OF FIGURES iv

ABSTRACT v

CHAPTER 1 : INTRODUCTION 1
1. Surface ocean pCO_2 and environmental controls 1
1.1. Thermodynamic effects 2
1.2. Biological activities 3
1.3. Ocean mixing 4
1.4. Air-Sea CO_2 exchange 5
2. Satellite estimation of surface ocean pCO_2 6
2.1. Satellite-derived environmental variables 6
2.2. Satellite mapping of surface pCO_2: current status 8
3. Study area 11
4. Objectives 13
5. Data sources 14
5.1. Field data 14
5.2. Satellite data 15
6. Approach and dissertation structure 16
7. Literature cited 17

CHAPTER 2 : ESTIMATING SURFACE PCO_2 IN SINGLE-PROCESS DOMINATED REGION FROM SATELLITES: THE WEST FLORIDA SHELF 33
1. Research overview 33

CHAPTER 3 : ESTIMATING SURFACE PCO_2 IN SINGLE-PROCESS DOMINATED REGION FROM SATELLITES: THE NORTHERN GOM 35
1. Research overview 35

CHAPTER 4: REMOTE ESTIMATION OF SEA SURFACE SALINITY IN THE GOM 37
1. Research overview 37

CHAPTER 5: A UNIFIED APPROACH TO ESTIMATE SURFACE OCEAN PCO_2 FROM SATELLITE MEASUREMENTS 39
1. Research overview 39

CHAPTER 6: DOMINANT CONTROLS OF SURFACE OCEAN PCO_2 IN COASTAL OCEANS: ANALYSIS OF IN SITU TIME SERIES DATA 50

1. Research overview 50

CHAPTER 7: RESEARCH IMPACTS AND CONCLUSIONS 52
1. Summary of findings 52
2. Research implications 55
2.1. Satellite mapping of surface pCO_2 55
2.2. Further implications 57
3. Future work 58
3.1. Research 58
3.2. Product delivery 59
4. Conclusions 60
5. Literature cited 61

APPENDIX A: REMOTE ESTIMATION OF SURFACE PCO_2 ON THE WEST FLORIDA SHELF 69

APPENDIX B: ESTIMATING SURFACE PCO_2 IN THE NORTHERN GULF OF MEXICO: WHICH REMOTE SENSING MODEL TO USE? 86

APPENDIX C: ESTIMATING SEA SURFACE SALINITY IN THE NORTHERN GULF OF MEXICO FROM SATELLITE OCEAN COLOR MEASUREMENTS 104

APPENDIX D: A MACHINE LEARNING APPROACH TO ESTIMATE SURFACE OCEAN PCO_2 FROM SATELLITE MEASUREMENTS 123

APPENDIX E: DOMINANT CONTROLS OF SURFACE OCEAN PCO_2 IN COASTAL OCEANS: ANALYSIS OF IN SITU TIME SERIES DATA 197

APPENDIX F: AUTHOR CONTRIBUTIONS AND COPYRIGHT CLEARANCES 252

APPENDIX G: PUBLICATIONS (PUBLISHED AND SUBMITTED) 256

LIST OF TABLES

Table 1: List of published satellite pCO_2 remote sensing algorithms for open ocean waters 8

Table 2: List of published satellite pCO_2 remote sensing algorithms for coastal ocean waters 9

LIST OF FIGURES

Figure 1.1: Study region of the Gulf of Mexico 12

Figure 5.1: Surface *p*CO_2 climatology in the GOM: monthly mean 41

Figure 5.2: Surface pCO_2 climatology in the GOM: monthly mean minus two standard deviations 42

Figure 5.3: Surface pCO_2 climatology in the GOM: monthly mean plus two standard deviations 43

Figure 5.4: Surface pCO_2 climatology in the GOM: monthly minima 44

Figure 5.5: Surface pCO_2 climatology in the GOM: monthly maxima 45

Figure 5.6: Sensitivity of the pCO_2 remote sensing algorithm to Chl and K_d 46

Figure 5.7: Sensitivity of the pCO_2 remote sensing algorithm to Chl and SSS 47

Figure 5.8: Sensitivity of the pCO_2 remote sensing algorithm to Chl and SST 47

Figure 5.9: Sensitivity of the pCO_2 remote sensing algorithm to K_d and SSS 48

Figure 5.10: Sensitivity of the pCO_2 remote sensing algorithm to K_d and SST 48

Figure 5.11: Sensitivity of the pCO_2 remote sensing algorithm to SSS and SST 49

ABSTRACT

Surface ocean partial pressure of CO_2 (pCO_2) is a critical parameter in the quantification of air-sea CO_2 flux, which further plays an important role in quantifying the global carbon budget and understanding ocean acidification. The demand for a clearer understanding of how, and how fast, the ocean is changing due to atmospheric CO_2 absorption, requires accurate and synoptic estimation of surface pCO_2.

Surface ocean pCO_2 is mainly controlled by four oceanic processes – thermodynamics, ocean mixing, biological activities, and air-sea CO_2 exchange. Surface ocean pCO_2 is therefore closely related to environmental variables that characterize each oceanic process. These variables include sea surface temperature (SST), sea surface salinity (SSS), chlorophyll-a concentration (Chl), diffuse attenuation of downwelling irradiance (K_d), and wind speed. Ocean color satellites provide a means by which the relationship between these environmental variables and surface pCO_2 can be developed. Yet, remote estimation of surface pCO_2 in coastal oceans has been difficult due to the dynamic and complex biogeochemical processes. To date, most of the published satellite-based pCO_2 models are developed for single-process dominated regions, therefore having poor applicability in other oceanic regions. Particularly, there is no unified approach, let alone unified model, to remotely estimate surface pCO_2 in oceanic regions that are dominated by different oceanic processes.

This work provides solutions to these challenging issues for the remote estimation of surface pCO_2 in the Gulf of Mexico (GOM), with the following objectives: 1) Develop satellite-

based surface pCO_2 models and data products for single-process dominated subregions of the GOM, and quantify the sensitivities of the pCO_2 algorithms to the input environmental variables; 2) Quantify the oceanic processes in controlling surface pCO_2 in the GOM, analyze the relationships between environmental variables and surface pCO_2, and understand the mechanisms of seasonal and interannual variations of surface pCO_2 and its driving factors; 3) Develop an improved SSS model and data products for most GOM waters, and quantify the sensitivities of the SSS model to the input variables; 4) Develop a unified pCO_2 model and data products for the GOM waters, and quantify the sensitivities of the pCO_2 model to the input environmental variables and their relationships; 5) Quantify the temperature and non-temperature effects on surface pCO_2 at different latitudes, analyze the dominant controls and the corresponding the driving factors of surface pCO_2. The data used in this dissertation include those from extensive cruise surveys, buoy measurements, and long-term measurements by the Moderate Resolution Imaging Spectroradiometer (MODIS).

Specifically, for single-process dominated regions, two separate algorithms are developed and validated, respectively, from MODIS measurements. One is focused on the ocean current-dominated West Florida Shelf (WFS) (Appendix A), and the other is on the river-dominated northern GOM (Appendix B). The former utilizes a multi-variate nonlinear regression approach to establish the relationship between surface pCO_2 and environmental variables of SST, Chl, and K_d. The latter relies on a mechanistic semi-analytical approach (MeSAA), modified from an existing algorithm published earlier. Both algorithms show satisfactory performance, yet the latter requires SSS as the model input, which is difficult to obtain from ocean color satellite measurements. Therefore, a multilayer perceptron neural network-based (MPNN) SSS model is developed and validated, which generates SSS maps at 1-km resolution for the GOM using MODIS

measurements (Appendix C). Finally, with the availability of SSS from MODIS for the GOM, a unified pCO_2 algorithm is developed and validated. The machine-learning algorithm is based on a random forest regression ensemble (RFRE), which is able to estimate surface pCO_2 from MODIS measurements with a Root Mean Square Error (RMSE) of < 10 µatm and R^2 of 0.95 for pCO_2 ranging between 145 and 550 µatm (Appendix D). Using this approach, The RFRE algorithm is shown to be applicable to the Gulf of Maine (a contrasting oceanic region to GOM) after local model tuning. The results show significant improvement over other models, suggesting that the RFRE approach may serve as a template for other oceanic regions once sufficient field-measured pCO_2 data are available for local model tuning.

To further improve the accuracy of satellite-derived surface pCO_2 from coastal oceans and to increase its capability in capturing the interannual variations of surface pCO_2 resulting from anthropogenic forcing, the dominant controls of surface pCO_2 over seasonal and interannual time scales need to be better understood. As such, *in situ* pCO_2 time series data along the coasts of the United States of America at different latitudes are analyzed (Appendix E). On a seasonal time scale, surface pCO_2 tends to be dominated by the temperature effect (pCO_2_T) through SST and wind speed (with some exceptions) in tropical and subtropical oceans, but appears to be dominated by the non-temperature effect (pCO_2_nonT) in subpolar regions. In contrast, in tropical and subtropical waters on interannual time scales, surface pCO_2 is primarily moderated by the non-temperature effect (through air-sea CO_2 exchange via atmospheric pCO_2), but conversely dominated by the temperature effect (i.e., SST increase) in subpolar regions. The effects of biological activities (i.e., algal blooms) need to be further investigated in the future.

Overall, this dissertation has developed several algorithms to estimate SSS and surface pCO_2, among which the unified pCO_2 algorithm for multi-processes dominated regions appears to

be able to serve as a template for many other regions after local model tuning. The derived surface pCO_2 data products for the GOM provide a fundamental basis to assess air-sea exchange of CO_2 and understand the carbon chemistry under a changing climate.

CHAPTER 1:

INTRODUCTION

1. Surface ocean pCO_2 and environmental controls

When CO_2 from the atmosphere enters seawater, a chain of reactions can occur, which can produce carbonic acid, bicarbonate, and carbonate (Kanwisher, 1960). The free aqueous CO_2 in seawater is quantified as partial pressure of CO_2 (pCO_2), which refers to the fugacity in most cases (Pilson, 2012). The term fugacity expresses the tendency of CO_2 to escape from the seawater.

Knowledge of spatial and temporal distributions of pCO_2 in surface ocean waters is essential to understanding of carbon cycling and ocean acidification (Borges, 2005; Bauer et al., 2013). Since the industrialization era, ocean acidity has increased by 30% (~0.1 decrease in pH units), corresponding to a 40% increase in atmospheric CO_2 (Sabine et al., 2004; Solomon et al., 2007; Feely et al., 2009; Pachauri and Meyer, 2014). As a result, a degradation of ecological environment and a decrease in marine biodiversity have been observed (Reynaud et al., 2003; Orr et al., 2005; Kleypas et al., 2006; Kleypas and Yates, 2009). Knowledge of surface pCO_2 also helps to quantify air-sea CO_2 flux (Borges et al., 2005; 2006; Cai et al., 2006). The benefits of quantifying air-sea CO_2 flux are twofold: 1) it can help to better understand the ocean acidification process; and 2) it can provide insight into carbon cycling. Synoptic and frequent surface pCO_2 measurements are critical to quantifying the air-sea CO_2 flux and ocean acidity.

The variation of surface pCO_2 is complex, being closely related to the carbonate parameters: pH, total dissolved inorganic carbon (DIC, μmol kg^{-1}) and total alkalinity (TA, μmol kg^{-1}) (Pilson,

2012). In a carbonate system, once sea surface temperature (SST, ˚C), sea surface salinity (SSS, practical salinity unit) and pressure are known, any two parameters of TA, DIC, pCO_2, and pH can be used to calculate the other two and CO_2 speciation (i.e., $[CO_3^{-2}]$ and thus the carbonate mineral saturation state) using the CO_2 System Program (CO2SYS) (Pierrot and Wallace 2006). In principle, surface water pCO_2 in the ocean is mainly controlled by four processes: physical mixing, thermodynamic effects, biological activities, and air-sea CO_2 exchange (Fennel et al., 2008; Ikawa et al., 2013; Xue et al., 2016). These processes usually do not affect surface pCO_2 independently, but in an interrelated fashion (Murata, 2006).

1.1. Thermodynamic effects

Ocean thermodynamic effect on surface pCO_2 is dependent on SST, which influences the solubility of gaseous CO_2 (Weiss, 1974). The relationship between surface pCO_2 and SST can be estimated with an exponential function ($pCO_{2@T2} = pCO_{2@T1} \times e^{0.0423\times(T_2-T_1)}$) (Takahashi et al., 2002; 2009) although the exact parameter can deviate slightly from 0.0423 in coastal waters (Bai et al., 2015; Joesoef et al., 2015). The equation shows that an increase of SST increases surface pCO_2, and vice versa. SST is primarily regulated by several physical processes such as solar energy radiation, air-sea heat exchanges, and vertical oceanic mixing (Takahashi et al., 2002). Studies show that SST is the dominant factor in controlling seasonal variations of surface pCO_2 in the subtropical oligotrophic ocean waters (Takahashi et al., 2002; Fay and McKinley, 2017).

1.2. Biological activities

Biological activities in the ocean such as photosynthesis, respiration, and calcification have direct effects on surface pCO_2 because photosynthesis consumes CO_2, respiration produces CO_2, and calcification depletes both TA and DIC in a 2 to 1 ratio (Murata and Takizawa, 2002).

Photosynthesis by phytoplankton is mainly controlled by the concentrations of surface nutrients (i.e., $[NO_3^-]$, $[SO_4^{-2}]$, $[Fe^{+2}]$), SST, and light availability, which are all set by the physical environment (Fay and McKinley, 2017). Under optimal conditions (i.e., sufficient nutrients and sunlight at proper water temperatures, usually in spring and fall), phytoplankton blooms occur. In most cases, phytoplankton blooms (e.g., cyanobacteria blooms) would bring a distinct decrease in surface pCO_2 due to the great consumption of CO_2 in the production of organic carbons (Schneider et al., 2006; Martz et al., 2009). However, there are some exceptions. For example, Shadwick et al. (2011) found that spring blooms could introduce a sharp drop of surface pCO_2 by ~ 180 µatm, while the blooms in fall did not appear to change the surface pCO_2. This lack of change has been mainly attributed to the competing effect of decreasing SST, though the bloom can be clearly detected from satellite images. Furthermore, for phytoplankton blooms that also produce calcium carbonate (e.g., coccolithophorid, *E. huxleyi*), it was found that such phytoplankton blooms could result in an increase in surface pCO_2 (Murata and Takizawa, 2002; Murata, 2006). In these type of algal blooms, both DIC and TA would decrease during the bloom. It has been observed that if the ratio of calcification to photosynthesis during the bloom is between 1:1 and 2:1, the production of CO_2 via calcification would balance and exceed the consumption of CO_2 through photosynthesis (Murata and Takizawa, 2002; Murata, 2006).

In general, the overall effect of biological activities on surface pCO_2 is quite complex. Currently, the most common proxies for this biological term include chlorophyll concentrations

(Chl, mg m^{-3}) and light attenuation coefficients (Salisbury et al., 2008; Zhu et al., 2009; Hales et al., 2012; Signorini et al., 2013; Fay and McKinley, 2017). In addition, studies show that the biologic effect on surface pCO_2 only dominates in high-latitude waters greater than 40˚ latitude in both hemispheres (Takahashi et al., 2002; Fay and McKinley, 2017).

1.3. Ocean mixing

Different water masses have specific carbonate characteristics such as TA and DIC. The horizontal and vertical mixing among these water masses can affect the surface pCO_2 distribution in a dynamic way. For example, the mixing between the ice meltwater (typically with a low DIC value) with the surrounding seawater in the Arctic Ocean would reduce pCO_2 by 50-60 µatm, which compensates the increase of pCO_2 caused by the water warming in summer (Cai et al., 2010). In river-dominated coastal oceans (e.g., the northern Gulf of Mexico and the East China Sea), the riverine water mass (i.e., river plume) has distinct water properties (i.e., SST, SSS, TA, DIC, and nutrients) relative to those of the seawater. The mixing between the fresh/brackish riverine waters and seawater have great impact on the variation of surface pCO_2, in terms of the conservative mixing of the carbonate properties (i.e., TA and DIC), as well as the nutrient-enhanced phytoplankton blooms (e.g., Lohrenz and Cai, 2006; Lohrenz et al., 2010; Bai et al., 2015). In addition, the surface cooling-induced, or wind-induced, vertical mixing and ocean upwelling also varies surface pCO_2. This is because vertical mixing and upwelling transport DIC enriched (mostly CO_2 enriched) waters to the surface where they generally release CO_2 into the atmosphere. However, in the presence of nutrient-enriched surface waters, phytoplankton production would be enhanced and uptake of atmospheric CO_2 would occur (e.g., Hales et al., 2005; Ikawa et al., 2013; Norman et al., 2013; Huang et al., 2015).

Oceanic water masses derived from melted ice and river sources typically have low SST and SSS. Oceanic water masses brought to the surface via vertical mixing and upwelling usually have lower temperature and salinity values. Therefore, SST and SSS are commonly used as proxies to quantify the effect of ocean mixing on surface pCO_2 (e.g., Lohrenz and Cai, 2006; Lohrenz et al., 2010; 2018; Hales et al., 2012; Signorini et al., 2013; Bai et al., 2015). In addition to SST and SSS, wind speed and the mixed layer depth was also used in some studies (Jamet et al., 2007; Chierici et al., 2009; Shadwick et al., 2010; Nakaoka et al., 2013).

1.4. Air-Sea CO_2 exchange

The difference between the surface ocean pCO_2 and atmospheric pCO_2 at the air-sea interface represents the thermodynamic driving potential for the CO_2 to transfer across the air-sea interface (Takahashi et al., 2002). The direction of the net CO_2 transfer is governed by the pCO_2 differences between the ocean's surface and its overlying atmosphere. On seasonal time scales, Lu et al. (2012) found that air-sea CO_2 exchange exceeded the role of SST and dominated the seasonal variations of surface pCO_2 in the northern South China Sea. On short time scales (i.e., a few days up to 3 weeks), extreme weather events such as hurricanes also have strong impact on surface pCO_2, via air-sea CO_2 exchange. It's known that the rate of air-sea CO_2 exchange depends on the gas transfer velocity, which is a function of wind speed. During high-wind events (i.e., hurricanes, and strong storms), the wind speed is usually greater than 10 m s^{-1}. Bates et al. (1998) found that hurricanes in the Sargasso Sea could greatly increase the outgassing of CO_2 from the ocean surface to the atmosphere and decrease the surface pCO_2 further, despite the strong cooling effect during the events (which would also decrease surface pCO_2 by ~60 µatm). However, Turk et al. (2013) shows that episodic high wind events would increase surface pCO_2 by 30-50 µatm, regardless of

the pre-event conditions of the upper ocean water mass (either stratified, non-stratified, oversaturated, or under-saturated).

In most cases (except extreme events), air-sea CO_2 exchange has little effect on the surface pCO_2 during short-time scales, mainly due to buffering of the carbonate system (Murata et al., 2002; Bai et al., 2015). However, during long-time scales, surface pCO_2 has changed with time, especially during the anthropogenic increase of atmospheric pCO_2 (Takahashi et al., 2002; 2009), and atmospheric pCO_2 can be used as a proxy to quantify how air-sea CO_2 exchange affects surface pCO_2 (Lefèvre and Taylor, 2002).

2. Satellite estimation of surface ocean pCO_2

Synoptic and frequent surface pCO_2 measurements are critical to quantifying the air-sea CO_2 flux and ocean acidification. Due to data scarcities of surface pCO_2 from ship-based measurements and their limitations in spatial and temporal coverages, large uncertainties exist in the resultant air-sea CO_2 fluxes (e.g., Takahashi et al., 2002; 2009; Tseng et al., 2011; Vandemark et al., 2011; Geilfus et al., 2012). Numerical models have been used to estimate surface pCO_2 (Xue et al., 2014; Arruda et al., 2015), however the model results are strongly dependent on the assumption of the initial conditions. In contrast, recent advances in satellite ocean color remote sensing have shown its capacity in synoptic and frequent mapping of surface pCO_2 through developing relationships between environmental variables and surface pCO_2.

2.1. Satellite-derived environmental variables

Although surface pCO_2 is mainly controlled by the four processes as described in Section 1, in practice, it is hard to accurately quantify each of them separately due to the interactions among

them. Therefore, most of the satellite mapping models of surface pCO_2 are empirical (see Section 2.2 for details), and the most commonly used environmental variables include SST, SSS, Chl (e.g., Lohrenz and Cai, 2006; Lohrenz et al., 2010; 2018; Hales et al., 2012; Signorini et al., 2013; Bai et al., 2015). SST and SSS are proxies for the thermodynamic and ocean mixing effects, and Chl is a proxy for biological activities. In addition to these variables, some studies also used a beam attenuation coefficient, absorption of the Colored Dissolved Organic Matter (CDOM), Mixed Layer Depth (MLD), and wind speed as auxiliary variables to quantify surface pCO_2 in some oceanic regions (e.g., Jamet et al., 2007; Salisbury et al., 2008; Chierici et al., 2009; Shadwick et al., 2010; Nakaoka et al., 2013; Parard et al., 2014).

Of the commonly used environmental variables, SST and ocean color data products (i.e., Chl, CDOM, diffuse attenuation coefficient of the downwelling irradiance (K_d, m^{-1})) are available from the ocean color satellites such as Moderate Resolution Imaging Spectroradiometer (MODIS). However, currently there is no standard SSS data from these ocean color satellites.

The satellites designed to "measure" SSS, such as the ESA SMOS (the Soil Moisture and Ocean Salinity) and NASA Aquarius/SAC-D, lack sufficient spatial (30-100 km) and temporal resolution ($\geq$ 3days revisit period), and they are not designed for dynamic coastal waters (Lagerloef et al., 2008; Font et al., 2010). Since CDOM is a good tracer of SSS in coastal oceans (e.g., Hu et al., 2003; Coble et al., 2004; Del Vecchio and Blough, 2004), several studies have demonstrated the potentials of ocean color satellites in deriving SSS via empirical models (e.g., Bai et al., 2013; Geiger et al., 2013; Qing et al., 2013; Vandermeulen et al., 2014; Zhao et al., 2017). However, these models are region-dependent and may have poor applicability in other coastal waters, considering the difference of optical complexities among coastal regions. Therefore, in order to

map the surface pCO_2 from satellites in different coastal ocean settings, SSS data products from ocean color need to be developed first.

2.2. Satellite mapping of surface pCO_2: current status

At present, most of the published literature correlate surface pCO_2 to the environmental variables (SST, SSS, Chl, etc.) via traditional empirical regression and machine learning approaches (i.e., neural network) with variable performance in different oceanic regions (e.g., Stephens et al., 1995; Rangama et al., 2005; Wanninkhof et al., 2007; Zhu et al., 2009; Chierici et al., 2009; Friedrich and Oschlies, 2009; Telszewski et al., 2009; Signorini et al., 2013; Nakaoka et al., 2013; Parard et al., 2014). Specifically, for the open oceans, the satellite pCO_2 models often yield results with Root Mean Square Error (RMSE) between 10 and 20 µatm (e.g., Table 1), while for the coastal oceans, the model RMSE is > 20 µatm in most cases (Table 2). Some studies also proposed semi-analytical approaches to estimate surface pCO_2, but with larger error (RMSE > 30 µatm) (Hales et al., 2012; Bai et al., 2015; Song et al., 2016).

Table 1: List of published satellite pCO_2 remote sensing algorithms for open ocean waters. It should include most, if not all, the published studies of surface pCO_2 from remote sensing in the open oceans.

Reference	Study area	Model input	Model	Model uncertainty
Stephens et al. (1995)	North Pacific	SST, LON	MPR	RMSE=±17 µatm (subtropical), RMSE=±40µatm (subpolar)
Sarma (2003)	Arabian Sea	SST, SSS, CHL	MLR for DIC and TA	errors=±5-30 µatm
Lefevre and Taylor (2002)	Atlantic Gyre	SST, LAT, LON, atmospheric pCO_2	MLR	R=0.95~0.99
Olsen et al. (2004)	Caribbean Sea	SST, LAT, LON	MLR	RMSE=9.5 µatm,R^2=0.8
Ono et al. (2004)	North Pacific	SST, CHL	MPR	RMSE=±14 µatm (subtropical), RMSE=±17 µatm (subpolar)
Rangama et al. (2005)	Southern ocean	SST, CHL	MLR	STD=2.6~7.9 µatm
Sarma et al. (2006)	North Pacific	SST, SSS, CHL	MLR for DIC and TA	RMSE=17~23 µatm

Table 1 (Continued)

Reference	Study area	Model input	Model	Model uncertainty
Jamet et al. (2007)	North Atlantic	SST, CHL, MLD	MLR	R=0.45~0.86, RMSE = 8.98~15.01 µatm
Berryman et al. (2008)	Central Pacific	SST, SSS, CHL	MLR	R^2=0.59, $p < 0.02$
Chierici et al. (2009)	Northern North Atlantic	SST, CHL, MLD	MPR	RMSE=10.8 µatm, R^2 =0.72
Telszewski et al. (2009)	North Atlantic	SST, CHL, MLD	SOM	RMSE=11.6 µatm
Friedrich and Oschlies (2009)	North Atlantic	SST, CHL	KFM	RMSE=19 µatm
Chen et al. (2011)	Southern Atlantic and Indian Ocean	SST, CHL	MLR	R^2=0.77, 0.85, STD=1.21, 21.0 µatm
Nakaoka et al. (2013)	North Pacific	SST, SSS, CHL, MLD	SOM	RMSE=17.6~20.2 µatm
Moussa et al. (2016)	Tropical Atlantic	SST, SSS, CHL	FNN	RMSE=8.7~9.6 µatm
Xu et al. (2017)	Southern Ocean	SST, CHL	MLR	RMSE=13.6~21.3 µatm
Note: MLR=Multiple Linear Regression; MPR=Multiple Polynomial Regression; SOM=Self Organising Map; KFM=Kohonen Feature Map; FNN=Feedforward Neural Network; STD=Standard Deviation; R=Correlation Coefficient; SST=Sear Surface Temperature, CHL=Chlorophyll concentration; MLD=Mixed Layer Depth; LAT=Latitude; LON=Longitude; TA=Total Alkalinity; DIC=Dissolved Inorganic Carbon.				

Table 2: List of published satellite pCO_2 remote sensing algorithms for coastal ocean waters. It should include most, if not all, the published studies of surface pCO_2 from remote sensing in the coastal oceans.

Reference	Study area	Model input	Model	Model uncertainty
Lefevre et al. (2002)	Coast off Chile	SST, SSS, CHL	MLR	STD=35 µatm, R^2=0.65
Lohrenz and Cai (2006)	Mississippi River delta	SST, SSS, CHL	PCA and MLR	R^2 =0.743, RMSE=50.2 µatm
Evans et al. (2008)	Oregon and Washington Shelf	SST, CHL	Not available	Not available
Zhu et al. (2009)	Northern South China Sea	SST, CHL	MPR	R^2=0.66~0.68, RMSE=4.6~25.1 µatm
Shadwick et al. (2010)	Scotian Shelf	SST, CHL, wind speed	MLR	STD=13 µatm,R^2=0.81
Borges et al. (2010)	Belgian coastal zone	SST, CHL	MPR	Not available
Lohrenz et al. (2010)	Mississippi River delta	SST, SSS, CHL	PCA and MLR	R^2=0.165~0.976, p<0.001
Karagali et al. (2010)	Peru and Namibia	SST, CHL	MPR	R^2=0.67~0.72
Wipf et al. (2012)	Santa Barbara Channel	SST, CHL, NO_3^-	MLR	Not available
Jo et al. (2012)	Northern South China Sea	SST, CHL, LAT, LON	FFBP	RMSE=6.9 µatm, R^2=0.98
Hales et al. (2012)	North American West Coast	SST, CHL	Quasi-mechanistic model	R=0.61~0.93, RMSE=6.6~65 µatm
Tao et al. (2012)	Huanghai Sea and Bohai Sea	SST, CHL	MPR	RMSE=15.82~31.74 µatm
Signorini et al. (2013)	North American East Coast	SST, SSS, CHL, Jday	MLR	R^2=0.42~0.82, RMSE=22.4~36.9 µatm
Marrec et al. (2014)	Western English Channel	SST,SSS,CHL,MLD,Jday,LAT,LON	MLR	RMSE=17.2, 21.5 µatm, R^2=0.71,0.79
Parard et al. (2014)	Baltic Sea	SST,CHL,CDOM,NPP,MLD,Jday	MLR and SOM	RMSE=35 µatm, R^2=0.93

Table 2 (Continued)

Reference	Study area	Model input	Model	Model uncertainty
Qin et al. (2014)	Yellow Sea	SST, CHL	MPR	RMSE=16.68~21.46 µatm
Bai et al. (2015)	East China Sea	TA, DIC, CHL	MeSAA	Not available, but large data scattering in validation
Marrec et al. (2015)	European shelf	SST, CHL, wind speed, PAR, MLD	MLR	RMSE=16, 17 µatm
Padhy et al. (2015)	Hooghly Estuary	SST, CHL	MPR	RMSE=18 µatm
Song et al. (2016)	Bering Sea	SST, CHL	MeSAA	STD=17.67~74.8 µatm
Lohrenz et al. (2018)	Mississippi River delta	SST, CDOM, CHL	Regression tree	RMSE = 30.8 µatm
Joshi et al. (2018)	Apalachicola Bay	SST, CDOM, CHL	MLR	Uncertainty = ±101 ppm and ±643 ppm

Note: MLR=Multiple Linear Regression; MPR=Multiple Polynomial Regression; SOM=Self Organising Map; KFM=Kohonen Feature Map; FNN=Feedforward Neural Network; FFBP= Feed Forward Back Propagation; MeSAA=Mechanistic Semi-Analytical Algorithm; PCA=Principal Component Analysis; STD=Standard Deviation; R=Correlation Coefficient; SST=Sear Surface Temperature, SSS=Sea Surface Salinity; CHL=Chlorophyll concentration; MLD=Mixed Layer Depth; LAT=Latitude; LON=Longitude; TA=Total Alkalinity; DIC=Dissolved Inorganic Carbon; CDOM=Colored Dissolved Organic Matter; NPP=Net Primary Production; PAR=Photosynthetically Active Radiation; Jday=Julian day.

Regardless if an empirical or semi-analytical approach is used, the resulting published satellite pCO_2 model depends on the assumptions made for a specific oceanic region (e.g., river dominated, ocean-current dominated, or upwelling dominated). To date, there is no unified pCO_2 approach, let alone a unified pCO_2 model with region-specific parameterization, available to estimate surface pCO_2 from satellites for a large oceanic domain (e.g., the Gulf of Mexico) that contains several different oceanic processes. The difficulty in obtaining a unified approach to estimate surface pCO_2 from satellites with relatively lower uncertainties is due mostly to the complexity and dynamics of the biogeochemical and physical processes in such regions.

In some of the published satellite-based pCO_2 models, the monthly mean satellite products or climatology for Chl are used as model inputs to compensate for the scarcities of concurrent and co-located satellite measurements of Chl. These satellite measurements are paired with *in situ* pCO_2 to develop a model. As a result, significant uncertainties could exist in the nonlinear pCO_2 models (Zhu et al., 2009; Jo et al., 2012; Hale et al., 2012; Signorini et al., 2013; Parard et al., 2014). Likewise, the sensitivity of the established models to each input variable has rarely been

studied (Lefèvre et al., 2002; Olsen et al., 2004; Zhu et al., 2009; Lohrenz and Cai, 2006; Lohrenz et al., 2010; Borges et al., 2010; Parard et al., 2014). As satellite-derived variables (i.e., SST, SSS, and Chl) have inherent uncertainties (Hu et al., 2009; Cannizzaro et al., 2013), error propagation in model-derived pCO_2 needs to be understood, especially for regions with potentially large uncertainties in these satellite-derived variables. Therefore, in this study, the uncertainties in satellite products used in the pCO_2 model will be quantified to better understand their error propagations.

3. Study area

As the largest semi-enclosed marginal sea of the western Atlantic, the Gulf of Mexico (GOM) encompasses the West Florida Shelf (WFS), Louisiana Shelf, Texas Shelf, Mexican Shelf, the Cuban Shelf, and the open Gulf, with a surface area of 1.6 million km^2, as shown in Figure 1.1. Each of these regions is dominated by different oceanic processes. The WFS is a broad carbonate-based shelf with gentle slope. It is mainly controlled by the coastal currents with little freshwater inputs. The offshore area of the WFS is also affected by the Loop current. The Louisiana Shelf is the most dynamic region of the GOM, with larger amounts of freshwater discharges from the Mississippi-Atchafalaya River system (MARS). Texas Shelf is very narrow and usually receives lots of freshwater from the MARS during spring. Mexican Shelf is also broad which is characterized by the coastal upwelling along the carbonate Campeche Bank. The Cuban shelf is narrow and is mainly affected by the Loop Current in the Florida Strait. The open Gulf is the mainly controlled by the Loop Current, and mesoscale eddies.

The GOM is a very productive marine ecosystem (estimated at 150-300 g C m^{-2} yr^{-1}; Heileman and Rabalais, 2008) and an important global reservoir of biodiversity and biomass of

fish, sea birds, and marine mammals (Widdicombe and Spicer, 2008; Xue et al., 2013), thus, it is important to quantify the role of the GOM in modulating CO_2 flux and ocean acidification through estimating surface pCO_2.

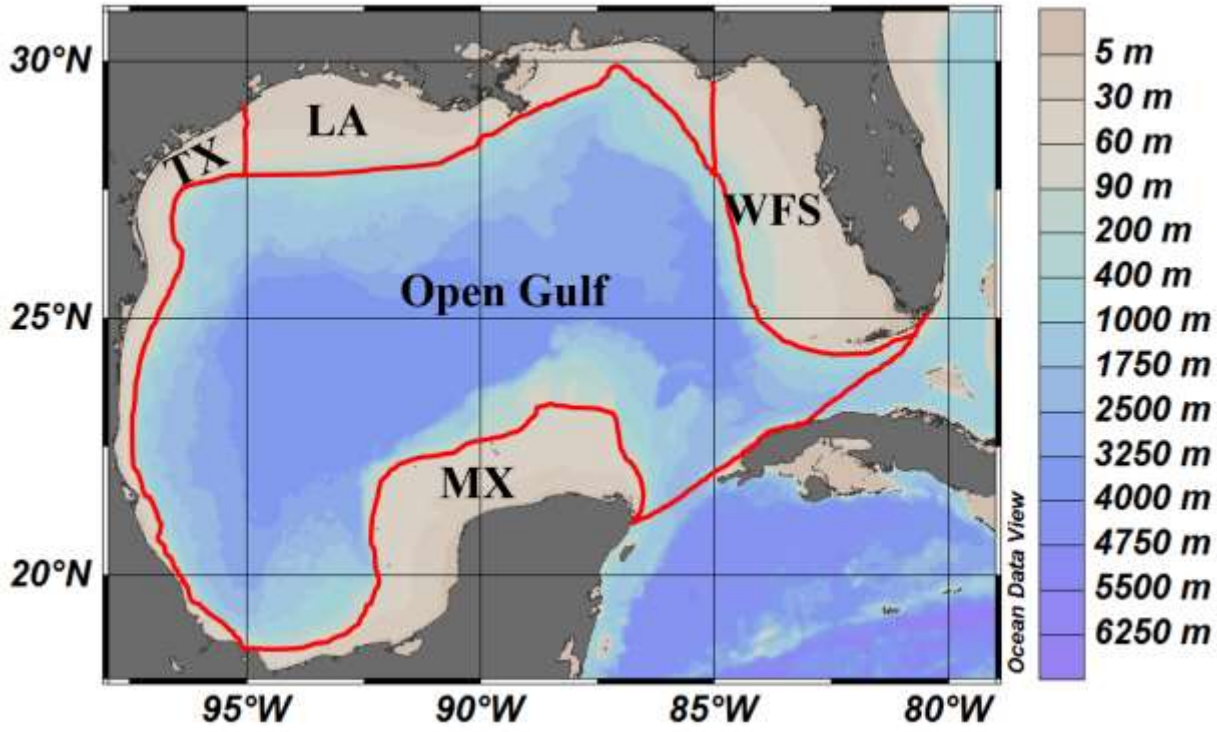

Figure 1.1: Study region of the Gulf of Mexico. The Gulf of Mexico encompasses the West Florida Shelf (WFS), Louisiana Shelf (LA), Texas Shelf (TX), Mexican Shelf (MX), Cuban Shelf, and the open Gulf.

In previous studies, contradictory results about the air-sea CO_2 flux in the GOM were obtained. For instance, based on field measurements, Takahashi et al. (2009) estimated the GOM to be a CO_2 source (CO_2 flux = 0.21 mol C/m^2/year). On the other hand, Xue et al. (2014) estimated the GOM to be a CO_2 sink (CO_2 flux = -0.84 mol C/m^2/year) using a 3-dimentional numerical model. Benway and Coble (2014) also concluded that the GOM is a CO_2 sink but with a smaller flux (CO_2 flux = -0.19 mol C/m^2/year). These discrepancies resulting from these studies show that

new methods need to be developed to better quantify the air-sea CO_2 flux and understand carbon cycling and ocean acidification in the GOM. Synoptic and frequent mapping of surface pCO_2 from satellites should play an important role in developing new methods.

In the northern GOM near the MARS, Lohrenz and Cai (2006) and Lohrenz et al. (2010; 2018) developed empirical pCO_2 models using satellite-derived SST, SSS and Chl. However, due to the complexities and dynamics of the northern GOM waters, these models all showed relatively large errors (i.e., RMSE > 30 μatm). Such errors would introduce large uncertainties in the quantification of air-sea CO_2 flux. Thus, model improvements are needed. In other GOM waters, uncertainties are greater because there are no satellite pCO_2 models or data products available.

4. Objectives

The overarching goals of this research are to advance satellite remote sensing technology by developing surface pCO_2 models and data products for most of the GOM waters, and to improve our understanding of the mechanisms and dominant factors in controlling surface pCO_2. Towards these goals, the specific research objectives are:

1) Develop satellite-based surface pCO_2 models and data products for single-process dominated subregions of the GOM, and quantify the sensitivities of the pCO_2 algorithms to the input environmental variables.

2) Quantify the oceanic processes in controlling surface pCO_2 in the GOM, analyze the relationships between environmental variables and surface pCO_2, and understand the mechanisms of seasonal and interannual variations of surface pCO_2 and its driving factors.

3) Develop an improved SSS model and data products for most GOM waters, and quantify the sensitivities of the SSS model to the input variables.

4) Develop a unified pCO_2 model and data products for the GOM waters, and quantify the sensitivities of the pCO_2 model to the input environmental variables.

5) Quantify the temperature and non-temperature effects on surface pCO_2 at different latitudes, analyze the dominant controls and the corresponding the driving factors of surface pCO_2.

5. Data sources

5.1. Field data

In the years between 2002 and 2017, over 220 cruise surveys have been conducted to collect flow-through surface pCO_2 data during different seasons in the GOM as well as one buoy time series data from the Coastal Mississippi Buoy. Most of these pCO_2 data were obtained from the NOAA National Centers for Environmental Information (NCEI) (https://www.nodc.noaa.gov/ocads/), and several cruise data were obtained from University of Columbia, Texas A andM University, and University of Delaware. All these surface pCO_2 data sources were compiled and quality controlled for the development of surface pCO_2 remote sensing algorithms in this research. Details of these data can be found in Appendixes of A, B, and D. It should be clarified that data collected before July 2002 were not used mainly because there is no MODIS data available for that period.

In addition to surface pCO_2, SSS was also measured and collected in all the field surveys mentioned above. To develop the SSS remote sensing algorithm for the GOM, the SSS data

collected from these field surveys was compiled and quality controlled. Other cruises that measured SSS but not surface pCO_2 were also used. Specifically, ship-based cruise data collected in the GOM by College of Marine Science University of South Florida, Florida Fish and Wildlife Conservation Commission (FWC), and buoy-based time series data collected in the GOM from NOAA National Data Buoy Center (NDBC) buoys were also compiled and quality controlled, and merged with the SSS datasets from the pCO_2 data surveys. Details of these data can be found in Appendix C.

To analyze the driving mechanisms of surface pCO_2 in different coastal ocean environments, *in situ* surface pCO_2 time series data collected from buoys located at different latitudes along the coasts of U. S. and its territories were compiled and quality controlled. These data were obtained from the NOAA NCEI. Details of these can be found in Appendix E.

5.2. Satellite data

NASA standard daily Level-2 data products (version R2014.0) for the period of Jul. 2002 – Dec. 2017 with a spatial resolution of ~1 km were downloaded from the NASA Goddard Space Flight Center (GSFC) (https://oceancolor.gsfc.nasa.gov/). These Level-2 data products were derived from measurements by the Moderate Resolution Imaging Spectroradiometer (MODIS) on the Aqua satellite, and they included Chl, SST, and spectral remote sensing reflectance (Rrs, sr^{-1}) in 7 bands between 412 and 678 nm. The spectral Rrs data were used to calculate K_d using the semi-analytical algorithm developed by Lee et al. (2005). The MODIS-derived environmental variables including Chl, K_d, SST, and SSS were used as inputs for the development of pCO_2 remote sensing algorithms. The spectral Rrs data and SST were used to develop the SSS remote sensing algorithm.

6. Approach and dissertation structure

This dissertation is arranged in chapters that detail the research conducted to fulfill these objectives. Chapters 2 and 3 focus on the estimation of surface pCO_2 from MODIS in single-process dominated regions of the GOM: the WFS and the northern GOM, respectively (Objective 1). For the WFS, a multi-variate nonlinear regression (MNR) model is developed to estimate surface pCO_2 from MODIS, and in the northern GOM, a previously developed mechanistic semi-analytical algorithm (MeSAA) is evaluated and locally-tuned, and compared with the performance of regression-based models. For both regions, the sensitivity of the developed pCO_2 models to the input environmental variables and their relationships are analyzed. The MeSAA model is developed through quantifying different oceanic processes that affect surface pCO_2 variations (Objective 2). The driving mechanisms of the seasonal and interannual variations of surface pCO_2 on the WFS are analyzed (Objective 2).

The satellite mapping of surface pCO_2 in the northern GOM waters requires the development of SSS data products from ocean color remote sensing (Objective 3). This work is completed using MODIS and SeaWiFS data, as described in Chapter 4. Briefly, a multilayer perceptron neural network (MPNN) is developed to estimate SSS from satellite-derived SST and remote sensing reflectance ($Rrs(\lambda)$, m^{-1}) in the visible bands. The sensitivity of the model to realistic model input errors is analyzed and quantified.

Most of the published satellite-based pCO_2 models are developed for single-process dominated oceanic regions, as described in Chapters 2 and 3. The availability of SSS data products from remote sensing in the GOM (Chapter 4) makes it possible to test the feasibility of developing a unified pCO_2 model for the multi-process dominated GOM (Objective 4). Chapter 5 details the

development of such a unified pCO_2 model for the GOM, which proves the possibility of using the proposed approach for other oceanic regions (e.g., Gulf of Maine). The seasonal and interannual variability of surface pCO_2 in the GOM, and the relationships between pCO_2 and environmental variables, as well as the underlying driving mechanisms, are also analyzed in Chapter 5 (Objective 2).

Chapter 6 details the decomposition of the effects of temperature and non-temperature on surface pCO_2 variations, based on buoy time series data at different latitudes in both open oceans and coastal oceans (Objective 5). The underlying driving mechanisms of the seasonal variations of surface pCO_2 as well as their temperature and non-temperature components are analyzed, where the relationships between surface pCO_2 and environmental variables are also quantified.

Finally, Chapter 7 summarizes the works and findings in the previous chapters, with particular focus on the implications of the dissertation as a whole. Overall implications are presented on both the successes and lessons learned from this work. Furthermore, Chapter 7 also discusses future research directions to broaden the findings of this work and to study CO_2 flux, carbon cycling, and ocean acidification using satellite data.

7. Literature cited

Arruda, R., Calil, P. H., Bianchi, A. A., Doney, S. C., Gruber, N., Lima, I., and Turi, G. (2015). Air-sea CO_2 fluxes and the controls on ocean surface pCO_2 seasonal variability in the coastal and open-ocean southwestern Atlantic Ocean: A modeling study. Biogeosciences, 12(19), 5793-5809.

Bai, Y., Pan, D., Cai, W. J., He, X., Wang, D., Tao, B., and Zhu, Q. (2013). Remote sensing of salinity from satellite-derived CDOM in the Changjiang River dominated East China Sea. Journal of Geophysical Research: Oceans, 118(1), 227-243.

Bai, Y., Cai, W. J., He, X., Zhai, W., Pan, D., Dai, M., and Yu, P. (2015). A mechanistic semi-analytical method for remotely sensing sea surface pCO_2 in river-dominated coastal oceans: A case study from the East China Sea. Journal of Geophysical Research: Oceans, 120(3), 2331-2349.

Bates, N. R., Knap, A. H., and Michaels, A. F. (1998). Contribution of hurricanes to local and global estimates of air-sea exchange of CO_2. Nature, 395 (6697), 58-61.

Bauer, J. E., Cai, W. J., Raymond P. A., Bianchi, T. S., Hopkinson, C. S., and Regnier, P. A. G. (2013). The changing carbon cycle of the coastal ocean. Nature, 504 (7478), 61-70.

Benway, H. M., and Coble, P. G. (2014). Report of the US Gulf of Mexico Carbon Cycle Synthesis Workshop, March 27-28, 2013. Ocean Carbon and Biogeochemistry Program and North American Carbon Program.

Berryman, A. D., Goudiaby, D., and Moore, P. (2008). A Multiple Linear Regression of pCO_2 against Sea-Surface Temperature, Salinity, and Chlorophyll *a* at Station ALOHA and its Potential for Estimate pCO_2 from Satellite Data. Elizabeth City, NC.

Borges, A. V. (2005). Do we have enough pieces of the Jigsaw to integrate CO_2 fluxes in the coastal ocean? Estuaries, 28(1), 3-27.

Borges, A. V., Delille, B., and Frankignoulle, M. (2005). Budgeting sinks and sources of CO_2 in the coastal ocean: Diversity of ecosystem counts. Geophysical Research Letters, 32(14), L14601.

Borges, A. V., Schiettecatte, L. S., Abril, G., Delille, B., and Gazeau, F. (2006). Carbon dioxide in European coastal waters. Estuarine, Coastal and Shelf Science, 70(3), 375-387.

Borges, A., Ruddick, K., Lacroix, G., Nechad, B., Asteroca, R., Rousseau, V., and Harlay, J. (2010). Estimating pCO_2 from remote sensing in the Belgian coastal zone. In ESA Living Planet Symposium: 28 June-2 July 2010, Bergen, Norway.

Cai, W. J., Dai, M., and Wang, Y. (2006). Air-sea exchange of carbon dioxide in ocean margins: A province‐based synthesis. Geophysical Research Letters, 33(12), L12603.

Cai, W. J., Chen, L., Chen, B., Gao, Z., Lee, S. H., Chen, J., Pierrot, D., Sullivan, K., Wang, Y., Hu, X., Huang, W. J., Zhang, Y., Xu, S., Murata, A., Grebmeier, J. M., Jones, E. P., and Zhang, H. (2010). Decrease in the CO_2 uptake capacity in an ice-free Arctic Ocean basin. Science, 1189338, 1-10.

Cannizzaro, J. P., Hu, C., Carder, K. L., Kelble, C. R., Melo, N., Johns, E. M., G. A. Vargo, G. A., and Heil, C. A. (2013). On the accuracy of SeaWiFS ocean color data products on the West Florida Shelf. Journal of Coastal Research, 29(6), 1257-1272.

Chen, L., Xu, S., Gao, Z., Chen, H., Zhang, Y., Zhan, J., and Li, W. (2011). Estimation of monthly air-sea CO_2 flux in the southern Atlantic and Indian Ocean using in-situ and remotely sensed data. Remote sensing of environment, 115(8), 1935-1941.

Chierici, M., Olsen, A., Johannessen, T., Trinañes, J., and Wanninkhof, R. (2009). Algorithms to estimate the carbon dioxide uptake in the northern North Atlantic using shipboard observations, satellite and ocean analysis data. Deep Sea Research Part II: Topical Studies in Oceanography, 56(8-10), 630-639.

Coble, P., Hu, C., Gould Jr, R. W., Chang, G., and Wood, A. M. (2004). Colored Dissolved Organic Matter in the Coastal Ocean: An Optical Tool for Coastal Zone Environmental Assessment and Management. Oceanography, 17(2), 50–59.

Del Vecchio, R., and Blough, N. V. (2004). Spatial and seasonal distribution of chromophoric dissolved organic matter and dissolved organic carbon in the Middle Atlantic Bight. Marine Chemistry, 89(1), 169-187.

Evans, W., Hales, B., Strutton, P. G., Sabine, C. L., and Feely, R. A. (2008). Seasonal Variability in Surface Ocean pCO_2 on the Oregon and Washington Shelf, American Geophysical Union, Fall Meeting 2008, abstract #OS53C-1326.

Fay, A. R., and McKinley, G. A. (2017). Correlations of surface ocean pCO_2 to satellite chlorophyll on monthly to interannual timescales. Global Biogeochemical Cycles, 31(3), 436-455.

Feely, R. A., Doney, S. C., and Cooley, S. R. (2009). Ocean acidification: Present conditions and future changes in a high-CO_2 world. Oceanography, 22(4), 36-47.

Fennel, K., Wilkin, J., Previdi, M., and Najjar, R. (2008). Denitrification effects on air-sea CO_2 flux in the coastal ocean: Simulations for the northwest North Atlantic, Geophysical Research Letters, 35, L24608.

Font, J., Camps, A., Borges, A., Martín-Neira, M., Boutin, J., Reul, N., and Mecklenburg, S. (2010). SMOS: The challenging sea surface salinity measurement from space. Proceedings of the IEEE, 98(5), 649-665.

Friedrich, T., and Oschlies, A. (2009). Neural network-based estimates of North Atlantic surface pCO_2 from satellite data: A methodological study, Journal of Geophysical Research, 114, C03020.

Geiger, E. F., Grossi, M. D., Trembanis, A. C., Kohut, J. T., and Oliver, M. J. (2013). Satellite-derived coastal ocean and estuarine salinity in the Mid-Atlantic. Continental Shelf Research, 63, S235-S242.

Geilfus, N. X., Carnat, G., Papakyriakou, T., Tison, J. L., Else, B., Thomas, H., Shadwick, E., and Delille, B. (2012). Dynamics of pCO_2 and related air-ice CO_2 fluxes in the Arctic coastal zone (Amundsen Gulf, Beaufort Sea). Journal of Geophysical Research: Oceans, 117, C00G10.

Hales, B., Takahashi, T., and Bandstra, L. (2005). Atmospheric CO_2 uptake by a coastal upwelling system. Global Biogeochemical Cycles, 19, GB1009.

Hales, B., Strutton, P. G., Saraceno, M., Letelier, R., Takahashi, T., Feely, R., Sabine, C., and Chavez, F. (2012). Satellite-based prediction of pCO_2 in coastal waters of the eastern North Pacific. Progress in Oceanography, 103, 1-15.

Heileman, S., and Rabalais, N. (2008). Gulf of Mexico LME, XV50. The UNEP Large Marine Ecosystem Report: A perspective on changing conditions in LME's of the World Regional Seas. UNEP Regional Seas Report and Studies: 673-698.

Hu, C., Muller-Karger, F. E., Biggs, D. C., Carder, K. L., Nababan, B., Nadeau, D., and Vanderbloemen, J. (2003). Comparison of ship and satellite bio-optical measurements on the continental margin of the NE Gulf of Mexico. International Journal of Remote Sensing, 24(13), 2597-2612.

Hu, C., Muller-Karger, F., Murch, B., Myhre, D., Taylor, J., Luerssen, R., Moses, C., Zhang, C., Gramer, L., and Hendee, J. (2009). Building an automated integrated observing system to detect sea surface temperature anomaly events in the Florida Keys. IEEE Transactions on Geoscience and Remote Sensing, 47(6), 1607-1620.

Huang, W. J., Cai, W. J., Wang, Y., Hu, X., Chen, B., Lohrenz, S. E., Chakraborty, S., He, R., Brandes, J., and Hopkinson, C. S. (2015). The response of inorganic carbon distributions and dynamics to upwelling-favorable winds on the northern Gulf of Mexico during summer. Continental Shelf Research, 111, 211-222.

Ikawa, H., Faloona, I., Kochendorfer, J., Paw, U., and Oechel, W. C. (2013). Air–sea exchange of CO_2 at a Northern California coastal site along the California Current upwelling system. Biogeosciences, 10(7), 4419-4432.

Jamet, C., Moulin, C., and Lefèvre, N. (2007). Estimation of the oceanic pCO_2 in the North Atlantic from VOS lines in-situ measurements: parameters needed to generate seasonally mean maps, Annales Geophysicae, 25, 2247-2257.

Jo, Y. H., Dai, M., Zhai, W., Yan, X. H., and Shang, S. (2012). On the variations of sea surface pCO_2 in the northern South China Sea: A remote sensing based neural network approach. Journal of Geophysical Research: Oceans, 117, C08022.

Joesoef, A., Huang, W. J., Gao, Y., and Cai, W. J. (2015). Air-water fluxes and sources of carbon dioxide in the Delaware Estuary: spatial and seasonal variability. Biogeosciences, 12(20), 6085-6101.

Joshi, I. D., Ward, N. D., D'Sa, E. J., Osburn, C. L., Bianchi, T. S., and Oviedo-Vargas, D. (2018). Seasonal trends in surface pCO_2 and air-sea CO_2 fluxes in Apalachicola Bay, Florida, from VIIRS ocean color. Journal of Geophysical Research: Biogeosciences, 123, 2466-2484.

Kanwisher, J. (1960). pCO_2 in sea water and its effect on the movement of CO_2 in nature. Tellus, 12(2), 209-215.

Karagali, I., Badger, M., and Sørensen, L. L. (2010). MERIS Ocean Colour Data for the Estimation of Surface Water pCO_2: The Case Studies of Peru and Namibia. In 2010 European Space Agency ESA Living Planet Symposium.

Kleypas, J.A., Feely, R.A., Fabry, V.J., Langdon, C., Sabine, C. L., and Robbins, L. L. (2006). Impacts of Ocean Acidification on Coral Reefs and Other Marine Calcifiers: A Guide for Future Research, report of a workshop held 18-20 April 2005, St. Petersburg, FL, sponsored by NSF, NOAA, and the U.S. Geological Survey, 88 pp.

Kleypas, J. A., and Yates K. K. (2009). Coral reefs and ocean acidification. Oceanography 22(4), 108-117.

Lagerloef, G., Colomb, F. R., Le Vine, D., Wentz, F., Yueh, S., Ruf, C., and Feldman, G. (2008). The Aquarius/SAC-D mission: Designed to meet the salinity remote-sensing challenge. Oceanography, 21(1), 68-81.

Lefèvre, N., and Taylor, A. (2002). Estimating pCO_2 from sea surface temperatures in the Atlantic gyres. Deep Sea Research Part I: Oceanographic Research Papers, 49(3), 539-554.

Lefèvre, N., Aiken, J., Rutllant, J., Daneri, G., Lavender, S., and Smyth, T. (2002). Observations of pCO_2 in the coastal upwelling off Chile: Spatial and temporal extrapolation using satellite data. Journal of Geophysical Research, 107(C6), 3055.

Lefèvre, N., and Taylor, A. (2002). Estimating pCO_2 from sea surface temperatures in the Atlantic gyres. Deep Sea Research Part I: Oceanographic Research Papers, 49(3), 539-554.

Lohrenz, S. E., and Cai, W. J. (2006). Satellite ocean color assessment of air‐sea fluxes of CO_2 in a river-dominated coastal margin. Geophysical Research Letters, 33(1), L01601.

Lohrenz, S. E., Cai, W. J., Chen, F., Chen, X., and Tuel, M. (2010). Seasonal variability in air-sea fluxes of CO_2 in a river-influenced coastal margin. Journal of Geophysical Research: Oceans, 115(C10), C10034.

Lohrenz, S. E., Cai, W. J., Chakraborty, S., Huang, W. J., Guo, X., He, R., Xue, Z., Fennel, K., Howden, S., and Tian, H. (2018). Satellite estimation of coastal pCO_2 and air-sea flux of carbon dioxide in the northern Gulf of Mexico. Remote Sensing of Environment, 207, 71-83.

Lu, Z., Gan, J., and Dai, M. (2012). Modeling seasonal and diurnal pCO_2 variations in the northern South China Sea. Journal of Marine Systems, 92(1), 30-41.

Martz, T. R., DeGrandpre, M. D., Strutton, P. G., McGillis, W. R., and Drennan, W. M. (2009). Sea surface pCO_2 and carbon export during the Labrador Sea spring-summer bloom: An *in situ* mass balance approach. Journal of Geophysical Research: Oceans, 114, C09008.

Marrec, P., Thierry, C., Eric, M., Pascal, M., Marc, V., and Yann, B. (2014, May). Dynamics of air-sea CO2 fluxes based on FerryBox measurements and satellite-based prediction of pCO2 in the Western English Channel. Geophysical Research Abstracts, 16, EGU2014-583.

Marrec, P., Cariou, T., Macé, É., Morin, P., Salt, L. A., Vernet, M., Taylor, B., Paxman, K., and Bozec, Y. (2015). Dynamics of air-sea CO_2 fluxes in the northwestern European shelf based on voluntary observing ship and satellite observations. Biogeosciences, 12(18), 5371-5391.

Moussa, H., Benallal, M. A., Goyet, C., and Lefèvre, N. (2016). Satellite-derived CO_2 fugacity in surface seawater of the tropical Atlantic Ocean using a feedforward neural network. International Journal of Remote Sensing, 37(3), 580-598.

Murata, A., and Takizawa, T. (2002). Impact of a coccolithophorid bloom on the CO_2 system in surface waters of the eastern Bering Sea shelf. Geophysical Research Letters, 29(11), 1547.

Murata, A., Kumamoto, Y., Saito, C., Kawakami, H., Asanuma, I., Kusakabe, M., and Inoue, H. Y. (2002). Impact of a spring phytoplankton bloom on the CO_2 system in the mixed layer of the northwestern North Pacific. Deep Sea Research Part II: Topical Studies in Oceanography, 49(24-25), 5531-5555.

Murata, A. (2006). Increased surface seawater pCO_2 in the eastern Bering Sea shelf: An effect of blooms of coccolithophorid Emiliania huxleyi? Global biogeochemical cycles, 20(4), GB4006.

Nakaoka, S., Telszewski, M., Nojiri, Y., Yasunaka, S., Miyazaki, C., Mukai, H., and Usui, N. (2013). Estimating temporal and spatial variation of ocean surface pCO_2 in the North

Pacific using a self-organizing map neural network technique. Biogeosciences, 10(9), 6093-6106.

Norman, M., Parampil, S. R., Rutgersson, A., and Sahlée, E. (2013). Influence of coastal upwelling on the air–sea gas exchange of CO_2 in a Baltic Sea Basin. Tellus B: Chemical and Physical Meteorology, 65(1), 21831.

Olsen, A., Triñanes, J. A., and Wanninkhof, R. (2004). Sea–air flux of CO_2 in the Caribbean Sea estimated using *in situ* and remote sensing data. Remote Sensing of Environment, 89(3), 309-325.

Ono, T., Saino, T., Kurita, N., and Sasaki, K. (2004). Basin-scale extrapolation of shipboard pCO_2 data by using satellite SST and Chl *a*. International Journal of Remote Sensing, 25(19), 3803-3815.

Orr, J. C., Fabry, V. J., Aumont, O., Bopp, L., Doney, S. C., Feely, R. A., Gnanadesikan, A., Gruber, N., Ishida, A., Joos, F., Key, R. M., Lindsay, K., Maier-Reimer, E., Matear, Patrick Monfray, R., Mouchet, A., Najjar, R. G., Plattner, G. K., Rodgers, K. B., Sabine, C. L., Sarmiento, J. L., Schlitzer, R., Slater, R. D., Totterdell, I. J., Weirig, M. F., Yamanaka, Y., and Yool A (2005). Anthropogenic ocean acidification over the twenty-first century and its impact on calcifying organisms. Nature, 437(7059), 681-686.

Pachauri, R. K., and Meyer, L. A. (2014). Climate Change 2014: Synthesis Report. IPCC, Geneva, Switzerland, 151 pp.

Padhy, P. C., Nayak, R. K., Dadhwal, V. K., Salim, M., Mitra, D., Chaudhury, S. B., Rao, P. R., and Dutt, C. B. S. (2015). Estimation of Partial Pressure of Carbon Dioxide and Air-Sea

Fluxes in Hooghly Estuary Based on In Situ and Satellite Observations. Journal of the Indian Society of Remote Sensing, 44(1), 135-143.

Parard, G., Charantonis, A. A., and Rutgerson, A. (2014). Remote sensing algorithm for sea surface CO_2 in the Baltic Sea. Biogeosci. Discuss, 11, 12255-12294.

Pierrot, D. E. L., and Wallace, D. W. R. (2006). MS Excel Program Developed for CO_2 System Calculations. ORNL/CDIAC-105. Carbon Dioxide Information Analysis Center, Oak Ridge National Laboratory, U. S. Department of Energy, Oak Ridge, Tennessee. Doi: 10.3334/CDIAC/otg.CO2SYS_XLS_CDIAC105a.

Pilson, M. E. (2012). An Introduction to the Chemistry of the Sea. Cambridge University Press. Chapter 7: Carbon Dioxide, 115-176.

Qin, B. Y., Tao, Z., Li, Z. W., and Yang, X. F. (2014). Seasonal changes and controlling factors of sea surface pCO_2 in the Yellow Sea. In IOP Conference Series: Earth and Environmental Science. IOP Publishing, 17(1), 012025.

Qing, S., Zhang, J., Cui, T., and Bao, Y. (2013). Retrieval of sea surface salinity with MERIS and MODIS data in the Bohai Sea. Remote Sensing of Environment, 136, 117-125.

Rangama, Y., Boutin, J., Etcheto, J., Merlivat, L., Takahashi, T., Delille, B., Frankignoulle, M., and Bakker, D. C. (2005). Variability of the net air-sea CO_2 flux inferred from shipboard and satellite measurements in the Southern Ocean south of Tasmania and New Zealand, Journal of Geophysical Research, 110, C09005.

Reynaud, S., Leclercq, N., Romaine-Lioud, S., Ferrier-Pagés, C., Jaubert, J., and Gattuso, J. P. (2003). Interacting effects of CO_2 partial pressure and temperature on photosynthesis and calcification in a scleractinian coral. Global Change Biology, 9(11), 1660-1668.

Sabine, C. L., Feely, R. A., Gruber, N., Key, R. M., Lee, K., Bullister, J. L., Wanninkhof, R., Wong, C. S., Wallace, D. W. R., Tilbrook, B., Millero, F. J., Peng, T., Kozyr, A., Ono, T., and Rios, A. F. (2004). The oceanic sink for anthropogenic CO_2. Science, 305 (5682), 367-371.

Salisbury, J. E., Vandemark, D., Hunt, C. W., Campbell, J. W., McGillis, W. R., and McDowell, W. H. (2008). Seasonal observations of surface waters in two Gulf of Maine estuary-plume systems: Relationships between watershed attributes, optical measurements and surface pCO_2. Estuarine, Coastal and Shelf Science, 77(2), 245-252.

Sarma, V. V. S. S. (2003). Monthly variability in surface pCO_2 and net air-sea CO_2 flux in the Arabian Sea. Journal of Geophysical Research: Oceans, 108(C8), 3255.

Sarma, V. V. S. S., Saino, T., Sasaoka, K., Nojiri, Y., Ono, T., Ishii, M., Inoue, H. Y., and Matsumoto, K. (2006). Basin-scale pCO_2 distribution using satellite sea surface temperature, Chl *a*, and climatological salinity in the North Pacific in spring and summer. Global biogeochemical cycles, 20(3), GB3005.

Schneider, B., Kaitala, S., and Maunula, P. (2006). Identification and quantification of plankton bloom events in the Baltic Sea by continuous pCO_2 and chlorophyll-a measurements on a cargo ship. Journal of Marine Systems, 59(3-4), 238-248.

Shadwick, E. H., Thomas, H., Comeau, A., Craig, S. E., Hunt, C. W., and Salisbury, J. E. (2010). Air-Sea CO_2 fluxes on the Scotian Shelf: Seasonal to multi-annual variability. Biogeosciences, 7(11), 3851-3867.

Shadwick, E. H., Thomas, H., Azetsu-Scott, K., Greenan, B. J., Head, E., and Horne, E. (2011). Seasonal variability of dissolved inorganic carbon and surface water pCO_2 in the Scotian Shelf region of the Northwestern Atlantic. Marine Chemistry, 124(1-4), 23-37.

Signorini, S. R., Mannino, A., Najjar, R. G., Friedrichs, M. A., Cai, W. J., Salisbury, J., Wang, Z. A., Thomas, H., and Shadwick, E. (2013). Surface ocean pCO_2 seasonality and sea-air CO_2 flux estimates for the North American east coast. Journal of Geophysical Research: Oceans, 118(10), 5439-5460.

Solomon, S., Qin, D., Manning, M., Chen, Z., Marquis, M., Averyt, K. B., Tignor, M., and Miller H. L. (2007). Climate Change 2007: The Physical Science Basis, Contribution of Working Group I to the Fourth Assessment Report of the Intergovernmental Panel on Climate Change. Cambridge Univ. Press, New York, 129-336.

Song, X., Bai, Y., Cai, W. J., Chen, C. T. A., Pan, D., He, X., and Zhu, Q. (2016). Remote Sensing of Sea Surface pCO_2 in the Bering Sea in Summer Based on a Mechanistic Semi-Analytical Algorithm (MeSAA). Remote Sensing, 8(7), 558.

Stephens, M. P., Samuels, G., Olson, D. B., Fine R. A., and Takahashi T. (1995). Sea-air flux of CO_2 in the North Pacific using shipboard and satellite data, Journal of Geophysical Research, 100(C7), 13571-13583.

Takahashi, T., Sutherland, S. C., Sweeney, C., Poisson, A., Metzl, N., Tilbrook, B., Bates, N., Wanninkhof, R., Feely, R. A., Sabine, C., Olafsson, J., and Nojiri, Y. (2002). Global sea-

air CO_2 flux based on climatological surface ocean pCO_2, and seasonal biological and temperature effects. Deep Sea Research Part II: Topical Studies in Oceanography, 49(9-10), 1601-1622.

Takahashi, T., Sutherland, S. C., Wanninkhof, R., Sweeney, C., Feely, R. A., Chipman, D. W., Hales, B., Friederich, G., Chavez, F., Sabine, C., Watson, A., Bakker, D. C. E., Schuster, U., Metzl, N., Yoshikawa-Inoue, H., Ishii, M., Midorikawa, T., Nojiri, Y., Körtzinger, a., Steinhoff, t., Hoppema, M., Olafsson, J., Arnarson, T. S., Tilbrook, B., Johannessen, T., Olsen, A., Bellerby, R., Wong, C. S., Delille, B., Bates, N. R., and de Baar, H. J. W. (2009). Climatological mean and decadal change in surface ocean pCO_2, and net sea–air CO_2 flux over the global oceans. Deep Sea Research Part II: Topical Studies in Oceanography, 56(8-10), 554-577.

Tao, Z., Qin, B., Li, Z., and Yang, X. (2012). Satellite observations of the partial pressure of carbon dioxide in the surface water of the Huanghai Sea and the Bohai Sea. Acta Oceanologica Sinica, 31(3), 67-73.

Telszewski, M., Chazottes, A., Schuster, U., Watson, A. J., Moulin, C., Bakker, D. C. E., González-Dávila, M., Johannessen, T., Körtzinger, A., Lüger, H., Olsen, A., Omar, A., Padin, X. A., Ríos, A. F., Steinhoff, T., Santana-Casiano, M., Wallace, D. W. R., and Wanninkhof, R. (2009). Estimating the monthly pCO_2 distribution in the North Atlantic using a self-organizing neural network. Biogeosciences, 6, 1405-1421

Tseng, C. M., Liu, K. K., Gong, G. C., Shen, P. Y., and Cai, W. J. (2011). CO_2 uptake in the East China Sea relying on Changjiang runoff is prone to change. Geophysical Research Letters, 38(24), L24609.

Turk, D., Book, J. W., and McGillis, W. R. (2013). pCO_2 and CO_2 exchange during high bora winds in the Northern Adriatic. Journal of Marine Systems, 117, 65-71.

Vandemark, D., Salisbury, J. E., Hunt, C. W., Shellito, S. M., Irish, J. D., McGillis, W. R., Sabine, C. L., and Maenner, S. M. (2011). Temporal and spatial dynamics of CO_2 air-sea flux in the Gulf of Maine. Journal of Geophysical Research: Oceans, 116, C01012.

Vandermeulen, R. A., Arnone, R., Ladner, S., and Martinolich, P. (2014). Estimating sea surface salinity in coastal waters of the Gulf of Mexico using visible channels on SNPP-VIIRS. International Society for Optics and Photonics, 9111, 911109.

Wanninkhof, R., Olsen, A., and Trinanes J. (2007). Air-Sea CO_2 Fluxes in the Caribbean Sea from 2002-2004, Journal of Marine Systems, 66, 272-284.

Weiss, R. F. (1974). Carbon dioxide in water and seawater: the solubility of a non-ideal gas, Marine chemistry, 2, 203-215.

Widdicombe, S., and Spicer J. I. (2008). Predicting the impact of ocean acidification on benthic biodiversity: What can animal physiology tell us? Journal of Experimental Marine Biology and Ecology, 366, 187-197.

Wipf, J., Palacios, S. L., and Kudela, R. M. (2012). Sink or Source? Evaluation of the CO_2 Air-Sea Flux in the Santa Barbara Channel Using Remote-Sensing Data. American Geophysical Union, Fall Meeting 2012, abstract #B13F-07.

Xue, Z., He, R., Fennel, K., Cai, W. J., Lohrenz, S., and Hopkinson, C. (2013). Modeling ocean circulation and biogeochemical variability in the Gulf of Mexico. Biogeosciences, 10(11), 7219-7234.

Xue, Z., He, R., Fennel, K., Cai, W. J., Lohrenz, S., Huang, W. J., and Tian, H. (2014). Modeling pCO_2 variability in the Gulf of Mexico, Biogeosciences Discussions, 11(8), 12673-12695.

Xue, L., Cai, W. J., Hu, X., Sabine, C., Jones, S., Sutton, A.J., Jiang, L. Q., and Reimer, J. J. (2016). Sea surface carbon dioxide at the Georgia time series site (2006-2007): Air-sea flux and controlling processes. Progress in Oceanography, 140, 14-26.

Zhao, J., Temimi, M., and Ghedira, H. (2017). Remotely sensed sea surface salinity in the hyper-saline Arabian Gulf: Application to landsat 8 OLI data. Estuarine, Coastal and Shelf Science, 187, 168-177.

Zhu, Y., Shang, S., Zhai, W., and Dai, M. (2009). Satellite-derived surface water pCO_2 and air–sea CO_2 fluxes in the northern South China Sea in summer. Progress in Natural Science, 19(6), 775-779.

CHAPTER 2:

ESTIMATING SURFACE *P*CO2 IN SINGLE-PROCESS DOMINATED REGION FROM SATELLITES: THE WEST FLORIDA SHELF

Note to Reader

This chapter have been previously published in *Continental Shelf Research*, 2016, 128: 10-25, and have been reproduced with permission from Elsevier Publishing.

1. Research overview

Appendix A – Remote estimation of surface pCO_2 on the West Florida Shelf (Chen et al., 2016)

As one of the broadest continental shelves of the U. S., the West Florida Shelf (WFS) should play a big role in modulating CO_2 flux in the Gulf of Mexico (GOM). However, despite significant efforts to collect surface pCO_2 data through numerous ship surveys, synoptic mapping of surface pCO_2 from satellites is available for the WFS. In this study, a multi-variable empirical surface pCO_2 model was firstly developed for satellite mapping of surface pCO_2 over the WFS, with a Root Mean Square Error (RMSE) of < 12 μatm and a R^2 of 0.88 for pCO_2 ranging from 300 to 550 μatm (N = 1,516). This model was based on concurrent MODIS estimates of surface chlorophyll concentrations, diffuse light attenuation at 490 nm, and sea surface temperature. The first spatial and temporal estimate of distributions of surface pCO_2 on the WFS were investigated and discussed in this study. However, while the general approach of empirical regression may work for waters in other

areas of the GOM, model coefficients will most likely need to be empirically determined in a similar fashion.

CHAPTER 3:

ESTIMATING SURFACE pCO_2 IN SINGLE-PROCESS DOMINATED REGION FROM SATELLITES: THE NORTHERN GOM

Note to Reader

This chapter have been previously published in *Continental Shelf Research*, 2017, 151: 94-110, and have been reproduced with permission from Elsevier Publishing.

1. Research overview

Appendix B – Estimating surface pCO_2 in the northern Gulf of Mexico: Which remote sensing model to use? (Chen et al., 2017a)

Various approaches and models have been proposed to remotely estimate surface pCO_2 in the ocean, with variable performance as they were designed for different environments. Among these, a recently developed mechanistic semi-analytical approach (MeSAA) has shown an advantage for its explicit inclusion of physical and biological forcing in the model, yet its general applicability is unknown. Here, with extensive *in situ* measurements of surface pCO_2, the MeSAA was tested in the northern GOM where river plumes dominate the coastal water's biogeochemical properties during summer. Specifically, the MeSAA-predicted surface pCO_2 was estimated by combining the dominating effects of thermodynamics, river-ocean mixing and biological activities on the surface pCO_2. The RMSE (root mean square error) was 22.94 µatm (5.91 %) and R^2 was 0.25 for pCO_2 ranging between 316 and 452 µatm (N=676). A locally-tuned MeSAA and regression

models showed a RMSE of 12.36 µatm (3.14 %) and 10.66 µatm (2.68%), and R^2 of 0.78 and 0.84, respectively. These results suggest that the locally-tuned MeSAA worked better in the river-dominated northern GOM than the original MeSAA, with slightly worse statistics but more meaningful physical and biogeochemical interpretations than the empirical regression model. Because data from abnormal upwelling are not used to train the models, the models are not applicable for waters with strong upwelling, yet the empirical regression approach has the potential to be further tuned to adapt to such cases.

CHAPTER 4:

REMOTE ESTIMATION OF SEA SURFACE SALINITY IN THE GOM

Note to Reader

This chapter have been previously published in *Remote Sensing of Environment*, 2017, 201: 115-132, and have been reproduced with permission from Elsevier Publishing.

1. Research overview

SSS is an important input to pCO_2 remote sensing models, but currently there is no satellite-based SSS data product covering coastal waters with 1-km resolution. Therefore, an important step in developing pCO_2 models is developing a model to estimate SSS from ocean color measurements. This work is presented in Appendix C below.

Appendix C – Estimating sea surface salinity in the northern Gulf of Mexico from satellite ocean color measurements (Chen and Hu, 2017b)

> Sea surface salinity (SSS) is an important parameter to characterize physical and biogeochemical processes, and it is also an important parameter to quantify the surface pCO_2 variation especially in the river-dominated regions, yet its remote estimation in coastal waters has been difficult because satellite sensors designed to "measure" SSS lack sufficient resolution, and higher-resolution ocean color measurements suffer from optical and biogeochemical complexity when used to estimate SSS. In the northern Gulf of Mexico (GOM), this challenge is addressed through modeling, validation, and extensive tests in contrasting environments. Specifically, using extensive SSS datasets collected by many

groups spanning > 10 years and MODIS (Moderate Resolution Imaging Spectroradiometer) and SeaWiFS (Sea-Viewing Wide Field-of-View Sensor) estimated remote sensing reflectance (Rrs(λ), m^{-1}) at 412, 443, 488 (490), 555, and 667 (670) nm and sea surface temperature (SST), a multilayer perceptron neural network-based (MPNN) SSS model has been developed and validated with a spatial resolution of ~1km. The model showed an overall performance of root mean square error (RMSE) = 1.2, with coefficient of determination (R^2) = 0.86, mean bias (MB) = 0.0, and mean ratio (MR) = 1.0 for SSS ranging between ~1 and ~37 (N=3640). The model was thoroughly evaluated under different scenarios with reasonable performance. The sensitivity of the model to realistic model input errors from satellite-derived SST and Rrs was also thoroughly examined, with uncertainties in the model-derived SSS being always < 1 for SSS > 30. The extensive validation, evaluation, and sensitivity test all indicated the robustness of the MPNN model in estimating SSS in most, if not all, coastal waters and offshore plumes in the northern GOM. Thus, the model provided a basis for generating near real-time 1-km resolution SSS maps from satellite measurements. However, the model showed limitations when applied to regions with known algal blooms or upwelling as they both led to low Rrs in the blue bands that may be falsely recognized as caused by low SSS.

CHAPTER 5:

A UNIFIED APPROACH TO ESTIMATE SURFACE OCEAN *P*CO_2 FROM SATELLITE MEASUREMENTS

1. Research overview

With all satellite-derived variables (SST, SSS, Chl, K_d) available as the model inputs, this chapter details the effort in using these variables to develop a unified approach to estimated *p*CO_2 in multi-process dominated regions. The steps and results are all presented in Appendix D below.

Appendix D – A machine learning approach to estimate surface ocean *p*CO_2 from satellite measurements (Chen et al., *submitted*)

> Surface ocean *p*CO_2 is a critical parameter in the quantification of air-sea CO_2 flux, which further plays an important role in quantifying the global carbon budget and understanding ocean acidification. Yet, to date there is no unified approach, let alone unified model, to remotely estimate surface *p*CO_2 in oceanic regions that are dominated by different oceanic processes. In the study area of the Gulf of Mexico (GOM), this challenge is addressed through the evaluation of different approaches, including multi-linear regression (MLR), multi-nonlinear regression (MNR), principle component regression (PCR), decision tree, supporting vector machines (SVMs), multilayer perceptron neural network (MPNN), and random forest based regression ensemble (RFRE). After modeling, validation, and extensive tests under different scenarios, the RFRE model performed the best. The RFRE model showed an overall performance of a root mean square error (RMSE) of 9.1 μatm,

with R^2 of 0.95, a unbiased percentage difference (UPD) of 0.07%, and a mean ratio difference (MRD) of 0.12% for pCO_2 ranging between 145 and 550 µatm. The model, with its original parameterization, has been tested with independent datasets collected over the entire GOM, with satisfactory performance in each case. The sensitivity of the RFRE-based pCO_2 model to input errors of each environmental variable was also thoroughly examined. The extensive validation, evaluation, and sensitivity analysis indicate the robustness of the RFRE model in estimating surface pCO_2 in most, if not all, GOM waters. The RFRE model approach was applied to the Gulf of Maine (a contrasting oceanic region to GOM), with local model training. The results showed significant improvement over other models for that area, suggesting that the RFRE may serve as a robust approach for other regions once sufficient field-measured pCO_2 data are available for model training.

While most results are presented in a submitted manuscript, further analysis of surface pCO_2 climatology and the pCO_2 model sensitivity to input variables (i.e., SST, SSS, Chl, and K_d) is presented below.

Specifically, the monthly pCO_2 maps derived from MODIS between July 2002 and December 2017 were averaged to derive the climatological pCO_2 monthly mean. Meanwhile, the standard deviations of the monthly surface pCO_2, as well as the monthly maxima and minima of surface pCO_2 over the study period were also quantified to express the variations of surface pCO_2 in each month. Figs. 5.1-5.5 are the monthly mean, monthly mean with two standard deviation added, monthly mean with two standard deviations subtracted, monthly maxima, and monthly minima, of surface pCO_2 in the GOM, respectively. These monthly surface pCO_2 maps should represent the typical variation range of surface pCO_2 in each month, and thus can be used as

references during the field surveys of surface pCO_2 in the GOM in the future. It should be noted that, there is some patchiness in the monthly mean pCO_2 maps; specifically where two standard deviation are added (Fig. 5.2), where two standard deviations are subtracted (Fig. 5.3), and monthly maxima (Fig. 5.4) and minima (Fig. 5.5). These extreme high (or low) pCO_2 values are mainly caused by the large variations of the monthly surface pCO_2 from year to year in those regions.

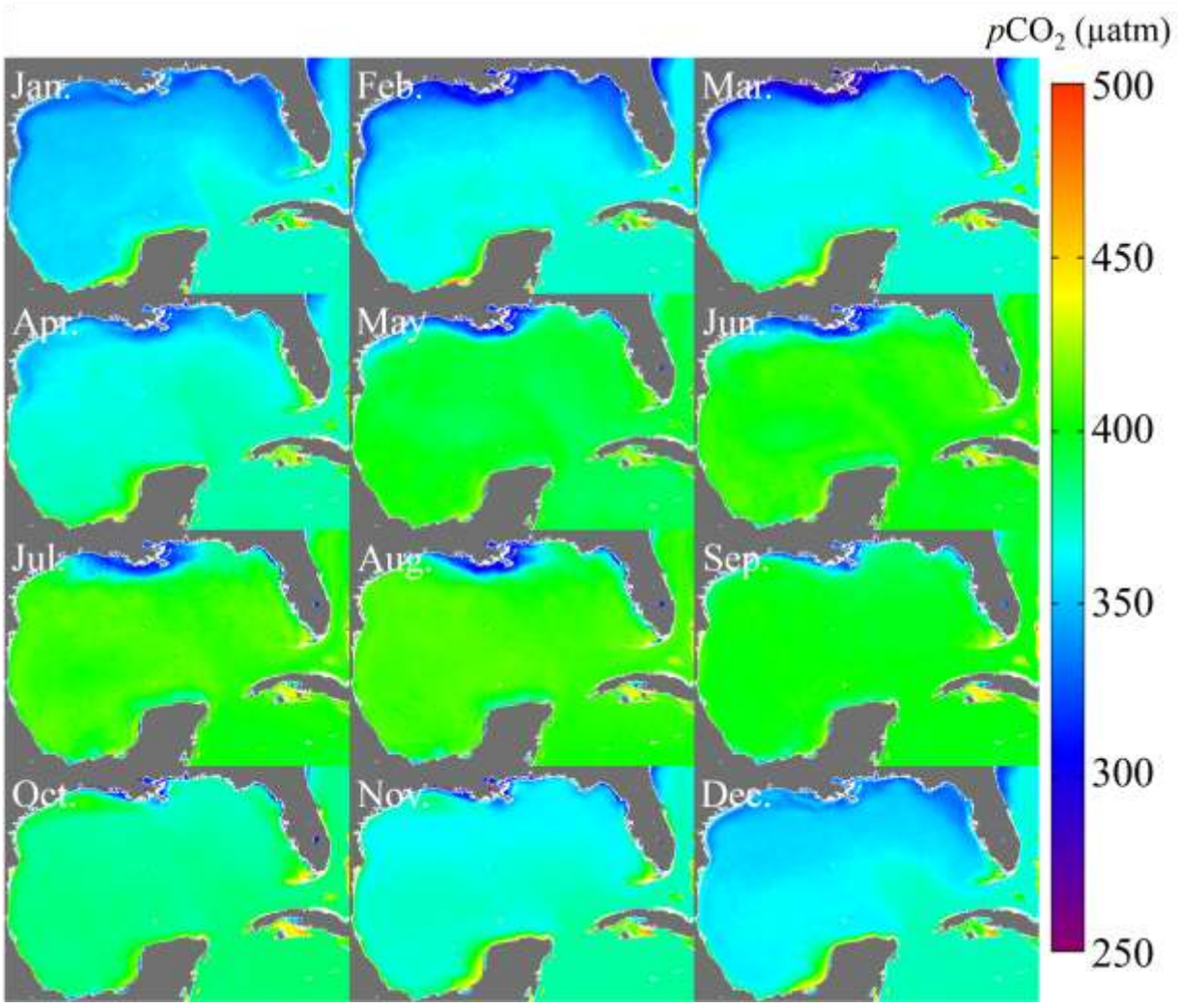

Figure 5.1: Surface pCO_2 climatology in the GOM: monthly mean. They are based on MODIS-derived surface pCO_2 between July 2002 and December 2017.

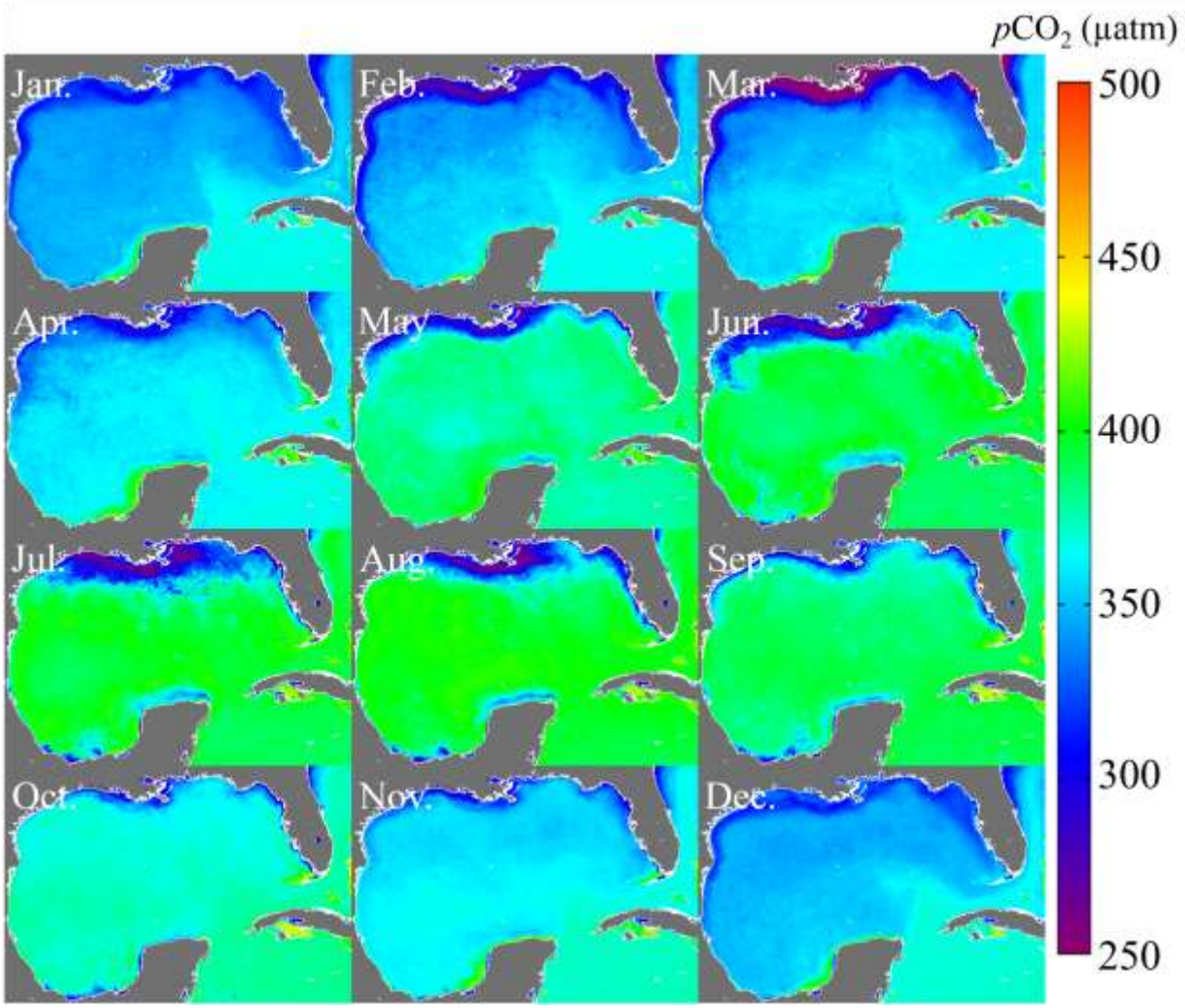

Figure 5.2: Surface pCO_2 climatology in the GOM: monthly mean minus two standard deviations. They are based on MODIS-derived surface pCO_2 between July 2002 and December 2017.

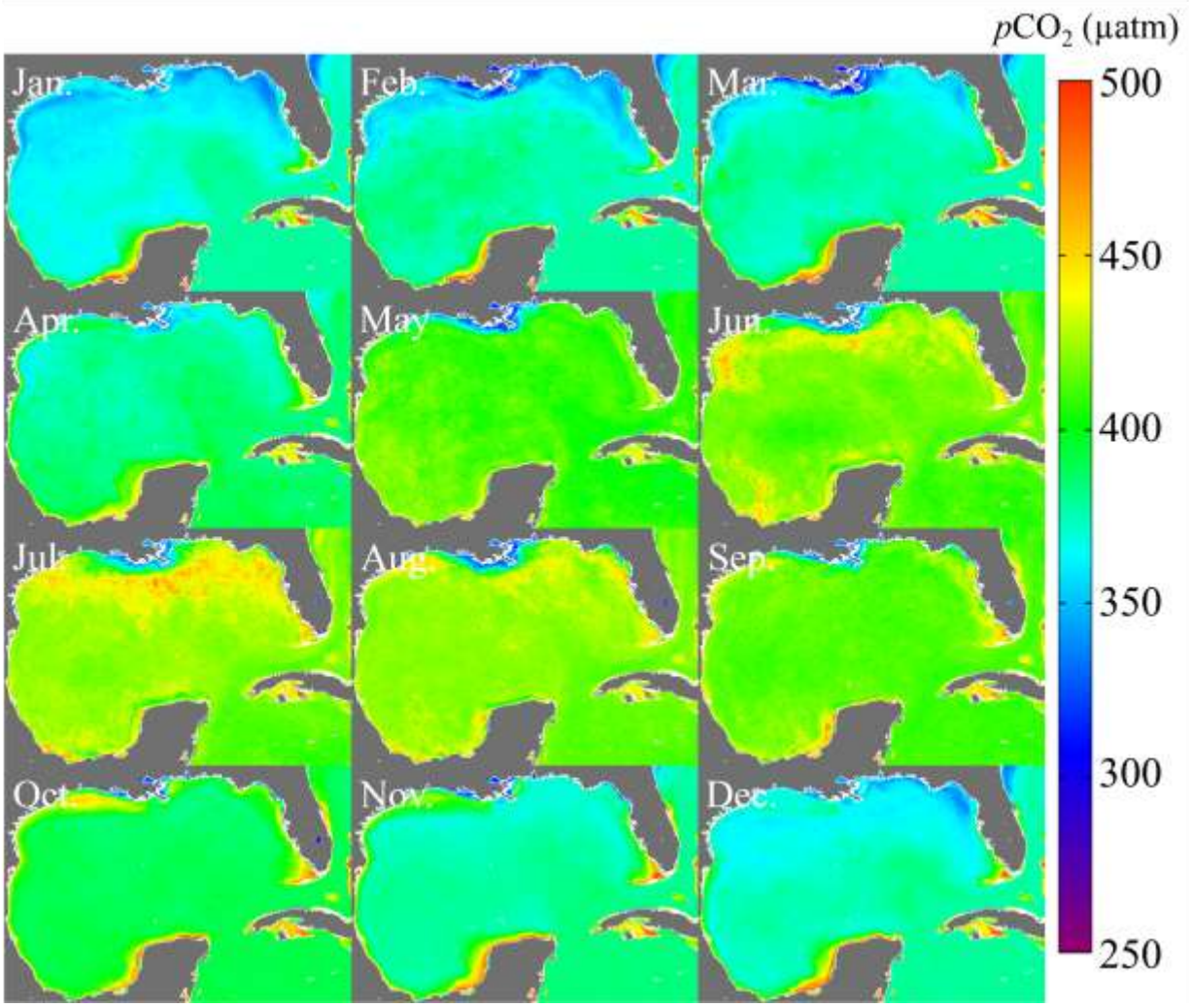

Figure 5.3: Surface pCO_2 climatology in the GOM: monthly mean plus two standard deviations. They are based on MODIS-derived surface pCO_2 between July 2002 and December 2017.

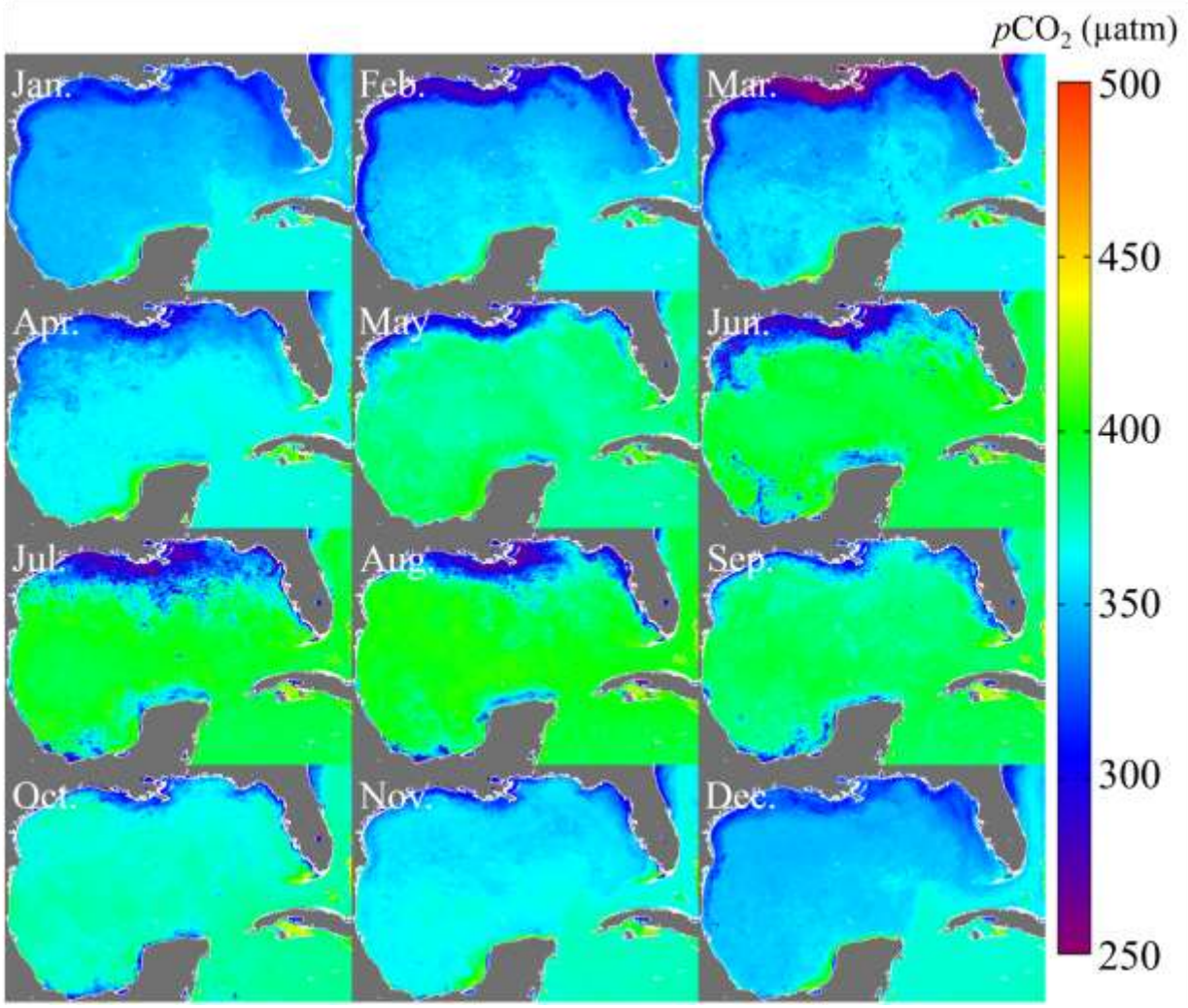

Figure 5.4: Surface pCO_2 climatology in the GOM: monthly minima. They are based on MODIS-derived surface pCO_2 between July 2002 and December 2017.

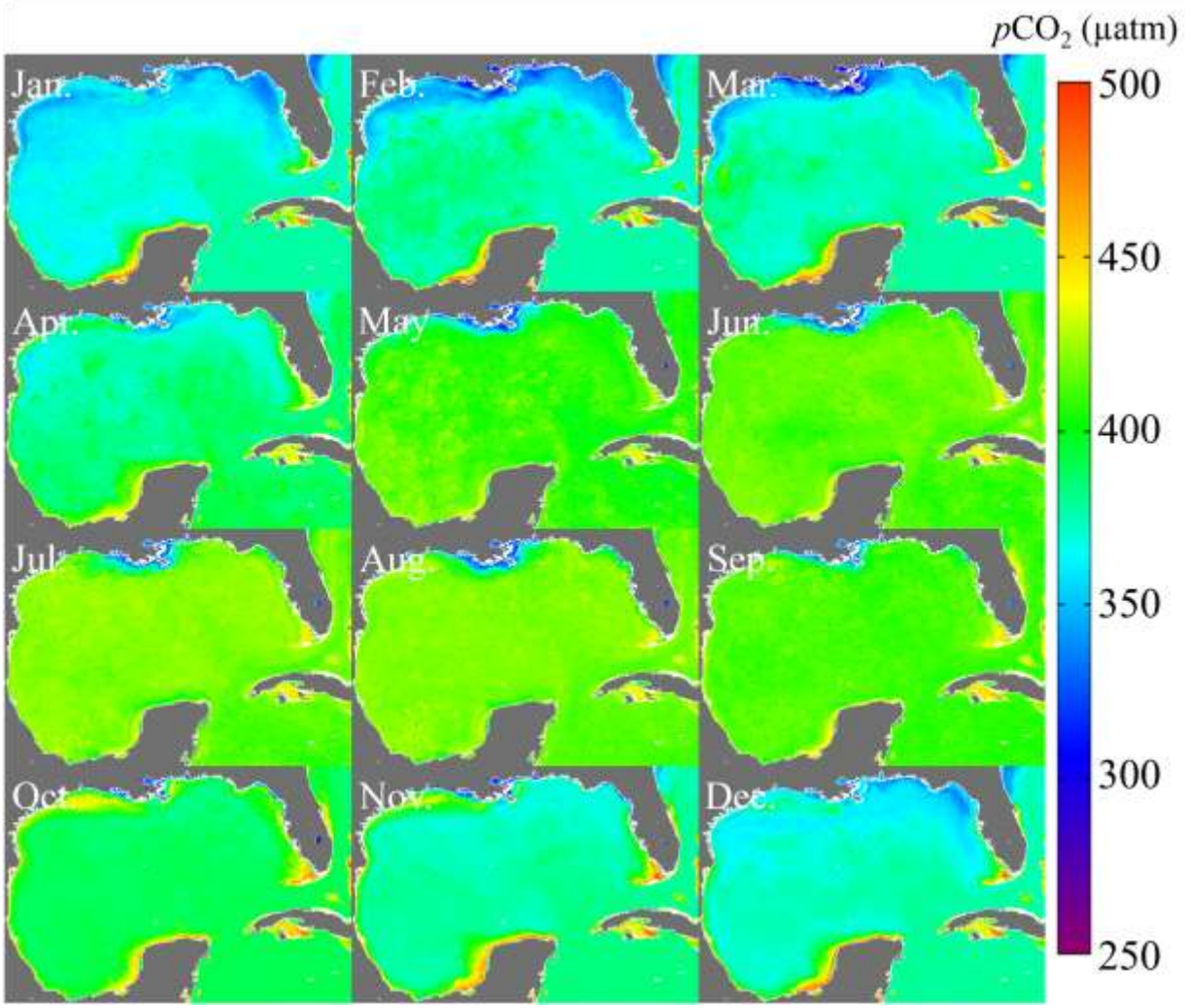

Figure 5.5: Surface pCO_2 climatology in the GOM: monthly maxima. They are based on MODIS-derived surface pCO_2 between July 2002 and December 2017.

In the manuscript, the sensitivity of the pCO_2 remote sensing algorithm to the input variables was quantified based on the training dataset used to develop the algorithm. This sensitivity analysis was conducted by varying one of the input variables by a certain amount while keeping the other variables unchanged (see Appendix D). Here I did a 3-dimensional (3D) sensitivity analysis via data simulation. For example, to examine the model sensitivity to both SST and SSS, a 2-dimensional (2D) arrays for both SST and SSS were generated by varying SST and

SSS within a typical range of each input (i.e., SST within 0~35 ˚C, and SSS within 0~40); thus, each value of SST corresponds to different SSS values in the SSS range, and each pair of SST and SSS values was referred to as a grid cell. Futrther, each grid cell was assigned fixed Chl and K_d values (e.g., Chl = 1.0 mg m^{-3}, Kd = 0.1 m^{-1}). A data matrix was generated, and each grid cell of the data matrix represented a data sample associated with SST, SSS, Chl, and K_d. Finally, the developed pCO_2 model was applied to this data matrix to calculate the surface pCO_2 value for each grid cell. Following the above steps, Fig. 5.6-5.12 are the 3D plots of the sensitivity of the developed pCO_2 model to environmental variable pairs of Chl and K_d, Chl and SSS, Chl and SST, K_d and SSS, K_d and SST, SST and SSS, respectively. These 3D plots allow the visualization of model-predicted pCO_2 varied against any other two of the four environmental variables (i.e., SST, SSS, Chl, and K_d). Similar to the sensitivity analysis in Appendix D, the pCO_2 algorithm is more sensitive to SST and SSS than to Chl and K_d. Surface pCO_2 showed large increase with an increase in SST and SSS, while the changes in surface pCO_2, in response to Chl and K_d variations, were gradual with smaller amplitudes.

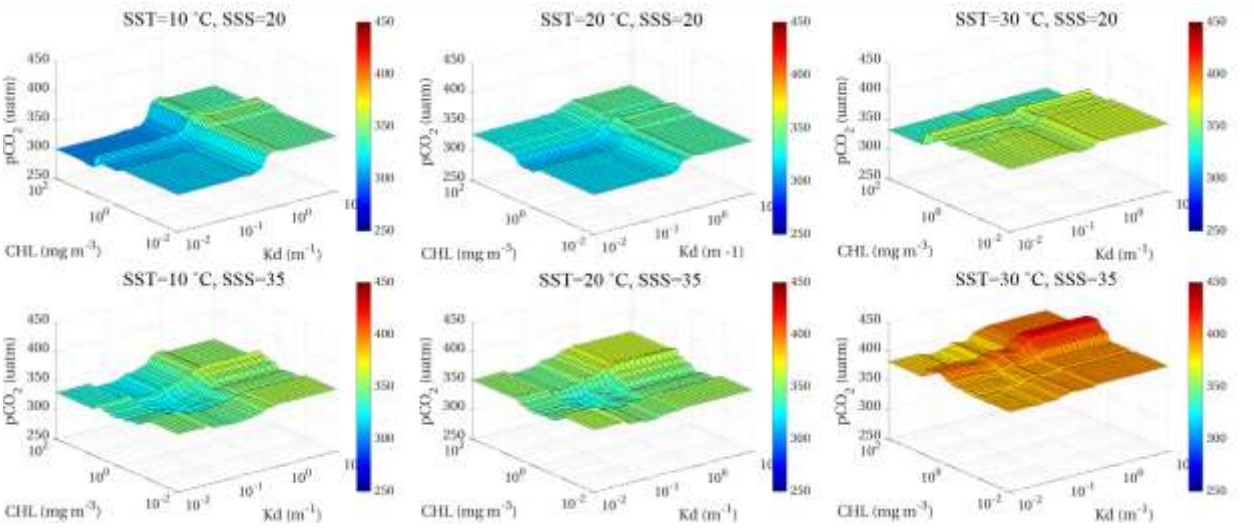

Figure 5.6: Sensitivity of the pCO_2 remote sensing algorithm to Chl and K_d. SST and SSS are fixed with a certain value.

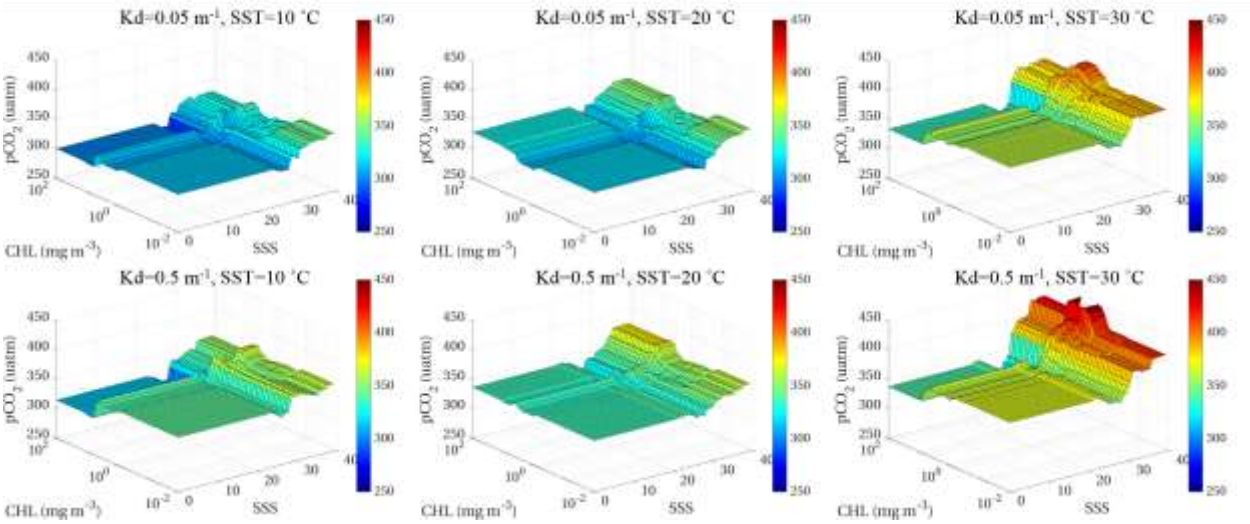

Figure 5.7: Sensitivity of the pCO_2 remote sensing algorithm to Chl and SSS. K_d and SST are fixed with a certain value.

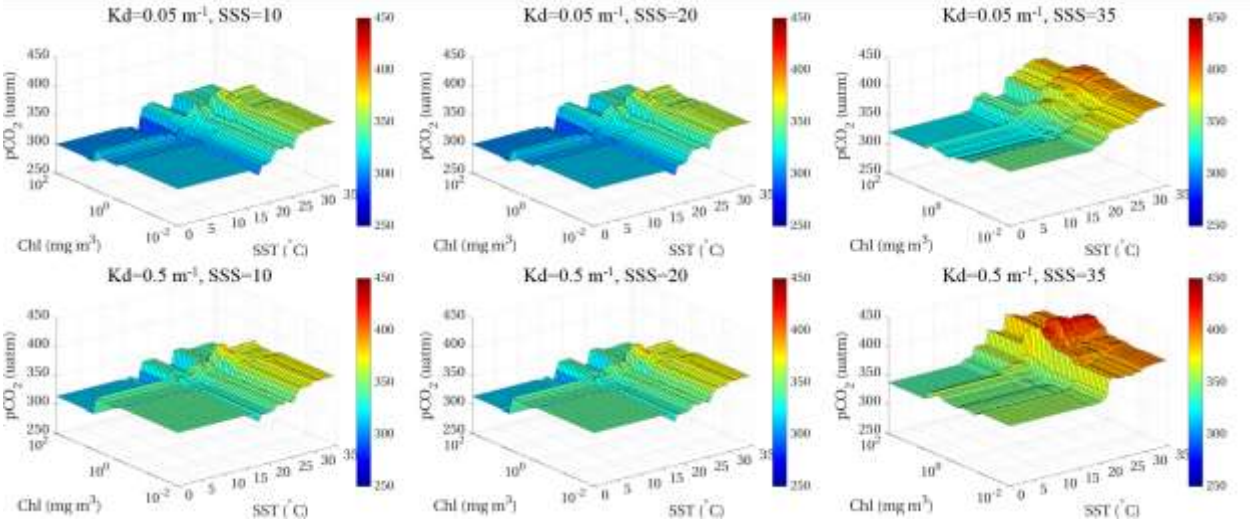

Figure 5.8: Sensitivity of the pCO_2 remote sensing algorithm to Chl and SST. K_d and SSS are fixed with a certain value.

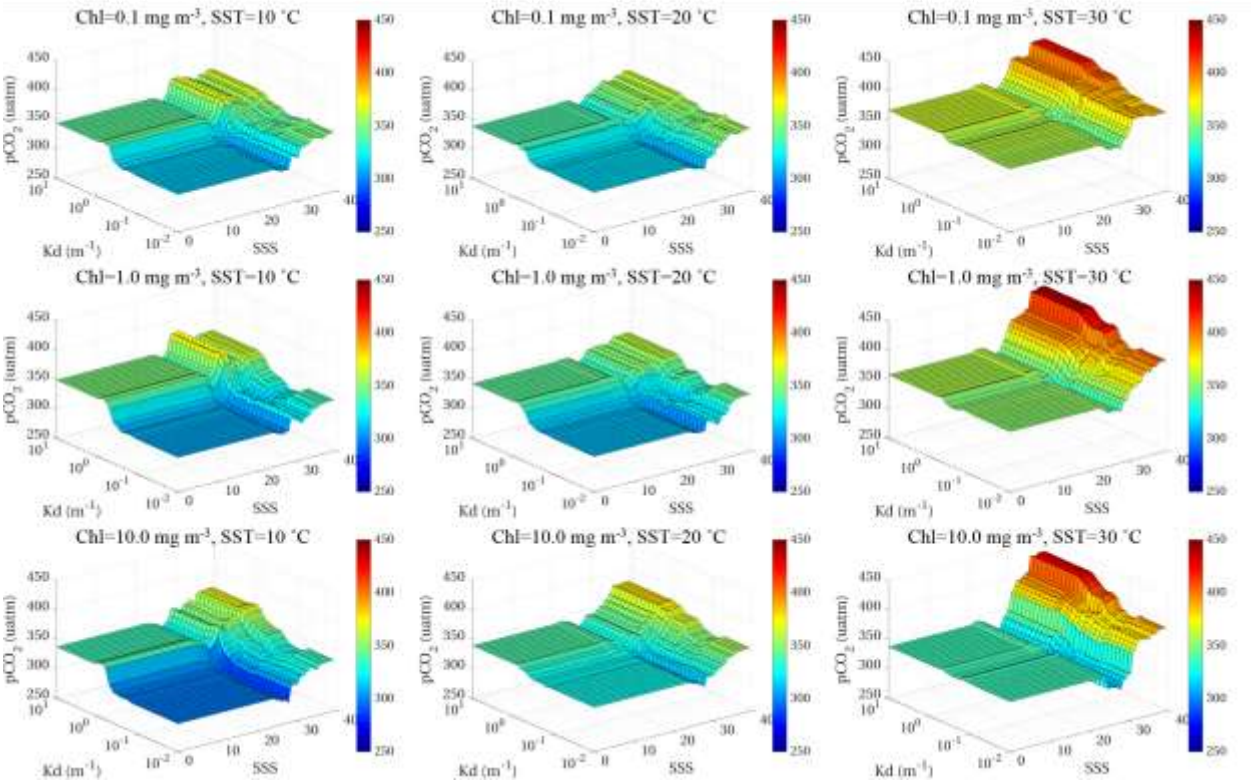

Figure 5.9: Sensitivity of the pCO_2 remote sensing algorithm to K_d and SSS. Chl and SST are fixed with a certain value.

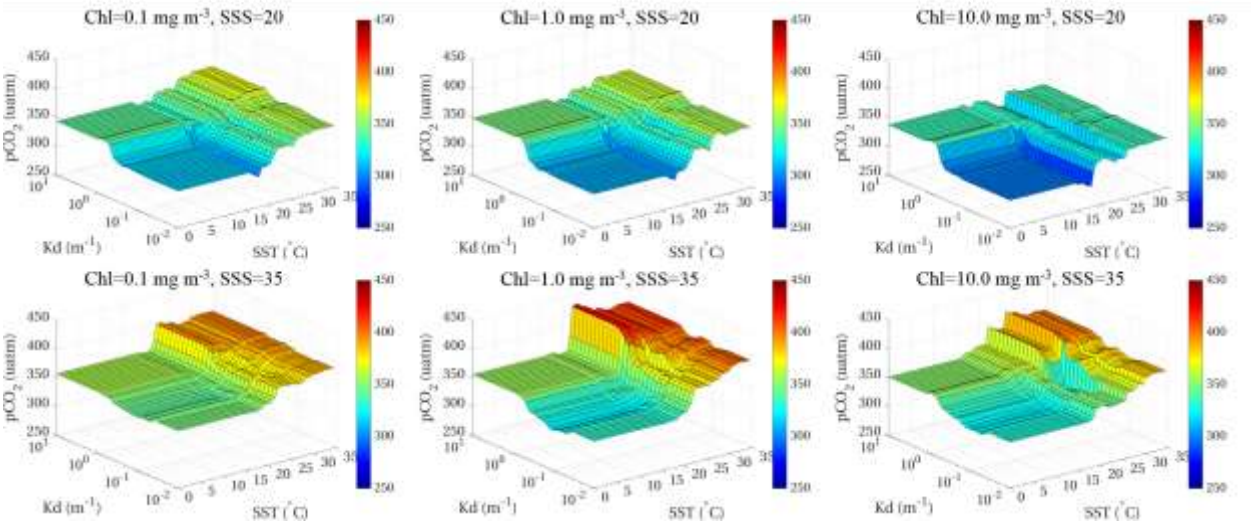

Figure 5.10: Sensitivity of the pCO_2 remote sensing algorithm to K_d and SST. Chl and SSS are fixed with a certain value.

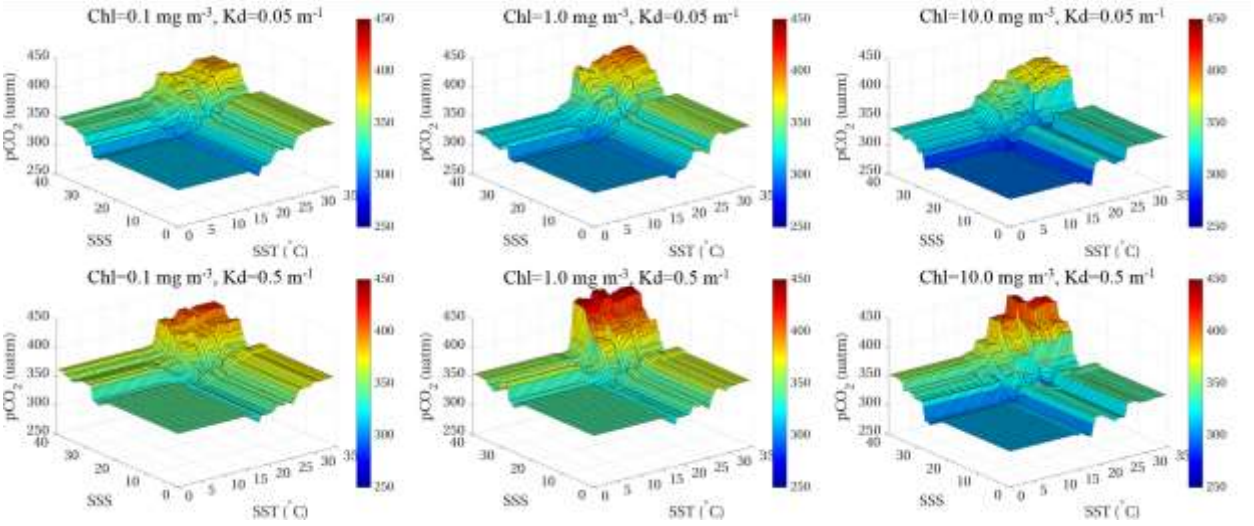

Figure 5.11: Sensitivity of the pCO_2 remote sensing algorithm to SSS and SST. Chl and K_d are fixed with a certain value.

CHAPTER 6:

DOMINANT CONTROLS OF SURFACE OCEAN *P*CO_2 IN COASTAL OCEANS: ANALYSIS OF *IN SITU* TIME SERIES DATA

1. Research overview

Appendix E – Dominant controls of surface water *p*CO_2 in different coastal environments (Chen and Hu, *prepared*)

Atmospheric *p*CO_2 has increased continuously since global industrialization. Satellite measurements allow for synoptic estimation of surface ocean *p*CO_2, which can be further used to quantify air-sea CO_2 flux and to understand ocean acidification under anthropogenic forcing. To improve the accuracy of satellite-derived surface *p*CO_2, the dominant controls of surface *p*CO_2 over seasonal and interannual time scales need to be better understood. As such, a time series of *in situ* *p*CO_2 data, together with other environmental variables from field or satellite measurements along the U. S coasts at different latitudes, are analyzed. On seasonal time scales, surface *p*CO_2 tends to be dominated by the temperature effect (*p*CO_2_T) through SST and wind speed (with exceptions in river-dominated, upwelling-dominated, or coral reef dominated regions) in tropical and subtropical oceanic waters, but by the non-temperature effect (*p*CO_2_nonT) in subpolar regions. At high latitudes, despite the covariations between *p*CO_2_nonT and atmospheric *p*CO_2 on seasonal scales, no statistically significant correlation is found between the two or between *p*CO_2_nonT and the environmental proxies of ocean mixing and biological activities. On interannual time scales, corresponding to the significant

increasing trends in atmospheric pCO_2 over the study period, surface pCO_2 also shows significant increasing trends (again with exceptions in river-dominated, upwelling-dominated, or coral reef dominated regions). In contrast to the dominant controls of the seasonal variations, interannual variability of surface pCO_2 is mainly controlled by the non-temperature effect (through air-sea CO_2 exchange via atmospheric pCO_2) in tropical and subtropical waters but by temperature effect (warming effect of SST) in subpolar regions. In river-dominated and upwelling-dominated coastal ocean systems where biological activities are expected to be intensive, surprisingly, no significant correlation is found between pCO_2_nonT and biological proxies (i.e., Chlorophyll concentration (Chl), diffuse attenuation coefficient of downwelling irradiance (K_d)). This may be mainly attributed to the data scarcities and large uncertainties in the satellite-derived Chl and K_d, and more importantly to the complexities of the dynamic physical and biogeochemical processes in such coastal environments. Therefore, the effects of biological activities (e.g., algal blooms) need to be further investigated.

CHAPTER 7:

RESEARCH IMPACTS AND CONCLUSIONS

1. Summary of findings

Due to the dynamic and complex physical and biogeochemical processes in coastal oceans, large uncertainties (i.e., Root Mean Square Error (RMSE) ≥ 20μatm) exist in satellite-derived surface pCO_2 (e.g., Lohrenz et al., 2010; 2018; Hales et al., 2012; Signorini et al., 2013; Bai et al., 2015). Most of the published satellite-based pCO_2 models are region specific and thus having poor applicability in other regions. In the Gulf of Mexico (GOM), no satellite-based pCO_2 models or data products are available except for a few preliminary attempts in the northern GOM waters around the Mississippi river delta (Lohrenz and Cai, 2006; Lohrenz et al., 2010; 2018), yet these attempts all show relatively large uncertainties (i.e., RMSE > 30 μatm). Here, an empirical surface pCO_2 remote sensing algorithm, based on multi-variate nonlinear regression (MNR), was developed for the West Florida Shelf (WFS) with RMSE of 10.98 μatm and R^2 of 0.86 for pCO_2 between 300 and 550 μatm. (Chen et al., 2016). For the northern GOM waters, a mechanistic semi-analytical approach (MeSAA) was attempted and the same MNR approach used for the WFS was also locally tuned for this region (Chen et al., 2017a). The MNR shows better performance with RMSE of 10.66 μatm and R^2 of 0.84 than the best MeSAA results (RMSE = 12.36 μatm, and R^2 = 0.78) for pCO_2 range of 315~450 μatm. Clearly studies of both the WFS and the northern GOM show greatly reduced errors when compared to the published studies. It should be clarified that, while a multi-variate nonlinear regression model was developed from this work, the MeSAA model was adapted from a previously published work

(Bai et al., 2015) but tuned using local parameterization. While they both appear to be able to estimate surface pCO_2 using satellite measurements, their advantages and disadvantages are discussed in Chen et al. (2017a). Specifically, while the MeSAA model can address the individual processes more explicitly, it also leads to higher uncertainties than the empirical model. On the other hand, because the complex and often unknown processes may be implicitly included in the model coefficients, empirical models often lead to lower uncertainties than MeSAA models, but at the price of being unable to explain the processes explicitly. One limitation of both models is their requirement of SSS as the model input (Chen et al., 2017a), where SSS at 1-km resolution is not readily available from satellite measurements.

To overcome this difficulty, a multilayer perceptron neural network (MPNN) is developed to estimate SSS from MODIS and SeaWiFS (Chen et al., 2017b). This SSS model is mainly based on the optical properties of the colored dissolved organic matter (CDOM) and its relationship with SSS (Vodacek et al., 1997; Hu et al., 2003; Coble et al., 2004; Del Vecchio and Blough, 2004). However, the CDOM characteristics depend on individual rivers, and the CDOM-SSS relationship also varies with space and time (Chen, 1999; Hu et al., 2003; Del Vecchio and Blough, 2004; Bowers and Brett, 2008; Bai et al., 2013; Geiger et al., 2013). To overcome these difficulties, the MPNN model developed in Chen et al. (2017b) bypasses the need of CDOM as an intermediate step, but estimates SSS directly from satellite-derived SST and remote sensing reflectance ($Rrs(\lambda)$, m^{-1}) in the visible bands. This model shows a RMSE of 1.2 PSU and R^2 of 0.86 for a wide range of SSS (i.e., 1~37) with uncertainties always < 1 PSU for SSS > 30, and therefore is being able to generate SSS data products at 1-km resolution to be used in surface pCO_2 models.

Most of the published satellite-based pCO_2 models (e.g., Hales et al., 2012; Signorini et al., 2013), as well as the models described in Chapters 2 and 3, are developed for single-process dominated regions. These regional pCO_2 models are developed using various approaches and different combinations of environmental variables. With the available SSS data products from ocean color remote sensing in the GOM (Chapter 4), the feasibility of developing a unified pCO_2 model for multi-process dominated regions (GOM, Gulf of Maine) is demonstrated (Chapter 5). Such a pCO_2 model leads to spatial and temporal (e.g., seasonal and interannual) distribution patterns of surface pCO_2 in the GOM that can be interpreted as being driven by different physical and biological processes. This unified satellite pCO_2 model has a RMSE of 9.1 µatm and R^2 of 0.95 for pCO_2 between 145 and 550 µatm.

Finally, to improve the accuracy of satellite mapping of surface pCO_2 in the complex coastal waters, the mechanisms and dominant controls of the variations in surface pCO_2 on seasonal and interannual time scales are further investigated using *in situ* time series data along the coasts of U. S. and its territories (Chapter 6). It is found that, in tropical and subtropical coastal waters, the seasonal variations of surface pCO_2 are mainly controlled by SST (with a few exceptions in the river-dominated, upwelling-dominated, and coral-reef-dominated systems), while in the subpolar or high latitude regions, the seasonal variations of surface pCO_2 are mainly dominated by non-temperature effects. In contrast, on interannual time scale, with the increase of the atmospheric pCO_2, surface pCO_2 also shows increasing trends over most of the sites selected for this study. In the tropical and subtropical coastal waters, the increasing trends in surface pCO_2 are mainly attributed to non-temperature effect, while in the subpolar or high latitude regions, they are mainly caused by the effect of SST. More biological data are required to better understand the biological effects on surface pCO_2 variations.

2. Research implications

2.1. Satellite mapping of surface pCO_2

In principle, surface ocean pCO_2 is mainly controlled by four oceanic processes: thermodynamics, ocean mixing, air-sea CO_2 exchange, and biological activities (Fennel et al., 2008; Ikawa et al., 2013; Xue et al., 2016). Therefore, any environmental variables related to these processes can be used to remotely estimate surface pCO_2. In practice, SST, SSS, Chl and K_d are determined to be the best variables to model surface pCO_2 in the GOM. The selection of these variables (except K_d) concurs with many of the published studies (e.g., Lohrenz and Cai, 2006; Lohrenz et al., 2010; 2018; Hales et al., 2012; Signorini et al., 2013; Bai et al., 2015). In this study, K_d is found to be an important biological proxy. More importantly, although the GOM encompasses several sub-regions that are dominated by distinct and complex physical and biogeochemical processes (Figure 1.1), SST, SSS, Chl and K_d are found to be the common environmental variables in affecting surface pCO_2 over the GOM. However, it is known that, in addition to these variables, other variables (e.g., mixed layer depth and wind speed) can also affect surface pCO_2 (e.g., Jamet et al., 2007; Salisbury et al., 2008; Chierici et al. 2009; Shadwick et al., 2010; Nakaoka et al., 2013; Parard et al., 2014). Therefore, in order to apply the developed pCO_2 model on a global scale, further investigations need to be conducted to examine the sufficiency of these four environmental variables (SST, SSS, Chl, and K_d) in estimating surface pCO_2. The significantly improved model performance from this effort suggest that many of the published pCO_2 models may need to be revisited.

Due to the dynamic and complex characteristics of the coastal oceans and prior to this work, the satellite estimated pCO_2 always showed relatively large uncertainties (e.g., RMSE >

20 µatm, or RMSE > 30 µatm in river-dominated regions). Furthermore, due to the lack of sufficient surface pCO_2 data, contradictory results about the air-sea CO_2 flux in the GOM have also been reported (Takahashi et al., 2009; Xue et al., 2014; Benway and Coble, 2014). In this dissertation, the considerable gaps of available synoptic pCO_2 data in the GOM are filled through extensive algorithm development effort. Various approaches, such as multi-nonlinear regression, principle component analysis and regression, neural network, supporting vector machines, regression tree, and random forest, are all thoroughly tested and compared toward an improved accuracy (e.g., RMSE < 10 µatm) in the satellite-derived pCO_2. With the synoptic surface pCO_2 at relatively high spatial and temporal resolutions available from satellites, it is now straightforward to calculate air-sea CO_2 flux in future works. This will lead to an improved understanding of the carbon budget and carbon cycling in the GOM. More importantly, the unified pCO_2 approach demonstrated here shows potentials for other regions (e.g., Gulf of Maine), and thus may greatly facilitate carbon-flux studies in other region.

Finally, with rapidly increasing atmospheric pCO_2 resulting from anthropogenic forcing, it is expected that surface pCO_2 would also show a similar or detectable increasing rate (Takahashi et al., 2009; 2014). However, no such clear trends are observed in either the satellite-derived pCO_2 for the GOM or *in situ* time series of pCO_2 data in the northern GOM (e.g., buoy C3 in Chapter 6). In other words, based on the results presented in this study, currently it is difficult to conclude whether there is a significantly increasing trend in the surface pCO_2 in the GOM, despite the fact that the satellite-based surface pCO_2 does show slight increases after 2012. This is possibly due to 1) the buoy-based time series data may not be representative of the entire GOM, especially for the open GOM waters, and 2) if the model inputs (SST, SSS, Chl, and K_d) do not show apparent trend, the modeled pCO_2 would not show any trend either. Therefore, in

future studies of surface pCO_2, in order to capture the response of surface pCO_2 to the increased atmospheric pCO_2 on interannual time scale, the latter should be used as the model input as well.

2.2. Further implications

The SSS work presented in this dissertation has implications beyond its use in satellite mapping of surface pCO_2. Accurate estimation of SSS from ocean color remote sensing is critical to characterizing many physical and biogeochemical processes in coastal ocean waters (Fennel et al., 2011; Xue et al., 2013). It can not only be used to examine the mixing characteristics between different water masses (e.g., riverine freshwater versus oceanic water) (Hu et al., 2004; Horner-Devine et al., 2015; Yang et al., 2015), but it can also be used to trace the pathways of the terrestrial runoffs into the ocean as well as to characterize the optical properties of the ocean waters related to hypoxia and algal blooms (Rabalais et al., 1996; 2002; Weisberg et al., 2014; 2016; Le et al., 2016). The SSS algorithm developed here (Chen et al., 2017b) may also be implemented within near-real time applications in monitoring water properties in the near future. Likewise, the general approach of using neural network to implicitly address relationships between spectral reflectance and SSS may be applied to other coastal regions to derive SSS from ocean color measurements.

Similar to the neural network approach used on SSS estimation, the approaches proposed in this dissertation to estimate surface pCO_2 may be extended to other regions as well. Although the relative importance of the four processes (thermodynamics, physical ocean mixing, biological activities, air-sea CO_2 exchange) that control the variations of surface pCO_2 may vary in different oceanic ecosystems (e.g., upwelling-dominated, river-dominated, or current-dominated), for example at different latitudes, the proposed machine learning approach used to generate the pCO_2

model for the multi-process dominated GOM waters shows great potential for estimating surface pCO_2 from other oceanic waters (Chapter 5, Chen et al., submitted). At present, due to the lack of synoptic and accurate mapping of surface pCO_2 in coastal margins, it is still difficult to quantify the role of coastal oceans in cycling atmospheric CO_2 as either a source or a sink (e.g., Borges, 2005; Cai et al., 2006). As such, the proposed approach in this dissertation can be implemented and tested on global continental margins as well as in global open-ocean waters to improve our knowledge of global oceanic carbon cycling.

3. Future work

3.1. Research

In the past, controversial results have been reported on whether the GOM acts as a CO_2 source or sink (Takahashi et al., 2009; Xue et al., 2014; Benway and Coble, 2014). Based on the synoptic and long-term satellite-based pCO_2 data products provided in this work, an important next step is to estimate the air-sea CO_2 flux in the GOM waters. Subsequently, the variations of the air-sea CO_2 fluxes in the past years (e.g., at least > 15 years from MODIS) can be analyzed towards a better understanding of the carbon cycling in the GOM.

With the increases of atmospheric pCO_2 resulting from anthropogenic forcing, how the ocean responds to such increases is one of the top concerns in marine carbonate studies (e.g., Doney et al., 2009). Therefore, future works on pCO_2 remote sensing must improve the model capacity in capturing interannual variations surface pCO_2 in response to changes in atmospheric pCO_2. In particular, based on the *in situ* time series data, surface pCO_2 shows clear increasing trends in most of the study sites along the U. S. However, based on the remotely sensed pCO_2 from this work, surface pCO_2 trends in the GOM are less conclusive. Considering the dynamic

and complex oceanic processes in the GOM, it could be possible that surface pCO_2 did not increase much over this study period; it could also be possible that the interannual changes in surface pCO_2 were not captured well by the environmental variables used in the developed pCO_2 models. As such, further investigation and improvement of the developed pCO_2 models are needed, possibly through the use of the atmospheric pCO_2 as one of the input variables.

Finally, to better quantify surface pCO_2 from satellite measurements, the biological effects on surface pCO_2 must be to be investigated in greater detail in the future. At present, Chl and K_d are used as general proxies of the biological activities in modulating surface pCO_2. However, due to the complex processes of the biological activities (e.g., photosynthesis, respiration, and calcification), the signals in Chl and K_d may not co-vary with surface pCO_2 on the same time scales. For example, it was surprising to find that Chl and K_d are insignificant to surface pCO_2 changes (Chapter 5). Such results could be caused by data scarcities and large uncertainties in the satellite-derived Chl and K_d, especially in coastal ocean waters. As such, more work is still needed to study the effects of biological activities on surface pCO_2. In particular, how surface pCO_2 changes, together with other environmental variables (e.g., apparent oxygen utilization, nutrients, dissolved oxygen, and Chl), before, during, and after algal blooms needs to be investigated.

3.2. Product delivery

Surface pCO_2 is a key parameter in assessing air-sea CO_2 flux and understanding ocean acidification. While algorithms and data products are developed in this study, effective delivery of these products to the end-users still requires more efforts, especially for a user groups of different needs. For example, the North American Carbon Program (NACP) is a multi-agency,

multidisciplinary scientific research program which focuses on carbon sources and sinks. The surface pCO_2 data products can be provided to researchers in this program to study carbon cycles. The NOAA Ocean Acidification Program (OAP) is dedicated to improving our understanding of how (and how fast) the ocean chemistry is changing. The interannual variations of the surface pCO_2 in different regions of the GOM (e.g., river-dominated northern GOM, WFS, and open GOM waters), after accounting for the anthropogenic factor, can help to understand the response of the GOM waters to anthropogenic forcing. Further, similar to the NOAA Pacific Marine Environmental Laboratory (PMEL) moored pCO_2 systems (Chapter 6), virtual buoy systems (VBS) presenting surface pCO_2 time series at pre-selected locations of the GOM may be developed (Hu et al., 2014) in coordination with the NOAA PMEL carbon program.

In addition to the major data products (surface pCO_2) developed here, SSS estimated from ocean color satellite measurements is also an important data product for many applications, from water quality monitoring to ecosystem research. Currently, SSS data products have been generated in retrospective mode, which can be shared with many research and environmental groups. Once SSS data products are generated and updated in near real-time, these products may be delivered to various user groups through the common web portal established at the University of South Florida Optical Oceanography Lab (https://optics.marine.usf.edu).

4. Conclusions

Ocean color satellites provide synoptic and frequent measurements of the surface ocean to study the changing ocean chemistry. Integrating satellite data with traditional ship- and buoy-based measurements can provide further insights into understanding of variations of surface pCO_2 and CO_2 flux. Compared with previous efforts in mapping surface pCO_2 from satellite measurements,

the most significant outcome of this research is its use of machine learning to establish models to estimate SSS and surface pCO_2 resulting in greatly reduced uncertainties even for multi-process dominated complex regions. The accurate surface pCO_2 data products enable a better understanding of controlling mechanisms of their spatial, seasonal, and inter-annual variations. The developed datasets of SSS and surface pCO_2 are expected to facilitate more studies of carbon cycling between atmosphere and ocean, for example to better quantify the role of continental margins as potential CO_2 sources or sinks, and to better quantify the ocean's role in absorbing atmosphere CO_2.

5. Literature cited

Bai, Y., Pan, D., Cai, W. J., He, X., Wang, D., Tao, B., and Zhu, Q. (2013). Remote sensing of salinity from satellite-derived CDOM in the Changjiang River dominated East China Sea. Journal of Geophysical Research: Oceans, 118(1), 227-243.

Bai, Y., Cai, W. J., He, X., Zhai, W., Pan, D., Dai, M., and Yu, P. (2015). A mechanistic semi-analytical method for remotely sensing sea surface pCO_2 in river-dominated coastal oceans: A case study from the East China Sea. Journal of Geophysical Research: Oceans, 120(3), 2331-2349.

Benway, H. M., and Coble, P.G. (2014). Report of the U. S. Gulf of Mexico carbon cycle synthesis workshop, March 27-28, 2013, Ocean Carbon and biogeochemistry Program and North American Carbon Program, 67 pp.

Borges, A. V. (2005). Do we have enough pieces of the Jigsaw to integrate CO_2 fluxes in the coastal ocean? Estuaries, 28, 3-27. Doi: 10.1007/BF02732750.

Bowers, D. G., and Brett, H. L. (2008). The relationship between CDOM and salinity in estuaries: an analytical and graphical solution. Journal of Marine systems, 73(1), 1-7.

Cai, W. J., M. Dai, and Y. Wang (2006). Air-sea exchange of carbon dioxide in ocean margins: A province-based synthesis, Geophysical Research Letters, 33, L12603.

Chen, R. F. (1999). *In situ* fluorescence measurements in coastal waters. Organic Geochemistry, 30(6), 397-409.

Chen, S., Hu, C., Byrne, R. H., Robbins, L. L., and Yang, B. (2016). Remote estimation of surface pCO_2 on the West Florida Shelf. Continental Shelf Research, 128, 10-25.

Chen, S., Hu, C., Cai, W. J., and Yang, B. (2017a). Estimating surface pCO_2 in the northern Gulf of Mexico: Which remote sensing model to use? Continental Shelf Research, 151, 94-110.

Chen, S., and Hu, C. (2017b). Estimating sea surface salinity in the northern Gulf of Mexico from satellite ocean color measurements. Remote Sensing of Environment, 201, 115-132.

Chen, S., Hu, C., Wanninkhof, R., Cai, W. J., and Barbero, L. (submitted). A machine learning approach to estimate surface ocean pCO_2 from satellite measurements. Remote Sensing of Environment.

Chierici, M., Olsen, A., Johannessen, T., Trinañes, J., and Wanninkhof, R. (2009). Algorithms to estimate the carbon dioxide uptake in the northern North Atlantic using shipboard observations, satellite and ocean analysis data. Deep Sea Research Part II: Topical Studies in Oceanography, 56(8-10), 630-639.

Coble, P., Hu, C., Gould Jr, R. W., Chang, G., and Wood, A. M. (2004). Colored Dissolved Organic Matter in the Coastal Ocean: An Optical Tool for Coastal Zone Environmental Assessment and Management. Oceanography, 17(2), 50-59.

Del Vecchio, R., and Blough, N. V. (2004). Spatial and seasonal distribution of chromophoric dissolved organic matter and dissolved organic carbon in the Middle Atlantic Bight. Marine Chemistry, 89(1), 169-187.

Doney, S. C., (2010). The Growing Human Footprint on Coastal and Open-Ocean Biogeochemistry. Science, 328(5985), 1512-1516.

Fennel, K., Wilkin, J., Previdi, M., and Najjar, R. (2008). Denitrification effects on air-sea CO_2 flux in the coastal ocean: Simulations for the northwest North Atlantic, Geophysical Research Letters, 35, L24608.

Fennel, K., Hetland, R., Feng, Y., and DiMarco, S. (2011). A coupled physical-biological model of the Northern Gulf of Mexico shelf: model description, validation and analysis of phytoplankton variability. Biogeosciences, 8(7), 1881-1899.

Geiger, E. F., Grossi, M. D., Trembanis, A. C., Kohut, J. T., and Oliver, M. J. (2013). Satellite-derived coastal ocean and estuarine salinity in the Mid-Atlantic. Continental Shelf Research, 63, S235-S242.

Hales, B., Strutton, P. G., Saraceno, M., Letelier, R., Takahashi, T., Feely, R., Sabine, C., and Chavez, F. (2012). Satellite-based prediction of pCO_2 in coastal waters of the eastern North Pacific. Progress in Oceanography, 103, 1-15.

Horner-Devine, A. R., Hetland, R. D., and MacDonald, D. G. (2015). Mixing and transport in coastal river plumes. Annual Review of Fluid Mechanics, 47, 569-594.

Hu, C., Muller-Karger, F. E., Biggs, D. C., Carder, K. L., Nababan, B., Nadeau, D., and Vanderbloemen, J. (2003). Comparison of ship and satellite bio-optical measurements on the continental margin of the NE Gulf of Mexico. International Journal of Remote Sensing, 24(13), 2597-2612.

Hu, C., Chen, Z., Clayton, T. D., Swarzenski, P., Brock, J. C., and Muller-Karger, F. E. (2004). Assessment of estuarine water-quality indicators using MODIS medium-resolution bands: Initial results from Tampa Bay, FL. Remote Sensing of Environment, 93(3), 423-441.

Hu, C., Barnes, B. B., Murch, B., and Carlson, P. R. (2013). Satellite-based virtual buoy system to monitor coastal water quality. Optical Engineering, 53(5), 051402.

Ikawa, H., Faloona, I., Kochendorfer, J., Paw, U., and Oechel, W. C. (2013). Air–sea exchange of CO_2 at a Northern California coastal site along the California Current upwelling system. Biogeosciences, 10(7), 4419-4432.

Jamet, C., Moulin, C., and Lefèvre, N. (2007). Estimation of the oceanic pCO_2 in the North Atlantic from VOS lines in-situ measurements: parameters needed to generate seasonally mean maps. Annales Geophysicae, European Geosciences Union. 25(11), 2247-2257.

Le, C., Lehrter, J. C., Hu, C., and Obenour, D. R. (2016). Satellite-based empirical models linking river plume dynamics with hypoxic area and volume. Geophysical Research Letters, 43, 2693-2699.

Lohrenz, S. E., and Cai, W. J. (2006). Satellite ocean color assessment of air‐sea fluxes of CO_2 in a river-dominated coastal margin. Geophysical Research Letters, 33(1), L01601.

Lohrenz, S. E., Cai, W. J., Chen, F., Chen, X., and Tuel, M. (2010). Seasonal variability in air-sea fluxes of CO_2 in a river-influenced coastal margin. Journal of Geophysical Research: Oceans, 115(C10), C10034.

Lohrenz, S. E., Cai, W. J., Chakraborty, S., Huang, W. J., Guo, X., He, R., Xue Z., Fennel K., Howden S., and Tian, H. (2018). Satellite estimation of coastal pCO_2 and air-sea flux of carbon dioxide in the northern Gulf of Mexico. Remote Sensing of Environment, 207, 71-83.

Nakaoka, S., Telszewski, M., Nojiri, Y., Yasunaka, S., Miyazaki, C., Mukai, H., and Usui, N. (2013). Estimating temporal and spatial variation of ocean surface pCO_2 in the North Pacific using a self-organizing map neural network technique. Biogeosciences, 10(9), 6093-6106.

Parard, G., Charantonis, A. A., and Rutgerson, A. (2014). Remote sensing algorithm for sea surface CO_2 in the Baltic Sea. Biogeosci. Discuss, 11, 12255-12294.

Rabalais, N. N., Turner, R. E., Justic, D., Dortch, Q., Wiseman, W. J., and Gupta, B. K. S. (1996). Nutrient changes in the Mississippi River and system responses on the adjacent continental shelf. Estuaries, 19(2), 386-407.

Rabalais, N. N., Turner, R. E., and Wiseman Jr, W. J. (2002). Gulf of Mexico hypoxia, AKA" The dead zone". Annual Review of ecology and Systematics, 235-263.

Salisbury, J. E., Vandemark, D., Hunt, C. W., Campbell, J. W., McGillis, W. R., and McDowell, W. H. (2008). Seasonal observations of surface waters in two Gulf of Maine estuary-plume systems: Relationships between watershed attributes, optical measurements and surface pCO_2. Estuarine, Coastal and Shelf Science, 77(2), 245-252.

Shadwick, E. H., Thomas, H., Comeau, A., Craig, S. E., Hunt, C. W., and Salisbury, J. E. (2010). Air-Sea CO_2 fluxes on the Scotian Shelf: seasonal to multi-annual variability. Biogeosciences, 7(11), 3851-3867.

Signorini, S. R., Mannino, A., Najjar, R. G., Friedrichs, M. A., Cai, W. J., Salisbury, J., Wang, Z. A., Thomas, H., and Shadwick, E. (2013). Surface ocean pCO_2 seasonality and sea-air CO_2 flux estimates for the North American east coast. Journal of Geophysical Research: Oceans, 118(10), 5439-5460.

Takahashi, T., Sutherland, S. C., Wanninkhof, R., Sweeney, C., Feely, R. A., Chipman, D. W., Hales, B., Friederich, G., Chavez, F., Sabine, C., Watson, A., Bakker, D. C. E., Schuster, U., Metzl, N., Yoshikawa-Inoue, H., Ishii, M., Midorikawa, T., Nojiri, Y., Körtzinger, a., Steinhoff, t., Hoppema, M., Olafsson, J., Arnarson, T. S., Tilbrook, B., Johannessen, T., Olsen, A., Bellerby, R., Wong, C. S., Delille, B., Bates, N. R., and de Baar, H. J. W. (2009). Climatological mean and decadal change in surface ocean pCO_2, and net sea-air CO_2 flux over the global oceans. Deep Sea Research Part II: Topical Studies in Oceanography, 56(8-10), 554-577.

Takahashi, T., Sutherland, S. C., Chipman, D. W., Goddard, J. G., Ho, C., Newberger, T., Sweeney, C., and Munro, D. R. (2014). Climatological distributions of pH, pCO_2, total CO_2,

alkalinity, and $CaCO_3$ saturation in the global surface ocean, and temporal changes at selected locations. Marine Chemistry, 164, 95-125.

Vodacek, A., Blough, N. V., DeGrandpre, M. D., Peltzer, E. T., and Nelson, R. K. (1997). Seasonal variation of CDOM and DOC in the Middle Atlantic Bight: Terrestrial inputs and photooxidation. Limnology and Oceanography, 42(4), 674-686.

Weisberg, R. H., Zheng, L., Liu, Y., Lembke, C., Lenes, J. M., and Walsh, J. J. (2014). Why no red tide was observed on the West Florida Continental Shelf in 2010. Harmful Algae, 38, 119-126.

Weisberg, R. H., Zheng, L., Liu, Y., Corcoran, A. A., Lembke, C., Hu, C., Lenes, J. M., and Walsh, J. J. (2016). Karenia brevis blooms on the West Florida Shelf: A comparative study of the robust 2012 bloom and the nearly null 2013 event. Continental Shelf Research, 120, 106-121.

Xue, Z., He, R., Fennel, K., Cai, W. J., Lohrenz, S., and Hopkinson, C. (2013). Modeling ocean circulation and biogeochemical variability in the Gulf of Mexico. Biogeosciences, 10(11), 7219-7234.

Xue, Z., He, R., Fennel, K., Cai, W. J., Lohrenz, S., Huang, W., and Tian, H. (2014). Modeling pCO_2 variability in the Gulf of Mexico, Biogeosciences Discussions, 11(8), 12673-12695.

Xue, L., Cai, W. J., Hu, X., Sabine, C., Jones, S., Sutton, A. J., Jiang, L. Q., and Reimer, J. J. (2016). Sea surface carbon dioxide at the Georgia time series site (2006–2007): Air-sea flux and controlling processes. Progress in Oceanography, 140, 14-26.

Yang, B., Byrne, R. H., and Wanninkhof, R. (2015). Subannual variability of total alkalinity distributions in the northeastern Gulf of Mexico. Journal of Geophysical Research: Oceans, 120(5), 3805-3816.

APPENDIX A:

REMOTE ESTIMATION OF SURFACE pCO_2 ON THE WEST FLORIDA SHELF

Chen, S., Hu, C., Byrne, R. H., Robbins, L. L., and Yang, B. (2016). Remote estimation of surface pCO_2 on the West Florida Shelf. *Continental Shelf Research, 128, 10-25*.

Continental Shelf Research 128 (2016) 10–25

Contents lists available at ScienceDirect

Continental Shelf Research

journal homepage: www.elsevier.com/locate/csr

Research papers

Remote estimation of surface pCO_2 on the West Florida Shelf

Shuangling Chen[a], Chuanmin Hu[a,*], Robert H. Byrne[a], Lisa L. Robbins[b], Bo Yang[c]

[a] College of Marine Science, University of South Florida, 140 7th Avenue, South, St. Petersburg, FL 33701, USA
[b] U. S. Geological Survey, 600 4th Street, South, St Petersburg, FL 33701, USA
[c] School of Oceanography, University of Washington, Seattle, WA 98105, USA

ARTICLE INFO

Keywords:
Surface pCO_2
Satellite remote sensing
MODIS
Chlorophyll
SST
Kd
WFS

ABSTRACT

Surface pCO_2 data from the West Florida Shelf (WFS) have been collected during 25 cruise surveys between 2003 and 2012. The data were scaled up using remote sensing measurements of surface water properties in order to provide a more nearly synoptic map of pCO_2 spatial distributions and describe their temporal variations. This investigation involved extensive tests of various model forms through parsimony and Principal Component Analysis, which led to the development of a multi-variable empirical surface pCO_2 model based on concurrent MODIS (Moderate Resolution Imaging Spectroradiometer) estimates of surface chlorophyll *a* concentrations (CHL, mg m^{-3}), diffuse light attenuation at 490 nm (Kd_Lee, m^{-1}), and sea surface temperature (SST, °C). Validation using an independent dataset showed a pCO_2 Root Mean Square Error (RMSE) of < 12 µatm and a 0.88 coefficient of determination (R^2) for measured and model-predicted pCO_2 ranging from 300 to 550 µatm. The model was more sensitive to SST than to CHL and Kd_Lee, with a 1 °C change in SST leading to a ~16 µatm change in the predicted pCO_2. Application of the model to the entire WFS MODIS time series between 2002 and 2014 showed clear seasonality, with maxima (~450 µatm) in summer and minima (~350 µatm) in winter. The seasonality was positively correlated to SST (high in summer and low in winter) and negatively correlated to CHL and Kd_Lee (high in winter and low in summer). Inter-annual variations of pCO_2 were consistent with inter-annual variations of SST, CHL, and Kd_Lee. These results suggest that surface water pCO_2 of the WFS can be estimated, with known uncertainties, from remote sensing. However, while the general approach of empirical regression may work for waters from other areas of the Gulf of Mexico, model coefficients need to be empirically determined in a similar fashion.

1. Introduction

Atmospheric CO_2 has increased by 40% since the industrialization era (Sabine et al., 2004; Solomon et al., 2007). Correspondingly, oceanic uptake of CO_2 has resulted in ocean acidification and decreased surface water pH (by ~0.1 units) (Sun et al., 2012; Pachauri and Meyer, 2014), leading to ecological degradation and a decrease of marine biodiversity (Widdicombe and Spicer, 2008; Orr et al., 2005; Feely et al., 2012). Due to large spatial and temporal variations in surface water CO_2 partial pressure (pCO_2), the magnitude and even the sign of air/sea CO_2 fluxes can be highly variable (Takahashi et al., 2002, 2009, 2014; Sarma, 2003; Borges et al., 2005; Hofmann et al., 2011; Sarma et al., 2012; Chen et al., 2013; Wanninkhof et al., 2013). Accurate knowledge of surface pCO_2 distributions is therefore essential to quantify the ocean's role in carbon cycling.

A large number of studies have used field measurements to estimate air-sea CO_2 fluxes for both the open ocean and coastal sites (e.g., Takahashi et al., 2002, 2009, 2014; Tseng et al., 2011; Jiang et al., 2008; Gelfus et al., 2012; Vandemark et al., 2011; Zhai et al., 2005). However, direct field observations are often limited in spatial and temporal coverage. While numerical models have also been used to estimate surface pCO_2 (e.g., Xue et al., 2014; Arruda et al., 2015), model results are strongly influenced by assumed initial conditions and can also be highly model-specific. In contrast, satellite remote sensing can provide frequent synoptic assessments of surface ocean properties, and in view of recent advances in surface pCO_2 algorithm development (e.g., Ono et al., 2004; Sarma et al., 2006; Jamet et al., 2007; Telszewski et al., 2009; Hales et al., 2012; Nakaoka et al., 2013; Signorini et al., 2013; Bai et al., 2015), there is potential for the use of satellite remote sensing to augment direct field assessments of air/sea CO_2 fluxes. Nevertheless, except for two studies that focused on nearshore waters off the Mississippi River delta (Lohrenz and Cai, 2006; Lohrenz et al., 2010), such remote sensing approaches have rarely been applied to major ocean basins such as the Gulf of Mexico (GOM), a semi-enclosed sea of environmental and economic importance.

* Corresponding author.
E-mail address: huc@usf.edu (C. Hu).

http://dx.doi.org/10.1016/j.csr.2016.09.004
Received 30 December 2015; Received in revised form 26 July 2016; Accepted 12 September 2016
Available online 13 September 2016

Nomenclature

CDIAC	Carbon Dioxide Information Analysis Center
CHL	Chlorophyll-a Concentration
GOM	Gulf of Mexico
Kd_Lee	Diffuse light attenuation coefficient at 490 nm
LC	Loop Current
MB	Mean Bias
MLR	Multi-variate Linear Regression
MNR	Multi-variate Nonlinear Regression
MODIS	Moderate Resolution Imaging Spectroradiometer
MR	Mean Ratio
PCA	Principle Component Analysis
PCR	Principle Component Regression
RMSE	Root Mean Square Error
SSS	Sea Surface Salinity
SST	Sea Surface Temperature
USGS	U.S. Geological Survey
WFS	West Florida Shelf

With a surface area of 1.6 million km^2, the GOM encompasses the West Florida Shelf (WFS), Louisiana Shelf, Texas Shelf, Mexican Shelf, and the open Gulf (Robbins et al., 2009; Coble et al., 2010). As one of the most productive areas for fisheries in the world, it is essential habitat for numerous fish and wildlife species, and is likely to be strongly impacted by ocean acidification (Cai, et al., 2011; Wanninkhof et al., 2015). Thus, it is important to quantify the role of the GOM in modulating CO_2 flux (Takahashi et al., 2009). Based on field measurements, Takahashi et al. (2009) estimated the GOM as a CO_2 source with a net flux of about 0.21 mol C/m^2/year. However, with additional field observations, Robbins et al. (2014) reported that the GOM is a CO_2 sink with a net flux near −0.19 mol C/m^2/year. Using a 3-dimensional numerical model, Xue et al. (2014) estimated the GOM as a sink with a flux of −0.84 mol C/m^2/year. Clearly, such discrepancies necessitate additional studies to better quantify CO_2 flux, and synoptic mapping of surface pCO_2 should play an important role. In particular, with continuous surface pCO_2 collections in the GOM in recent years (see below for data sources), the application of satellite remote sensing can strongly contribute to a better understanding of surface pCO_2 distributions and CO_2 flux.

Within the GOM, of particular importance is the WFS between 24–31 °N and 80–85 °W (Fig. 1). The WFS is a broad carbonate-based shelf with a width of 220–275 km and a gentle slope, influenced by the Loop Current (LC) system as well as upwelling, river discharge, blooms of both harmful and non-harmful algae, summer and winter storms, and groundwater influx (Jolliff et al., 2003; Weisberg and He, 2003; Hu et al., 2005; Hu et al., 2006; Walsh et al., 2006; Benway and Coble, 2014). Although the GOM is typically characterized as being oligotrophic, the WFS is one of the most productive continental shelves in the United States, supporting numerous fisheries and diverse organisms (Saul et al., 2013; Chagaris et al., 2015). As one of the broadest continental shelves of United States (He and Weisberg, 2002), the WFS may play a big role in modulating CO_2 flux in the GOM, and knowledge of synoptic surface pCO_2 distributions as well as their temporal changes can help to quantify air-sea CO_2 fluxes, biochemical and ocean acidification processes. However, despite significant efforts to collect surface pCO_2 data through numerous ship surveys, and one study (Xue et al., 2014) to model pCO_2 variability on the Louisiana Shelf and the GOM as a whole, little information is available for the WFS.

The objectives of this study are thus two-fold: (a) development of a remote sensing model to scale up ship-based surface pCO_2 observations in order to take advantage of the more synoptic and frequent remote sensing observations for the WFS, and (b) application of the model to long-term remote sensing data to examine spatial-temporal distributions of surface pCO_2 on the WFS. The present work is directed toward bridging knowledge gaps by providing, for the first time, monthly pCO_2 distribution maps at medium resolution (1-km) and their temporal variations on the WFS.

2. Data and methods

2.1. A brief review of pCO_2 remote sensing

While the details of different methods to estimate surface pCO_2

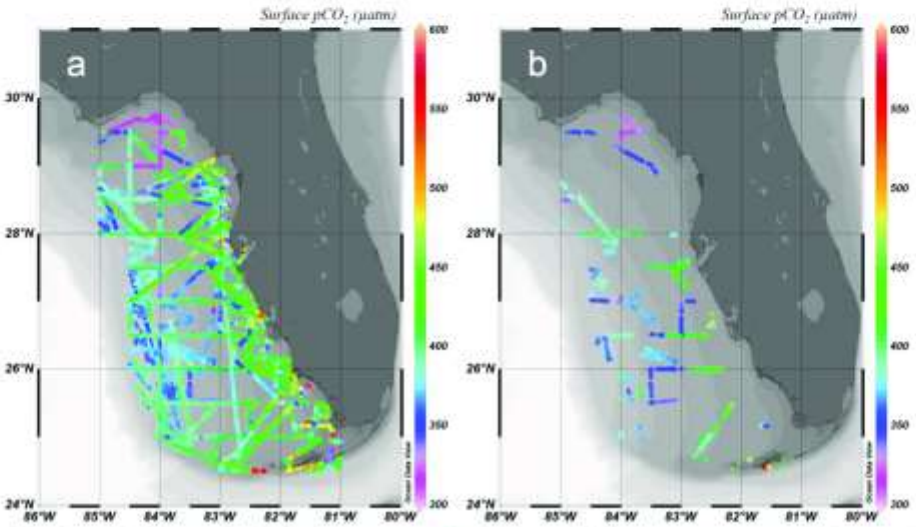

Fig. 1. (a) Spatial distributions of the field-measured pCO_2 along the ship transects (Table 2). (b) The same field data where near-concurrent (±6 h) high-quality MODIS data exist.

Table 1
List of published works on remote sensing of surface ocean pCO_2 arranged in chronological order. Note that studies of surface ocean pCO_2 without the use of remote sensing are not listed here.

Reference	Study area	Model input	Model	Model uncertainty
Stephens et al. (1995)	North Pacific	SST, LON	MPR	RMSE = ± 17 μatm (subtropical); RMSE= ± 40 μatm (subpolar)
Lefèvre et al. (2002)	Coast off Chile	SST, SSS, CHL	MLR	STD=35 μatm, R^2=0.65
Sarma (2003)	Arabian Sea	SST, SSS, CHL	MLR for DIC and TA	errors= ± 5–30 μatm
Olsen et al. (2004)	Caribbean Sea	SST, LAT, LON	MLR	RMSE=9.5 μatm,R^2=0.8
Ono et al. (2004)	North Pacific	SST, CHL	MPR	RMSE = ± 14 μatm (subtropical); RMSE= ± 17 μatm (subpolar)
Rangama et al. (2005)	Southern ocean	SST, CHL	MLR	STD=2.6–7.9 μatm
Sarma et al. (2006)	North Pacific	SST, SSS, CHL	MLR for DIC and TA	RMSE=17–23 μatm
Lohrenz and Cai (2006)	Mississippi River delta	SST, SSS, CHL	PCA and MLR	R^2=0.743, RMSE=50.2 μatm
Jamet et al. (2007)	North Atlantic	SST, CHL, MLD	MLR	R=0.45–0.86, RMSE=8.98–15.01 μatm
Watanabe (2007)	East China Sea	SST, CHL, SSS	MPR for TA and DIC	Not available
Berryman et al. (2008)	Central Pacific	SST, SSS, CHL	MLR	R^2=0.59, $p < 0.02$
Evans et al. (2008)	Oregon and Washington Shelf	SST, CHL	Not available	Not available
Zhu et al. (2009)	Northern South China Sea	SST, CHL	MPR	R^2=0.66, RMSE=25.1 μatm, R^2=0.68 RMSE=4.6 μatm
Chierici et al. (2009)	Northern North Atlantic	SST, CHL, MLD	MPR	RMSE=10.8 μatm, R^2=0.72
Takahashi et al. (2009)	North Atlantic	SST, CHL, MLD	SOM	RMSE=11.6 μatm
Friedrich and Oschlies (2009)	North Atlantic	SST, CHL	KFM	RMSE=19 μatm
Shadwick et al. (2010)	Scotian Shelf	SST, CHL, wind speed	MLR	STD=13 μatm,R^2=0.81
Borges et al. (2010)	Belgian coastal zone	SST, CHL	MPR	Not available
Lohrenz et al. (2010)	Mississippi River delta	SST, SSS, CHL	PCA and MLR	R^2=0.165–0.976, $p < 0.001$
Kanuguh et al. (2010)	Peru and Namibia	SST, CHL	MPR	R^2=0.67–0.72
Chen et al. (2011)	Southern Atlantic and Indian Ocean	SST, CHL	MLR	R^2=0.77, 0.85, STD=1.21, 21.0 μatm
Wijf et al. (2012)	Santa Barbara Channel	SST, CHL, NO_3^-	MLR	Not available
Jo et al. (2012)	Northern South China Sea	SST, CHL, LAT, LON	FFBP	RMSE=6.9 μatm, R^2=0.98
Hales et al. (2012)	North American West Coast	SST, CHL	Quasi-mechanistic model	R=0.61–0.93, RMSE=6.6–65 μatm
Tao et al. (2012)	Huanghai Sea and Bohai Sea	SST, CHL	MPR	RMSE=15.82–31.74 μatm
Nakaoka et al. (2013)	North Pacific	SST, SSS, CHL, MLD	SOM	RMSE=17.6–20.2 μatm
Signorini et al. (2013)	North American East Coast	SST, SSS, CHL, Jday	MLR	R^2=0.42–0.82, RMSE=22.4–36.9 μatm
Marrec et al. (2014)	Western English Channel	SST, SSS, CHL, MLD, Jday, LAT, LON	MLR	RMSE=17.2, 21.5 μatm, R^2=0.73,0.79
Parard et al. (2014)	Baltic Sea	SST, CHL, CDOM, NPP, MLD, Jday	MLR and SOM	RMSE=35 μatm, R^2=0.93
Qin et al. (2014)	Yellow Sea	SST, CHL	MPR	RMSE=16.68–21.46 μatm
Bai et al. (2015)	East China Sea	TA, DIC, CHL	Mechanistic semi-analytical model	Not available, but large uncertainty can be detected from the model validation.
Marrec et al. (2015)	European shelf	SST, CHL, wind speed, PAR, MLD	MLR	RMSE=16, 17 μatm
Padin et al. (2015)	Hooghly Estuary	SST, CHL	MPR	RMSE=18 μatm
Moussa et al. (2016)	Tropical Atlantic	SST, SSS, CHL	FNN	RMSE=8.7–9.6 μatm

Note: MLR=Multiple Linear Regression; MPR=Multiple Polynomial Regression; PCA=Principal Component Analysis; SOM=Self Organizing Map; FFBP=Feed Forward Back Propagation; KFM=Kohonen Feature Map; FNN=Feedforward Neural Network; STD=Standard Deviation; CDOM=Colored Dissolved Organic Matter; NPP=Net Primary Production; PAR=Photosynthetically Active Radiation; Jday=Julian day; R=Correlation Coefficient.

from remote measurements can be found in the literature (as listed in Table 1), for completeness the methods are briefly described here.

In terms of model inputs, most published works correlated surface pCO_2 to physical and biological parameters such as sea surface temperature (SST), sea surface salinity (SSS), mixed layer depth (MLD, m), and chlorophyll *a* concentration (CHL, mg m^{-3}) (e.g., Stephens et al., 1995; Rangama et al., 2005; Wanninkhof et al., 2007; Watanabe, 2007; Berryman et al., 2008; Zhu et al., 2009; Friedrich and Oschlies, 2009; Hales et al., 2012; Tao et al., 2012; Signorini et al., 2013; Qin et al., 2014; Bai et al., 2015, Marrec et al., 2015; Padhy et al., 2015; Moussa et al., 2016). These parameters all have the potential to affect surface pCO_2, because: 1) SST and SSS can influence the solubility of CO_2 and the dissociation constants of the carbonate system (Weiss, 1974; Lee et al., 1998; Millero et al., 2006); 2) CHL can be a good tracer of the influence of biological processes on surface pCO_2 as CHL increases (e.g., in algal blooms) can cause significant decreases in surface pCO_2 (Sarma et al., 2006; Jamet et al., 2007; Friedrich and Oschlies, 2009); and 3), MLD can be a good indicator of wind stress and convective mixing, and as a result, carbonate properties of subsurface waters brought to surface by strong mixing are usually different from those of the surface (Jamet et al., 2007; Chierici et al., 2009; Signorini et al., 2013). In some studies, wind speed (Shadwick et al., 2010) and atmospheric pCO_2 (Lefevre and Taylor, 2002) were used to model the effect of air-sea CO_2 flux on surface pCO_2. Parard et al. (2014) and Marrec et al. (2014) estimated surface pCO_2 seasonal variations as a function of Julian day, and net primary production (Parard et al., 2014) was used to describe biological effects. Several other studies correlated surface pCO_2 with latitude and longitude (Olsen et al., 2004; Jo et al., 2012; Marrec et al., 2014). The work of Salisbury et al. (2008) related surface pCO_2 to optical measurements (beam attenuation at 660 nm, c-660, m^{-1}, provided an indication of the turbidity of the water column), and showed that high pCO_2 was associated with low c-660. It is reasonable and generally necessary to correlate surface pCO_2 to the parameters mentioned above (possibly excluding geo-locations) because it is difficult to directly describe pCO_2 in more mechanistic terms (physical, biological and chemical relationships).

In terms of methods and model uncertainties, both empirical regression and neural network approaches have been used to relate surface pCO_2 to SST, SSS, CHL and MLD in the open ocean (Ono et al., 2004; Sarma et al., 2006; Jamet et al., 2007; Telszewski et al., 2009; Nakaoka et al., 2013; Marrec et al., 2015; Padhy et al., 2015; Moussa et al., 2016). Such parameterizations have provided pCO_2 with Root Mean Square Errors (RMSE) less than 17 µatm. In coastal margins, in addition to the empirical regression and neural network approaches, a mechanistic semi-analytical method (Bai et al., 2015) was also examined by modeling the ocean processes that control surface pCO_2. Unlike empirical models, mechanistic methods explicitly explain the physical and biogeochemical processes that control surface pCO_2 in the model. Although the mechanistic method was more meaningful than the empirical regression and neural network approaches, it has generally been effective only in regions where river discharge was the dominant influencing factor on pCO_2 (Bai et al., 2015). The pCO_2 RMSE uncertainties of these models for coastal oceans can reach 88.6 µatm (Hales et al., 2012), and the coefficient of determination (R^2) can be as low as 0.165 (Lohrenz et al., 2010). Therefore, while remote estimation of surface pCO_2 for the open ocean is relatively mature due to less variable environmental conditions (mainly controlled by mesoscale ocean circulation), due to the complex dynamics of coastal regions (e.g., including river discharge, ocean tides, coastal upwelling, groundwater discharge and biological factors) (Richey et al., 2002; Bauer et al., 2013; Cyronak et al., 2014), remote estimation of surface pCO_2 is still challenging.

The monthly mean satellite products or climatology used as inputs in most published works can introduce significant uncertainties in nonlinear pCO_2 models. Likewise, the sensitivity of established models to individual input variables has rarely been studied. As satellite-derived SST and CHL have inherent uncertainties (0.5–1.0 °C for SST (Hu et al., 2009) and 12–24% for CHL in waters of > 5 m bottom depth (Cannizzaro et al., 2013)), error propagation in model-derived pCO_2 needs to be understood, especially for coastal waters. The developments in the present study are based on daily satellite data, and a sensitivity analysis was conducted to understand the principal factors that control pCO_2 and how errors in input parameters influence the final pCO_2 estimates.

2.2. Field data

The twenty five cruises used to obtain the underway surface water pCO_2 data used in this study are described in Table 2. These data, obtained between Sep. 2003 and Sep. 2012, are found at the Carbon Dioxide Information Analysis Center (CDIAC) (http://cdiac.ornl.gov/) and the U.S. Geological Survey (USGS). Seawater samples for measurements of pCO_2, SSS and SST were collected at a depth of 5 m using a shipboard flow-through seawater system (31,137 observations of each parameter). Full cruise tracks with color-coded surface pCO_2 values are shown in Fig. 1a. Surface pCO_2 data were measured with either a non-dispersive, infrared analyzer Li-COR™ (Feely et al., 1998; Pierrot et al., 2009) or with a Multiparameter Inorganic Carbon Analyzer (MICA; Wang et al., 2007). The Li-COR™ data had an accuracy of 2 µatm (or better) with a measurement interval near 2 min, and the MICA data had an accuracy of 2.5 µatm (or better) and a measurement interval around 2 min (Wang et al., 2007). The details of data collection, processing, and quality control can be found in Feely et al. (1998), Pierrot et al. (2009) and Wang et al. (2007). Corresponding SSS and SST data were obtained using a CTD (SBE-21 or SBE-38, Seabird Inc., USA, YSI 6600) integrated in the underway pCO_2 system.

All cruise data obtained from CDIAC/SOCAT has undergone quality control analysis. These data were converted into uniform format with an Interactive Data Language (IDL) program, and were visualized and quality controlled (i.e., by viewing data quality flags and metadata files) to discard apparent errors (e.g., individual spikes due to instrument malfunction or other factors). Surface pCO_2 that fluctuated greatly for consecutive measurements while other variables (SST, SSS) remained stable (e.g., part of the data collected over GU1005_Leg2 and WS1202) were assumed to be prone to measurement errors and were therefore discarded. Less than 0.1% of the available observations were discarded via this quality control protocol. A total of 31,137 pCO_2 observations were selected for model development and validation (see Section 2.4).

2.3. MODIS satellite data

Standard NASA Level-2 data products (version R2014.0) between July 2002 and December 2014 were downloaded from NASA Goddard Space Flight Center (http://oceancolor.gsfc.nasa.gov/). These Level-2 data products obtained by the Moderate Resolution Imaging Spectroradiometer (MODIS) on the Aqua satellite included SST and ocean color data such as CHL and spectral remote sensing reflectance (Rrs, sr^{-1}) in 7 spectral bands between 412 and 678 nm. The spectral Rrs data were used to calculate the diffuse attenuation coefficient at 490 nm (Kd_Lee, m^{-1}) and the absorption coefficient of colored dissolved organic matter at 440 nm (a_{g440}, m^{-1}) using the semi-analytical algorithm developed by Lee et al. (2005). This algorithm was selected because it is more accurate than empirical Kd algorithms for the large Kd range (0.03–1.29 m^{-1}) that is typical of turbid coastal waters in the eastern GOM. Kd_Lee has an estimated uncertainty of about 13% (Zhao et al., 2013). Data quality flags - another Level-2 MODIS data product - were used to screen low-quality data. Statistics between 2003 and 2014 showed that after discounting cloud cover, sun glint, and other factors that affect data quality, for any given location in the GOM there was, on average, a valid CHL (or Kd_Lee) observation every 5–10 days and a valid SST observation every 3–5 days (Feng and

Table 2
Underway pCO_2 measurements used in this study. All the cruise tracks listed here are shown in Fig. 1a. The cruises marked in italics were selected for model development together with concurrent (±6 h) satellite measurements, as shown in Fig. 1b. The cruises marked in bold had no concurrent satellite measurements, thus were not used for this study.

Cruise ID	Ship name[a]	Date range	# of observations
GU0801	*NOAA ship Gordon Gunter*	*2008/04/04–2008/04/07*	*2281*
GU0802_Leg2	**NOAA ship Gordon Gunter**	**2008/05/13–2008/05/14**	**344**
08FSH01	**M/V Here Today**	**2008/8/11–2008/8/15**	**1594**
GU0805_leg2_2	*NOAA ship Gordon Gunter*	*2008/11/05–2008/11/12*	*4628*
GU0805_Leg3	*NOAA ship Gordon Gunter*	*2008/11/14–2008/11/19*	*1734*
09FSH01	*M/V Here Today*	*2009/2/24–2009/2/28*	*1067*
GU0901_leg2	*NOAA ship Gordon Gunter*	*2009/03/01–2009/03/13*	*3327*
GU0902_Leg3	**NOAA ship Gordon Gunter**	**2009/03/15–2009/05/16**	**246**
09FSH02	*M/V Here Today*	*2009/8/17–2009/8/21*	*1504*
GU0904_Leg1	**NOAA ship Gordon Gunter**	**2009/09/06–2009/09/08**	**683**
GU0904_Leg2	*NOAA ship Gordon Gunter*	*2009/09/17–2009/09/28*	*3046*
GU0905_Leg2	*NOAA ship Gordon Gunter*	*2009/11/07–2009/11/08*	*383*
GU1001L2	**NOAA ship Gordon Gunter**	**2010/04/30–2010/05/01**	**280**
GU1005_Leg1_DWH	*NOAA ship Gordon Gunter*	*2010/10/16–2010/10/25*	*409*
GU1005_Leg2	*NOAA ship Gordon Gunter*	*2010/09/18–2010/09/28*	*3651*
RB0905	**NOAA ship Ronald Brown**	**2009/8/20**	**111**
RB0905T	**NOAA ship Ronald Brown**	**2009/09/15–2009/09/16**	**150**
RB0305	**NOAA ship Ronald Brown**	**2003/09/03–2003/09/04**	**152**
RB0306	**NOAA ship Ronald Brown**	**2003/09/09–2003/09/12**	**486**
RB0606A	**NOAA ship Ronald Brown**	**2006/7/30**	**97**
RB0705	**NOAA ship Ronald Brown**	**2007/07/15–2007/07/16**	**196**
WS1116	*R/V Walton Smith*	*2011/10/21–2011/10/24*	*1240*
WS1202	*R/V Walton Smith*	*2012/02/28–2012/03/02*	*1130*
WS1209	**R/V Walton Smith**	**2012/6/29**	**344**
WS1214	*R/V Walton Smith*	*2012/09/08–2012/09/12*	*2054*
Total from all cruises			31,137
Total used in model development and validation			26,734

[a] The original data and metadata for the cruises of NOAA ship Gordon Gunter; NOAA ship Ronald H Brown and R/V Walton Smith can be found at http://www.aoml.noaa.gov/ocd/ocdweb/occ.html, These data were acquired with funding from the NOAA Climate Program Office. The original data and metadata for the USGS cruises of M/V Here Today can be found at http://pubs.usgs.gov/ds/. These data were acquired with funding from USGS Coastal and Marine Geology Program.

Hu, 2016).

2.4. Algorithm development and validation

Although the field measurements included several key properties (e.g., SST, SSS, and CHL) that can be used to model surface pCO_2, MODIS-derived data products for SST, CHL, a_{g440}, and Kd_Lee were preferred for use in multi-variate regression against field-measured pCO_2. One advantage of this choice is that uncertainties in the MODIS-derived data products will be implicitly included in the regression coefficients. When the same data products are used with these coefficients for pCO_2 predictions, such uncertainties will be canceled to a large extent.

To obtain concurrent field data and MODIS data, a time window of ± 6 h was used. In order to assure satellite data quality an image pixel was discarded if it was associated with any one of the following quality control flags (Barnes and Hu, 2015): atmospheric correction failure, land, sun glint, high radiance, large sensor viewing angle (> 60°), stray light, cloud/ice, high solar zenith angle, low water-leaving radiance (low nLw_555), questionable navigation, CHL > 64 or < 0.01 mg/m^{-3}, suspicious atmospheric correction, dark pixel (scan line error) and navigation failure. Although SST is more tolerant than ocean color data to non-optimal observing conditions as defined in the quality flags (Feng and Hu, 2016), for consistency these criteria were applied to SST as well. Because the pixel size of the MODIS data used in this work is about 1 km, the pCO_2 field within the pixel was averaged to match the satellite data.

After the strict quality control and field data binning, for the period between Apr. 2008 and Sep. 2012 1516 conjugate observations of field-measured pCO_2 and MODIS data products were available for algorithm development and validation (Fig. 1b). In this dataset, field-measured pCO_2 ranged between 305.7 and 552.4 µatm, field-measured SSS ranged between 31.75 and 36.56, satellite SST ranged between 15.1 and 31.4 °C, satellite CHL ranged between 0.076 and 3.624 mg/m^{-3}, satellite a_{g440} ranged between 0.009 and 0.185 m^{-1}, and satellite Kd_Lee ranged between 0.030 and 0.590 m^{-1}. Most of the variables in this dataset showed normal distributions with equal variance except for a few outliers. This dataset was divided randomly into two groups, with one group used for model development and coefficient tuning, and the other for model validation.

To determine the appropriate forms to relate the dependent variable (surface pCO_2) and the independent variables, two exercises were conducted. Following the principle of parsimony, a stepwise multiple linear regression (MLR) was first conducted to examine which independent variables {SST, SSS, CHL, Kd_Lee, a_{g440}, Julday} should be used to predict surface pCO_2. Although Julday was not a real biochemical variable (more of a "tuning" parameter), it was selected and normalized sinusoidally to emphasize the seasonal cycle of surface pCO_2 (Friedrich and Oschlies, 2009; Lefèvre et al., 2005; Signorini et al., 2013). Because CHL, Kd_Lee and a_{g440} tend to be log-normal in their large-scale distributions (Campbell, 1995), these three variables were scaled logarithmically in the regression model. The results are presented in Table 3. All independent variables except CHL and Kd_Lee could be selected with 95% confidence ($p \leq 0.05$) in the final stepwise MLR model, with RMSE of 14.83 µatm and R^2 of 0.75. However, the scatterplot between predicted pCO_2 and field-measured pCO_2 (not shown here, but with statistics listed in Table 3) indicated that the predicted pCO_2 tended to plateau at high pCO_2: for pCO_2 > 420 µatm, the mean bias (MB) and mean ratio (MR) between model-predicted and field-measured pCO_2 from the stepwise MLR were −39.336 µatm and 0.916, respectively, suggesting that pCO_2 was significantly underestimated for pCO_2 > 420 µatm, thus the performance of the MLR approach was not satisfactory and further improvement was required.

Exclusion of CHL and Kd_Lee in the MLR model was consistent with the parsimony step-wise test, even though they were used in other studies to model surface pCO_2 (see Section 2.1). To further examine the reason and to investigate whether the independent variables are

Table 3
Statistics of the stepwise multiple linear regression (MLR). With 95% confidence ($p \leq 0.05$), all variables except CHL and Kd_Lee were selected in the final MLR model (*p* values with CHL or Kd_Lee added in the model are marked in italics). Clearly, the stepwise MLR underestimated surface pCO_2 for $pCO_2 > 420$ µatm. Therefore, this model was not applied in this study.

Model inputs*	Variable added	Decision to the new-added variable	*p* value	RMSE (µatm)	MB (µatm)		MR		R^2
					$pCO_2 >$ 420 µatm	$pCO_2 \leq$ 420 µatm	$pCO_2 >$ 420 µatm	$pCO_2 \leq$ 420 µatm	
Inputs1	SST	In	0.000	16.06	−45.251	1.120	0.903	1.004	0.703
Inputs2	log10(a_{g440})	In	0.000	15.16	−37.025	0.916	0.921	1.004	0.736
Inputs3	SSS	In	0.000	14.86	−39.282	0.972	0.916	1.004	0.746
Inputs4	cos(Julday)	In	0.042	14.83	−39.336	0.973	0.916	1.004	0.748
Inputs5	$\log_{10}$(CHL)	Out	*0.644*	14.78	−39.443	0.976	0.916	1.004	0.748
Inputs6	$\log_{10}$(Kd_Lee)	Out	*0.135*	14.75	−38.822	0.961	0.917	1.004	0.749

* inputs1=[SST]; inputs2=[SST, $\log_{10}(a_{g440})$]; Inputs3=[SST, $\log_{10}(a_{g440})$, SSS]; Inputs4=[SST, $\log_{10}(a_{g440})$, SSS, cos(Julday)]; Inputs5=[SST, $\log_{10}(a_{g440})$, SSS, cos(Julday), $\log_{10}$(CHL)]; Inputs6=[SST, $\log_{10}(a_{g440})$, SSS, cos(Julday), $\log_{10}$(Kd_Lee)].

orthogonal, correlations among the independent variables (SST, SSS, CHL, Kd_Lee, a_{g440}, Julday) and dependent variable (surface pCO_2) were examined and listed in Table 4. With 95% confidence ($p \leq 0.05$), most of the independent variables were inter-correlated, suggesting that a principal component analysis (PCA) may be needed to remove the redundant information from these variables (see below). Correlation analysis also showed high correlation between a_{g440} and CHL (or Kd_Lee), and higher correlation between surface pCO_2 and a_{g440} than between surface pCO_2 and CHL (or Kd_Lee). Therefore, once a_{g440} was explicitly included in the MLR model, CHL and Kd_Lee were implicitly included.

Considering the non-satisfactory performance of the MLR and the high correlations among the independent variables, PCA was used to determine the dominant, orthogonal modes that could be used to construct the model. As shown in Table 5, the derived six principal components (PCs) are orthogonal, and the first three PCs can explain > 98% of the variance in the independent variables. Thus, a principal component regression (PCR) model was developed to predict surface pCO_2 using the six PCs. The RMSE and R^2 of the PCR were 14.69 µatm and 0.75, respectively. Similar to the MLR results, the predicted pCO_2 tended to plateau at high pCO_2 values: for $pCO_2 > 420$ µatm, MB and MR of the PCR were −38.695 µatm and 0.917, respectively, indicating model deficiency of the PCR and a necessity for further effort to improve the model.

The non-satisfactory performance of the MLR and PCR methods indicated that linear regressions through either the independent variables or the orthogonal PCs could not explain the entire variance of the dependent variable, and that some non-linear forms may be required. Therefore, the following model development and tuning were based on multi-variate nonlinear regression (MNR) between field-measured pCO_2 and the independent variables. After extensive trial and error, it was found that the use of MODIS-derived SST, CHL, and Kd_Lee provided optimal results (Table 6). Other parameters, such as MODIS-derived a_{g440} (often inversely related to SSS in coastal waters due to conservative mixing) and field-measured SSS, did not improve the efficiency of the model because of the limited model predictive

Table 5
Coefficients between each principal component (PC) and the independent variables, as well as the percentage of variance explained by each PC.

Variables	PC1	PC2	PC3	PC4	PC5	PC6
SST	0.996	−0.066	0.024	0.053	0.014	−0.004
$\log_{10}$(CHL)	−0.037	−0.063	−0.022	0.702	−0.089	0.702
$\log_{10}$(Kd_Lee)	−0.023	−0.040	0.005	0.497	−0.642	−0.583
$\log_{10}(a_{g440})$	−0.044	−0.081	−0.012	0.495	0.761	−0.409
SSS	0.063	0.972	−0.198	0.104	0.029	−0.015
cos(Julday)	−0.013	0.196	0.980	0.038	0.016	0.011
Variance explained (%)	90.59	6.69	2.15	0.53	0.02	0.01

capability at high pCO_2 (Table 6). The functional relationship between field-measured pCO_2 and the satellite data was modeled by a multi-variate nonlinear (quadratic polynomial) regression, implemented in the Interactive Data Language (IDL). The regression equation was determined as:

$$pCO_2 = k_0x_1 + k_1x_2 + k_2x_3 + k_3x_4 + k_4x_1x_2 + k_5x_1x_3 + k_6x_1x_4 + k_7x_2x_3 + k_8x_2x_4 + k_9x_3x_4 + k_{10}x_1^2 + k_{11}x_2^2 + k_{12}x_3^2 + k_{13}x_4^2 \quad (1)$$

where x_1*=SST,* x_2*=log* $_{10}$*(Kd_Lee),* x_3*=log* $_{10}$*(CHL),* x_4*=cos(2π(Julday−γ)/365).*

In the equation above, γ was optimized by iteration (ranging from 0 to 365) until the minimum RMSE was obtained.

During the model tuning phase, several different forms of Eq. (1) were examined to determine the best form of the regression function. These included use of field-measured SSS or MODIS-derived a_{g440} instead of satellite Kd_Lee, and use of original CHL or Kd_Lee instead of logarithmic CHL or Kd_Lee. The results from these alternative functional forms were slightly worse than those from Eq. (1) (Table 6) except for the combinations of SSS and CHL, a_{g440} and CHL, and a_{g440} and SSS (last three rows in Table 6). However, models with combinations of a_{g440} and CHL, and a_{g440} and SSS tended to plateau for high pCO_2 values (> 420 µatm), with MB of −18.303 µatm and −16.305 µatm, and MR of 0.962 and 0.966, respectively, indicating

Table 4
Correlation coefficients among independent variables and dependent variables used in the selected model in this work, with 95% confidence. Coefficients with < 95% confidence are marked in italics, and the corresponding *p* values are listed in the parentheses.

Variables	SST	$\log_{10}$ (CHL)	$\log_{10}$ (Kd_Lee)	$\log_{10}$ (a_{g440})	SSS	cos (Julday)	pCO_2
SST	1	−0.532	−0.471	−0.681	0.212	−0.081	0.839
$\log_{10}$(CHL)	−0.532	1	0.950	0.927	−0.342	*−0.073 (0.052)*	−0.324
$\log_{10}$(Kd_Lee)	−0.471	0.950	1	0.858	−0.314	*−0.009 (0.812)*	−0.266
$\log_{10}(a_{g440})$	−0.681	0.927	0.858	1	−0.475	−0.077	−0.438
SSS	0.212	−0.342	−0.314	−0.475	1	0.198	*0.007 (0.852)*
cos(Julday)	−0.081	*−0.073 (0.052)*	*−0.009 (0.812)*	−0.077	0.198	1	−0.154
pCO_2	0.839	−0.324	−0.266	−0.438	*0.007 (0.852)*	−0.154	1

Table 6
Model performance for different combinations of input parameters using regression formula in Eq. 1. Note that although the last two rows show the same R^2 values as the first row with even lower RMSE, both tend to plateau for $pCO_2 > 420$ µatm (i.e., negatively biased MB and MR values). The third row from bottom shows slightly lower MB for $pCO_2 > 420$ µatm than the first row, but this row also shows higher RMSE, lower R^2, and plateaued performance for $pCO_2 > 480$ µatm (MB=−23.804 µatm, MR=0.957). Because currently SSS is difficult to derive from satellites for coastal waters, **the first row was selected as the final pCO_2 model in this study**.

Model inputs[a]	R^2	RMSE (µatm/%)	MB (µatm)		MR		Relationship between modeled pCO_2 and in situ pCO_2	Range of modeled pCO_2 (µatm)
			$pCO_2 >$ 420 µatm	$pCO_2 \leq 420$ µatm	$pCO_2 >$ 420 µatm	$pCO_2 \leq 420$ µatm		
Inputs1	0.89	10.98/2.9	−8.536	0.561	0.981	1.002	Y=0.899X+38.1	312.5–558.0
Inputs1[b]	0.62	19.98/5.0	−37.922	1.917	0.916	1.007	Y=0.605X+147.57	312.3–516.2
Inputs2	0.87	11.60/3.1	−12.269	0.628	0.973	1.002	Y=0.871X+48.1	312.9–566.1
Inputs3	0.84	13.10/3.4	−11.590	0.703	0.974	1.003	Y=0.856X+54.1	316.5–529.0
Inputs4	0.84	13.12/3.4	−9.187	0.933	0.979	1.003	Y=0.887X+42.6	310.3–562.1
Inputs5	0.86	11.94/3.1	−6.251	0.765	0.987	1.002	Y=0.911X+33.7	315.6–498.2
Inputs6	0.89	9.97/2.6	−18.303	0.369	0.962	1.001	Y=0.880X+44.7	311.9–477.8
Inputs7	0.89	9.86/2.6	−16.305	0.303	0.966	1.001	Y=0.889X+40.4	311.2–488.2

[a] Inputs1=[SST, $\log_{10}$(Kd_Lee), $\log_{10}$(CHL), cos(Julday)]; Inputs2=[SST, Kd_Lee, $\log_{10}$(CHL), cos(Julday)];Inputs3=[SST, $\log_{10}$(Kd_Lee), CHL, cos(Julday)]; Inputs4=[SST, Kd_Lee, CHL, cos(Julday)]; Inputs5=[SST, SSS, $\log_{10}$(CHL), cos(Julday)]; Inputs6=[SST, $\log_{10}(a_{\phi+\text{dg}})$, $\log_{10}$(CHL), cos(Julday)]; Inputs7=[SST, $\log_{10}(a_{\phi+\text{dg}})$, SSS, cos(Julday)].
[b] This model was a stepwise MNR, as shown in Eq. (2).

underestimation at high pCO_2 values. Although the model with combination of SSS and CHL showed a slightly lower MB for $pCO_2 >$ 420 µatm as compared to the model in Eq. (1), this model had a slightly higher RMSE and lower R^2, and its pCO_2 prediction was significantly biased for $pCO_2 > 480$ µatm (MB=−23.804 µatm, MR=0.957). Furthermore, it is currently difficult to estimate SSS from satellite measurements over coastal waters. Therefore, Eq. (1) was preferred as the potential pCO_2 model for this study. For reference and to follow the principle of model parsimony, again a stepwise MNR against all terms in Eq. (1) was conducted. The model formula did become concise as shown in Eq. (2) (compared to the formula in Eq. (1)). However, the statistics in Table 6 showed that the stepwise MNR had a RMSE of 19.98 µatm (5.0%) and a R^2 of 0.62, and its ability in estimating pCO_2 for $pCO_2 > 420$ µatm was also limited (MB=−37.922 µatm, MR=0.916). Therefore, this stepwise MNR did not show improvement over the stepwise MLR or PCR or MNR above, and was not selected in this study to model surface pCO_2.

$$pCO_2 = 2.0105x_1 + 339.2493x_2 + 0.5330x_1x_2 - 0.1784x_1x_3 - 0.0035x_1^2 + 234.2682x_2^2 - 86.8151x_3^2 \quad (2)$$

where x_1=*SST*, x_2=$\log_{10}$*(Kd_Lee)*, x_3=$\log_{10}$*(CHL)*.

Table 7 is a summary of the model performance with the stepwise MLR, PCR, stepwise MNR, and MNR. Clearly, the MNR model with Eq. (1) showed the best performance in terms of RMSE, R^2, MB, MR, the relationship between modeled and measured pCO_2, and the range of modeled versus measured pCO_2. Thus, the final empirical pCO_2 model was determined as:

$$pCO_2 = -124.076x_1 + 790.201x_2 - 753.952x_3 + 704.22x_4 + 35.217x_1x_2 - 7.044x_1x_3 - 34.737x_1x_4 - 1075.65x_2x_3 - 108.248x_2x_4 - 10.091x_3x_4 + 3.525x_1^2 + 947.627x_2^2 + 285.986x_3^2 + 105.661x_4^2 \quad (3)$$

where x_1=*SST*, x_2=$\log_{10}$*(Kd_Lee)*, x_3=$\log_{10}$*(CHL)*, x_4=$\cos(2\pi$ *(Julday −255)/365)*.

The MNR model in Eq. (3) was subsequently applied to the half of the dataset that was not used in the model development. The model-predicted pCO_2 was compared with the field-measured pCO_2, where R^2, RMSE, MR and MB were used to gauge model performance. A histogram of the difference between field-measured pCO_2 and model-predicted pCO_2 was generated to examine the error distributions.

To examine which independent variable is mostly responsible for the predictive capacity of the pCO_2 model, the variance that is explained by each variable was investigated by comparing the full model (Eq. (3), with all the four variables selected) to a reduced model (i.e., after removal of a certain variable). Using the same regression format (quadratic polynomial), a total of 4 reduced models were developed with the exclusion of SST, CHL, Kd_Lee, and Julday, respectively. In each case, variance in the surface pCO_2 explained by the selected variables was calculated and compared with that of the full model, with the difference regarded as the variance explained by the excluded variable.

2.5. Spatial-temporal pCO_2 distributions derived from MODIS

The model in Eq. (3) was applied to the daily Level-2 MODIS data for the period of July 2002–December 2014 to generate daily surface pCO_2 maps. The daily maps were used to compose monthly mean pCO_2 maps for each year, and these monthly mean maps were then used to compose monthly pCO_2 climatology. All parameters, including monthly pCO_2, CHL, Kd_Lee, and SST, were averaged over the WFS to examine long-term trends and inter-annual changes.

Table 7
Comparison of model performance. The stepwise MNR and MNR are both based on Eq. (1), with model coefficients shown in Eqs. (2) and (3), respectively. Clearly, the stepwise MLR, PCR, and stepwise MNR all show large underestimations for $pCO_2 > 420$ µatm. Therefore, the MNR model was selected as the final pCO_2 model in this study (Eq. (3)).

Model type	R^2	RMSE (µatm)	MB (µatm)		MR		Relationship between modeled pCO_2 and in situ pCO_2	Range of modeled pCO_2 (µatm)
			$pCO_2 >$ 420 µatm	$pCO_2 \leq 420$ µatm	$pCO_2 >$ 420 µatm	$pCO_2 \leq 420$ µatm		
Stepwise MLR	0.75	14.83	−39.336	0.973	0.916	1.004	Y=0.748X+93.7	323.2–416.5
PCR	0.75	14.69	−38.695	0.958	0.917	1.004	Y=0.751X+92.6	323.4–414.6
Stepwise MNR	0.62	19.98	−37.922	1.917	0.916	1.007	Y=0.605X+147.57	312.3–516.2
MNR	**0.89**	**10.98**	**−8.536**	**0.561**	**0.981**	**1.002**	**Y=0.899X+38.1**	**312.5–558.0**

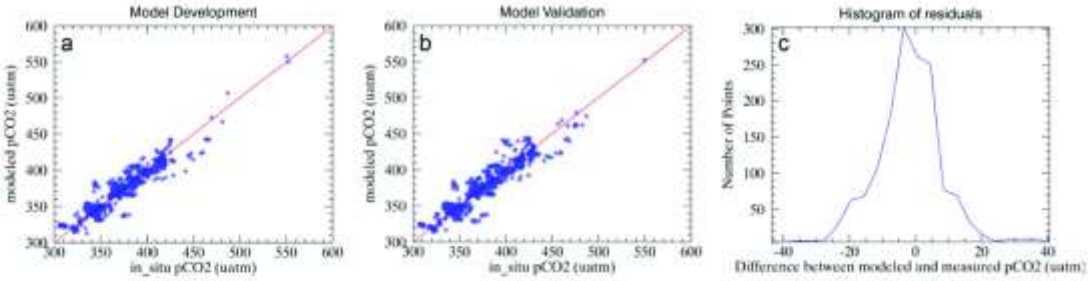

Fig. 2. (a) pCO_2 model development, where the modeled pCO_2 (y-axis) was estimated through coefficient tuning using the multi-variate regression Eq. (3). (b) pCO_2 model validation using a separate dataset that was not used for model development. (c) Histogram of error distributions for both model development and validation.

3. Results

3.1. Model performance

Fig. 2a shows the MNR model for pCO_2 prediction. The RMSE during model training was 10.51 µatm, with a coefficient of variation (CV) of 2.8% and R^2 of 0.89. Fig. 2b shows the model validation obtained with the data that were not used in the model training. Statistical results for the validation data are similar to those for the model training, with an RMSE of 11.79 µatm, CV of 3.1% and R^2 of 0.88. The validation showed that model-predicted pCO_2 was almost non-biased, as MR (which was 1.0006) was close to 1 and MB (which was 0.033 µatm) was close to 0 µatm. A histogram of residuals (measured pCO_2 minus predicted pCO_2) for the combined datasets (both model training and validation data) is shown in Fig. 2c. The histogram shows that 97.6% of the residuals were smaller than the observed 32.45 µatm pCO_2 standard deviation (+/−sigma).

The results shown in Table 8 indicated that variables used in our model (the full model) could explain 88.92% of the pCO_2 variance. When SST was excluded in the model, the remaining variables could only explain 68.62% of the pCO_2 variance. When Julday was excluded in the model, 74.45% pCO_2 variance could be explained. Similarly, exclusion of CHL or Kd_Lee would reduce the explained variance to 82.06% and 79.63%, respectively. Clearly, SST was the most responsible variable in our model (exclusion of SST would reduce the explained variance by 20.3%), followed by Julday. This is consistent with those reported in previous studies (Friedrich and Oschlies, 2009; Lefevre et al., 2005; Signorini et al., 2013). CHL and Kd_Lee were the least important variables in explaining the pCO_2 variance, consistent with later sensitivity analysis (see Section 4.1). Note that although Julday is not a real biochemical variable, its use improved the model performance more than the use of CHL or Kd_Lee.

3.2. Temporal and spatial variation of surface pCO_2

Fig. 3 shows mean monthly pCO_2, CHL, Kd_Lee and SST over the entire WFS where pCO_2 is within the model range. Monthly climatologic maps of surface pCO_2 are presented in Fig. 4, with the model range outlined by red dashes. Distinct seasonal pCO_2 patterns can be seen in both Figs. 3 and 4, corresponding to the seasonal variation of CHL, Kd_Lee and SST.

On a temporal scale the seasonal variation of pCO_2 was positively correlated with SST (in phase), and negatively correlated with CHL and Kd_Lee. In summer, surface pCO_2 can reach a maximum around 450 µatm. During this period, primary production is inhibited mainly by a deficiency of nutrients caused by ocean stratification. Thus CO_2 removal through photosynthesis is reduced in the summer, and the balance between respiration and photosynthesis is strongly shifted toward the former by increasing SST. In winter, surface pCO_2 attains a minimum of around 350 µatm. During this time, with the breakdown of the thermocline and increase of MLD (> ~50 m; Liu and Weisberg, 2007), phytoplankton blooms can occur as nutrients are brought to the surface by upwelling. Combined with the decrease of SST, which would by itself strongly decrease pCO_2 (see Section 4), surface pCO_2 would be expected to significantly decrease. However, another factor needs to be considered because deep water brought to the surface by wintertime vertical mixing is rich in dissolved inorganic carbon as a result of decomposition of organics in deep waters and also submarine groundwater discharge (Hu et al., 2006; Cyronak et al., 2014). Thus the combined effect of enhanced vertical mixing and decreased SST is that pCO_2 reaches a minimum during winter but is not severely diminished. Although the interannual patterns of pCO_2, SST, CHL and Kd_Lee are generally similar throughout our study period, certain exceptions can be noted. In September of 2005, due to an intense red tide bloom that was triggered on the west-central Florida Shelf by two hurricanes combined with other influencing parameters (Hu et al., 2006), CHL peaked at 2.27 mg/m−3 (Fig. 3c). Concomitantly, surface pCO_2 estimates decreased by 38 µatm relative to pCO_2 estimates in the previous month, but did not reach a minimum. The highest value of surface pCO_2 was attained in 2010 June (Fig. 3a) and was about 58 µatm higher than the previous month. Considering that there was almost no change in CHL and Kd_Lee, and Julian day was only a small adjusting factor, this increase was likely caused by the observed 3.4 °C increase of SST. Combined with the sensitivity analysis demonstrating that an increase of 1 °C in SST by itself can lead to an increase of about 15.7 µatm in surface pCO_2, the appearance of the pCO_2 maximum in June was reasonable. Comparing this interannual variability of spatially averaged pCO_2 on the WFS to modeled pCO_2 results for the whole

Table 8
Statistics of the full model and reduced models for explaining variance in the estimated surface pCO_2. The first row represents the full model (Eq. (3)) used in this study, while other rows represent models with one variable excluded. The last column shows the reduced variance (compared to the full model) when a variable was excluded.

Model inputs	Excluded variable	Variance explained (%)	Variance explained by the excluded variable (%)
SST, log(Kd_Lee), log(CHL), Julday	NaN	88.92	NaN
log(Kd_Lee), log(CHL), Julday	SST	68.62	20.3
SST, log(CHL), Julday	Kd_Lee	79.63	9.29
SST, log(Kd_Lee), Julday	CHL	82.06	6.86
SST, log(Kd_Lee), log(CHL)	Julday	74.45	14.47

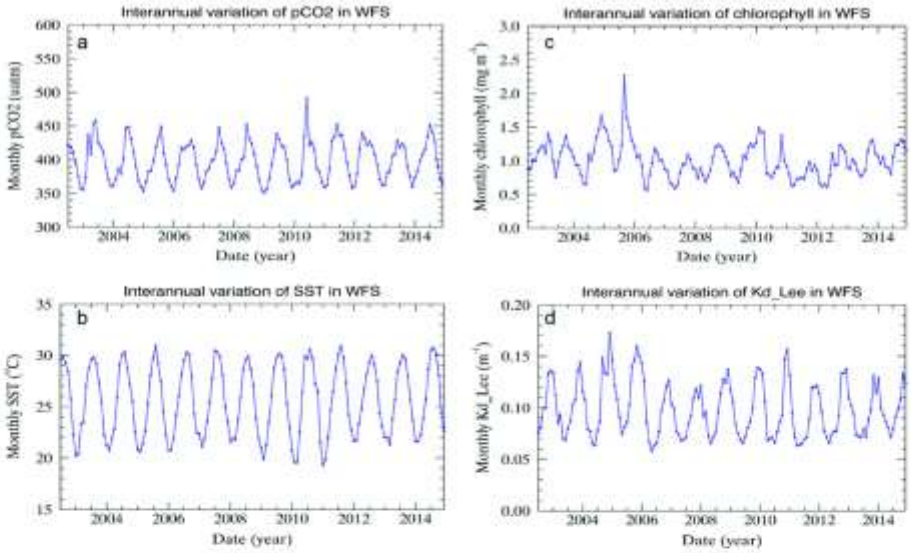

Fig. 3. Monthly time series showing seasonality and inter-annual variations of pCO_2, CHL, Kd_Lee, and SST on the West Florida Shelf (calculated from the entire WFS, outlined in Fig. 4). The data were generated from monthly mean satellite data products from July 2002 to December 2014.

GOM (Xue et al., 2014), a similar pattern of seasonal variations with highs in summer and lows in winter was detected. However, the model sensitivity analysis and uncertainty and accuracy assessment that is described below (Section 4.1) indicates that the results obtained in the present work exhibits improved accuracy and less uncertainty.

In terms of observations on spatial scales (Fig. 4), although there were distinct gradients in CHL and Kd_Lee climatologic maps (not explicitly shown here), pCO_2 climatologic maps showed small gradients from inshore to offshore during winter and early spring (November to March) when SST was low. Other interesting features of Fig. 4 included two regions with elevated pCO_2 relative to their surroundings (red solid circles in Fig. 4). Among other possible influences, because there are large springs in this region (Rosenau et al., 1977) with low temperature and high pCO_2, this could be due to upwelling of submarine groundwater discharge, as pCO_2 is usually higher in fresh groundwater than surroundings (Macpherson, 2009; Cyronak et al., 2014). From early spring to late fall (April to October), obvious pCO_2 gradients were observed, changing from high to low in the offshore direction. High pCO_2 in near shore regions can be related to tidal mixing and river runoff, carrying elevated DIC to coastal surface waters. Although DIC in coastal areas can be diminished by photosynthesis, high nearshore pCO_2 values are commonly observed. However, the extremely high pCO_2 values (> 550 μatm) in the nearshore regions of South Florida may not be reliable, as there was little pCO_2 data in this region and the pCO_2 model developed here was only valid for pCO_2 ranging from 300 to 550 μatm. On the other hand, such extremely high pCO_2 values could be realistic as pCO_2 had a positive response to SST changes and SST in this region was higher than in offshore waters. In the offshore region during our observation period, due to the combined effects of thermocline development and decreases in SST, surface pCO_2 was lower than for inshore waters. Nevertheless, in temporal terms, offshore surface pCO_2 values during the summer are higher than offshore pCO_2 values in the winter and early spring. In the area around the Florida Keys, pCO_2 values were high relative to other regions year round. This can be attributed to the influence of the LC in the Florida Strait (clearly shown in the SST climatology map) and potentially submarine groundwater discharge in this very shallow region. Compared with the modeled multi-year pCO_2 maps in Xue et al. (2014), the results shown here exhibit distinctive spatial distribution patterns across nearshore and offshore waters.

4. Discussion

4.1. Model sensitivity to environmental forcing and model uncertainty

The distribution of surface ocean pCO_2 is mainly controlled by ocean thermodynamics, physical processes, biological processes, and air-sea exchange (Takahashi et al., 2002; Inoue et al., 2003; Rangama et al., 2005; Bai et al., 2015). Ocean thermodynamic effects are dependent on SST, and the relationship between surface pCO_2 and SST can be estimated using a simple exponential relationship: ($pCO_{2@T2}=pCO_{2@T1}$*exp[0.0423*(T_2-T_1)]) (Takahashi et al., 2002, 2009). Physical processes such as advection, upwelling and water mixing affect pCO_2 mainly by transport and mixing of different water masses with distinctive chemical and physical properties such as total alkalinity (TA), dissolved inorganic carbon (DIC), SST and SSS. Biological processes, including consumption of CO_2 by photosynthesis, production of CO_2 by respiration, and utilization of carbonate during calcification also have important direct effects on the pCO_2 of seawater (Reynaud et al., 2003). Air/sea CO_2 exchange can exert especially strong controls on surface pCO_2 under strong wind conditions (Bates et al., 1998; Bates and Merlivat, 2001; Turk et al., 2013). Nevertheless, in a limited case study, only one or two processes were observed to dominate the pattern of sea surface pCO_2 (Bai et al., 2015).

In order to better understand how surface pCO_2 responds to input variables, a sensitivity analysis was conducted. For each analysis, one input variable was varied while the others remained constant. Surface pCO_2 predictions were compared to examine the magnitudes of change with variations in SST, CHL and Kd_Lee. Considering the uncertainties observed during retrieval of satellite products, we varied CHL and Kd_Lee by ± 20% and SST by ± 1 °C. These are the upper bounds of the MODIS data product uncertainties over the WFS. The model response results are shown in Figs. 5 and 6, and additional statistics

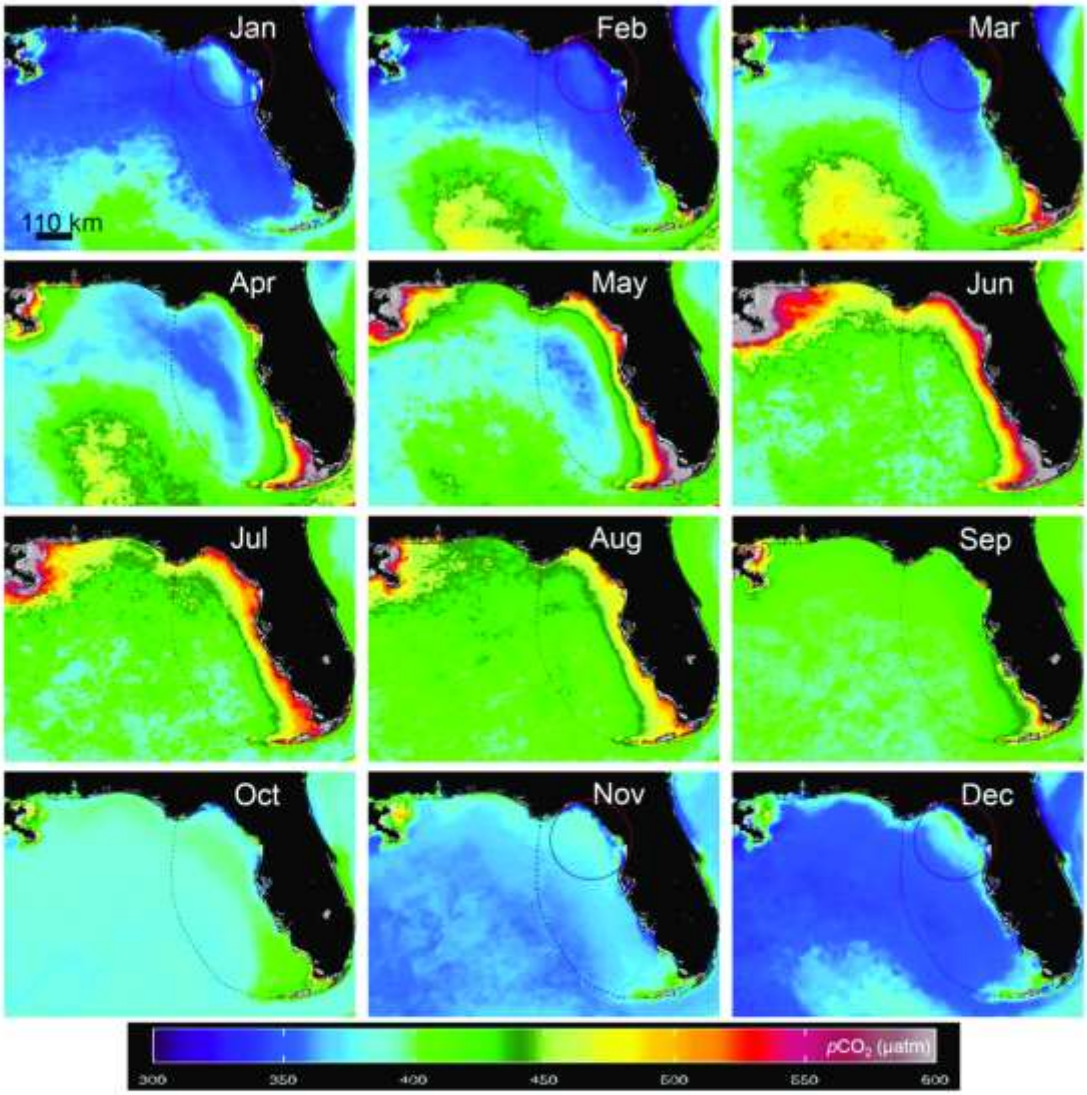

Fig. 4. pCO_2 monthly climatology derived from satellite data using the multi-variate regression model for the period of July 2002 to December 2014. The maps showed the eastern Gulf of Mexico between 24 °N to 31 °N and 90 °W to 80 °W. The West Florida Shelf is outlined by the red dashed line. The red solid circles outline some high-spatial gradient features that were possibly caused by upwelling.

such as RMSE, MR, and MB are listed in Table 9.

A visual interpretation of Figs. 5 and 6 indicates that the model is more sensitive to input changes in CHL when CHL is >1.5 mg m^{-3}. For CHL greater than 1.5 mg m^{-3}, a 20% increase in CHL (Figs. 5a and 6a) produced pCO_2 predictions that were lower than the original pCO_2, while for CHL less than 1.5 mg m^{-3} the same 20% increase in CHL caused a substantially smaller change in the predicted pCO_2. For the entire data range tested in this analysis (Table 9), the RMSE, MR and MB were 10.34 µatm, 1.022, and 8.06 µatm, indicating that a 20% increase in CHL resulted in an 8.06 µatm pCO_2 overestimate. For data with CHL >1.5 mg m^{-3}, the RMSE, MR and MB were 16.44 µatm, 0.968, and −12.44 µatm. In contrast, for data with CHL ≤ 1.5 mg m^{-3}, the RMSE, MR and MB were 10.07 µatm, 1.024, and 8.79 µatm, respectively. A similar disparity in model sensitivity was observed for a 20% decrease in CHL when CHL >1.5 mg m^{-3} and CHL ≤ 1.5 mg m^{-3} (Figs. 5b and 6b). For the entire data range, RMSE, MR, and MB were 9.36 µatm, 0.986, and −4.98 µatm. For data with CHL >1.5 mg m^{-3}, pCO_2 was overestimated, with RMSE, MR, and MB being 24.09 µatm, 1.053 and 20.11 µatm. Consistent with the observations described above, for data with CHL ≤ 1.5 mg m^{-3} the model showed much reduced sensitivity to a 20% decrease in CHL, with an RMSE of 8.40 µatm, an MR of 0.984, and an MB of −5.87 µatm. Based on the characteristics shown in Figs. 5a, 6a, 5b and 6b, the pCO_2 algorithm is especially sensitive to CHL at high concentrations. To

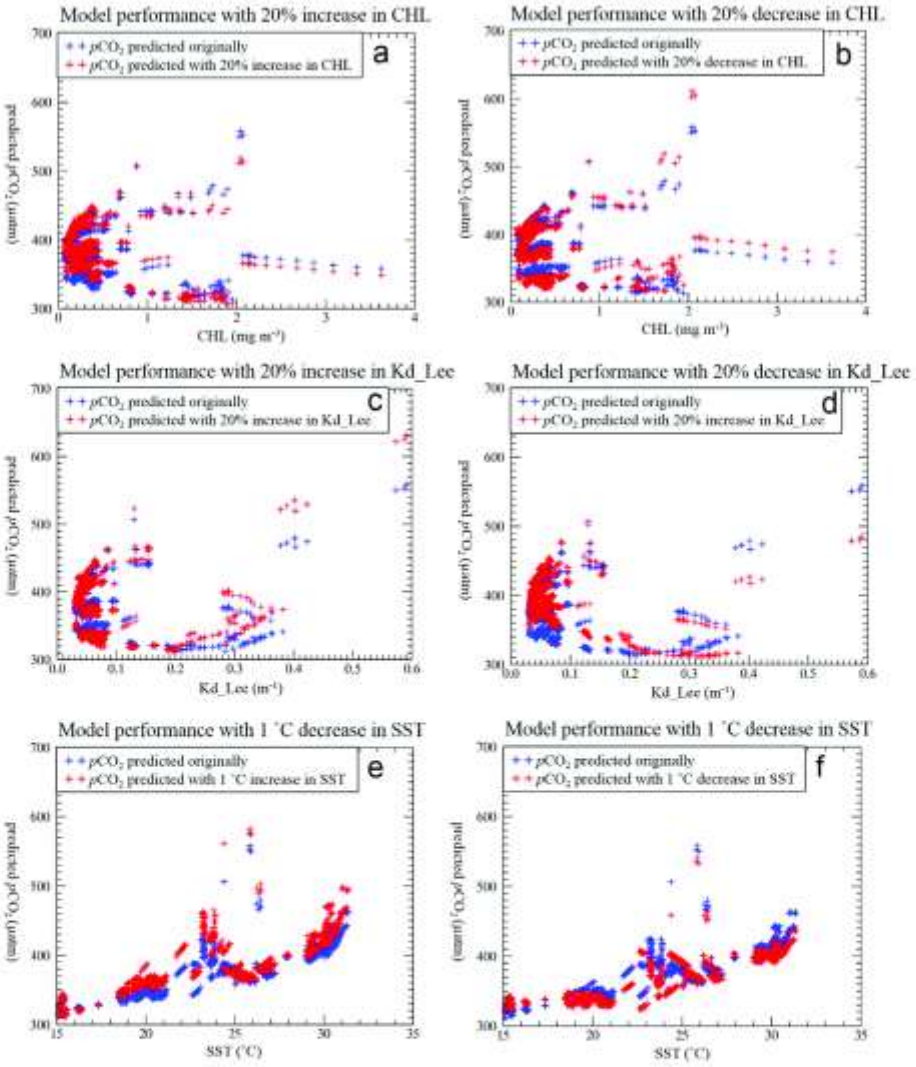

Fig. 5. pCO_2 model sensitivity to changes in CHL, Kd_Lee, or SST. Data used here are from both model development and model validation. In all panels, blue points represent the original prediction while red points represent the prediction corresponding to the artificial changes in either CHL (± 20%) (a and b), Kd_Lee (± 20%) (c and d), or SST (± 1 °C) (e and f) while all other algorithm input variables are kept the same. Statistical results are listed in Table 9.

some extent, this reflects the complex role of CHL in controlling surface pCO_2.

As Kd_Lee is not entirely independent from CHL, it is also clearly seen that the pCO_2 algorithm is more sensitive to Kd_Lee as this variable becomes larger (> 0.2 m^{-1}). For Kd_Lee values greater than 0.2 m^{-1}, a 20% increase in Kd_Lee (Figs. 5c and 6c) resulted in substantial increases in predicted pCO_2, while for Kd_Lee values less than 0.2 m^{-1}, a 20% increase in Kd_Lee produced pCO values close to the original pCO_2 prediction. When all data were used in the analysis the RMSE, MR and MB values for this experiment were 10.02 μatm, 0.997, and −0.68 μatm. For data with Kd_Lee > 0.2 m^{-1}, they were 29.43 μatm, 1.066, and 24.51 μatm, while for data with Kd_Lee ≤0.2 m^{-1} the RMSE, MR and MB were 8.13 μatm, 0.994, and −1.83 μatm. Likewise, with a 20% decrease in Kd_Lee (Figs. 5d and 6d), pCO_2 was predicted to be lower than the original pCO_2 if Kd_Lee values were greater than 0.2 m^{-1} (RMSE=24.04 μatm, MR=0.966, MB=−13.83 μatm) but higher if Kd_Lee values were less than 0.2 m^{-1} (RMSE=20.81 μatm, MR=1.050, MB=18.41 μatm). When all data were used in the calculation, RMSE, MR and MB were 20.95 μatm, 1.047, and 17.01 μatm. The differences in model sensitivity for Kd_Lee > 0.2 m^{-1} and Kd_Lee ≤0.2 m^{-1} are consistent with those for CHL changes, as coastal waters typically have higher CHL and Kd_Lee than offshore waters.

The sensitivity of the pCO_2 model to SST varied over the modeled range of SST. For SST greater than 16 °C (Figs. 5e and 6e), a 1 °C increase in SST produced pCO_2 predictions higher than the original

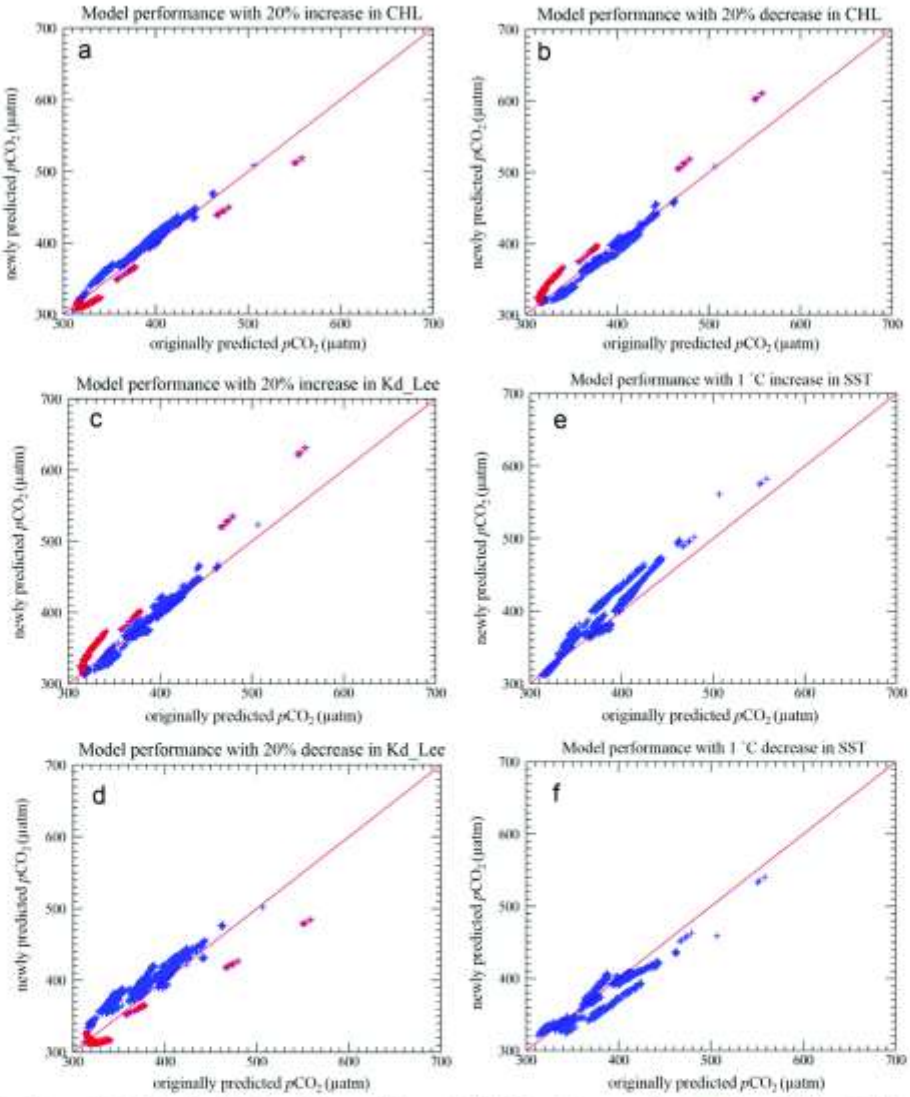

Fig. 6. Comparison between original pCO_2 and predicted pCO_2 with incremental changes in CHL, Kd_Lee, or SST, corresponding to Fig. 5. The red solid line is the 1:1 line, red points in panel a and b represent data with CHL above 1.5 mg/m^{-3}, and red points in panel c and d represent data with Kd_Lee above 0.2 m^{-1}.

pCO_2, while for SST less than 16 °C, the predicted pCO_2 was much closer to the original prediction. As would be expected from the above analyses, a 1 °C decrease in SST (Figs. 5f and 6f) for SST greater than 16 °C resulted in predicted pCO_2 values that were lower than the original pCO_2 while for SST less than 16 °C pCO_2 predictions were closer to the original pCO_2. The RMSE values for these two experiments (1 °C increase and 1 °C decrease in SST) were 16.03 and 11.98 µatm, with MR values of 1.030 and 0.989 and MB values of 11.57 and −4.52 µatm.

In summary, pCO_2 variations created by a 1 °C change in SST, 20% variations in CHL and 20% variations in Kd_Lee were all within or close to the RMSE of the model although, notably, the model sensitivity varies with the model input range. Only in the case of Kd_Lee did 20% variations produce pCO_2 variations somewhat higher than the RMSE of the model. However, considering the range of SST in this region (minimum around 15 °C, maximum around 35 °C), a 1 °C temperature variation corresponds to a 6% variation in SST, whereby it is seen that the model is far more sensitive to SST than to CHL and Kd_Lee. Indeed, although coastal waters may occasionally have SST < 16 °C, CHL > 1.5 mg m^{-3}, and Kd_Lee > 0.2 m^{-1}, when the entire WFS is considered as a whole at monthly intervals, these conditions are rarely met (Fig. 3), suggesting that the model uncertainties are within those specified in the model evaluation.

Because we chose to use satellite data products directly as the

Table 9
Model sensitivity to CHL, Kd_Lee and SST. For each case, the variable was set to artificially increase or decrease by 20% or 1 °C while other variables were kept the same. RMSE, MR (mean ratio between model-predicted pCO_2 and field-measured pCO_2) and MB (mean bias between model-predicted pCO_2 and field-measured pCO_2) were calculated by comparing the new-predicted pCO_2 with the original-predicted pCO_2. The model was more sensitive to changes in the input variables when CHL was > 1.5 mg m^{-3}, Kd_Lee was > 0.2 m^{-1}, or SST was > 16 °C.

Cases	RMSE (μatm)	MR	MB (μatm)
20% increase in CHL	10.34	1.022	8.06
20% decrease in CHL	9.36	0.986	−4.98
20% increase in Kd_Lee	10.02	0.997	−0.68
20% decrease in Kd_Lee	20.95	1.047	17.01
1 °C increase in SST	16.03	1.030	11.57
1 °C decrease in SST	11.98	0.989	−4.52

model input during model development, systematic errors (e.g., bias) other than random noise in the satellite data products are implicitly accounted for in the model coefficients. Thus, considering the combined effects of uncertainties in the satellite data products and the sensitivity test results, the uncertainties of the pCO_2 model should be between 10.5 and 21.0 μatm for typical data ranges. However, these uncertainties represent RMSE values for each data point. When the data are averaged over large scales in either space or time, the uncertainties in the mean products should be much smaller.

The empirical model developed for the WFS here shows improvement over published works (Table 1) in terms of RMSE and R^2, but not necessarily for other regions in the GOM (see below). Furthermore, the model is applicable all year round because data collected from different months were used in tuning the model coefficients. Therefore, with daily measurements from satellites, the model may be used study the impacts of extreme events on surface pCO_2 distributions (e.g., 2005 algal blooms and storms), although no such events were considered in the model tuning or validation. In addition, air-sea CO_2 flux (F_{CO2}=$kK_0(pCO_{2sw}-pCO_{2air})$, where k is the gas transfer velocity of CO_2, and K_0 is the solubility coefficient of CO_2) can be calculated with auxiliary wind speed and atmospheric pCO_2 data, allowing broad-scale assessments of the extent to which the WFS serves as a CO_2 source or sink. Similarly pH (pH=$-\log_{10}([H^+]_T)$, where $[H^+]_T$ is the total concentration of hydrogen ions) or carbonate ion concentrations ($[CO_3^{2-}]_T$) and carbonate saturation states ($[Ca^{2+}]_T$ $[CO_3^{2-}]_T$/ Ksp)) can be derived from modeled pCO_2 and regional assessments of salinity-normalized TA on the WFS.

However, one shortcoming of the model, as is the case for any other empirical models, is that the model is good only for the data range within which it was tuned. Specifically, all data used in the tuning had pCO_2 values between 300 and 550 μatm as the lower and upper bounds of the model's applicability. Field data showed that pCO_2 could occasionally be > 600 μatm or even > 1000 μatm in nearshore waters. As these data had no concurrent satellite data, they were not used in the model tuning. Nevertheless, in the derived maps most values are indeed within the range of applicability except for some very nearshore waters (e.g., in Florida Bay). Thus, the pCO_2 model should be appropriate to most of the data over the WFS.

4.2. Model testing in other regions of GOM

With the auxiliary underway pCO_2 measurements in other regions of GOM between April 2002 and May 2014 (obtained from http://cdiac.ornl.gov/oceans/Coastal/ and http://www.aoml.noaa.gov/ocd/gcc/), we also tested how the algorithm (Eq. (3)) performed in other GOM waters. Based on the distributions of cruise data after matching up with satellite products, the validation was examined mainly in three regions (see Fig. 7): around the Mississippi delta, the northwestern GOM, and LC affected regions (open GOM, northern Caribbean and the Florida Strait). For region around the Mississippi River delta (Figs. 7a, b and 8a), predictions for the offshore region were better than the inshore. For the inshore region, predicted pCO_2 deviated substantially from the in situ pCO_2. This result was not unexpected since water

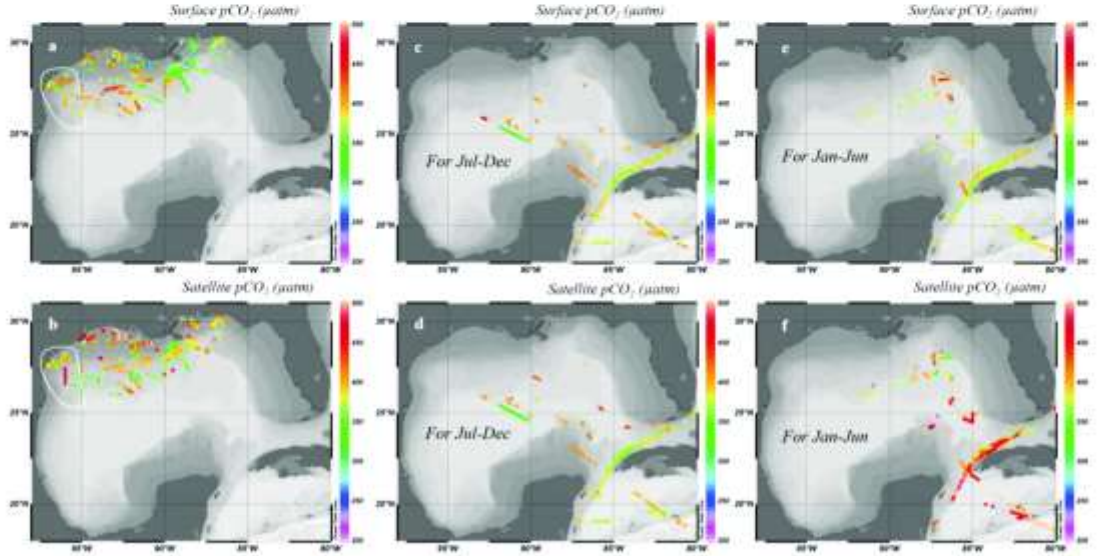

Fig. 7. Spatial distribution of in situ and satellite-predicted pCO_2 in other GOM regions except WFS, with in situ measurements after matchup with concurrent satellite products shown in top panels and the corresponding satellite prediction below. This validation is divided into three parts according to the location: northwestern GOM (white circles in panel a and b), the region near the Mississippi delta (all points outside the white circles in panels a and b), and LC affected region (panel c–f), based on different backgrounds. Validation for LC affected region is divided into two time regimes with Jul-Dec showed in panel c and d, and Jan–Jun shown in panel e and f. The time span of all the in situ measurements shown here is from April 2002 to May 2014.

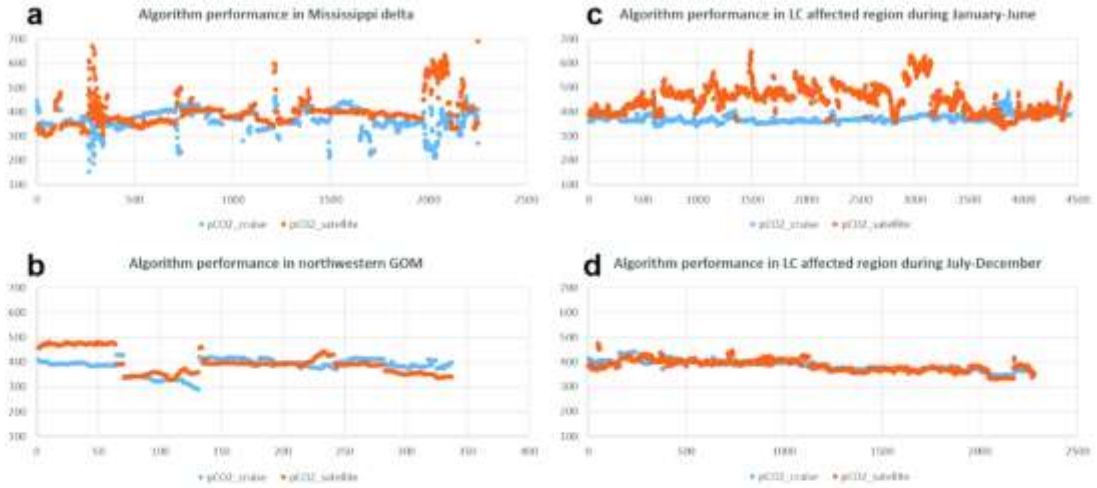

Fig. 8. Algorithm performances in the region near the Mississippi delta, northwestern GOM, and the LC affected region as specified in Fig. 7. X axis is the pixel number, and Y axis is pCO_2 in unit of μatm.

residence times are much shorter inshore, and dynamic salinity variations caused by extensive large river discharge create large variations in surface pCO_2. Compared with the satellite-derived pCO_2 map for Mississippi delta generated by Lohrenz and Cai (2006) for June 2003, the offshore patterns show general consistency but the results obtained in the present work reveal temporal and spatial variations in greater detail. For predictions in the northwestern GOM (Figs. 7a, b and 8b), the modeled pCO_2 generally followed the in situ pCO_2 variations, but with an RMSE of 44.1 μatm. For prediction in the LC affected region, pCO_2 was well estimated (RMSE of 13.7 μatm) between July and December (Figs. 7c, d and 8d), while between January and June (Figs. 7e, f and 8c), the estimation was poor with an RMSE of 79.8 μatm. For the January to June period of high uncertainty, we propose that dominant influences on pCO_2 influencing mechanisms may be different from the mechanisms that are dominant between July and December. Accordingly, pCO_2 variations are not well represented by the parameters used in our model. To some extent, this hypothesis is demonstrated by examining the monthly distribution of the LC (http://www7320.nrlssc.navy.mil/GLBhycom1-12_mosd/navo/arc_list_glfmexspdcurMN.html). The extension of the LC shows different distribution patterns during these two periods. Because the controlling mechanisms for surface pCO_2 can vary across geographic regions, region-specific algorithms need to be developed. For the Mississippi delta, river and ocean mixing are likely to strongly affect surface pCO_2 distributions, and SSS is a good tracer for mixing effects. Due to the complexity of this region, much further research needs to be done. For the LC affected region, parameters that reflect the characteristics of LC need to be found in order to better estimate surface pCO_2. For both the western and southern GOM, additional in situ data are needed for algorithm development.

5. Conclusion

With extensive field and satellite observations and after testing several algorithm approaches, an empirical algorithm for predicting the surface pCO_2 on the West Florida Shelf was developed and validated. The algorithm took Julian day and MODIS-derived CHL, Kd_Lee, and SST as inputs, and determined algorithm coefficients through multivariate nonlinear regression against concurrent in situ pCO_2 measurements. The algorithm showed reasonably good performance and was used to derive spatial distribution maps of surface pCO_2 distributions on the WFS as well as their seasonality and interannual changes. Observed distributions and temporal changes can be well explained based on a sensitivity analysis for the input parameters. Application of the algorithm to other GOM waters showed variable performance, indicating that different pCO_2 controlling mechanisms exist in different regions.

Acknowledgments

This work was supported by a USGS (G14PD00047) fellowship and a University South Florida fellowship-Gulf Oceanographic Charitable Trust Endowed Fellowship in College of Marine Science. We thank Dr. Xinping Hu (Texas A & M University) for sharing one cruise data in western GOM. LLR thanks the U.S. Geological Survey Coastal and Marine Geology Program and NASA grant NNH13ZDA001N for funding data collection and the compilation of GOM data which the authors then used. The pCO_2 data can be found at the Surface Ocean CO_2 Atlas v3 (SOCAT), which is an international effort, supported by the International Ocean Carbon Coordination Project (IOCCP), the Surface Ocean Lower Atmosphere Study (SOLAS), and the Integrated Marine Biogeochemistry and Ecosystem Research program (IMBER), to deliver a uniformly quality-controlled surface ocean CO_2 database. The many researchers and funding agencies responsible for the collection of data and quality control are thanked for their contributions to SOCAT. We also thank NASA for providing MODIS satellite data and processing software. Any use of trade, firm, or product names is for descriptive purposes only and does not imply endorsement by the U.S. Government. The efforts of two anonymous reviewers, who provided extensive comments and suggestions to improve the manuscript, is greatly appreciated.

Appendix A. Supporting information

Supplementary data associated with this article can be found in the online version at doi:10.1016/j.csr.2016.09.004.

References

Arruda, R., Calil, P.H.R., Bianchi, A.A., Doney, S.C., Gruber, N., Lima, I., Turi, G., 2015. Air-sea CO_2 fluxes and the controls on ocean surface pCO_2 seasonal variability in the coastal and open-ocean southwestern Atlantic Ocean: A modeling study. Biogeosciences 12, 5793–5809.

Bai, Y., Cai, W., He, X., Zhai, W., Pan, D., Dai, M., Yu, P., 2015. A mechanistic semi-analytical method for remotely sensing sea surface pCO_2 in river-dominated coastal oceans: a case study from the East China Sea. J. Geophys. Res. Oceans 120, 2331–2349. http://dx.doi.org/10.1002/2014JC010632.

Barnes, B.B., Hu, C., 2015. Cross-sensor continuity of satellite-derived water clarity in the Gulf of Mexico: Insights into temporal aliasing and implications for long-term water clarity assessment. IEEE Trans. Geosci. Remote Sens. 53, 1761–1772.

Bates, N., R., Merlivat, L., 2001. The influence of short-term wind variability on air-sea CO_2 exchange. Geophys. Res. Lett. 28 (17), 3281–3284.

Bates, N.R., Knap, A.H., Michaels, A.F., 1998. Contribution of hurricanes to local and global estimates of air-sea exchange of CO_2. Nature 395, 58–61.

Bauer, J.E., Cai, W., Raymond, P.A., Bianchi, T.S., Hopkinson, C.S., Regnier, P.A.G., 2013. The changing carbon cycle of the coastal ocean. Nature 504, 61–70. http://dx.doi.org/10.1038/nature12857.

Benway, H.M., Coble, P.G., 2014. Report of the U. S. Gulf of Mexico carbon cycle synthesis workshop, March 27–28, 2013, ocean carbon and biogeochemistry program and North American Carbon Program. pp. 67.

Berryman, A.D., Goudiabe, D., Moore, P., 2008. A multiple linear regression of pCO_2 against sea-surface temperature, salinity, and chlorophyll a at station ALOHA and its potential for estimate pCO_2 from satellite data. Elizabeth City, NC,

Borges, A.V., Delille, B., Frankignoulle, M., 2005. Budgeting sinks and sources of CO_2 in the coastal ocean: diversity of ecosystems counts. Geophys. Res. Lett. 32, L14601. http://dx.doi.org/10.1029/2005GL023053,

Borges, A.V., Ruddick, K., Lacroix, G., Nechad, B., Astereca, R., Rousseau, V., Harlay, J., 2010. Estimating pCO_2 from remote sensing in the Belgian coastal zone. ESA Special Publications SP, 686, http://hdl.handle.net/2268/81111,

Cai, W., Hu, X., Huang, W., Murrell, M.C., Lehrter, J.C., Lohrenz, S.E., Chou, W., Zhai, W., Hollibaugh, J.T., Wang, Y., Zhao, P., Guo, X., Gundersen, K., Dai, M., Gong, G., 2011. Acidification of subsurface coastal waters enhanced by eutrophication. Nat. Geosci. 4 (11), 766–770.

Campbell, J.W., 1995. The lognormal distribution as a model for bio-optical variability in the sea. J. Geophys. Res. 100 (C7), 13237–13254. http://dx.doi.org/10.1029/95JC00458.

Cannizzaro, J., Hu, C., Carder, K.L., Kelble, C.R., Melo, N., Johns, E.M., Vargo, G.A., Heil, C.A., 2013. On the accuracy of SeaWiFS ocean color data products on the West Florida Shelf. J. Coast. Res. 29 (6), 1257–1272. http://dx.doi.org/10.2112/JCOASTRES-d-12-00223.1.

Chagaris, D.D., Mahmoudi, B., Walters, C.J., Allen, M.S., 2013. Simulating the trophic impacts of fishery policy options on the West Florida Shelf using ecopath with Ecosim. Mar. Coast. Fish. 7 (1), 44–58.

Chen, C.T.A., Huang, T., Chen, Y., Bai, Y., He, X., Kang, Y., 2013. Air–sea exchanges of CO_2 in the world's coastal seas. Biogeosciences 10, 6509–6544. http://dx.doi.org/10.5194/bg-10-6509-2013,

Chen, L., Xu, S., Gao, Z., Chen, H., Zhang, Y., Zhan, J., Li, W., 2011. Estimation of monthly air-sea CO_2 flux in the southern Atlantic and Indian Ocean using in-situ and remotely sensed data. Remote Sens. Environ. 115 (8), 1935–1941,

Chierici, M., Olsen, A., Johannessen, T., Trinanes, J., Wanninkhof, R., 2009. Algorithms to estimate the carbon dioxide uptake in the northern North Atlantic using shipboard observations, satellite and ocean analysis data,. Deep-Sea Res. II 56, 630–639. http://dx.doi.org/10.1016/j.dsr2.2008.12.014,

Coble, P.G., Robbins, L.L., Daly, K.L., Cai, W.J., Fennel, K., Lohrenz S.E., 2010. A Preliminary Carbon Budget for the Gulf of Mexico. Fall 2010 issue of the OCB newsletter.

Cyronak, T., Santos, I.R., Erler, D.V., Maher, D.T., Eyre, B.D., 2014. Drivers of pCO_2 variability in two contrasting coral reef lagoons: The influence of submarine groundwater discharge. Glob. Biogeochem. Cycles 28, 398–414. http://dx.doi.org/10.1002/2013GB004598,

Evans, W., Hales, B., Strutton, P.G., Sabine, C.L., Feely R.A., 2008. Seasonal variability in surface ocean pCO_2 on the oregon and washington shelf, American geophysical union, fall meeting 2008, abstract #OS53C-1326.

Feely, R.A., Wanninkhof, R., Milburn, H.B., Cosca, C.E., Stapp, M., Murphy, P.P., 1998. A new automated underway system for making high precision pCO_2 measurements onboard research ships. Anal. Chim. Acta 377 (2–3), 185–191,

Feely, R.A., Sabine, C.L., Byrne, R.H., Millero, F.J., Dickson, A.G., Wanninkhof, R., Murata, A., Miller, L.A., Greeley, D., 2012. Decadal changes in the aragonite and calcite saturation state of the Pacific Ocean. Glob. Biogeochem. Cycles 26, GB3001. http://dx.doi.org/10.1029/2011GB004157.

Feng, L., Hu, C., 2016. Comparison of valid ocean data coverage between MODIS Terra and Aqua observations over the global oceans. IEEE Trans. Geosci. Remote Sens. 54, 1575–1585. http://dx.doi.org/10.1109/TGRS.2015.2483500,

Friedrich, T., Oschlies, A., 2009. Neural network-based estimates of North Atlantic surface pCO_2 from satellite data: a methodological study. J. Geophys. Res. 114, C03020. http://dx.doi.org/10.1029/2007JC004646,

Geilfus, N.X., Carnat, G., Papakyriakou, T., Tison, J.L., Else, B., Thomas, H., Shadwick, E., Delille, B., 2012. Dynamics of pCO_2 and related air-ice CO_2 fluxes in the Arctic coastal zone (Amundsen Gulf, Beaufort Sea). J. Geophys. Res. 117, C00G10. http://dx.doi.org/10.1029/2011JC007138,

Hales, B., Strutton, P.G., Saraceno, M., Letelier, R., Takahashi, T., Feely, R., Sabine, C., Chavez, F., 2012. Satellite-based prediction of pCO_2 in coastal waters of the eastern North Pacific, Prog. Oceanogr. 103, 1–15. http://dx.doi.org/10.1016/j.pocean.2012.03.001,

He, R., Weisberg, R.H., 2002. Tides on the west Florida shelf. J. Phys. Oceanogr. 32 (12), 3455–3473,

Hofmann, E.E., Cahill, B., Fennel, K., Friedrichs, M.A.M., Hyde, K., Lee, C., Mannino, A., Najjar, R.G., O'Reilly, J.E., Wilkin, J., Xue, J., 2011. Modeling the Dynamics of Continental Shelf Carbon. Annu. Rev. Mar. Sci. 3, 93–122. http://dx.doi.org/10.1146/annurev-marine-120709-142740,

Hu, C., Muller-Karger, F.E., Taylor, C.J., Carder, K.L., Kelble, C., Johns, E., Heil, C.A., 2005. Red tide detection and tracing using MODIS fluorescence data: A regional example in SW Florida coastal waters. Remote Sensing of Environment 97 (3), 311–321.

Hu, C., Muller-Karger, F.E., Swarzenski, W., 2006. Hurricanes, submarine groundwater discharge, and Florida's red tides. Geophys. Res. Lett. 33, L11601. http://dx.doi.org/10.1029/2005GL025440,

Hu, C., Muller-Karger, F.E., Murch, B., Myhre, D., Taylor, J., Luerssen, R., Moses, C., Zhang, C., Graemer, L., Hendee, J., 2009. Building an automated integrated observing system to detect sea surface temperature anomaly events in the Florida Keys. IEEE Trans. Geosci. Remote Sens. 47, 1607–1620.

Inoue, H.Y., Ishii, M., Matsueda, H., Kawano, T., Murata, A., Takasugi, Y., 2003. Distribution of the partial pressure of CO_2 in surface water (pCO_2^w) between Japan and the Hawaiian Islands: pCO_2^w–SST relationship in the winter and summer. Tellus 55B, 456–465,

Jamet, C., Moulin, C., Lefèvre, N., 2007. Estimation of the oceanic pCO_2 in the North Atlantic from VOS lines in-situ measurements: parameters needed to generate seasonally mean maps. Ann. Geophys. 25, 2247–2257,

Jiang, L., Cai, W., Wanninkhof, R., Wang, Y., Lüger, H., 2008. Air-sea CO_2 fluxes on the U.S. South Atlantic Bight: spatial and seasonal variability. J. Geophys. Res. 113, C07019. http://dx.doi.org/10.1029/2007JC004366,

Jo, Y.H., Dai, M., Zhai, W., Yan, X., Shang, S., 2012. On the variations of sea surface pCO_2 in the northern South China Sea: A remote sensing based neural network approach. J. Geophys. Res. 117, C08022. http://dx.doi.org/10.1029/2011JC007745,

Jolliff, J.K., Walsh, J.J., He, R., Weisberg, R., Stovall-Leonard, A., Coble, P.G., Conmy, R., Heil, C., Nababan, B., Zhang, H., Hu, C., Muller-Karger, F.E., 2003. Dispersal of the Suwannee River plume over the West Florida shelf: Simulation and observation of the optical and biochemical consequences of a flushing event. Geophys. Res. Lett. 30 (13). http://dx.doi.org/10.1029/2003GL016964,

Karagali, I., Badger, M., Sørensen, L.L., 2010. MERIS ocean colour data for the estimation of surface water pCO_2: the case studies of Peru and Namibia. European Space Agency, ESA Proceedings.

Lee, K., Wanninkhof, R., Takahashi, T., Doney, S.C., Feely, R.A., 1998. Low interannual variability in recent oceanic uptake of atmospheric carbon dioxide. Nature 396, 155–159,

Lee, Z., Darecki, M., Carder, K.L., Davis, C.O., Stramski, D., Rhea, W.J., 2005. Diffuse attenuation coefficient of downwelling irradiance: An evaluation of remote sensing methods. J. Geophys. Res. 110, C02017,

Lefèvre, N., Taylor, A., 2002. Estimating pCO_2 from sea surface temperatures in the Atlantic gyres. Deep-Sea Res. I 49, 539–554,

Lefèvre, N., Watson, A.J., Watson, A.R., 2005. A comparison of multiple regression and neural network techniques for mapping in situ pCO_2 data. Tellus 57B, 375–384,

Lefèvre, N., Aiken, J., Rutllant, J., Daneri, G., Lavender, S., Smyth, T., 2002. Observations of pCO_2 in the coastal upwelling off Chile: Spatial and temporal extrapolation using satellite data. J. Geophys. Res. 107 (C6), 3055. http://dx.doi.org/10.1029/2000JC000094,

Liu, Y., Weisberg, R.H., 2007. Ocean currents and sea surface heights estimated across the West Florida Shelf. J. Phys. Oceanogr. 37 (6), 1697–1713,

Lohrenz, S.E., Cai, W., 2006. Satellite ocean color assessment of air-sea fluxes of CO_2 in a river-dominated coastal margin. Geophys. Res. Lett. 33, L01601. http://dx.doi.org/10.1029/2005GL023942,

Lohrenz, S.E., Cai, W., Chen, F., Chen, X., Tuel, M., 2010. Seasonal variability in air-sea fluxes of CO_2 in a river-influenced coastal margin. J. Geophys. Res. 115, C10034. http://dx.doi.org/10.1029/2009JC005608,

Macpherson, G.L., 2009. CO_2 distribution in groundwater and the impact of groundwater extraction on the global C cycle. Chem. Geol. 264, 328–336. http://dx.doi.org/10.1016/j.chemgeo.2009.03.018,

Marrec, P., Cariou, T., Macé, E., Morin, P., Salt, L.A., Vernet, M., Bozec, Y., 2015. Dynamics of air-sea CO_2 fluxes in the northwestern European shelf based on voluntary observing ship and satellite observations. Biogeosciences 12 (18), 5371–5391,

Marrec, P., Thierry, C., Eric, M., Pascal, M., Marc, V., Yann, B., 2014. Dynamics of air-sea CO_2 fluxes based on FerryBox measurements and satellite-based prediction of pCO_2 in the Western English Channel, Geophysical Research Abstracts. 16: EGU2014-583.

Millero, F.J., Graham, T.B., Huang, F., Bustos-Serrano, H., Pierrot, D., 2006. Dissociation constants of carbonic acid in seawater as a function of salinity and temperature. Mar. Chem. 100, 80–94,

Mousa, H., Benallal, M.A., Goyet, C., Lefèvre, N., 2016. Satellite-derived CO_2 fugacity in surface seawater of the tropical Atlantic Ocean using a feedforward neural network. Int. J. Remote Sens. 37 (3), 580–598,

Nakaoka, S., Telszewski, M., Nojiri, Y., Yasunaka, S., Miyazaki1, C., Mukai, H., Usui, N., 2013. Estimating temporal and spatial variation of ocean surface pCO_2 in the North Pacific using a self-organizing map neural network technique. Biogeosciences 10, 6093–6106. http://dx.doi.org/10.5194/bg-10-6093-2013,

Olsen, A., Trinanes, J.A., Wanninkhof, R., 2004. Sea–air flux of CO_2 in the Caribbean Sea estimated using in situ and remote sensing data. Remote Sens. Environ. 89, 309–325 , http://dx.doi.org/10.1016/j.rse.2003.10.011,

Ono, T., Saino, T., Kurita, N., Sasaki, K., 2004. Basin-scale extrapolation of shipboard

pCO_2 data by using satellite SST and Chla. Int. J. Remote Sens. 25 (19), 3803–3815. http://dx.doi.org/10.1080/0143116031000115175.
Orr, J.C., Fabry, V.J., Aumont, O., Bopp, L., Doney, S.C., Feely, R.A., Gnanadesikan, A., Gruber, N., Ishida, A., Joos, F., Key, R.M., Lindsay, K., Maier-Reimer, E., Matear, R., Monfray, P., Mouchet, A., Najjar, R.G., Plattner, G.K., Rodgers, K.B., Sabine, C.L., Sarmiento, J.L., Schlitzer, R., Slater, R.D., Totterdell, I.J., Weirig, M.F., Yamanaka, Y., Yool, A., 2005. Anthropogenic ocean acidification over the twenty-first century and its impact on calcifying organisms. Nature 437, 681–686.
Pachauri, R.K., Meyer L. A., 2014. Climate Change 2014: Synthesis Report. IPCC, Geneva, Switzerland, 151
Padhy, P.C., Nayak, R.K., Dadhwal, V.K., Salim, M., Mitra, D., Chaudhury, S.B., Dutt, C.B.S., 2015. Estimation of partial pressure of carbon dioxide and air-sea fluxes in Hooghly Estuary based on in situ and satellite observations. J. Indian Soc. Remote Sens., 1–9.
Parard, G., Charantonis, A.A., Rutgerson, A., 2014. Remote sensing algorithm for sea surface CO_2 in the Baltic Sea. Biogeosci. Discuss. 11, 12255–12294. http://dx.doi.org/10.5194/bgd-11-12255-2014.
Pierrot, D., Neill, C., Sullivan, K., Castle, R., Wanninkhof, R., Lüger, H., Johannessen, T., Olsen, A., Feely, R.A., Cosca, C.E., 2009. Recommendations for autonomous underway pCO_2 measuring systems and data-reduction routines. Deep-Sea Res. II 56, 512–522.
Qin, B.Y., Tao, Z., Li, Z.W., Yang, X.F., 2014. Seasonal changes and controlling factors of sea surface pCO_2 in the Yellow Sea. In: Proceedings of the IOP Conference Series: Earth and Environmental Science, IOP Publishing, vol. 17, no. 1, p. 012025..
Rangama, Y., Boutin, J., Etcheto, J., Merlivat, L., Takahashi, T., Delille, B., Frankignoulle, M., Bakker, D.C.E., 2005. Variability of the net air–sea CO_2 flux inferred from shipboard and satellite measurements in the Southern Ocean south of Tasmania and New Zealand. J. Geophys. Res. 110, C09005. http://dx.doi.org/10.1029/2004JC002619.
Reynaud, S., Leclercq, N., Romaine-Lioud, S., Ferrier-Pages, C., Jaubert, J., Gattuso, J.P., 2003. Interacting effects of CO_2 partial pressure and temperature on photosynthesis and calcification in a scleractinian coral. Glob. Change Biol. 9, 1660–1668. http://dx.doi.org/10.1046/j.1529-8817.2003.00678.x.
Richey, J.E., Melack, J.M., Aufdenkampe, A.K., Ballester, V.M., Hess, L.L., 2002. Outgassing from Amazonian rivers and wetlands as a large tropical source of atmospheric CO_2. Lett. Nat. 416, 617–620.
Robbins, L.L., Coble, P., Clayton, T., Cai, W.-J., 2009. Ocean Biogeochemistry Scoping Workshop, Terrestrial and Coastal. Carbon Fluxes Gulf Mex., Workshop Rep., St. Petersburg, Fl. USA 6–8 May 2008: Open File Rep. 2009–1070, 46 (http://pubs.usgs.gov/of/2009/1070/).
Robbins, L.L., Wanninkhof, R., Barbero, L., Hu, X., Mitra, S., Yvon-Lewis, S., Cai, W.J., Huang, W.J., Ryerson T., 2014. Air-Sea Exchange. In: Benway, H.M., Coble, P.G., (Eds.), 2014, Report of the U.S. Gulf of Mexico Carbon Cycle Synthesis Workshop, March 27–28, 2013, Ocean Carbon and Biogeochemistry Program and North American Carbon Program. pp. 17–23. (http://www.us-ocb.org/publications/GMx_report_FINAL.pdf).
Rosenau, J.C., Faulkner, G.L., Hendry, C.W., Jr., Hull, R.W., 1977. Springs of Florida, Fla. Geol. Surv. Bull. 31, 438–453.
Sabine, C.L., Feely, R.A., Gruber, N., Key, R.M., Lee, K., Bullister, J.L., Wanninkhof, R., Wong, C.S., Wallace, D.W.R., Tilbrook, B., Millero, F.J., Peng, T., Kozyr, A., Ono, T., Rios, A.F., 2004. The oceanic sink for anthropogenic CO_2. Science 305 (5682), 367–371. http://dx.doi.org/10.1126/science.1097403.
Salisbury, J.E., Vandemark, D., Hunt, C.W., Campbell, J.W., McGillis, W.R., McDowell, W.H., 2008. Seasonal observations of surface waters in two Gulf of Maine estuary-plume systems: Relationships between watershed attributes, optical measurements and surface pCO_2. Estuar. Coast. Shelf Sci. 77, 245–252.
Sarma, V.V.S.S., 2003. Monthly variability in surface pCO_2 and net air-sea CO_2 flux in the Arabian Sea. J. Geophys. Res. 108 (C8), 3255. http://dx.doi.org/10.1029/2001JC001062.
Sarma, V.V.S.S., Saino, T., Sasaoka, K., Nojiri, Y., Ono, T., Ishii, M., Inoue, H.Y., Matsumoto, K., 2006. Basin-scale pCO_2 distribution using satellite sea surface temperature, Chl a, and climatological salinity in the North Pacific in spring and summer. Glob. Biogeochem. Cycles 20, GB3005. http://dx.doi.org/10.1029/2005GB002594.
Sarma, V.V.S.S., Krishna, M.S., Rao, V.D., Viswanadham, R., Kumar, N.A., Kumari, T.R., Gawade, L., Ghatkar, S., Tari, A., 2012. Sources and sinks of CO_2 in the west coast of Bay of Bengal. Tellus B 64, 1–10. http://dx.doi.org/10.3402/tellusb.v64i0.10961.
Saul, S.E., Walter, J.F., Die, D.J., Nasr, D.F., Donahue, B.T., 2013. Modeling the spatial distribution of commercially important reef fishes on the West Florida Shelf. Fish. Res. 143, 12–20.
Shadwick, E.H., Thomas, H., Comeau, A., Craig, S.E., Hunt, C.W., Salisbury, J.E., 2010. Air-Sea CO_2 fluxes on the Scotian Shelf: seasonal to multi-annual Variability. Biogeosciences 7, 3851–3867. http://dx.doi.org/10.5194/bg-7-3851-2010.
Signorini, S.R., Mannino, A., Najjar, R.G., Jr., Friedrichs, M.A.M., Cai, W., Salisbury, J., Wang, Z.A., Thomas, H., Shadwick, E., 2013. Surface ocean pCO_2 seasonality and sea-air CO_2 flux estimates for the North American east coast. J. Geophys. Res. 118, 5439–5460. http://dx.doi.org/10.1002/jgrc.20369.
Solomon, S., Qin, D., Manning, M., Chen, Z., Marquis, M., Averyt, K.B., Tignor, M., Miller, H.L., 2007. Climate Change 2007: The Physical Science Basis. Contribution of Working Group I to the Fourth Assessment Report of the Intergovernmental Panel on Climate Change. Cambridge Univ. Press, New York.
Stephens, M.P., Samuels, G., Olson, D.B., Fine, R.A., Takahashi, T., 1995. Sea-air flux of CO_2 in the North Pacific using shipboard and satellite data. J. Geophys. Res. 100 (C7), 13571–13583.
Sun, Q., Tang, D., Wang, S., 2012. Remote-sensing observations relevant to ocean acidification. Int. J. Remote Sens. 22 (23), 7542–7558.
Takahashi, T., Sutherland, S.C., Chipman, D.W., Goddard, J.G., Ho, C., Newberger, T., Sweeney, C., Munro, D.R., 2014. Climatological distributions of pH, pCO_2, total CO_2, alkalinity, and $CaCO_3$ saturation in the global surface ocean, and temporal changes at selected locations. Mar. Chem. 164, 95–125. http://dx.doi.org/10.1016/j.marchem.2014.06.004.
Takahashi, T., Sutherland, S.C., Sweeney, C., Metzl, A.P.N., Tilbrook, B., Bates, N., Wanninkhof, R., Feely, R.A., Sabine, C., Olafsson, J., Nojiri, Y., 2002. Global sea–air CO_2 flux based on climatological surface ocean pCO_2, and seasonal biological and temperature effects. Deep-Sea Res. II 49, 1601–1622.
Takahashi, T., Sutherland, S.C., Wanninkhof, R., Sweeney, C., Feely, R.A., Chipman, D.W., Hales, B., Friederich, G., Chavez, F., Chris, S., Watson, A.J., Bakker, D., Schuster, U., Metzl, N., Yoshikawa-Inoue, H., Ishii, M., Midorikawa, T., Nojiri, Y., Aens, K., Tobias, S., Hoppeman, M., Olafsson, J., Arnarson, T.S., Tilbrook, B., Johannessen, T., Olsen, A., Bellerby, R., Wong, C.S., Delille, B., Bates, N.R., Baar, H., 2009. Climatological mean and decadal change in surface ocean pCO_2, and net sea–air CO_2 flux over the global oceans. Deep-Sea Res. II 56, 554–577.
Tao, Z., Qin, B., Li, Z., Yang, X., 2012. Satellite observations of the partial pressure of carbon dioxide in the surface water of the Huanghai Sea and the Bohai Sea. Acta Oceanol. Sin. 31 (3), 67–73.
Telszewski, M., Chazottes, A., Schuster, U., Watson, A.J., Moulin, C., Bakker, D.C.E., Gonzalez-Davila, M., Johannessen, T., Kortzinger, A., Lager, H., Olsen, A., Omar, A., Padin, X.A., Rios, A.F., Steinhoff, T., Santana-Casiano, M., Wallace, D.W.R., Wanninkhof, R., 2009. Estimating the monthly pCO_2 distribution in the North Atlantic using a self-organizing neural network. Biogeosciences 6, 1405–1421.
Tseng, C., Liu, K., Gong, G., Shen, P., Cai, W., 2011. CO_2 uptake in the East China Sea relying on Changjiang runoff is prone to change. Geophys. Res. Lett. 38, L24609. http://dx.doi.org/10.1029/2011GL049774.
Turk, D., Book, J.W., McGillis, W.R., 2013. pCO_2 and CO_2 exchange during high bora winds in the Northern Adriatic. J. Mar. Syst. 117–118, 65–71. http://dx.doi.org/10.1016/j.jmarsys.2013.02.010.
Vandemark, D., Salisbury, J.E., Hunt, C.W., Shellito, S.M., Irish, J.D., McGillis, W.R., Sabine, C.L., Maenner, S.M., 2011. Temporal and spatial dynamics of CO_2 air-sea flux in the Gulf of Maine. J. Geophys. Res. 116, C01012. http://dx.doi.org/10.1029/2010JC006408.
Walsh, J.J., Jolliff, J.K., Darrow, B.P., Lenes, J.M., Milroy, S.P., Remsen, A., Weisberg, R.H., 2006. Red tides in the Gulf of Mexico: where, when, and why? J. Geophys. Res. Oceans 111 (C11).
Wang, Z.A., Liu, X., Byrne, R.H., Wanninkhof, R., Bernstein, R.E., Kaltenbacher, E.A., Patten, J., 2007. Simultaneous spectrophotometric flow-through measurements of pH, carbon dioxide fugacity, and total inorganic carbon in seawater. Anal. Chim. Acta 1, 23–26. http://dx.doi.org/10.1016/j.aca.2007.05.048.
Wanninkhof, R., Olsen, A., Trinanes, J., 2007. Air-Sea CO_2 Fluxes in the Caribbean Sea from 2002–2004. J. Mar. Syst. 66, 272–284. http://dx.doi.org/10.1016/j.jmarsys.2005.11.014.
Wanninkhof, R., Barbero, L., Byrne, R., Cai, W., Huang, W., Zhang, J., Baringer, M., Langdon, C., 2015. Ocean acidification along the Gulf Coast and East Coast of the USA. Cont. Shelf Res. 98, 54–71.
Wanninkhof, R., Park, G.H., Takahashi, T., Sweeney, C., Feely, R., Nojiri, Y., Gruber, N., Doney, S.C., McKinley, G.A., Lenton, A., Le Quere, C., Heinze, C., Schwinger, J., Graven, H., Khatiwala, S., 2013. Global ocean carbon uptake: magnitude, variability and trends. Biogeosciences 10, 1983–2000. http://dx.doi.org/10.5194/bg-10-1983-2013.
Watanabe, A., 2007. pCO_2 distribution in the East China Sea continental shelf estimated from satellite sea surface temperature, Chla, and climatological salinity. Geophys. Res. Abstr. 9, 01680.
Weisberg, R.H., He, R., 2003. Local and deep-ocean forcing contributions to anomalous water properties on the West Florida Shelf. J. Geophys. Res. 108, 3184. http://dx.doi.org/10.1029/2002JC001407.
Weiss, R.F., 1974. Carbon dioxide in water and seawater: the solubility of a non-ideal gas. Mar. Chem. 2, 203–215.
Widdicombe, S., Spicer, J.I., 2008. Predicting the impact of ocean acidification on benthic biodiversity: what can animal physiology tell us? J. Exp. Mar. Biol. Ecol. 366, 187–197. http://dx.doi.org/10.1016/j.jembe.2008.07.024.
Wipf, J., Palacios, S.L., Kudela R.M., 2012. Sink or Source? Evaluation of the CO_2 Air-sea flux in the santa barbara channel using remote-sensing data, American Geophysical Union, fall meeting 2012, abstract #B13F-07.
Xue, Z., He, R., Fennel, K., Cai, W., Lohrenz, S., Huang, W., Tian, H., 2014. Modeling pCO_2 variability in the Gulf of Mexico. Biogeosciences 11, 12673–12695. http://dx.doi.org/10.5194/bgd-11-12673-2014.
Zhai, W., Dai, M., Cai, W., Wang, Y., Hong, H., 2005. The partial pressure of carbon dioxide and air–sea fluxes in the northern South China Sea in spring, summer and autumn. Mar. Chem. 96, 87–97. http://dx.doi.org/10.1016/j.marchem.2004.12.002.
Zhao, J., Barnes, B., Melo, N., English, D., Lapointe, B., Muller-Karger, F., Schaeffer, B., Hu, C., 2013. Assessment of satellite-derived diffuse attenuation coefficients and euphotic depths in south Florida coastal waters. Remote Sens. Environ. 131, 38–50.
Zhu, Y., Shang, S., Zhai, W., Dai, M., 2009. Satellite-derived surface water pCO_2 and air–sea CO_2 fluxes in the northern South China Sea in summer. Prog. Nat. Sci. 19 (6), 775–779. http://dx.doi.org/10.1016/j.pnsc.2008.09.004.

APPENDIX B:

ESTIMATING SURFACE pCO_2 IN THE NORTHERN GULF OF MEXICO: WHICH REMOTE SENSING MODEL TO USE?

Chen, S., Hu, C., Cai, W. J., and Yang, B. (2017a). Estimating surface pCO_2 in the northern Gulf of Mexico: Which remote sensing model to use? *Continental Shelf Research, 151, 94-110.*

Continental Shelf Research 151 (2017) 94–110

Contents lists available at ScienceDirect

Continental Shelf Research

journal homepage: www.elsevier.com/locate/csr

Estimating surface pCO_2 in the northern Gulf of Mexico: Which remote sensing model to use?

Shuangling Chen[a], Chuanmin Hu[b,*], Wei-Jun Cai[b], Bo Yang[c]

[a] College of Marine Science, University of South Florida, 140 7th Avenue, South, St. Petersburg, FL 33701, USA
[b] College of Earth, Ocean, & Environment, University of Delaware, 111 Robinson Hall, Newark, DE 19716, USA
[c] School of Oceanography, University of Washington, Seattle, WA 98105, USA

ARTICLE INFO

Keywords:
Surface pCO_2
TA
DIC
Northern GOM
MODIS
Remote sensing

ABSTRACT

Various approaches and models have been proposed to remotely estimate surface pCO_2 in the ocean, with variable performance as they were designed for different environments. Among these, a recently developed mechanistic semi-analytical approach (MeSAA) has shown its advantage for its explicit inclusion of physical and biological forcing in the model, yet its general applicability is unknown. Here, with extensive in situ measurements of surface pCO_2, the MeSAA, originally developed for the summertime East China Sea, was tested in the northern Gulf of Mexico (GOM) where river plumes dominate water's biogeochemical properties during summer. Specifically, the MeSAA-predicted surface pCO_2 was estimated by combining the dominating effects of thermodynamics, river-ocean mixing and biological activities on surface pCO_2. Firstly, effects of thermodynamics and river-ocean mixing ($pCO_{2@mixing}$) were estimated with a two-endmember mixing model, assuming conservative mixing. Secondly, pCO_2 variations caused by biological activities ($\Delta pCO_{2@bio}$) was determined through an empirical relationship between sea surface temperature (SST)-normalized pCO_2 and MODIS (Moderate Resolution Imaging Spectroradiometer) 8-day composite chlorophyll concentration (CHL). The MeSAA-modeled pCO_2 (sum of $pCO_{2@mixing}$ and $\Delta pCO_{2@bio}$) was compared with the field-measured pCO_2. The Root Mean Square Error (RMSE) was 22.94 μatm (5.91%), with coefficient of determination (R^2) of 0.25, mean bias (MB) of −0.23 μatm and mean ratio (MR) of 1.001, for pCO_2 ranging between 316 and 452 μatm. To improve the model performance, a locally tuned MeSAA was developed through the use of a locally tuned $\Delta pCO_{2@bio}$ term. A multivariate empirical regression model was also developed using the same dataset. Both the locally tuned MeSAA and the regression models showed improved performance comparing to the original MeSAA, with R^2 of 0.78 and 0.84, RMSE of 12.36 μatm (3.14%) and 10.66 μatm (2.68%), MB of 0.00 μatm and −0.10 μatm, MR of 1.001 and 1.000, respectively. A sensitivity analysis was conducted to study the uncertainties in the predicted pCO_2 as a result of the uncertainties in the input variables of each model. Although the MeSAA was more sensitive to variations in SST and CHL than in sea surface salinity (SSS), and the locally tuned MeSAA and the empirical regression models were more sensitive to changes in SST and SSS than in CHL, generally for these three models the bias induced by the uncertainties in the empirically derived parameters (river endmember total alkalinity (TA) and dissolved inorganic carbon (DIC), biological coefficient of the MeSAA and locally tuned MeSAA models) and environmental variables (SST, SSS, CHL) was within or close to the uncertainty of each model. While all these three models showed that surface pCO_2 was positively correlated to SST, the MeSAA showed negative correlation between surface pCO_2 and SSS and CHL but the locally tuned MeSAA and the empirical regression showed the opposite. These results suggest that the locally tuned MeSAA worked better in the river-dominated northern GOM than the original MeSAA, with slightly worse statistics but more meaningful physical and biogeochemical interpretations than the empirical regression model. Because data from abnormal upwelling were not used to train the models, they are not applicable for waters with strong upwelling, yet the empirical regression approach showed ability to be further tuned to adapt to such cases.

* Corresponding author.
E-mail address: hu@usf.edu (C. Hu).

https://doi.org/10.1016/j.csr.2017.10.013
Received 14 March 2017; Received in revised form 6 September 2017; Accepted 30 October 2017
Available online 06 November 2017

Nomenclature

AOML	Atlantic Oceanographic and Meteorological Laboratory
CDIAC	Carbon Dioxide Information Analysis Center
CDOM	Colored Dissolved Organic Matter
CHL	Chlorophyll-a Concentration
CO2SYS	CO_2 System Program
DIC	Dissolved Inorganic Carbon
ECS	East China Sea
GOM	Gulf of Mexico
IDL	Interactive Data Language
LDEO	Lamont-Doherty Earth Observatory
MARS	Mississippi-Atchafalaya River System
MB	Mean Bias
MeSAA	Mechanistic Semi-Analytical Algorithm
MLD	Mixed Layer Depth
MR	Mean Ratio
MODIS	Moderate Resolution Imaging Spectroradiometer
NBS	National Bureau of Standards
R^2	Coefficient of Determination
RMSE	Root Mean Square Error
SOMs	Self-Organizing Maps
SSS	Sea Surface Salinity
SST	Sea Surface Temperature
TA	Total Alkalinity
USGS	U. S Geological Survey
WFS	West Florida Shelf

1. Introduction

Coastal air-sea CO_2 flux plays an important role in the global carbon budget (Borges et al., 2005; Cai et al., 2006, Cai, 2011; Chen et al., 2007). Due to the complexity of biogeochemical and physical processes in coastal margins (Lefevre et al., 2002; Fennel et al., 2008; Dai et al., 2009; Zhai et al., 2009; Atkins et al., 2013; Bauer et al., 2013; Ikawa et al., 2013; Marotta et al., 2010; Norman et al., 2013), large uncertainties still exist in coastal air-sea CO_2 flux estimation (Bauer et al., 2013; Chen et al., 2013). On the other hand, oceanic uptake of CO_2 has resulted in ocean acidification or decreased surface water pH (by − 0.1 units) (Caldeira and Wickett, 2003; Orr et al., 2005; Doney et al., 2009; Sun et al., 2012; Pachauri and Meyer, 2014), leading to a decrease in marine biodiversity and decline in ecosystems and environments (Widdicombe and Spicer, 2008; Doney, 2010; Dickinson et al., 2012). Surface pCO_2 is a critical term in understanding coastal ocean acidification and air-sea CO_2 flux calculation (Bauer et al., 2013; Feely et al., 2010; Cai et al., 2011), thus it is important to quantify surface pCO_2 with high accuracy.

In principle, surface water pCO_2 in coastal oceans is mainly controlled by four processes: physical mixing, thermodynamic effect, biological activities, and air-sea CO_2 exchange (Fennel et al., 2008; Ikawa et al., 2013; Xue et al., 2016). Different water masses have specific carbonate characteristics such as total alkalinity (TA, μmol kg^{-1}) and dissolved inorganic carbon (DIC, μmol kg^{-1}). The horizontal and vertical mixing among these water masses can affect the surface pCO_2 distribution in a dynamic way. In a carbonate system, once sea surface temperature (SST, °C), sea surface salinity (SSS, practical salinity unit) and pressure are known, any two parameters of TA, DIC, pCO_2, and pH can be used to calculate the others and CO_2 speciation (e.g., $[CO_3^{-2}]$ and thus carbonate mineral saturation state) using the CO_2 System Program (CO2SYS) (Pierrot and Wallace, 2006). Ocean thermodynamic effect is dependent on SST, and the relationship between surface pCO_2 and SST can be estimated with an exponential function ($pCO_{2@T2} = pCO_{2@T1} \times e^{0.0423\times(T_2-T_1)}$) (Takahashi et al., 2002, 2009) although the exact parameter can deviate slightly from 0.0423 in coastal waters (Bai et al., 2015; Joesoef et al., 2015). Biological activities such as photosynthesis, respiration, and calcification have direct effects on surface pCO_2 (Reynaud et al., 2003) because photosynthesis consumes CO_2, respiration produces CO_2, and calcification depletes both TA and DIC in a 2 to 1 ratio. The air-sea CO_2 exchange can also impact surface pCO_2 values during extreme events (e.g., hurricane, storms) (Bates et al., 1998; Bates and Merlivat, 2001; Turk et al., 2013). However, it is difficult and challenging to quantify all these complicated processes separately.

Closely linked to the above processes, several environmental variables can affect surface water pCO_2, such as SST, SSS, mixed layer depth (MLD, m), and chlorophyll-a concentration (CHL, mg m^{-3}). With these variables as model inputs, various approaches such as empirical regression (Lohrenz and Cai, 2006; Lohrenz et al., 2010; Marrec et al., 2015; Chen et al., 2016) and feedforward neural network (Jo et al., 2012) have been developed to model surface pCO_2 in coastal oceans. In addition, surface pCO_2 models have been developed for different oceanic regions through the use of self-organizing maps (SOMs), either pattern recognition neural network based (Lefevre et al., 2005; Friedrich and Oschlies, 2009a, 2009b; Telszewski et al., 2009; Nakaoka et al., 2013) or linear regression based (Signorini et al., 2013; Parard et al., 2015, 2016). Generally, these empirical approaches can predict surface pCO_2 with relatively low uncertainties ($\leq$ 40 μatm) and can be applied to different kinds of coastal margins (e.g., river-dominated, upwelling-dominated, and current-dominated) when the model coefficients are tuned locally. However, as with any other empirical approaches, the disadvantage of these models is that each model is only applicable to the modeled data range and environment, and the predicted result is hard to interpret physically, biologically, or chemically.

With the aim to overcome the problems inherited in empirical models, recently, a nonlinear semi-mechanistic model together with SOMs has been developed and used in the upwelling dominated US western margins (Hales et al., 2012). In this model, temperature is used as a main parameter to measure vertical mixing which varies in different upwelling subregions; changes in DIC and TA caused by mixing and thermal forcing are modeled with changes in SST and CHL; and then surface pCO_2 is calculated from DIC and TA using CO2SYS. This method overcomes the nonlinearity of the marine carbonate system, but errors in the modeled DIC and TA could propagate through the calculation of surface pCO_2. Also recently, a mechanistic semi-analytical algorithm (MeSAA) was developed to model summertime surface pCO_2 in a river-dominated coastal ocean, namely the East China Sea (ECS) (Bai et al., 2015), to study pCO_2 variations in response to various controlling mechanism during summertime. The main idea is to quantify the effects of dominant processes (horizontal river-ocean mixing, thermodynamic effect, and biological activities) on surface pCO_2 in summer when river discharge plays a significant role in affecting ocean properties. In the work of Bai et al. (2015), the effects of river-ocean mixing and thermodynamics were estimated by assuming conservative mixing between river and ocean end members, and the biological effect was parameterized by an empirical relationship between SST-normalized surface pCO_2 and CHL developed in the adjacent open ocean. Song et al. (2016) applied the MeSAA method to the Bering Sea in summertime, when it is dominated by oceanic waters. They modified the MeSAA by removing the river-ocean mixing term and adding a reference term that has relatively stable temperature with minimal influence from mixing and biological processes. Although both results showed relatively high uncertainties, such approach may still provide a new way in quantifying surface pCO_2 variations, especially for river-dominated regions. However, the applicability of this type of mechanistic approach to other river-dominated regions is unknown.

Compared with the ECS which is affected by only one big river

(Yangtze River), the northern Gulf of Mexico (GOM) (Fig. 1) receives river inputs from the Mississippi-Atchafalaya River System (MARS) as well as several smaller rivers, resulting in a more complicated environment. Massive input of organic and inorganic terrestrial carbon and large amounts of nutrients enhance the biological activities in this area, which may lead to very low surface pCO_2 levels and a corresponding large uptake of atmospheric CO_2 (Cai, 2003; Lohrenz and Cai, 2006; Cai and Lohrenz, 2010; Huang et al., 2015b). In summertime, the northern GOM exhibits maximum stratification where thermodynamics, strong biological activities and horizontal mixing along salinity gradient are dominant factors in influencing surface pCO_2 (Rabalais et al., 2002; Morey et al., 2003; Huang et al., 2015a, 2015b). The MARS plume is not constrained on the continental shelf in summertime (Hu et al., 2003), instead, the plume can reach the slope areas and to the Florida Straits (Ortner et al., 1995; Hu et al., 2005). Therefore, river-ocean mixing may play a major role in influencing surface pCO_2 distributions in the northern GOM.

The primary objective of this paper is thus to test the applicability of the MeSAA model to another river-dominated margin, the northern GOM where river discharge plays an important role in affecting the ocean's biogeochemical properties. However, different from that of the East China Sea, the northern GOM is also a warmer, more closed marginal sea with more complex river end member conditions. Therefore, another objective is to compare the MeSAA model results with results from a locally tuned MeSAA model and a conventional empirical regression model, both specifically tuned for the same region. Although some work has been done in modeling surface pCO_2 in this area (Lohrenz and Cai, 2006; Lohrenz et al., 2010), due to lack of long-term in situ data, more work is required to develop improved models for synoptic mapping of surface pCO_2 with high accuracy via satellite remote sensing. In this study, the original MeSAA, the locally tuned MeSAA, and the empirical regression approaches are applied using an extensive dataset collected from the northern GOM to 1) test the applicability of the MeSAA approach in the northern GOM, 2) understand the effects of river-ocean mixing and biological processes on surface pCO_2, 3) develop a locally tuned MeSAA model for the northern GOM, and 4) compare the performance of the MeSAA, locally tuned MeSAA, and a locally tuned empirical regression model. The ultimate goal is to make recommendations on model development for this complex region, where the findings may also be extended to other river dominated margins.

The manuscript is structured as follows. The background and motivation of this work are introduced above. Section 2 presents the data and data processing methods; Section 3 describes the methods used in developing each model (original MeSAA, locally tuned MeSAA, and empirical regression); Section 4 presents the performance evaluation of each model; Section 5 discusses the model sensitivities (to uncertainties of the input variables) and strengths/weaknesses of each model; Finally, Section 6 summarizes the main findings with conclusions.

2. Data sources and data processing

2.1. Field data

Several cruise surveys collected underway surface water pCO_2 data from the northern GOM waters and the GOM open waters. These are described in Tables 1 and 2, respectively. None of these data were used in a recent effort to estimate surface pCO_2 on the West Florida Shelf (WFS) (Chen et al., 2016). Data from the northern GOM was collected between 2003 and 2013 in July–September, and data from the GOM open waters was collected between 2006 and 2013 in February–April and December. These data were obtained from the Carbon Dioxide Information Analysis Center (CDIAC) (http://cdiac.ornl.gov/) (Wanninkhof et al., 2013a, 2013b; Sabine et al., 2014; Cai et al., 2012a, 2012b, 2014;), the NOAA's Atlantic Oceanographic and Meteorological Laboratory (AOML) (http://www.aoml.noaa.gov/ocd/ocdweb/occ.html) (Wanninkhof et al., 2009, 2010, 2012a, 2012b, 2012c, 2013c), and the Lamont-Doherty Earth Observatory (LDEO) of Columbia University (http://www.ldeo.columbia.edu/res/pi/CO2/carbondioxide/pages/pCO2data.html) (Sutherland et al., 2013). For pCO_2 data collected in the northern GOM, due to abnormal upwelling in July 2009 (Zhang et al., 2012; Huang et al., 2015a), pCO_2 data collected around the Mississippi River mouth and adjacent offshore region (red boxes in Figs. 1b and 1c) showed much lower pCO_2 values than those collected

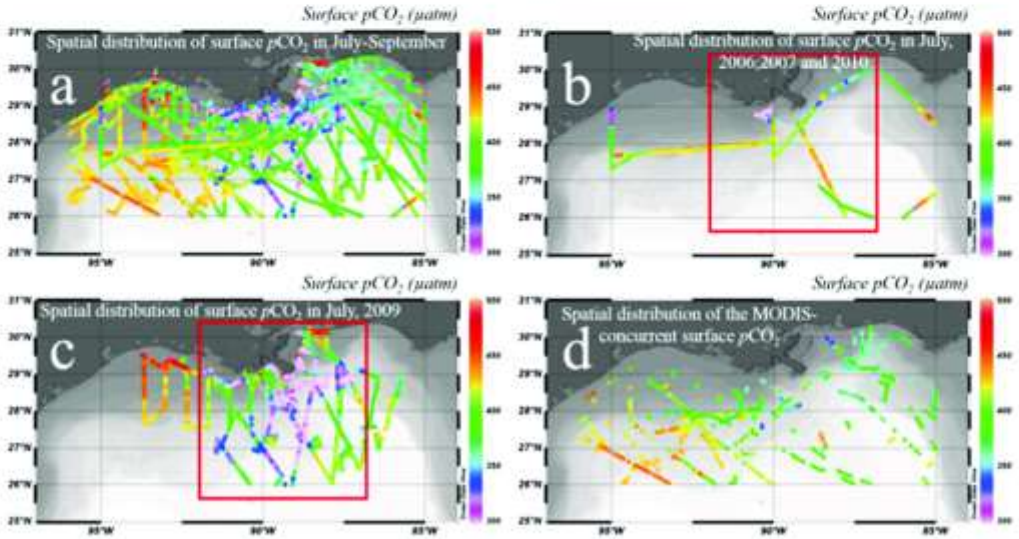

Fig. 1. Spatial distributions of the field-measured pCO_2 along the ship transects in the northern GOM (Table 1). (a) All cruise tracks; (b) and (c) are for July 2006, 2007 and 2010, and July 2009, respectively. Note that around the Mississippi River delta and offshore region (red boxes in b and c), due to abnormal upwelling in July 2009 (Huang et al., 2015a), pCO_2 data collected in July 2009 in this area were not used in this study; (d) Same field data as shown in (a) where high-quality MODIS L3 8 day CHL data encompassed the field measurement date.

Table 1
Underway pCO_2 measurements in the northern GOM during summer (July–September) at a depth of 5 m, with a measurement interval of ~ 2 or 3 min. For each cruise survey, the number of observations was greatly reduced when concurrent MODIS standard Level-3 8 day CHL composite data was found. Corresponding cruise tracks are shown in Fig. 1. Note that pCO_2 data collected in July 2009 around the Mississippi River delta and offshore region (red boxes in Figs. 1b and 1c) was not used in this study, due to abnormal upwelling in July 2009 (Huang et al., 2015a) in this area, but data collected outside this region in July 2009 were still used. Also note that data listed in this table were not used in Chen et al. (2016) to develop a pCO_2 model for the WFS.

Cruise_ID	Ship name	Date range	# of observations	# of observations with matching MODIS data
CoastalMS	Coastal Mississippi Buoy	7/1/2009–9/29/2009	684	0
MS_89W_30N	Coastal Mississippi Buoy	7/1/2011–9/30/2011	719	0
MS_89W_30N	Coastal Mississippi Buoy	7/11/2013–9/30/2013	645	1
GM0906	OSV Bold	9/6/2006–9/11/2006	7137	8
GM0708	OSV Bold	8/18/2007–8/24/2007	14,841	7
GM0907	R/V Cape Hatteras	7/19/2009–7/30/2009	6968	34
GU0804_Leg2	R/V Gordon Gunter	9/21/2008–9/22/2008	203	0
GU0903_Leg2	R/V Gordon Gunter	7/1/2009–7/20/2009	8267	25
GU0903_Leg3	R/V Gordon Gunter	8/1/2009–8/13/2009	4905	110
GU0904_Leg1	R/V Gordon Gunter	9/1/2009–9/10/2009	2670	38
GU0904_Leg2	R/V Gordon Gunter	9/15/2009–9/29/2009	1046	25
LasCuevas_10-09	M/V Las Cuevas	9/16/2009–9/20/2009	637	38
LasCuevas_10-10	M/V Las Cuevas	8/7/2010–8/18/2010	707	51
LasCuevas_11-10	M/V Las Cuevas	9/1/2010–9/8/2010	814	42
LasCuevas_12-10	M/V Las Cuevas	9/21/2010–9/28/2010	366	6
LasCuevas_9-10	M/V Las Cuevas	7/13/2010–7/18/2010	627	13
RB200306	R/V Brown	9/13/2003–9/19/2003	1172	32
RB200307	R/V Brown	9/21/2003–9/30/2003	1282	48
RB0606A	R/V Brown	7/31/2006–8/16/2006	972	32
RB200606B	R/V Brown	8/22/2006–9/11/2006	1692	1
RB200606T	R/V Brown	9/14/2006–9/15/2006	216	48
RB200705	R/V Brown	7/11/2007–7/17/2007	882	16
RB0905	R/V Brown	8/21/2009–9/12/2009	9855	82
RB0905T	R/V Brown	9/14/2009–9/15/2009	362	19
Total			67,669	676

Table 2
Underway pCO_2 measurements in the GOM open waters during spring (Feb–Apr) and winter (Dec), which were used to model the biological effect on surface pCO_2. These data were measured at a depth of 5 m, with a measurement interval of ~ 2 min. Data collected in summer was not used, due to the oligotrophic characteristics of the GOM open waters in summertime. For each cruise survey, the number of observations was greatly reduced when concurrent MODIS standard Level-3 8 day CHL composite data was found. Corresponding cruise tracks are shown in Figs. 2a & 2b. Note that these data were not used in Chen et al. (2016) to develop a pCO_2 model for the WFS.

Cruise_ID	Ship name	Date range	# of observations	# of observations with matching MODIS data
GU0802_Leg1	R/V Gordon Gunter	4/23/2008–4/30/2008	4238	141
GU0901_leg1	R/V Gordon Gunter	2/16/2009	233	0
GU0901_leg2	R/V Gordon Gunter	3/5/2009	174	6
GU0902_leg1	R/V Gordon Gunter	4/7/2009–4/13/2009	3104	116
GU0902_leg2	R/V Gordon Gunter	4/22/2009–4/30/2009	3774	45
LasCuevas_2-10	M/V Las Cuevas	2/3/2010–2/14/2010	1398	64
LasCuevas_5-10	M/V Las Cuevas	4/19/2010–4/20/2010	518	40
LasCuevas_14-10	M/V Las Cuevas	12/18/2010–12/20/2010	747	103
M131SFC	R/V Marcus G. Langseth	3/19/2013–3/20/2013	443	28
M132SFC	R/V Marcus G. Langseth	4/1/2013–4/3/2013	586	55
Total			15,215	598

in July of 2006, 2007 and 2010, as shown in Figs. 1b and 1c. Because this abnormal upwelling condition did not meet the conditions in the original MeSAA approach (horizontal river-ocean mixing, thermodynamic effects, and biological activities dominate the variations of surface pCO_2 in the summertime northern GOM) and abnormal upwelling may change the direction of air-sea CO_2 flux (Huang et al., 2015a), these low pCO_2 values were not selected in this study. Data from the GOM open waters were selected in order to model the biological effect on surface pCO_2. Note that due to the weak biological activities in the GOM open waters during summertime (CHL < 0.15 mg/m^3), data in July–September were not selected in modeling the biological effect. Seawater samples for measurements of pCO_2, SSS and SST in both the northern GOM and the GOM open waters were collected at a depth of ≤ 5 m using a shipboard flow-through seawater system. The full cruise tracks in the northern GOM and GOM open waters with color-coded in situ pCO_2 are shown in Figs. 1a and 2a, respectively. Surface pCO_2 was measured with a combination of a gas equilibrator and a non-dispersive, infrared analyzer Li-COR™ (model 6251 or 6262 or 7000 or 840A or 820) (Feely et al., 1998; Pierrot et al., 2009) with an accuracy of 2 μatm (or better) and a measurement interval of 2 or 3 min. The details of data collection, processing, and quality control can be found in Feely et al. (1998) and Pierrot et al. (2009) and Huang et al. (2015b). In addition to pCO_2, SSS and SST data were collected using a CTD (SBE-16 or SBE-21 or SBE-38 or SBE-45, Seabird Inc., USA, YSI 6600) integrated in the underway pCO_2 system.

All cruise data obtained from CDIAC, AOML and LDEO have undergone quality control analysis. These data were converted into the same format with an Interactive Data Language (IDL) program, and were visualized and quality controlled (i.e., by examining data quality flags and metadata files) to discard apparent errors (e.g., individual spikes due to instrument malfunction or other factors). A total of 67,669 pCO_2 observations were selected for the northern GOM to develop and validate the MeSAA and empirical models, and a total of 15,215 observations were selected for the GOM open waters to model the biological effect on surface pCO_2 for the MeSAA.

The MeSAA has two explicit components on modeling physical and

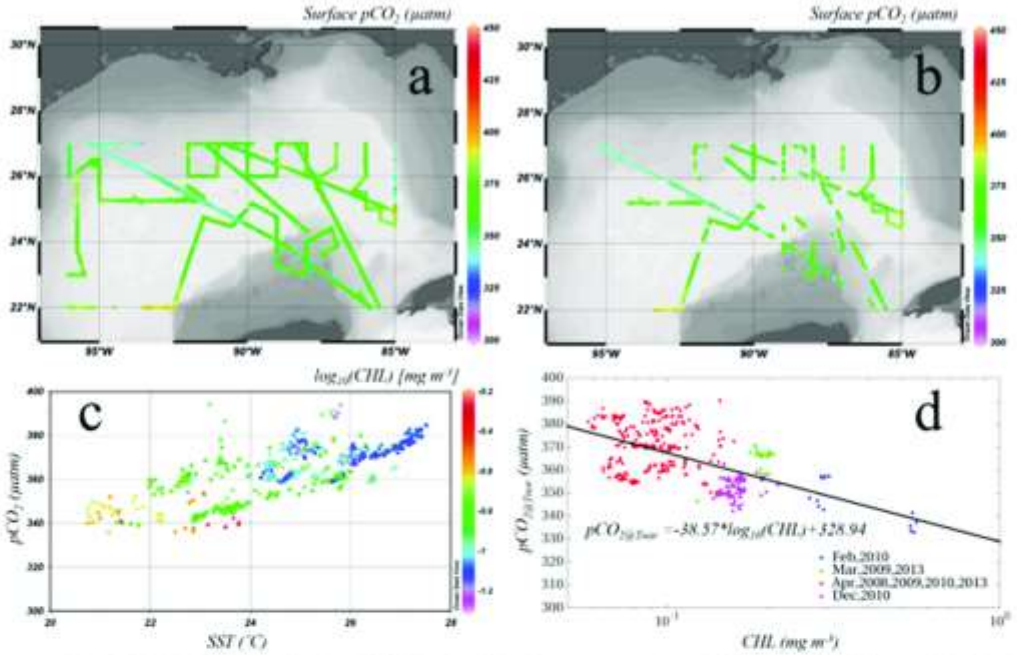

Fig. 2. Parameterization of the biological effect on surface pCO_2 with field data collected from the GOM open waters. (a) Spatial distributions of the field-measured pCO_2 along the ship transects in the GOM open waters (Table 2); (b) The same field data where high-quality MODIS L3 8 day CHL data encompassed the field measurement date; (c) Relationship between surface pCO_2 and SST, with CHL color coded in logarithmic scale. The corresponding surface pCO_2 spatial distribution is shown in (b). The strong dependency of surface pCO_2 on SST indicted the necessity of removing the thermodynamic effects for the quantification of the biological effect on surface pCO_2; (d) Relationship between SST-normalized pCO_2 ($pCO_{2@Tmon}$) and CHL. Note that to remove the thermodynamic effects on surface pCO_2, only data with SST restricted to within ± 1 °C of the monthly mean SST were applied.

biological effects, respectively. To model the physical effect, namely the effect of horizontal river and ocean mixing on surface pCO_2, through a two-endmember mixing model, TA and DIC data of the river and ocean endmembers were carefully selected. Specifically, river endmember TA_0 of 2420 μmol/kg and DIC_0 of 2450 μmol/kg at SSS_0 = 0.1, and ocean endmember TA_{ocean} of 2399.3 μmol/kg and DIC_{ocean} of 2082.8 μmol/kg at SSS_{ocean} = 36.04 from Huang et al. (2015a) were applied in this study. DIC_0 was assumed to be 30 μmol/kg higher than TA_0 (Guo et al., 2012; Cai et al., 2013), and oceanic TA and DIC were linearly normalized to salinity of 35 using Eqs. (1) and (2) (marked as TA_{35} and DIC_{35}, e.g., Yang et al., 2015) with the river endmember TA_0 and DIC_0 at SSS_0 = 0.1 as the intercepts, respectively. To quantify the variations of riverine TA of the Mississippi and Atchafalaya Rivers, TA data of both rivers between May 2006 and Feb 2015, were obtained from the U. S Geological Survey (USGS) water quality database (http://nwis.waterdata.usgs.gov/usa/nwis/qwdata). TA data for Atchafalaya River was the average of two stations (USGS Station 07381590 in Wax Lake Outlet at Calumet, LA, 29°41'52"N, 91°22'22"W, and Station 07381600 in Lower Atchafalaya River at Morgan City, LA, 29°41'33.4"N, 91°12'42.6"W), and TA data for the Mississippi River was from USGS Station 07374525 in Mississippi River at Belle Chasse, LA, (29°51'25"N, 89°58'40"W). As shown in Fig. 3, between May 2006 and Feb 2015, the TA ranges of Mississippi river and Atchafalaya River were 1204.0–2940.0 μmol/kg and 1014.0–3170.0 μmol/kg, respectively. In

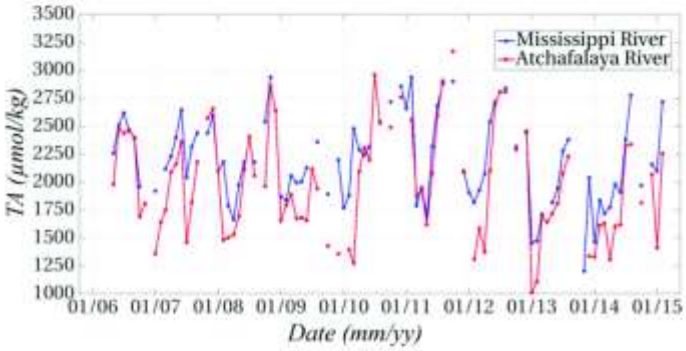

Fig. 3. Variations of TA of the Mississippi and Atchafalaya rivers between May 2006 and Feb 2015. Data for Atchafalaya River was the average of two stations (USGS Station 07381590 in Wax Lake Outlet at Calumet, LA (29°41'52"N, 91°22'22"W), and Station 07381600 in Lower Atchafalaya River at Morgan City, LA (29°41'33.4"N, 91°12'42.6"W). Data for Mississippi River was from the USGS Station 07374525 in Mississippi River at Belle Chasse, LA (29°51'25"N, 89°58'40"W).

summertime during this period, the TA range of Mississippi river was 2040–2880 μmol/kg, and the TA range of Atchafalaya River was 1460–2960 μmol/kg. According to the river flow rates of both rivers in summertime between May 2006 and Feb 2015, the Mississippi river contributed around 82% to the total river discharge to the northern GOM (data not shown here), thus the variation of river endmember TA_0 was 1935.6–2894.4 μmol/kg. The uncertainties of the parameterizations of TA_0 and DIC_0 caused by the variations in riverine TA and DIC in summertime were analyzed and quantified in Section 5.1.

$$TA_{35} = \frac{(TA_{ocean} - TA_0)}{(SSS_{ocean} - SSS_0)} \times (35 - SSS_0) + TA_0 \quad (1)$$

$$DIC_{35} = \frac{DIC_{ocean} - DIC_0}{SSS_{ocean} - SSS_0} \times (35 - SSS_0) + DIC_0 \quad (2)$$

2.2. MODIS data

To quantify the effect of biological activities on surface pCO_2, standard NASA Level-3 CHL data (version R2014.0) between 2003 and 2013 were obtained from the NASA Goddard Space Flight Center (http://oceancolor.gsfc.nasa.gov/). The use of satellite CHL was not only because there was no field CHL data available, but more importantly, the pCO_2 models were developed for satellite applications. Therefore, if satellite-derived CHL was used to train the models (see Sections 5.1–5.3) the errors in satellite-derived CHL would be implicitly included in the model coefficients. The 8-day composite Level-3 CHL data at 9-km resolution were generated from measurements by the Moderate Resolution Imaging Spectroradiometer (MODIS) on the Aqua satellite using community-accepted standard algorithms. Specifically, the Gordon and Wang (1994) algorithm was used to remove the atmospheric effects, after which a combination of band-ratio algorithm (O'Reilly et al., 2000) and band-subtraction algorithm (Hu et al., 2012) was used to estimate CHL. Various data quality flags (e.g., straylight, sun glint, etc.) were used to screen low-quality data when generating the global composite data (Patt et al., 2003). In general, comparison between satellite-derived CHL and field measured CHL showed uncertainties ranging from 5% to 33% (Gregg and Casey, 2004; Bailey and Werdell, 2006; Melin et al., 2007; Cannizzaro et al., 2013a).

3. Methods in model development

Concurrent and collocated MODIS and field data were used to develop and test all three models: the original MeSAA with its parameterization as presented in Bai et al. (2015), a modified MeSAA with locally-tuned parameterization, and an empirical regression model. Here "concurrent" means that the time of the field data collection is within the MODIS 8-day period, and "collocated" means that the field pCO_2 data within a 9-km MODIS pixel was averaged to match the satellite data.

After the strict quality control and field data binning, for the period between 2003 and 2013, 676 conjugate observations of field-measured pCO_2 and MODIS CHL data were available for the northern GOM (Fig. 1d), and 598 conjugate observations of field-measured pCO_2 and MODIS CHL data for the period between 2006 and 2013 were available for the GOM open waters (Fig. 2b). In the matched dataset for the northern GOM, field-measured pCO_2 ranged between 316.13 and 451.70 μatm, field-measured SST ranged between 27.95 and 31.51 °C, field-measured SSS ranged between 26.85 and 36.67, and satellite CHL ranged between 0.043 and 1.609 mg/m^3. In the matched dataset for the GOM open waters, the range of field-measured surface pCO_2, field-measured SST, field-measured SSS, and satellite-measured CHL were 336.22–394.04 μatm, 22.50–26.35 °C, 35.06–36.57, and 0.058–0.560 mg/m^3, respectively. These matched datasets were used to develop and validate the following pCO_2 models.

For both the original and locally tuned MeSAA models, pCO_2 was derived from the estimation of the influences from thermodynamics, river-ocean mixing, and biological activities. Field-measured pCO_2 was not used in the model development but used for model evaluation only. For the empirical regression model, the 2003–2013 pCO_2 dataset was divided randomly into two groups with one for model training and the other for model validation.

3.1. A brief description of the MeSAA

The details of this satellite remote sensing pCO_2 model – MeSAA – can be found in Bai et al. (2015), but for completeness a brief description is provided here.

For the physical aspect of river-ocean mixing ($pCO_{2@Mixing}$), conservative mixing of TA and DIC was assumed (Cai et al., 2010; Wang et al., 2013; Yang et al., 2015), and TA and DIC at certain salinity level were estimated with a linear river-ocean mixing model as shown in Eq. (3) (Jiang et al., 2008; Bai et al., 2015; Yang et al., 2015). Each pair of TA and DIC with ancillary SST, SSS and pressure was used to calculate a pCO_2 value with Eq. (4) using the CO2SYS (Pierrot and Wallace, 2006). Carbonic acid dissociation constants (K_1 and K_2) of Millero et al. (2006), Dickson's $KHSO_4$, pH scale of the National Bureau of Standards (NBS), and $[B]_T$ value of Uppstrom (1974) were applied in the CO2SYS pCO_2 calculation.

$$TA = \frac{TA_{35} - TA_0}{35} \times SSS + TA_0,\ DIC = \frac{DIC_{35} - DIC_0}{35} \times SSS + DIC_0 \quad (3)$$

To avoid redundancy, the thermodynamic effect on surface pCO_2 variation, through the use of SST, was also included.

$$pCO_{2@Mixing} = CO2SYS(TA, DIC, SST, SSS) \quad (4)$$

As shown in Fig. 2c, there is a clear trend showing the relationship between SST and surface pCO_2. To model the effect of biological activities on surface pCO_2, this thermodynamic effect needs to be removed first. To do so, pCO_2 data in the GOM open waters was restricted to within ± 1 °C of the monthly averaged SST of each month, and normalized to the monthly averaged SST using Eq. (5) (Takahashi et al., 2002, 2009).

$$pCO_{2@Tnor} = pCO_{2@Tobs} \times e^{0.0423 \times (T_{nor} - T_{obs})} \quad (5)$$

where T is SST in °C, and subscripts 'nor' and 'obs' symbol the normalized and observed values.

The variation of SST-normalized surface pCO_2 ($pCO_{2@Tnor}$) was supposed to be caused by the biological activities, which were related to changes in CHL. Thus, $pCO_{2@Tnor}$ was regressed against $\log_{10}$(CHL) by linear regression as shown in Eq. (6) and Fig. 2d. CHL was scaled logarithmically because CHL tends to be log-normal in large-scale distributions (Campbell, 1995).

$$pCO_{2@Tnor} = -38.57 \times log_{10}CHL + 328.94 \quad (6)$$

The integration of the changing rates in $pCO_{2@Tnor}$ over changes in CHL was regarded as the effect of biological activities on surface pCO_2. Therefore, to model the changing rates of surface pCO_2 corresponding to CHL changes, partial derivatives (over CHL) on both sides of Eq. (6) were calculated, and then the variation of surface pCO_2 caused by biological activities ($\Delta pCO_{2@bio}$) was obtained using Eq. (7) (CHL_0 was empirically set to 0.01 mg/m^3) by integrating the derived partial derivatives over the ranges of CHL. However, the final modeled pCO_2 via such integration alone showed large difference from the field-measured pCO_2. Therefore, different from Bai et al. (2015), two empirical coefficients (a and b) were added in Eq. (7) to account for the different pCO_2 response to biological activities between the northern GOM and GOM open waters through empirical regression, thus the total biological coefficient (B), which was the coefficient of $\log_{10}$(CHL) in the biological term $\Delta pCO_{2@bio}$, was 96.04.

$$\Delta pCO_{2@bio} = -38.57 \times (\log_{10} CHL - \log_{10} CHL_0) \times a + b \quad (7)$$

where a = 2.49, b = 2.57, and CHL_0 = 0.01 mg/m^3.

For model evaluation, the sum of river-ocean mixing and biological activities was used to represent the MeSAA-predicted surface pCO_2, as specified in Eq. (8), even though the biological component was based on empirical data fitting (Bai et al., 2015). The model-predicted pCO_2 was compared with the field-measured pCO_2, where coefficient of determination (R^2), root mean square error (RMSE), mean ratio (MR), and mean bias (MB) were used to gauge model performance. A histogram of the difference between field-measured pCO_2 and model-predicted pCO_2 was also generated to examine the error distributions.

$$pCO_2 = pCO_{2@Hmixing} + \Delta pCO_{2@bio} \quad (8)$$

3.2. Locally tuned MeSAA

The original MeSAA used an empirical relationship trained in the adjacent open ocean, where river-ocean mixing is minimum, to model the effects of biological activities on surface pCO_2 in the ECS (Bai et al., 2015). The extrapolation from open-ocean to the river-dominated northern GOM may be problematic. Therefore, in the locally tuned MeSAA this open-ocean based modeling component for the biological effect was replaced with a locally-trained empirical relationship between $\Delta pCO_{2@bio}$ and SSS and CHL, while the modeling of the river-ocean horizontal mixing ($pCO_{2@Hmixing}$) was kept the same as in the original MeSAA. Specifically, the residuals between the field-measured pCO_2 and $pCO_{2@Hmixing}$, expressed as ΔpCO_2, was calculated first using Eq. (9). Then, the relationships between ΔpCO_2 and environmental parameters such as SST, SSS, and CHL were examined. Finally, ΔpCO_2 was regressed against SSS and $\log_{10}$(CHL) by an empirical linear regression, and the calculated pCO_2 by Eq. (10) was regarded as the effect of biological activities on surface pCO_2, namely $\Delta pCO_{2@bio}$.

$$\Delta pCO_2 = pCO_{2@measured} - pCO_{2@Hmixing} \quad (9)$$

$$\Delta pCO_{2@bio} = 19.54 \times SSS + 8.31 \times \log_{10} CHL - 777.40 \quad (10)$$

Similar to the original MeSAA, for model evaluation, the sum of $pCO_{2@Hmixing}$ and $\Delta pCO_{2@bio}$ was used to represent the surface pCO_2 estimated from the locally tuned MeSAA. RMSE, R^2, MB and MR were calculated to gauge the model performance. A histogram of the difference between field-measured pCO_2 and modeled pCO_2 was generated to examine the error distributions.

3.3. Empirical regression

Chen et al. (2016) showed a multi-variate statistical approach to model surface pCO_2 on the WFS. The same approach was used to develop the relationship between surface pCO_2 and environmental variables (SST, SSS, CHL) as well as day of the year (Julday) for the northern GOM. The dataset was divided randomly into two groups, with one group used for model training and coefficient tuning, and the other for model validation. The relationships between surface pCO_2 and environmental variables were examined.

After extensive trial and error tests using various functional forms and model inputs, the regression equation was determined as:

$$pCO_2 = k_0x_1 + k_1x_2 + k_2x_3 + k_3x_4 + k_4x_1x_2 + k_5x_1x_3 + k_6x_1x_4 + k_7x_2x_3 + k_8x_2x_4 + k_9x_3x_4 + k_{10}x_1^2 + k_{11}x_2^2 + k_{12}x_3^2 + k_{13}x_4^2 + Constant \quad (11)$$

where x_3 = SST, x_2 = SSS, x_3 = $\log_{10}$(CHL), x_4 = cos (2π(Julday − γ)/365).

In this equation, Julday was sinusoidally normalized to reflect the seasonal feature (Friedrich and Oschlies, 2009a; Lefevre et al., 2005; Signorini et al., 2013), and γ was a tuning parameter ranging from 0 to 365 days, and was determined to be 330 by iteration until the minimum root mean square error (RMSE) between modeled and measured pCO_2 was reached. The final empirical pCO_2 model was thus determined as:

$$\begin{aligned} pCO_2 = & -202.75x_1 + 21.24x_2 + 426.12x_3 - 122.59x_4 \\ & + 1.53x_1x_2 - 3.06x_1x_3 + 2.86x_1x_4 - 12.68x_2x_3 \\ & + 0.85x_2x_4 + 7.67x_3x_4 + 2.77x_1^2 - 0.99x_2^2 \\ & - 72.31x_3^2 + 1.96x_4^2 + 2814.11 \end{aligned} \quad (12)$$

where x_1 = SST, x_2 = SSS, x_3 = $\log_{10}$(CHL), x_4 = cos (2π(Julday − 330)/365).

The model was subsequently applied to the other half of the dataset that was not used in the model development. RMSE, R^2, MB and MR were calculated to quantify the model performance in both model development and model validation. A histogram of the difference between field-measured pCO_2 and modeled pCO_2 was generated to examine the error distributions.

Note that although the model form in Eq. (12) is the same as in Chen et al. (2016), the model coefficients are specifically tuned for this dataset, thus different from those in Chen et al. (2016) for the WFS.

4. Results

In this section, the performance of each of the three models (original MeSAA, locally tuned MeSAA, and empirical regression) is examined and compared, in terms of statistical measures and spatial distribution patterns of modeled pCO_2.

4.1. Original MeSAA

Fig. 4a shows the comparison between $pCO_{2@Hmixing}$ calculated with the river-ocean mixing model and field-measured surface pCO_2. Clearly, the values of $pCO_{2@Hmixing}$ was higher than the field-measured surface pCO_2 across the SSS range (26.85–36.67) used in this study, but such a discrepancy was reduced at high SSS. This is because that the effect of biological uptake of CO_2 is strong and has not been taken into account yet, and at high SSS the TA and DIC values were getting close to those of the ocean endmember, thus $pCO_{2@Hmixing}$ values were getting close to the field-measured pCO_2. The variation of the biological term ($\Delta pCO_{2@bio}$) along with SSS in Fig. 4b demonstrated that the biological CO_2 removal at low SSS was more intense than at high SSS as $\Delta pCO_{2@bio}$ could reach − 209 µatm at low SSS. This is consistent with the high $pCO_{2@Hmixing}$ values at low salinity as shown in Fig. 4a and reported in the literature (Huang et al., 2013, 2015b).

The MeSAA-modeled pCO_2 (sum of $pCO_{2@Hmixing}$ and $\Delta pCO_{2@bio}$) was compared with the field-measured pCO_2 in Fig. 4c. Generally the modeled pCO_2 followed the in situ pCO_2 variations quite well at SSS > 30 with RMSE of 22.03 µatm (5.59%), MB of − 1.32 µatm and MR of 0.998 (Table 3). For SSS ≤ 30, surface pCO_2 was strongly overestimated with RMSE of 47.48 µatm (13.72%), MB of 42.08 µatm and MR of 1.121 (Table 3). Statistics for the whole SSS range used in this study showed a R^2 of 0.25, RMSE of 22.94 µatm (5.91%), MB of − 0.23 µatm and MR of 1.001 (Table 3). The strong overestimation in surface pCO_2 at SSS ≤ 30 (~ 7% of the northern GOM has such low salinity, the statistics was derived based on a salinity study that has not been published) was assumed to be caused either by the variations in the river endmember TA_0 and DIC_0 which could have a larger influence in the modeling of $pCO_{2@Hmixing}$ at low SSS, or by the non-sufficient modeling of the biological removal of CO_2. Quantification of the effect of the variations in TA_0 and DIC_0 in Section 5.1 demonstrated that the overestimation in surface pCO_2 at SSS ≤ 30 was mainly due to the variations in TA_0 and DIC_0. The histogram of the modeled pCO_2 residuals in Fig. 5c shows that 73.7% of the residuals were smaller than the standard deviation of the observed pCO_2 (± 26.43 µatm).

Comparing with the results of previously published works (Lohrenz and Cai, 2006; Lohrenz et al., 2010), the results from the MeSAA showed significant improvement, where for the same pCO_2 ranges

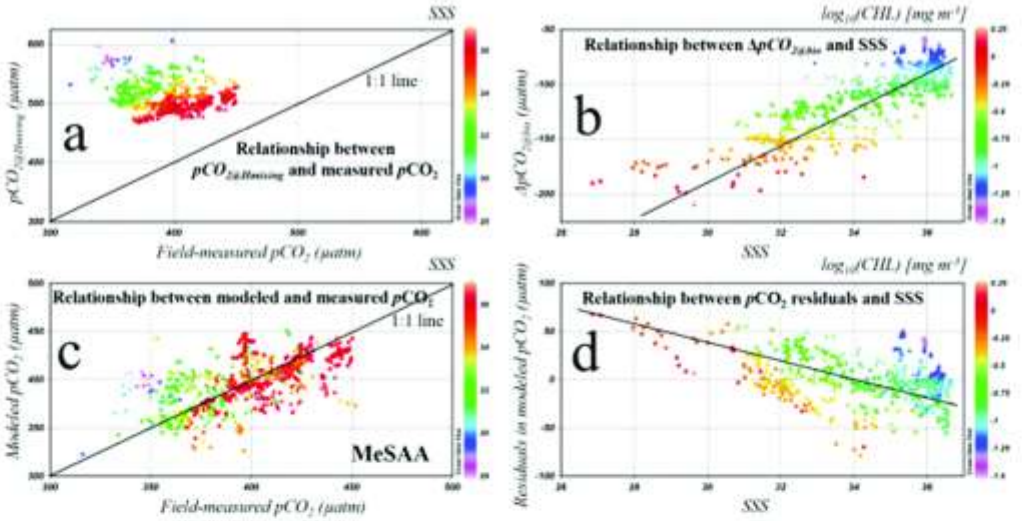

Fig. 4. Model performance of the original MeSAA. (a) Comparison between $pCO_{2@Henry}$ and field-measured pCO_2. $pCO_{2@Henry}$ was higher than the field-measured surface pCO_2, and with the decrease of SSS, the increase of the difference between $pCO_{2@Henry}$ and field-measured pCO_2 indicated that there should be stronger biological uptake of CO_2 at lower SSS; (b) Relationship between the modeled biological uptake of CO_2 ($\Delta pCO_{2@bio}$) and SSS, where the intense biological removal of CO_2 at lower SSS corresponded to higher $pCO_{2@Henry}$ at lower SSS; (c) Comparison between the MeSAA modeled pCO_2 and field-measured pCO_2; (d) Relationship between the MeSAA modeled pCO_2 residuals in (c) and SSS. The general linear relationship between the two indicated that either $pCO_{2@Henry}$ or $\Delta pCO_{2@bio}$ may not capture all the signals in pCO_2 variations caused either by horizontal mixing or by biological activities, respectively. Note that the statistics of this model performance were listed in Table 3.

RMSE reduced from 50.2 μatm in Lohrenz and Cai (2006) to 22.94 μatm in this study. Even though R^2 from the MeSAA was lower than in Lohrenz et al. (2010), the results here are still encouraging as the study region in Lohrenz et al. (2010) was much smaller and pCO_2 variation was much larger than the study here.

The spatial distribution of the MeSAA-predicted pCO_2 is shown in Fig. 5a. Compared with the in situ pCO_2 distribution (Fig. 1d), the MeSAA model appeared to be able to regenerate the spatial pCO_2 patterns, especially for the inshore-offshore pCO_2 gradient. The relatively low pCO_2 values (320–350 μatm) near the Mississippi River month and in the east of the MARS as well as the relatively high pCO_2 values in the west of the northern GOM were all predicted well. On the other hand, the distribution of the pCO_2 residuals shown in Fig. 5b revealed that in some locations (e.g., east of the northern GOM or to the east of 90°W) surface pCO_2 was either overestimated or underestimated. Such a discrepancy could be due to the rapid changes of the river plumes in response to wind and coastal currents, which in turn influenced the biological activities and therefore surface pCO_2. Clearly, the river-ocean mixing model or the biological effect model did not capture such changes very well, and in such a complex environment it is challenging to model the surface pCO_2 with very high accuracy (e.g., RMSE < 10 μatm).

To further examine the possible causes of the relatively large uncertainties in the MeSAA-modeled surface pCO_2, the relationships between the pCO_2 residuals and the environmental parameters (SST, SSS, and CHL) were investigated. As shown in Fig. 4d, there was a general

Table 3
Performance statistics of the MeSAA, locally tuned MeSAA, and the empirical regression models. The range of field-measured pCO_2 is 316.13–451.70 μatm. Y refers to modeled pCO_2 while X refers to measured pCO_2.

Methods			R^2	RMSE (μatm)	RMSE (%)	MB (μatm)	MR	Relationship between modeled and measured pCO_2	Range of modeled pCO_2 (μatm)	N (# of data)
MeSAA	**Whole SSS range**		**0.25**	**22.94**	**5.91**	**− 0.23**	**1.001**	$Y = 0.57X + 167.52$	**322.68–450.93**	**676**
	SSS > 30		0.25	22.03	5.59	− 1.32	0.998	$Y = 0.622X + 149.56$	326.63–450.93	659
	SSS ≤ 30		− 7.42	47.48	13.72	42.08	1.121	$Y = 0.555X + 198.77$	322.68–408.68	17
Locally tuned MeSAA	**Whole SSS range**		**0.78**	**12.36**	**3.14**	**0.00**	**1.001**	$Y = 0.782X + 86.82$	**335.34–435.59**	**676**
	SSS > 30		0.76	12.44	3.16	− 0.15	1.001	$Y = 0.871X + 91.07$	341.85–435.59	659
	SSS ≤ 30		0.67	9.41	2.75	5.70	1.017	$Y = 0.990X + 44.38$	335.34–403.90	17
Empirical Regression	Model development	Whole SSS range	0.84	10.35	2.62	− 0.00	1.001	$Y = 0.842X + 62.83$	329.01–443.82	338
		SSS > 30	0.83	10.40	2.63	0.07	1.001	$Y = 0.824X + 70.45$	349.39–443.82	331
		SSS ≤ 30	− 0.44	8.80	2.51	− 3.58	0.990	$Y = 0.884X + 36.96$	329.01–361.22	7
	Model validation	Whole SSS range	0.83	10.98	2.73	− 0.21	1.000	$Y = 0.816X + 73.21$	326.11–442.50	328
		SSS > 30	0.82	10.90	2.71	− 0.06	1.001	$Y = 0.792X + 83.21$	351.35–442.50	331
		SSS ≤ 30	0.56	13.89	3.72	− 5.02	0.987	$Y = 0.451X + 187.56$	326.11–364.03	10
	Both model development and validation	**Whole SSS range**	**0.84**	**10.66**	**2.68**	**− 0.10**	**1.000**	$Y = 0.829X + 68.15$	**326.11–443.82**	**676**
		SSS > 30	0.83	10.64	2.67	0.01	1.001	$Y = 0.818X + 76.87$	349.39–443.82	659
		SSS ≤ 30	0.49	11.73	3.19	− 4.43	0.988	$Y = 0.483X + 176.80$	326.11–364.03	17

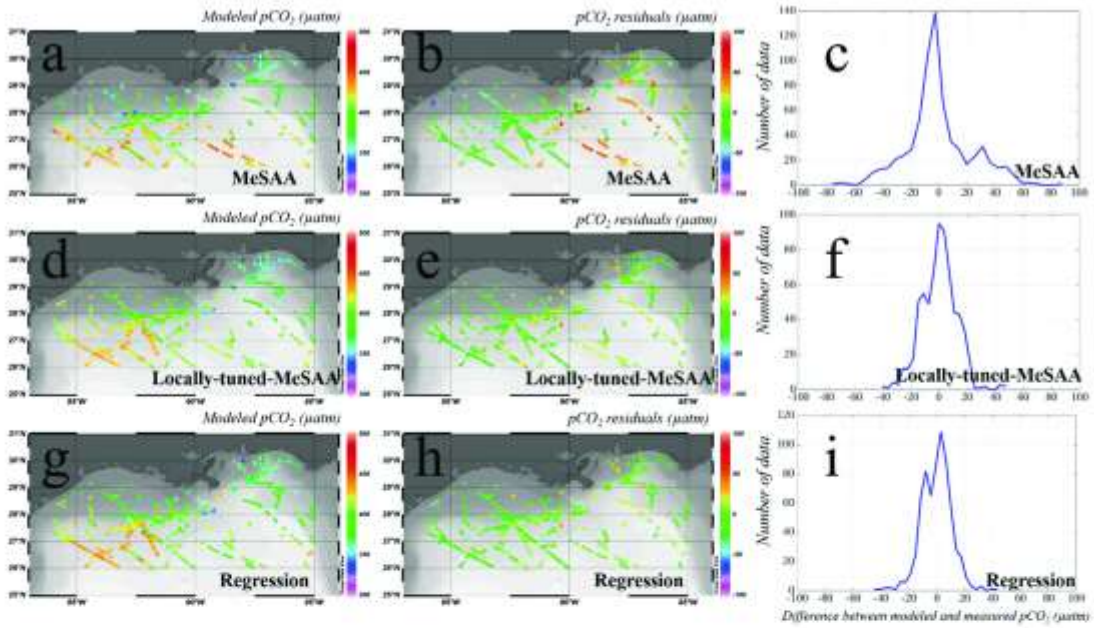

Fig. 5. Spatial distributions of the modeled surface pCO_2 and pCO_2 residuals (difference between modeled and measured pCO_2) in the northern GOM, and the histograms of the pCO_2 residuals, using the MeSAA (a–c), locally tuned MeSAA (d–f), and the empirical regression (g–i), respectively.

linear relationship between the pCO_2 residuals and SSS. This indicated that, although SSS could modulate the biological term $\Delta pCO_{2@bio}$ (Fig. 4b) and SSS was also used in the parameterization of $pCO_{2@Tmixing}$, the effect of SSS in the MeSAA-modeled pCO_2 was still not sufficiently expressed. The relationship between $pCO_{2@Tnor}$ and CHL in Eq. (6) assumed that variations in the normalized pCO_2 were dominated by the biological effects. However, in reality other possible factors such as the dynamic effects of mesoscale eddies, Loop Current, and vertical mixing of surface pCO_2 could also play a role, as shown in the data scattering in Fig. 2d. Furthermore, the effects of the biological activities may work differently in the northern GOM coastal waters from the GOM open waters, thus direct application of the biological relationship developed from the latter to the former may be questionable, requiring modification of the MeSAA.

4.2. Locally tuned MeSAA

Fig. 6e shows the comparison between modeled $\Delta pCO_{2@bio}$ using the locally tuned MeSAA and the residuals (ΔpCO_2) in the field-measured pCO_2 after subtracting the horizontal mixing term $pCO_{2@Hmixing}$. At SSS ≤ 35, the model performed reasonably well, but at SSS > 35 the biological removal of surface CO_2 appeared to be too strong. The comparison between the modeled pCO_2 (from the locally tuned MeSAA) and field-measured pCO_2 in Fig. 6d also showed similar patterns for data with SSS ≤ 35 and SSS > 35.

Statistically (Table 3), the locally tuned MeSAA showed better performance than the original MeSAA in estimating surface pCO_2 regardless of the SSS range considered. At SSS ≤ 30, the mean bias in the estimated pCO_2 was 5.70 μatm, possibly due to variations in the TA_0 and DIC_0 parameterizations, yet such a positive bias was much smaller than that of the original MeSAA (MB = 42.08 μatm) due to different ways in modeling the biological term $\Delta pCO_{2@bio}$. Such a greatly reduced underestimation in surface pCO_2 at SSS ≤ 30 indicated that, although the modeled result of Eq. (10) (based on Figs. 6a and 6b) was regarded as the biological term $\Delta pCO_{2@bio}$, it may also include some pCO_2 residuals in the mixing term that was not fully accounted for in the quantification of $pCO_{2@Hmixing}$ or in other weak but non-ignorable processes (e.g., vertical mixing), all of which were included implicitly in the empirical coefficients of Eq. (10). The histogram of the pCO_2 residuals (Fig. 5f) shows that 97.3% of the residuals were smaller than the standard deviation of the observed pCO_2 (± 26.43 μatm), which also indicated that the locally tuned MeSAA had improved performance comparing to the original MeSAA.

Figs. 5d and 5e show the spatial distributions of surface pCO_2 and pCO_2 residuals derived from the locally tuned MeSAA model. Compared with the field-measured pCO_2 distributions, the spatial distributions along the inshore-offshore gradient showed similar patterns, which also showed more detailed features and higher accuracies than from the original MeSAA model. In addition, the relatively low pCO_2 values near the river mouth and in the east of the northern GOM as well as the relatively high pCO_2 values in the west of the northern GOM were all revealed clearly. Compared with the pCO_2 residual distributions from the original MeSAA, the residual distributions from the locally tuned MeSAA in Fig. 5e showed lower uncertainties, suggesting improved model performance.

4.3. Empirical regression

Figs. 7a–7c show the relationships between surface pCO_2 and environmental variables (CHL, SSS and SST), and Figs. 7d–7f show the multi-variate regression model (Eq. (12)) for the pCO_2 prediction. For the model development (Fig. 7d), RMSE was 10.35 μatm (2.62%), with a R^2 of 0.84, MB of − 0.00 μatm and MR of 1.001. There was negligible overestimation at SSS > 30 (RMSE = 10.40 μatm (2.63%), MB = 0.07 μatm, and MR = 1.001) and slight underestimation at SSS ≤ 30 (RMSE = 8.80 μatm (2.51%), MB = − 3.58 μatm, and MR = 0.990). Fig. 7e shows the model validation with data not used in the model training. Performance measures are similar to those for the model

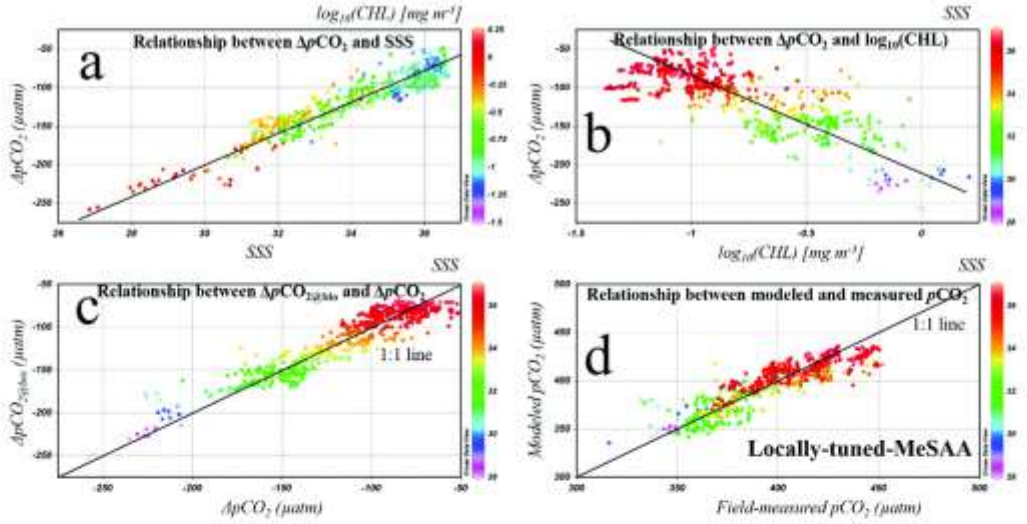

Fig. 6. Model performance of the locally tuned MeSAA. (a) Relationship between ΔpCO_2 (field-measured pCO_2 minus $pCO_{2@thermal}$) and SSS; (b) Relationship between ΔpCO_2 and SSS; (c) Comparison between MeSAA modeled $\Delta pCO_{2@bio}$ and ΔpCO_2; (d) Comparison between the modeled pCO_2 (from locally-tuned-MeSAA) and field-measured pCO_2. Note that the statistics of this model performance were listed in Table 3.

training, with an RMSE of 10.98 μatm (2.73%), R^2 of 0.83, MB of − 0.21 μatm and MR of 1.000. RMSE for the combined datasets (both model development and model validation) was 10.66 μatm (2.68%), with an R^2 of 0.84, MB of − 0.10 μatm, and MR of 1.000 (Table 3). The histogram of residuals for the combined datasets (Fig. 5i) shows that 97.9% of the residuals were smaller than the standard deviation of the observed pCO_2 (± 26.43 μatm).

Figs. 5g and 5h show the spatial distribution of empirically-modeled surface pCO_2 and the pCO_2 residuals. Similar to those from the locally tuned MeSAA, the spatial patterns along the inshore-offshore gradient agreed with those determined from in situ measurements, and they also showed more detailed features than those provided by the original MeSAA.

In summary, the empirical regression method showed slightly better performance than the locally tuned MeSAA, and both models showed improvements over the original MeSAA.

5. Discussion

In this section, the sensitivities of the mechanistic models (original MeSAA and locally tuned MeSAA) and the empirical model (empirical regression) to the empirical coefficients and uncertainties in the model inputs are analyzed, and strengths and weaknesses of each model as well as the controls of surface pCO_2 in summertime northern GOM are discussed.

5.1. Sensitivity analysis of the MeSAA

5.1.1. Model sensitivity to empirical coefficients

The parameterization of the MeSAA included two types of empirically derived coefficients: the first included the TA and DIC values of the river and ocean endmembers, which affected the horizontal mixing term $pCO_{2@thmixing}$, and the second included the biological coefficient of biological activities to surface pCO_2, which influenced the biological term $\Delta pCO_{2@bio}$.

As described in Section 2.1, the variation of the river endmember TA_0 was 1935.6–2894.4 μmol/kg, about 20% lower or higher than the TA_0 value (2420 μmol/kg) used in this study. Therefore, in order to evaluate the model sensitivity to changes in TA_0 and DIC_0, river endmember TA_0 was varied by ± 20% with the assumption that DIC_0 was about 30 μmol/kg higher than TA_0, while all other parameters remained unchanged. In addition, TA and DIC values for the ocean endmember were fixed because the Loop Current water was stable.

Visual inspection of Figs. 8a and 8b indicate that the MeSAA was more sensitive to changes in TA_0 and DIC_0 at lower SSS. For SSS ≤ 30, a 20% increase in TA_0 (Fig. 8a) produced about 47.60 μatm higher pCO_2, while for SSS > 30 the same 20% increase in TA_0 and DIC_0 caused a much smaller change (MB = 8.15 μatm) in the predicted pCO_2. A similar disparity in the model sensitivity was observed for a 20% decrease in TA_0 when data were partitioned to SSS ≤ 30 and SSS > 30 (Fig. 8b). The detailed statistics in Table 4 also suggested that the MeSAA was more sensitive to TA_0 and DIC_0 for low-SSS (SSS ≤ 30) waters than for high-SSS (SSS > 30) waters. Therefore, the overestimation in the MeSAA-modeled pCO_2 at SSS ≤ 30 in Section 4.1 could be attributed to the variations in river endmember TA_0 and DIC_0. However, on the other hand, based on the statistics over the whole SSS range used in this study, the uncertainties in the MeSAA-predicted pCO_2 due to changes in TA_0 and DIC_0 were within the RMSE uncertainties of the MeSAA.

Similar to the sensitivity analysis of the MeSAA to TA_0 and DIC_0, to examine the effect of the variations in the biological coefficient (B = 96.04) on the MeSAA-modeled pCO_2, B was varied by ± 20%. As shown in Figs. 8c and 8d and Table 4, a 20% increase (decrease) in B produced about − 22.51 μatm (22.51 μatm) lower (higher) pCO_2, with bigger changes in modeled pCO_2 at lower SSS (≤ 30). Either with a 20% increase or decrease in B, in each case, the RMSE at the whole SSS range, SSS > 30, and SSS ≤ 30 were 23.38 μatm, 22.91 μatm and 38.25 μatm, respectively. Compared with the statistics of the MeSAA model itself, these results indicate that the MeSAA was sensitive to the biological coefficient B, and the sensitivity decreased with increasing SSS.

5.1.2. Model sensitivity to environmental parameters

Field SST, SSS, and satellite CHL were used during the development of the MeSAA. In order to better understand how the MeSAA model responds to these input variables, a sensitivity analysis was conducted. For each test, one input variable was varied while the others remained

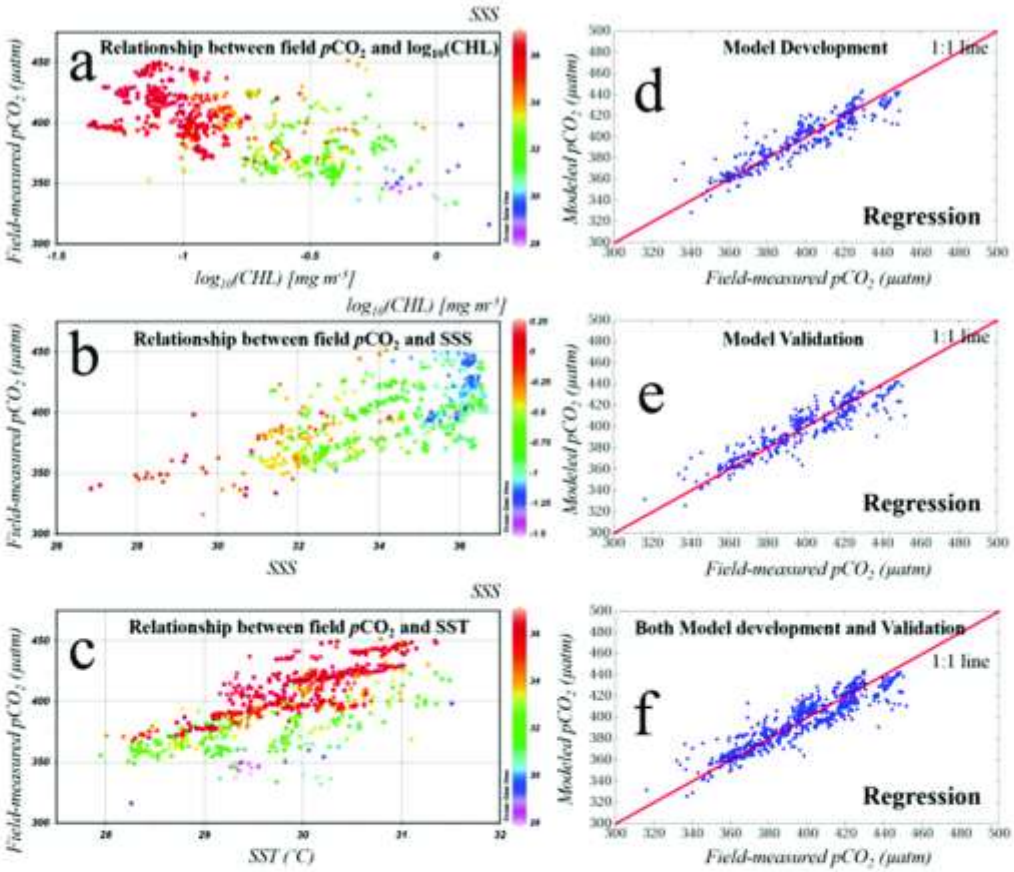

Fig. 7. Model performance of the empirical regression. (a)–(c) Relationships between field-measured pCO_2 and $\log_{10}$ (CHL), SSS, and SST, respectively. (d)–(f) Scatterplots of modeled pCO_2 (Y-axis) versus field-measured pCO_2 (X-axis) during model development, model validation, and both model development and validation, respectively. Note that the statistics of this model performance were listed in Table 3.

unchanged. Considering the typical uncertainties of satellite-derived SST and CHL, SST was varied by ± 1 °C, SSS by ± 1, and CHL by ± 35%. Note that although field-measured SSS was used in the model due to the lack of satellite-derived high-resolution SSS, in the future such SSS could be derived from ocean color data with a possible uncertainty of ± 1. The model response results are shown in Figs. 8e–8j, with statistics such as RMSE, MR, and MB listed in Table 4.

Variations in SST and SSS would only affect the horizontal mixing term $pCO_{2@Hmixing}$ of the MeSAA. As shown in Figs. 8e–8h, the sensitivities of the MeSAA to SST and SSS changes are similar. A 1 °C increase produced higher pCO_2 (MB = 19.65 μatm, Fig. 8e), and a 1 °C decrease produced lower pCO_2 (MB = − 19.01 μatm, Fig. 8f). Likewise, a 1 increase (decrease) in SSS produced lower (higher) pCO_2 (MB = − 10.00 μatm or − 10.64 μatm, Figs. 8g and 8h), with slightly higher pCO_2 decrease (increase) for SSS ≤ 30 than for SSS > 30. These results suggest that the MeSAA is more sensitive to SST changes than to SSS changes.

Variations in CHL would only influence the biological term $\Delta pCO_{2@bio}$ of the MeSAA. Figs. 8i and 8j demonstrate that the MeSAA had the same sensitivity to CHL changes at different SSS values, with MB of − 12.52 μatm and 17.97 μatm for 35% increase and decrease in CHL, respectively.

In short, the sensitivity analysis showed that pCO_2 variations caused by the assumed changes in both the model coefficients and input environmental variables were all within or close to the RMSE uncertainties of the MeSAA model itself, although the model showed relatively higher sensitivity to the biological coefficient B and SST. Thus, unless the uncertainties in these model inputs are systematic biases instead of random noise – which is unlikely according to the validation result of satellite data products – these uncertainties would not have a significant influence on the MeSAA-predicted pCO_2 when large regions are considered as a whole.

5.2. Sensitivity analysis of the locally tuned MeSAA

Based on the parameterizations of the locally tuned MeSAA in Section 4.2, the sensitivities of the locally tuned MeSAA to TA_0 and DIC_0 and SST were the same as the MeSAA. Therefore, only sensitivities of the locally tuned MeSAA to SSS and CHL were analyzed.

Figs. 9a and 9b show the sensitivity of the locally tuned MeSAA to SSS, with statistics shown in Table 4. Note that since SSS was included in both the physical mixing term $pCO_{2@Hmixing}$ and the biological term $\Delta pCO_{2@bio}$ in the locally tuned MeSAA, the variation in SSS would influence both terms. As a result, the locally tuned MeSAA showed the

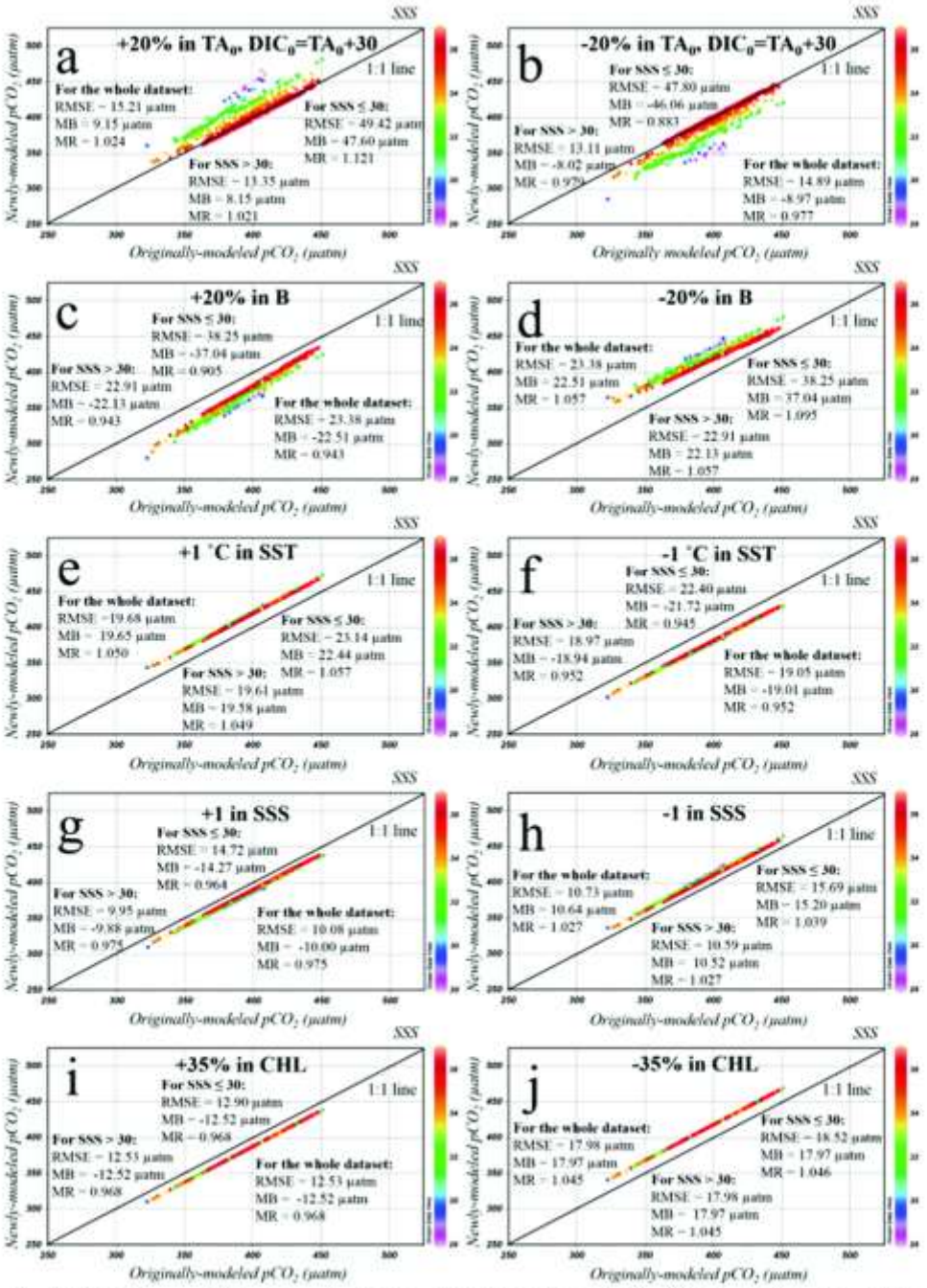

Fig. 8. Sensitivity of the MeSAA to the parameterizations of river endmember TA_0 (a and b), the biological coefficient (B) (c and d), SST (e and f), SSS (g and h), and CHL (i and j). Data used here are from the dataset of the northern GOM (Table 1 and Fig. 1d). In each panel, only one parameter was varied while all others were kept unchanged, and the newly-modeled pCO_2 corresponding to each set of parameterization variation is compared with the originally-modeled pCO_2. Note that the statistics of each analysis were shown in each panel, as listed in Table 4.

Table 4
Performance statistics in each sensitivity analysis of the MeSAA, locally tuned MeSAA, and the empirical regression models. For each case, one of the model inputs was artificially increased or decreased by a certain amount while other model inputs remained unchanged. RMSE, MR and MB were calculated by comparing the newly-predicted pCO_2 with the originally-predicted pCO_2. Note that the statistics of the sensitivities of the locally tuned MeSAA to TA_0 and SST are the same as those of the original MeSAA because TA_0 and SST only affect $pCO_{2\text{diffusion}}$ and both models had the same calculation of $pCO_{2\text{diffusion}}$.

Cases		RMSE (μatm)[a]			RMSE (%)[a]			MB (μatm)[a]			MR[a]		
+20% in TA_0	Whole SSS range	15.21			3.95			9.15			1.024		
	SSS > 30	13.35			3.48			8.15			1.021		
	SSS ≤ 30	49.42			12.54			47.60			1.121		
-20% in TA_0	Whole SSS range	14.89			3.86			-8.97			0.977		
	SSS > 30	13.11			3.42			-8.02			0.979		
	SSS ≤ 30	47.80			12.13			-46.06			0.883		
+20% in B	Whole SSS range	23.38			6.05			-22.51			0.943		
	SSS > 30	22.91			5.93			-22.13			0.943		
	SSS ≤ 30	38.25			9.84			-37.04			0.905		
-20% in B	Whole SSS range	23.38			6.05			22.51			1.057		
	SSS > 30	22.91			5.93			22.13			1.057		
	SSS ≤ 30	38.25			9.84			37.04			1.095		
+1 °C in SST	Whole SSS range	19.68	19.68	21.86	4.97	4.97	5.36	19.65	4.97	20.92	1.050	4.97	1.052
	SSS > 30	19.61	19.61	22.10	4.95	4.95	5.41	19.58	4.95	21.29	1.049	4.95	1.053
	SSS ≤ 30	23.14	23.14	8.28	5.91	5.91	2.33	22.44	5.91	6.84	1.057	5.91	1.019
-1 °C in SST	Whole SSS range	19.05	19.05	16.62	4.81	4.81	4.05	-19.01	4.81	-15.38	0.952	4.81	0.962
	SSS > 30	18.97	18.97	16.82	4.79	4.79	4.09	-18.94	4.79	-15.75	0.952	4.79	0.961
	SSS ≤ 30	22.40	22.40	4.54	5.72	5.72	1.27	-21.72	5.72	-1.30	0.945	5.72	0.997
+1 in SSS	Whole SSS range	10.08	9.64	8.41	2.56	2.41	2.11	-10.00	9.55	8.04	0.975	1.024	1.020
	SSS > 30	9.95	9.72	8.38	2.52	2.43	2.09	-9.88	9.66	8.01	0.975	1.024	1.020
	SSS ≤ 30	14.72	5.49	9.95	3.75	1.54	2.89	-14.27	5.28	9.38	0.964	1.015	1.027
-1 in SSS	Whole SSS range	10.73	9.01	10.34	2.72	2.25	2.59	10.64	-8.90	-10.04	1.027	0.978	0.975
	SSS > 30	10.59	9.10	10.30	2.68	2.27	2.57	10.52	-9.02	-10.00	1.027	0.977	0.975
	SSS ≤ 30	15.69	4.54	11.95	4.00	1.28	3.47	15.20	-4.34	-11.37	1.039	0.988	0.967
+35% in CHL	Whole SSS range	12.53	1.09	3.70	3.17	0.27	0.94	-12.52	1.09	0.95	0.968	1.003	1.002
	SSS > 30	12.53	1.09	3.67	3.16	0.27	0.927	-12.52	1.09	1.07	0.968	1.003	1.003
	SSS ≤ 30	12.90	1.12	4.99	3.30	0.31	1.43	-12.52	1.09	-3.95	0.968	1.003	0.989
-35% in CHL	Whole SSS range	17.98	1.56	7.65	4.54	0.39	1.90	17.97	-1.55	-5.67	1.045	0.996	0.986
	SSS > 30	17.98	1.56	7.72	4.54	0.39	1.91	17.97	-1.55	-5.85	1.045	0.996	0.986
	SSS ≤ 30	18.52	1.60	4.39	4.74	0.45	1.26	17.97	-1.55	1.36	1.046	0.996	1.004

[a] Columns with grey, blue, and green shading are statistics of the MeSAA, locally-tuned-MeSAA, and the empirical regression, respectively.

opposite sensitivity effect to SSS, comparing to the original MeSAA. Specifically, an increase (decrease) of 1.0 in SSS produced higher (lower) pCO_2 (MB = 9.55 μatm or − 8.90 μatm), with slightly higher pCO_2 increases (decreases) for SSS > 30 than for SSS ≤ 30.

As shown in Figs. 9c and 9d and Table 4, the locally tuned MeSAA showed little sensitivity to changes in CHL. With a 35% increase (decrease) in CHL, pCO_2 was modeled to be 1.09 μatm (− 1.55 μatm) higher (lower) than the originally-modeled pCO_2.

5.3. Sensitivity analysis of the empirical regression

Similar to the sensitivity analysis of the MeSAA and the locally tuned MeSAA, the performance of the empirical model was also evaluated against changes in the input parameters, with SST, SSS, and CHL varied by ± 1 °C, ± 1, and ± 35%, respectively. The results are presented in Fig. 10 and Table 4.

Figs. 10a and 10b indicate that the empirical model was more sensitive to changes in SST at high SSS (> 30) than at low SSS (≤ 30). A 1 °C increase resulted in MB of 21.29 μatm for SSS > 30, but only led to MB of 6.84 μatm for SSS ≤ 30. Similarly, a 1 °C decrease in SST resulted in MB of − 15.75 μatm for SSS > 30 but only − 1.30 μatm for SSS ≤ 30. The sensitivity to SSS changes is the opposite, with slightly higher sensitivity for the data group with SSS ≤ 30. A 1 increase in SSS resulted in MB of 8.01 μatm in the predicted pCO_2 for SSS > 30 but MB of 9.38 μatm for SSS ≤ 30 (Fig. 10c). A 1 decrease in SSS resulted in MB of − 10.00 μatm for SSS > 30 but MB of − 11.37 μatm for SSS ≤ 30 (Fig. 10d).

The empirical model is not sensitive to CHL changes over the modeled data range. With either 35% increase or 35% decrease in CHL, the predicted pCO_2 did not show much difference from the original predictions (Figs. 10e and 10f), where the MB of these two experiments were 0.95 μatm and − 5.67 μatm, respectively.

In summary, the predicted pCO_2 variations induced by a 1 change in SSS and a 35% change in CHL were all within or close to the RMSE of the empirical model. Only in the case of SST changes of 1 °C did the modeled pCO_2 variations exceed the RMSE of the model. In general the empirical model was more sensitive to SST and SSS than to CHL. Considering the combined effects of uncertainties in the satellite data products and the sensitivity test results, uncertainties in the empirically modeled pCO_2 should be between 10.66 and 21.86 μatm for typical data ranges. However, these uncertainties represent RMSE values for individual data points instead of systematic biases. When the data are averaged over large scales in either space or time, the uncertainties in the mean products should be much smaller.

5.4. Mechanistic or empirical approach

Statistically, the locally tuned MeSAA (R^2 = 0.78, RMSE = 12.36 μatm, MB = 0.00 μatm, and MR = 1.001) and the empirical regression model (R^2 = 0.84, RMSE = 10.66 μatm, MB = − 0.10 μatm, and MR = 1.000) showed similar but better performance than the original MeSAA model (R^2 = 0.25, RMSE = 22.94 μatm, MB = − 0.23 μatm, and MR = 1.001). This is also revealed in the scatterplots for these three models (Figs. 4c, 6d, and 7f). Similarly, although all these three models reproduced the spatial distribution patterns of pCO_2 well, the locally tuned MeSAA and the empirical regression models showed more details and improved accuracy (Fig. 5).

The sensitivity analyses showed that the MeSAA model was sensitive to both the empirical coefficients (river endmember TA_0 and DIC_0, and biological coefficient B) and the three environmental variables

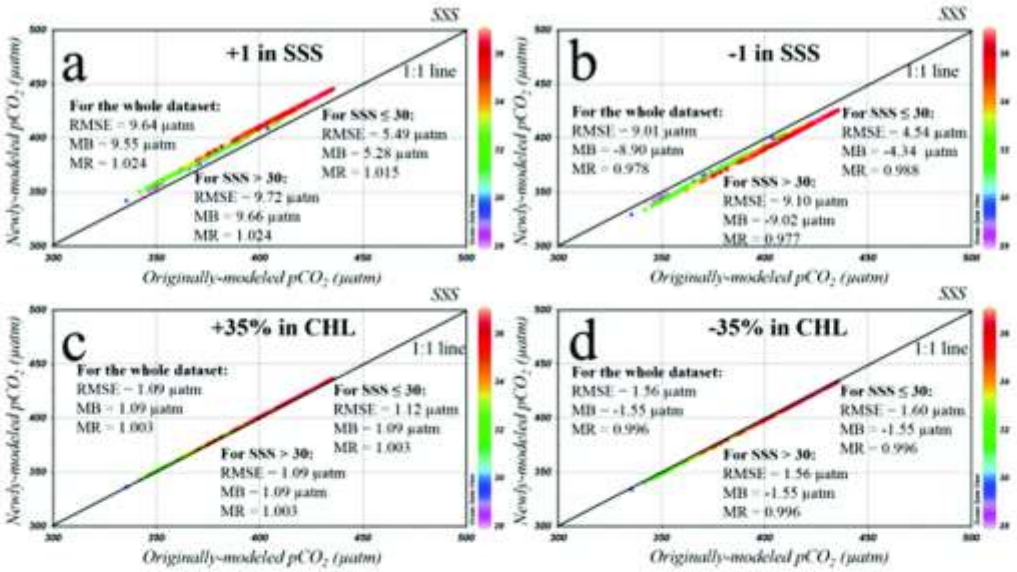

Fig. 9. Sensitivity of the locally tuned MeSAA to changes in SSS (a and b) and CHL (c and d). Note that the sensitivity of the locally tuned MeSAA to TA0 and SST are the same as that of the original MeSAA. In each panel, only one parameter was varied while all others were kept unchanged, and the newly-modeled pCO_2 corresponding to each set of parameterization variation is compared with the originally-modeled pCO_2. Note that the statistics of each analysis were shown in each panel, as listed in Table 4.

(SST, SSS, CHL), and the locally tuned MeSAA was sensitive to the river endmember TA_0 and DIC_0, and sensitive to SST and SSS but not to CHL. The MeSAA was more sensitive to the biological coefficient B while the locally tuned MeSAA and the empirical regression models were more sensitive to SST. All three models showed positive correlations between surface pCO_2 and SST, but the MeSAA showed negative correlations with SSS and CHL while the locally tuned MeSAA and the empirical regression models showed the opposite signs in the same correlations. However, all these uncertainties in the predicted surface pCO_2 are within the model uncertainties except for the case of SST in the empirical model.

Overall, while the empirical regression model resulted in slightly better performance than the locally tuned MeSAA in predicting surface pCO_2, interpretation of the model drivers is more straightforward with the latter, as both physical and biological forcing in the latter are explicitly expressed. Indeed, both the original MeSAA and the locally-tuned-MeSAA showed encouraging results in terms of model accuracy and physical interpretation over the northern GOM. However, currently only an empirical relationship was used to quantify the biological term in both models, thus requiring further improvement in quantifying the biological effect in a more meaningful way. In addition, when extending the MeSAA approach to other seasons (the current study was only conducted for summertime) in the northern GOM or to other similar systems, the locally-tuned-MeSAA may be more practical than the original MeSAA because of local tuning in determining the biological effect. However, a major limitation in both the original MeSAA and the locally tuned MeSAA that implemented in this study is that one of the model inputs, namely SSS, is from the field measurements due to lack of community-accepted algorithms to estimate SSS from high-resolution (1-km) satellite measurements. This deficiency in remote sensing algorithm makes it difficult to generate synoptic maps using satellite data alone. Clearly, an immediate need is to develop and validate a remote sensing SSS algorithm in order to derive surface pCO_2 maps using the established models here. The changing relationship between SSS and the absorption coefficient of colored dissolved organic matter (CDOM) in the northern GOM in recent studies (Hu et al., 2003; Del Castillo and Miller, 2008; Lohrenz et al., 2010; Cannizzaro et al., 2013b) indicated that empirical regression modeling may not be sufficient to derive a general relationship applicable to the whole northern GOM. More advanced empirical techniques such as neural network or support vector machine may be tried instead (e.g., Chen and Hu, 2017). In the end, because data from upwelling cases were excluded in all three models in order to satisfy the conditions in the original MeSAA approach (summertime East China Sea where river-ocean mixing dominates the processes), the models are not expected to work in regions with strong upwelling. Indeed, if all three models were to be applied to the upwelling case shown in Fig. 1c (July 2009 around the Mississippi River delta), the predicted pCO_2 would show large deviations from the field-measured pCO_2, with RMSE of 103.60–166.31 μatm. However, if data from this event were used together with all other data during training of the empirical regression model, the result would show significant improvement in the predicted pCO_2, with RMSE of 14.75 μatm and R^2 of 0.79 for the entire dataset, and RMSE of 63.17 μatm for the upwelling data ($N = 13$). Clearly, the applicability of the empirical regression model strongly depends on the data used in the model training, and more field data collected under upwelling cases are required to further tune the empirical regression model for general application with high confidence.

5.5. Controls of surface pCO_2 in the summertime northern GOM

While the focus of the paper is on comparison of models in estimating surface pCO_2 in order to provide guidance on future model selection when applying to remote sensing data, understanding of model uncertainties requires knowledge of the various controlling mechanisms in affecting surface pCO_2. As described in Section 1, surface pCO_2 can be affected by ocean mixing (both horizontal and vertical), biological activities, thermodynamics, and air-sea exchange. In summertime northern GOM, horizontal river-ocean mixing, biological activities and thermodynamics are the dominant factors in influencing surface pCO_2,

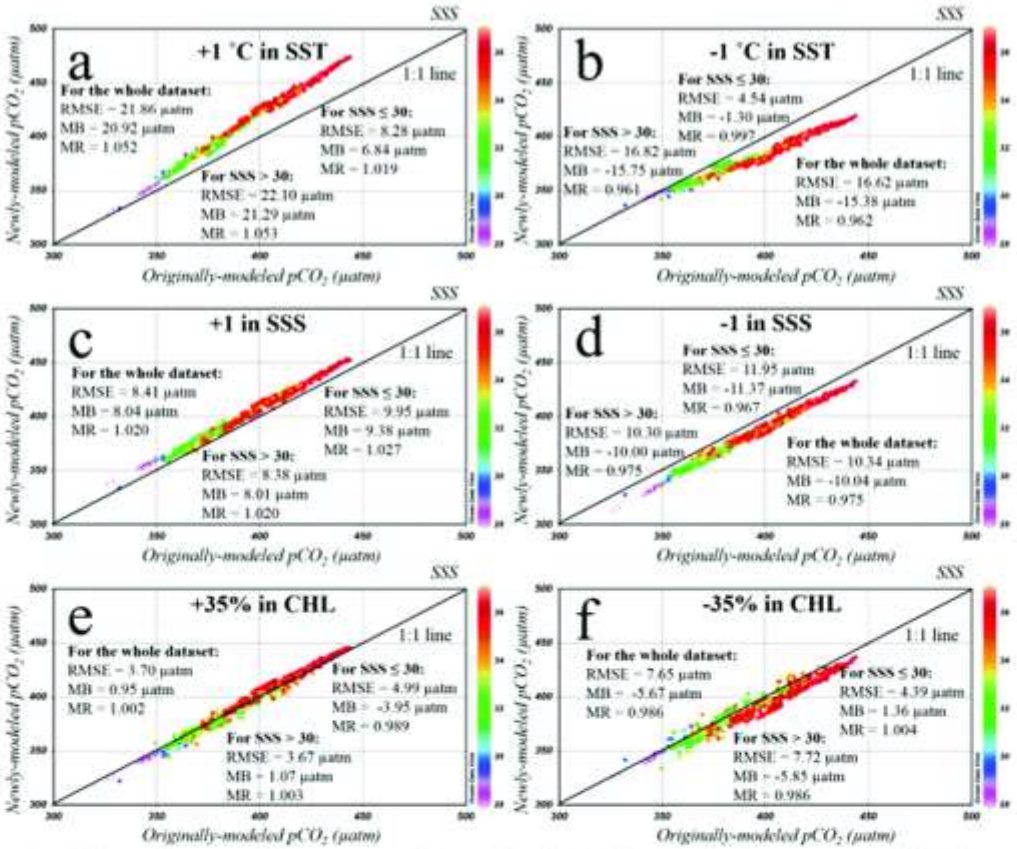

Fig. 10. Sensitivity of the empirical regression model to changes in SST (a and b), SSS (c and d), and CHL (e and f). In each panel, only one parameter was varied while all others were kept unchanged, and the newly-modeled pCO_2 corresponding to each set of parameterization variation is compared with the originally-modeled pCO_2. Note that the statistics of each analysis were shown in each panel, as listed in Table 4.

and all these three factors were included in the parameterization of the original and locally tuned MeSAA. However, vertical mixing and air-sea exchange are also likely to cause some variations in surface pCO_2, especially during and after extreme events (e.g., hurricanes, storms). Such processes were not considered in the parameterization of the MeSAA. On the other hand, in the parameterization of the MeSAA, conservative river-ocean mixing was assumed first, and the biological effect was then removed from the mixing term to derive the modeled surface pCO_2. These two processes may not occur on the same time scale and/or spatial scale, causing large uncertainties in the modeled surface pCO_2.

6. Conclusion

Using extensive field and satellite data, several models to predict surface pCO_2 using SST, SSS, and CHL were thoroughly tested over the northern GOM, with the ultimate goal of understanding model performance and sensitivity to uncertainties in the input variables. These include a recently established mechanistic model (i.e., MeSAA) originally developed for the East China Sea, a locally tuned MeSAA with local tuning to determine the biological effect, and a statistical empirical model. While the empirical model led to slightly better performance than the locally tuned MeSAA because the unknown factors driving the model uncertainties may be accounted for in the empirical coefficients, the physical and biological effect on the surface pCO_2 can only be explicitly interpreted by the mechanistic model. Additionally, the empirical regression approach could be further tuned for regions with upwelling. The study also suggests future directions in model development as well as in satellite-based SSS algorithms in order to derive accurate surface pCO_2 maps for river-dominated coastal regions. For example, instead of using a biological term determined from open-ocean waters a locally tuned biological term ($\Delta pCO_{2(Bio)}$) may be used in the MeSAA to account for pCO_2 residuals in the horizontal mixing and biological processes as well as other processes (e.g., vertical mixing).

Acknowledgements

This work was supported by a USGS fellowship, a University of South Florida fellowship, and the U.S. NASA (NNX14AM37G and NNX17AH03G to C. Hu, NNH13ZDA001N and NNX14AM37G to W.-J. Cai). We also thank CDIAC, NOAA AOML, and LDEO for providing all the available cruise data, and thank NASA for providing MODIS satellite data. Two anonymous reviewers provided comments and suggestions to help improve this manuscript, whose efforts are appreciated.

References

Atkins, M.L., Santos, I.R., Ruiz-Halpern, S., Maher, D.T., 2013. Carbon dioxide dynamics driven by groundwater discharge in a coastal floodplain creek. J. Hydrol. 493, 30–42. http://dx.doi.org/10.1016/j.jhydrol.2013.04.008.

Bai, Y., Cai, W., He, X., Zhai, W., Pan, D., Han, M., Yu, P., 2015. A mechanistic semi-analytical method for remotely sensing sea surface pCO_2 in river-dominated coastal oceans: a case study from the East China Sea. J. Geophys. Res. 120 (3), 2331–2349. http://dx.doi.org/10.1002/2014JC010023.

Bailey, S.W., Werdell, P.J., 2006. A multi-sensor approach for the on-orbit validation of ocean color satellite data products. Remote Sens. Environ. 102, 12–23.

Bates, N.R., Knap, A.H., Michaels, A.F., 1998. Contribution of hurricanes to local and global estimates of air-sea exchange of CO_2. Nature 395.

Bates, N.R., Merlivat, L., 2001. The influence of short-term wind variability on air-sea CO_2 exchange. Geophys. Res. Lett. 28 (17), 3281–3284.

Bauer, J.E., Cai, W.J., Raymond, P.A., Bianchi, T.S., Hopkinson, C.S., Regnier, P.A.G., 2013. The changing carbon cycle of the coastal ocean. Nature 504, 61–70. http://dx.doi.org/10.1038/nature12857.

Borges, A.V., Delille, B., Frankignoulle, M., 2005. Budgeting sinks and sources of CO_2 in the coastal ocean: diversity of ecosystem counts. Geophys. Res. Lett. 32, L14601. http://dx.doi.org/10.1029/2005GL023053.

Cai, W.J., 2003. Riverine inorganic carbon flux and rate of biological uptake in the Mississippi River plume. Geophys. Res. Lett. 30, 1997–2000. http://dx.doi.org/10.1029/2002GL016312.

Cai, W.J., Dai, M., Wang, Y., 2006. Air-sea exchange of carbon dioxide in ocean margins: a province-based synthesis. Geophys. Res. Lett. 33), 1–4. http://dx.doi.org/10.1029/2006GL026219.

Cai, W.J., Lohrenz, S.E., 2010. The Mississippi River plume and adjacent margin in the Gulf of Mexico. In: Liu, K.-K. (Ed.), Carbon and Nutrient Fluxes in the Continental Margins: A Global Synthesis. Springer, Berlin, pp. 406–422.

Cai, W.J., Hu, X., Huang, W.J., Jiang, L.Q., Wang, Y., Peng, T.H., Zhang, X., 2010. Alkalinity distribution in the western North Atlantic Ocean margins. J. Geophys. Res. 115 (C08014), 1–15. http://dx.doi.org/10.1029/2009JC005482.

Cai, W.J., 2011. Estuarine and coastal ocean carbon paradox: CO_2 sinks or sites of terrestrial carbon incineration? Annu. Rev. Mar. Sci. 3 (1), 123–145.

Cai, W.J., Hu, X., Huang, W.J., Murrell, M.C., Lehrter, J.C., Lohrenz, S.E., Chou, W.C., Zhai, W., Hollibaugh, J.T., Wang, Y., Zhan, P., Guo, X., Gundersen, K., Dai, M., Gong, G.C., 2011. Acidification of subsurface coastal waters enhanced by eutrophication. Nat. Geosci. 4 (11), 766–770.

Cai, W.-J., Wang, Y., Huang, W.-J., 2012a. Sea Surface pCO_2 measurements in the Gulf of Mexico during the Ocean Survey Vessel Bold cruises in 2006. (http://cdiac.ornl.gov/ftp/oceans/UG_GoM_UW_Data/2006.data). Carbon Dioxide Information Analysis Center, Oak Ridge National Laboratory, US Department of Energy, Oak Ridge, Tennessee. (http://dx.doi.org/10.3334/CDIAC/OTG.UG_GOM_UW_2006).

Cai, W.-J., Wang, Y., Huang, W.-J., 2012b. Sea Surface pCO_2 measurements in the Gulf of Mexico during the Ocean Survey Vessel Bold cruises in 2007. (http://cdiac.ornl.gov/ftp/oceans/UG_GoM_UW_Data/2007.data). Carbon Dioxide Information Analysis Center, Oak Ridge National Laboratory, US Department of Energy, Oak Ridge, Tennessee. (http://dx.doi.org/10.3334/CDIAC/OTG.UG_GOM_UW_2007).

Cai, W.J., Chen, C.T.A., Borges, A., 2013. Carbon dioxide dynamics and fluxes in coastal waters influenced by river plumes. Biogeochem. Dyn. Major River-Coast. Interfaces Link. Glob. Change.

Cai, W.-J., Wang, Y., Huang, W.-J., 2014. Sea surface pCO_2 survey in the Gulf of Mexico during the R/V Cape Hatteras cruises in 2009 and 2010. (http://cdiac.ornl.gov/ftp/oceans/Cape_Hatteras_GM/), Carbon Dioxide Information Analysis Center, Oak Ridge National Laboratory, US Department of Energy, Oak Ridge, Tennessee. (https://dx.doi.org/10.3334/CDIAC/OTG.Cape_Hatteras_GM).

Caldeira, K., Wickett, M.E., 2003. Oceanography: anthropogenic carbon and ocean pH. Nature 425 (6956) (365–365).

Campbell, J.W., 1995. The lognormal distribution as a model for bio-optical variability in the sea. J. Geophys. Res. 100 (C7), 13237–13254. http://dx.doi.org/10.1029/95JC00458.

Cannizzaro, J.P., Hu, C., Garder, K.L., Kelble, C.R., Melo, N., Johns, E.M., Vargo, G.A., Heil, C.A., 2013a. On the accuracy of SeaWIFS ocean color data products on the west Florida shelf. J. Coast. Res. 292, 1257–1272. http://dx.doi.org/10.2112/JCOASTRES-D-12-00223.1.

Cannizzaro, J.P., Carlson, P.R., Yarbro, L.A., Hu, C., 2013b. Optical variability along a river plume gradient: implications for management and remote sensing. Estuar. Coast. Shelf Sci. 131, 149–161.

Chen, F., Cai, W.J., Benitez-Nelson, C., Wang, Y., 2007. Sea surface pCO_2-SST relationships across a cold-core cyclonic eddy: implications for understanding regional variability and air-sea gas exchange. Geophys. Res. Lett. 34, L10603. http://dx.doi.org/10.1029/2006GL028058.

Chen, C.T.A., Huang, T.H., Chen, Y.C., Bai, Y., He, X., Kang, Y., 2013. Air-sea exchanges of CO_2 in the world's coastal seas. Biogeosciences 10, 6509–6544. http://dx.doi.org/10.5194/bg-10-6509-2013.

Chen, S., Hu, C., Byrne, R.H., Robbins, L.L., Yang, B., 2016. Remote estimation of surface pCO_2 on the west Florida shelf. Cont. Shelf Res. 128, 10–25.

Chen, S., Hu, C., 2017. Estimating sea surface salinity in the northern Gulf of Mexico from satellite ocean color measurements. Remote Sens. Environ. 201, 115–132. http://dx.doi.org/10.1016/j.rse.2017.09.004.

Dai, M., Lu, Z., Zhai, W., Chen, B., Cao, Z., Zhou, K., Cai, W.J., Chen, C.T.A., 2009. Diurnal variations of surface seawater pCO_2 in contrasting coastal environments. Limnol. Oceanogr. 54 (3), 735–745. http://dx.doi.org/10.4319/lo.2009.54.3.0735.

Del Castillo, C.E., Miller, R.L., 2008. On the use of ocean color remote sensing to measure the transport of dissolved organic carbon by the Mississippi River Plume. Remote Sens. Environ. 112 (3), 836–844.

Dickinson, G.H., Ivanina, A.V., Matoo, O.B., Portner, H.O., Lannig, G., Bock, C., Beniash, E., Sokolova, I.M., 2012. Interactive effects of salinity and elevated CO_2 levels on juvenile eastern oysters, Crassostrea virginica. J. Exp. Biol. 215 (1), 29–43.

Doney, S.C., Balch, W.M., Fabry, V.J., Feely, R.A., 2009. Ocean acidification: a critical emerging problem for the ocean sciences. Oceanography 22 (4), 16–25.

Doney, S.C., 2010. The growing human footprint on coastal and open-ocean biogeochemistry. Science 328 (5985), 1512–1516.

Feely, R.A., Wanninkhof, R., Milburn, H.B., Cosca, C.E., Stapp, M., Murphy, P.P., 1998. A new automated underway system for making high precision pCO_2 measurements onboard research ships. Anal. Chim. Acta 377 (2–3), 185–191.

Feely, R.A., Alin, S.R., Newton, J., Sabine, C.L., Warner, M., Devol, A., Krembs, C., Maloy, C., 2010. The combined effects of ocean acidification, mixing, and respiration on pH and carbonate saturation in an urbanized estuary. Estuar. Coast. Shelf Sci. 88 (4), 442–449.

Fennel, K., Wilkin, J., Previdi, M., Najjar, R., 2008. Denitrification effects on air-sea CO_2 flux in the coastal ocean: simulations for the northwest North Atlantic. Geophys. Res. Lett. 35, L24608. http://dx.doi.org/10.1029/2008GL036147.

Friedrich, T., Oschlies, A., 2009a. Neural network-based estimates of North Atlantic surface pCO_2 from satellite data: a methodological study. J. Geophys. Res. 114, C03020. http://dx.doi.org/10.1029/2007JC004646.

Friedrich, T., Oschlies, A., 2009b. Basin-scale pCO2 maps estimated from ARGO float data: a model study. J. Geophys. Res. 114, C10012. http://dx.doi.org/10.1029/2009JC005322.

Gordon, H.R., Wang, M., 1994. Retrieval of water-leaving radiance and aerosol optical thickness over the oceans with SeaWIFS: a preliminary algorithm. Appl. Opt. 33, 443–452.

Gregg, W.W., Casey, N.W., 2004. Global and regional evaluation of the SeaWiFS chlorophyll data set. Remote Sens. Environ. 93, 463–479.

Guo, X., Cai, W.J., Huang, W.J., Wang, Y., Chen, F., Murrell, M.C., Lin, Q., 2012. Carbon dynamics and community production in the Mississippi River plume. Limnol. Oceanogr. 57 (1), 1–17.

Hales, B., Strutton, P.G., Saraceno, M., Letelier, R., Takahashi, T., Feely, R., Sabine, C., Chavez, F., 2012. Satellite-based prediction of pCO_2 in coastal waters of the eastern North Pacific. Prog. Oceanogr. 103 (1), 15. http://dx.doi.org/10.1016/j.pocean.2012.03.001.

Hu, C., Muller-Karger, F.E., Biggs, D.C., Carder, K.L., Nababan, B., Nadeau, D., Vanderbloemen, J., 2003. Comparison of ship and satellite bio-optical measurements on the continental margin of the NE Gulf of Mexico. Int. J. Remote Sens. 24 (13), 2597–2612.

Hu, C., Nelson, J.R., Johns, E., Chen, Z., Weisberg, R.H., Muller-Karger, F.E., 2005. Mississippi River water in the Florida Straits and in the Gulf Stream off Georgia in summer 2004. Geophys. Res. Lett. 32 (14), 1–5.

Hu, C., Lee, Z., Franz, B., 2012. Chlorophyll algorithms for oligotrophic oceans: a novel approach based on three-band reflectance difference. J. Geophys. Res.: Oceans 117 (C1).

Huang, W.J., Cai, W.J., Castelao, R.M., Wang, Y., Lohrenz, S.E., 2013. Impacts of a wind-driven cross-shelf large river plume on biological production and CO_2 uptake in the Gulf of Mexico during spring. Limnol. Oceanogr. 58 (5), 1727–1735.

Huang, W.J., Cai, W.J., Wang, Y., Hu, X., Chen, B., Lohrenz, S.E., Chakraborty, S., He, R., Brandes, J., Hopkinson, C.S., 2015a. The response of inorganic carbon distributions and dynamics to upwelling-favorable winds on the northern Gulf of Mexico during summer. Cont. Shelf Res. 111, 211–222.

Huang, W.J., Cai, W.J., Wang, Y., Lohrenz, S.E., Murrell, M.C., 2015b. The carbon dioxide system on the Mississippi River-dominated continental shelf in the northern Gulf of Mexico: 1. Distribution and air-sea CO_2 flux. J. Geophys. Res.: Oceans 120 (2), 1429–1445.

Ikawa, H., Faloona, I., Kochendorfer, J., Paw U, K.T., Oechel, W.C., 2013. Air-sea exchange of CO_2 at a Northern California coastal site along the California current upwelling system. Biogeosciences 10, 4419–4432. http://dx.doi.org/10.5194/bg-10-4419-2013.

Jiang, L.Q., Cai, W.J., Wang, Y., 2008. A comparative study of carbon dioxide degassing in river and marine-dominated estuaries. Limnol. Oceanogr. 53 (6), 2603.

Jo, Y.H., Dai, M., Zhai, W., Yan, X.H., Shang, S., 2012. On the variations of sea surface pCO_2 in the northern South China Sea: a remote sensing based neural network approach. J. Geophys. Res. 117 (1), 13. http://dx.doi.org/10.1029/2011JC007745.

Joesoef, A., Huang, W.J., Gao, Y., Cai, W.J., 2015. Air-water fluxes and sources of carbon dioxide in the Delaware Estuary: spatial and seasonal variability. Biogeosciences 12 (20), 6085–6101.

Lefevre, N., Aiken, J., Rutllant, J., Daneri, G., Lavender, S., Smyth, T., 2002. Observations of pCO_2 in the coastal upwelling off Chile: spatial and temporal extrapolation using satellite data. J. Geophys. Res. 107 (C6), 1–15. http://dx.doi.org/10.1029/2000JC000095.

Lefevre, N., Watson, A.J., Watson, A.R., 2005. A comparison of multiple regression and neural network techniques for mapping in situ pCO_2 data. Tellus 57B, 375–384.

Lohrenz, S.E., Cai, W.J., 2006. Satellite ocean color assessment of air-sea fluxes of CO_2 in a river-dominated coastal margin. Geophys. Res. Lett. 33, L01601. http://dx.doi.org/10.1029/2005GL023942.

Lohrenz, S.E., Cai, W., Chen, F., Chen, X., Tuel, M., 2010. Seasonal variability in air-sea fluxes of CO_2 in a river-influenced coastal margin. J. Geophys. Res. 115, C10034. http://dx.doi.org/10.1029/2009JC005608.

Marotta, H., Duarte, C.M., Pinho, L., Enrich-Prast, A., 2010. Rainfall leads to increased pCO_2 in Brazilian coastal lakes. Biogeosciences 7, 1607–1614. http://dx.doi.org/10.5194/bg-7-1607-2010.

Marrer, P., Carton, T., Macé, E., Morin, P., Salt, L.A., Vernet, M., Taylor, B., Pasman, E.,

Borges, V., 2015. Dynamics of air-sea CO_2 fluxes in the North-West European shelf based on Voluntary Observing Ship (VOS) and satellite observations. Biogeosci. Discuss. 12 (7), 5371–5391.
Melin, F., Zibordi, G., Berthon, J.F., 2007. Assessment of satellite ocean color products at a coastal site. Remote Sens. Environ. 110, 192–215.
Millero, F.J., Graham, T.B., Huang, F., Bustos-Serrano, H., Pierrot, D., 2006. Dissociation constants of carbonic acid in seawater as a function of salinity and temperature. Mar. Chem. 100 (1), 80–94.
Morey, S.L., Martin, P.J., O'Brien, J.J., Wallcraft, A.A., Zavala-Hidalgo, J., 2003. Export pathways for river discharged fresh water in the northern Gulf of Mexico. J. Geophys. Res.: Oceans 108 (C10).
Nakaoka, S., Telszewski, M., Nojiri, Y., Yasunaka, S., Miyazaki, C., Mukai, H., Usui, N., 2013. Estimating temporal and spatial variation of ocean surface pCO_2 in the North Pacific using a self-organizing map neural network technique. Biogeosciences 10 (9), 6093.
Norman, M., Parampil, S.R., Rutgersson, A., Sahlee, E., 2013. Influence of coastal upwelling on the air–sea gas exchange of CO_2 in a Baltic Sea basin. Tellus B 65, 1–16. http://dx.doi.org/10.3402/tellusb.v65i0.21831.
O'Reilly, J.E., et al., 2000. Ocean color chlorophyll a algorithms for SeaWiFS, OC2 and OC4: version 4, NASA tech. Memo. 2000-206892. In: Hooker, S.B., Firestone, E.R. (Eds.), SeaWiFS Postlaunch Calibration and Validation Analyses 11 NASA Goddard Space Flight Center, Greenbelt, MD, USA.
Orr, J.C., Fabry, V.J., Aumont, O., Bopp, L., Doney, S.C., Feely, R.A., Gnanadesikan, A., Gruber, N., Ishida, A., Joos, F., Key, R.M., Lindsay, K., Maier-Reimer, E., Matear, R., Monfray, P., Mouchet, A., Najjar, R.G., Plattner, G.-K., Rodgers, K.B., Sabine, C.L., Sarmiento, J.L., Schlitzer, R., Slater, R.D., Totterdell, I.J., Weirig, M.-F., Yamanaka, Y., Yool, A., 2005. Anthropogenic ocean acidification over the twenty-first century and its impact on calcifying organisms. Nature 437 (7059), 681–686.
Omstedt, Peter B., Lee, T.N., Milne, P.J., Zika, R.G., Clarke, M.E., Podesta, G.P., Swart, P.K., Tester, P.A., Atkinson, L.P., Johnson, W.R., 1995. Mississippi River flood waters that reached the Gulf Stream. J. Geophys. Res.: Oceans 100 (C7), 13595–13601.
Pachauri, R.K., Meyer, L.A., 2014. Climate Change 2014: Synthesis Report. IPCC, Geneva, Switzerland, pp. 151.
Parard, G., Charantonis, A.A., Rutgersson, A., 2015. Remote sensing the sea surface CO_2 of the Baltic Sea using the SOMLO methodology. Biogeosciences 12 (11), 3369–3384.
Parard, G., Charantonis, A.A., Rutgersson, A., 2016. Using satellite data to estimate partial pressure of CO_2 in the Baltic Sea. J. Geophys. Res.: Biogeosci. 121 (3), 1002–1015.
Patt, F.S., et al., 2003. Algorithm updates for the fourth SeaWiFS data reprocessing. NASA tech memo 2003-206892. In: Hooker, S.B., Firestone, E.R. (Eds.), SeaWiFS Postlaunch Technical Report Series 22 NASA, Greenbelt, MD, USA.
Pierrot, D.E.L., Wallace, D.W.R., 2006. MS Excel Program Developed for CO_2 System Calculations (ORNL/CDIAC-105). Carbon Dioxide Information Analysis Center, Oak Ridge National Laboratory, U.S. Department of Energy, Oak Ridge, Tennessee. http://dx.doi.org/10.3334/CDIAC/otg.CO2SYS_XLS_CDIAC105a.
Pierrot, D., Neill, C., Sullivan, K., Castle, R., Wanninkhof, R., Lueger, H., Johannessen, T., Olsen, A., Feely, R.A., Cosca, C.E., 2009. Recommendations for autonomous underway pCO_2 measuring systems and data-reduction routines. Deep-Sea Res. II 56, 512–522.
Rabalais, N.N., Turner, R.E., Wiseman, W.J., 2002. Gulf of Mexico hypoxia, A.K.A. "The dead zone". Annu. Rev. Ecol. Syst. 33, 235–263.
Reynaud, S., Leclercq, N., Romaine-Lioud, S., Ferrier-Pages, C., Jaubert, J., Gattuso, J.P., 2003. Interacting effects of CO_2 partial pressure and temperature on photosynthesis and calcification in a scleractinian coral. Glob. Change Biol. 9, 1660–1668. http://dx.doi.org/10.1046/j.1529-8817.2003.00678.x.
Sabine, C., Maenner, S., Sutton, A., 2014. High-resolution ocean and atmosphere pCO2 time-series measurements from mooring CoastalMS_88W_30N. (http://cdiac.ornl.gov/ftp/oceans/Moorings/CoastalMS_88W_30N/). Carbon Dioxide Information Analysis Center, Oak Ridge National Laboratory, US Department of Energy, Oak Ridge, Tennessee. (http://dx.doi.org/10.3334/CDIAC/OTG.TSM_COASTALMS_88W_30N).
Signorini, S.R., Mannino, A., Najjar, R.G., Friedrichs, M.A.M., Cai, W.J., Salisbury, J., Wang, Z.A., Thomas, H., Shadwick, E., 2013. Surface ocean pCO_2 seasonality and sea-air CO_2 flux estimates for the North American east coast. J. Geophys. Res.: Oceans 118, 5439–5460. http://dx.doi.org/10.1002/jgrc.20369.
Song, X., Bai, Y., Cai, W.J., Chen, C.T.A., Pan, D., He, X., Zhu, Q., 2016. Remote sensing of sea surface pCO_2 in the Bering sea in summer based on a mechanistic semi-analytical algorithm (MeSAA). Remote Sens. 8 (7), 558.
Sun, Q., Tang, D., Wang, S., 2012. Remote-sensing observations relevant to ocean acidification. Int. J. Remote Sens. 22 (23), 7542–7558.
Sutherland, S.C., Newberger, T., Takahashi, T., Sweeney, C., 2013. Underway pCO_2 Measurements in Surface Waters and the Atmosphere in the Gulf of Mexico and Along the West Coast of North America During February–May 2013. Lamont-Doherty Earth Observatory of Columbia University, Palisades, New York. (http://www.ldeo.columbia.edu/res/pi/CO2/carbondioxide/pages/2013Bangarth.html).
Takahashi, T., Sutherland, S.C., Sweeney, C., Metzl, A.P.N., Tilbrook, B., Bates, N., Wanninkhof, R., Feely, R.A., Sabine, C., Olafsson, J., Nojiri, Y., 2002. Global sea–air CO_2 flux based on climatological surface ocean pCO_2, and seasonal biological and temperature effects. Deep-Sea Res. II 49, 1601–1622.
Takahashi, T., Sutherland, S.C., Wanninkhof, R., Sweeney, C., Feely, R.A., Chipman, D.W., Hales, B., Friederich, G., Chavez, F., Chris, S., Watson, A.J., Bakker, D., Schuster, U., Metzl, N., Yoshikawa-Inoue, H., Ishii, M., Midorikawa, T., Nojiri, Y., Arne, K., Tobias, S., Huppenman, M., Olafsson, J., Arnarson, T.S., Tilbrook, B., Johannessen, T., Olsen, A., Bellerby, R., Wong, C.S., Delille, B., Bates, N.R., Baar, H., 2009. Climatological mean and decadal change in surface ocean pCO_2, and net sea–air CO_2 flux over the global oceans. Deep-Sea Res. II 56, 554–577.
Telszewski, M., Chazottes, A., Schuster, U., Watson, A.J., Moulin, C., Bakker, D.C.E., González-Davila, M., Johannessen, T., Kortzinger, A., Lueger, H., Olsen, A., Omar, A., Padin, X.A., Rios, A.F., Steinhoff, T., Santana-Casiano, M., Wallace, D.W.R., Wanninkhof, R., 2009. Estimating the monthly pCO_2 distribution in the North Atlantic using a self-organizing neural net- work. Biogeosciences 6, 1405–1421. http://dx.doi.org/10.5194/bg-6-1405-2009.
Turk, D., Book, J.W., McGillis, W.R., 2013. pCO_2 and CO_2 exchange during high bora winds in the Northern Adriatic. J. Mar. Syst. 117–118, 65–71. http://dx.doi.org/10.1016/j.jmarsys.2013.02.010.
Uppstrom, L.R., 1974. The boron/chlorinity ratio of deep-sea water from the Pacific Ocean. Deep Sea Res. Oceanogr. Abstr. 21, 161–162.
Wang, Z.A., Wanninkhof, R., Cai, W.J., Byrne, R.H., Hu, X., Peng, T.H., Huang, W.J., 2013. The marine inorganic carbon system along the Gulf of Mexico and Atlantic coasts of the United States: insights from a transregional coastal carbon study. Limnol. Oceanogr. 58 (325), 242.
Wanninkhof, R., Pierrot, D., Sullivan, K., 2009. Sea Surface and Atmospheric fCO_2 data measured in the Gulf of Mexico, Atlantic and Caribbean waters during the M/V Las Cuevas 2009 cruises. (http://www.aoml.noaa.gov/ocd/gcc/lascuevas_data2009.php).
Wanninkhof, R., Pierrot, D., Sullivan, K., 2010. Sea Surface and Atmospheric fCO_2 data measured in the Gulf of Mexico, Atlantic and Caribbean waters during the M/V Las Cuevas 2010 cruises. (http://www.aoml.noaa.gov/ocd/gcc/lascuevas_data2010.php).
Wanninkhof, R., Castle, R.D., Shannahoff, J., 2012a. Carbon dioxide, temperature, salinity, and other variables collected via surface underway survey from NOAA Ship RONALD H. BROWN in the North Atlantic Ocean, North American Coastline-South and others from 2003-02-06 to 2003-11-21 (NODC Accession 0081017). Version 2.2. National Oceanographic Data Center, NOAA. Dataset.
Wanninkhof, R., Castle, R.D., Shannahoff, J., 2012b. Carbon dioxide, temperature, salinity, and other variables collected via surface underway survey from NOAA Ship RONALD H. BROWN in the North Atlantic Ocean, North American Coastline-South and others from 2006-02-16 to 2006-12-02 (NODC Accession 0081021). Version 2.2. National Oceanographic Data Center, NOAA. Dataset.
Wanninkhof, R., Castle, R.D., Shannahoff, J., 2012c. Carbon dioxide, temperature, salinity, and other variables collected via surface underway survey from NOAA Ship RONALD H. BROWN in the North Atlantic Ocean, North American Coastline-South and others from 2007-03-23 to 2008-01-18 (NODC Accession 0081023). Version 2.2. National Oceanographic Data Center, NOAA. Dataset.
Wanninkhof, R., Pierrot, D., Sullivan, K., Huss, B., 2013a. Sea Surface and Atmospheric fCO_2 data measured in the Gulf of Mexico during the R/V Gordon Gunter 2008 cruises. (http://cdiac.ornl.gov/ftp/oceans/Gordon_Gunter/2008/). Carbon Dioxide Information Analysis Center, Oak Ridge National Laboratory, US Department of Energy, Oak Ridge, Tennessee. (http://dx.doi.org/10.3334/CDIAC/OTG.COAST_GU2008).
Wanninkhof, R., Pierrot, D., Sullivan, K., Huss, B., 2013b. Sea Surface and Atmospheric fCO_2 data measured in the Gulf of Mexico during the R/V Gordon Gunter 2009 cruises. (http://cdiac.ornl.gov/ftp/oceans/Gordon_Gunter/2009/). Carbon Dioxide Information Analysis Center, Oak Ridge National Laboratory, US Department of Energy, Oak Ridge, Tennessee. (http://dx.doi.org/10.3334/CDIAC/OTG.COAST_GU2009).
Wanninkhof, R., Castle, R.D., Shannahoff, J., 2013c. Partial pressure (or fugacity) of carbon dioxide, salinity and other variables collected from underway – surface observations using Carbon dioxide (CO_2) gas analyzer, Shower head chamber equilibrator for autonomous carbon dioxide (CO_2) measurement and other instruments from NOAA Ship RONALD H. BROWN in the Caribbean Sea, Gulf of Mexico and others from 2009-04-17 to 2009-10-18 (NODC Accession 0109931). Version 1.1. National Oceanographic Data Center, NOAA. Dataset.
Widdicombe, S., Spicer, J.I., 2008. Predicting the impact of ocean acidification on benthic biodiversity: what can animal physiology tell us? J. Exp. Mar. Biol. Ecol. 366, 187–197. http://dx.doi.org/10.1016/j.jembe.2008.07.024.
Xue, L., Cai, W.J., Hu, X., Sabine, C., Jones, S., Sutton, A.J., Jiang, L.Q., Reimer, J.J., 2016. Sea surface carbon dioxide at the Georgia time series site (2006–2007): air–sea flux and controlling processes. Prog. Oceanogr. 140, 14–26.
Yang, B., Byrne, R.H., Wanninkhof, R., 2015. Subannual variability of total alkalinity distributions in the northeastern Gulf of Mexico. J. Geophys. Res.: Oceans 120, 3805–3816. http://dx.doi.org/10.1002/2015JC010780.
Zhai, W.D., Dai, M., Cai, W.J., 2009. Coupling of surface pCO_2 and dissolved oxygen in the northern South China Sea: impacts of contrasting coastal processes. Biogeosciences 6, 6249–6269. http://dx.doi.org/10.5194/bgd-6-6249-2009.
Zhang, X., Hetland, R.D., Marta-Almeda, M., DiMarco, S.F., 2012. A numerical investigation of the Mississippi and Atchafalaya freshwater transport, filling and flushing times on the Texas-Louisiana Shelf. J. Geophys. Res.: Oceans 117 (C11).

APPENDIX C:

ESTIMATING SEA SURFACE SALINITY IN THE NORTHERN GULF OF MEXICO FROM SATELLITE OCEAN COLOR MEASUREMENTS

Chen, S., and Hu, C. (2017b). Estimating sea surface salinity in the northern Gulf of Mexico from satellite ocean color measurements. *Remote Sensing of Environment, 201, 115-132*.

Remote Sensing of Environment 201 (2017) 115–132

Contents lists available at ScienceDirect

Remote Sensing of Environment

journal homepage: www.elsevier.com/locate/rse

Estimating sea surface salinity in the northern Gulf of Mexico from satellite ocean color measurements

Shuangling Chen, Chuanmin Hu*

College of Marine Science, University of South Florida, 140 Seventh Avenue, South, St. Petersburg, FL, USA 33701

ARTICLE INFO

Keywords:
Sea surface salinity
MODIS
SeaWiFS
Gulf of Mexico
Remote sensing reflectance
Neural network

ABSTRACT

Sea surface salinity (SSS) is an important parameter to characterize physical and biogeochemical processes, yet its remote estimation in coastal waters has been difficult because satellite sensors designed to "measure" SSS lack sufficient resolution and coverage, and higher-resolution ocean color measurements suffer from optical and biogeochemical complexity when used to estimate SSS. In the northern Gulf of Mexico (GOM), this challenge is addressed through modeling, validation, and extensive tests in contrasting environments. Specifically, using extensive SSS datasets collected by many groups spanning > 10 years and MODIS (Moderate Resolution Imaging Spectroradiometer) and SeaWiFS (Sea-Viewing Wide Field-of-View Sensor) estimated remote sensing reflectance (Rrs) at 412, 443, 488 (490), 555, and 667 (670) nm and sea surface temperature (SST), a multilayer perceptron neural network-based (MPNN) SSS model has been developed and validated with a spatial resolution of ~1 km. The MPNN was selected over many other empirical approaches such as principle component analysis (PCA), multi-nonlinear regression (MNR), decision tree, random forest, and supporting vector machines (SVMs) after extensive evaluations. The MPNN was trained by a back-propagation learning technique with Levenberg-Marquardt optimization and Bayesian regularization. The model showed an overall performance of root mean square error (RMSE) = 1.2, with coefficient of determination (R^2) = 0.86, mean bias (MB) = 0.0, and mean ratio (MR) = 1.0 for SSS ranging between ~1 and ~37 (N = 3640). Validation using an independent dataset showed a RMSE of 1.1, MB of 0.0, and MR of 1.0 for SSS ranging between ~27 and ~37 (N = 412). The model with its original parameterization has been tested in the Mississippi-Atchafalaya coastal region, Florida's Big Bend region, and in the offshore Mississippi River plume, with satisfactory performance obtained in each case. Comparison with concurrent Aquarius-derived SSS maps (110-km resolution) showed similar agreement in offshore waters as indicated above, but the new 1-km resolution SSS maps revealed more finer-scale features as well as salinity gradients in coastal waters. The sensitivity of the model to realistic model input errors in satellite-derived SST and Rrs was also thoroughly examined, with uncertainties in the model-derived SSS being always < 1 for SSS > 30. The extensive validation, evaluation, and sensitivity test all indicated the robustness of the MPNN model in estimating SSS in most, if not all, coastal waters and offshore plumes in the northern GOM. Thus, the model provided a basis for generating near real-time 1-km resolution SSS maps from satellite measurements. However, the model showed limitations when applied to regions with known algal blooms or upwelling as they both led to low Rrs in the blue bands that may be falsely recognized as caused by low SSS.

1. Introduction

1.1. Challenge in mapping sea surface salinity of coastal waters

Sea surface salinity (SSS) is an important parameter in understanding many physical and biogeochemical processes in coastal waters (Fennel et al., 2011; Xue et al., 2013). SSS data is used in support of studies examining the mixing between riverine freshwater and offshore oceanic water and changes in other water properties (Hu et al., 2004; Palacios et al., 2009; Devlin et al., 2015; Horner-Devine et al., 2015; Yang et al., 2015). Further, SSS is an important parameter in tracing the pathway of the riverine-delivered terrestrial substance (e.g. organic and inorganic carbon, nutrients) into the ocean, as well as examining the intensity of stratification and studying variations in water's optical properties, hypoxia, and algal blooms in coastal margins (Rabalais et al., 1996, 2002; Cannizzaro et al., 2013; Weisberg et al., 2014; O'Connor et al., 2016; Le et al., 2016).

However, obtaining SSS at synoptic scales with frequent coverage in

* Corresponding author.
E-mail address: huc@usf.edu (C. Hu).

http://dx.doi.org/10.1016/j.rse.2017.09.004
Received 5 February 2017; Received in revised form 17 July 2017; Accepted 2 September 2017
0034-4257/

coastal waters has proved difficult due to inadequate ship-based measurements (that lack of appropriate resolutions) or failures in satellite SSS measurement algorithms. The two existing satellite sensors, based on microwave remote sensing and designed to "measure" SSS from space, are the ESA SMOS (the Soil Moisture and Ocean Salinity) and NASA Aquarius/SAC-D. Yet the coarse spatial resolution (30–100 km) and low revisit frequency (3 days or more), along with the issue of land contamination, limit their use in observing the dynamic variations in SSS in coastal waters (Koblinsky et al., 2003; Lagerloef et al., 2008; Font et al., 2010; Kerr et al., 2010).

Recent advances in ocean color remote sensing have shown potentials in synoptic and frequent mapping of SSS (Wong et al., 2007; Ahn et al., 2008; Palacios et al., 2009; Marghany and Hashim, 2011; Urquhart et al., 2012; Bai et al., 2013; Geiger et al., 2013; Qing et al., 2013; Vandermeulen et al., 2014; Zhao et al., 2017). In these studies, SSS was modeled from apparent optical properties (AOPs) such as spectral remote sensing reflectance (Rrs, sr^{-1}), inherent optical properties (IOPs) such as absorption coefficient, or other satellite parameters such as Sea Surface Temperature (SST, °C) and chlorophyll-a concentrations (CHL, mg m^{-3}). Regardless of the method, the underlying principle is that colored dissolved organic matter (CDOM) is a good tracer of SSS in coastal oceans (Vodacek et al., 1997; Hu et al., 2003; Coble et al., 2004; Del Vecchio and Blough, 2004), and CDOM absorption coefficient (a_{CDOM}, m^{-1}) can be, at least in theory, estimated from ocean color measurements and then used to estimate SSS assuming conservative mixing for both (e.g., Siddorn et al., 2001; Johnson et al., 2003; Chen and Gardner, 2004; Hong et al., 2005; Guo et al., 2007; Bowers and Brett, 2008). Indeed, in river-dominated coastal regions, CDOM mainly comes from terrestrial inputs through river discharges and non-point source land runoff (Chester, 1990; Nelson et al., 2007). This plays a key role in determining the optical properties (especially Rrs) of coastal ocean waters. However, due to the distinct CDOM characteristics of each local river endmember and its seasonality, the relationship between a_{CDOM} and SSS may vary in space and time (Chen, 1999; Hu et al., 2003; Del Vecchio and Blough, 2004; Bowers and Brett, 2008; Bai et al., 2013; Geiger et al., 2013), making it impossible to apply a locally designed SSS algorithm to other regions. Adding to this difficulty are the uncertainties in the satellite-retrieved Rrs and a_{CDOM}; these uncertainties can cause a well-established, ship-based a_{CDOM} – SSS relationship to become unreliable. Such difficulties can be clearly seen from Fig. S1 in the supplemental materials for the northern Gulf of Mexico when satellite-derived a_{CDOM} was used to estimate SSS. Thus, in general, mapping SSS in coastal waters from space still represents a major challenge for the ocean color research community.

1.2. Study region and objectives

The study region is the northern Gulf of Mexico (GOM) that receives discharge from numerous rivers. The Mississippi River provides the largest river discharge into northern GOM. Ranking as the world's 8th largest river in freshwater discharge and sediment delivery, the Mississippi River system drains 41% of the land in the United States (Milliman and Meade, 1983). About 70% of the river's flow drains through the lower Mississippi River into the GOM, with the remaining 30% delivered to the Atchafalaya basin, and finally into the GOM (U. S. Army Corps of Engineers, 2008) forming the Mississippi/Atchafalaya River system (MARS). In addition to the MARS, there are some smaller rivers along the coast of the northern GOM, such as Suwannee, Pensacola, and Apalachicola Rivers; these also play significant roles in affecting the coastal water properties (Mattraw and Elder, 1984; Averett et al., 1994; Murrell et al., 2002). With large seasonal loadings of freshwater, inorganic and organic matters, and nutrients, from the MARS and other rivers, the northern GOM maintains an active ecosystem with dynamic physical and biogeochemical processes. Here, SSS plays an important role in the physical mixing between the MARS and GOM open waters (Xue et al., 2013), the hypoxia phenomenon induced by intensified biological activities and vertical stratification (Wiseman et al., 1997; Rabalais et al., 2002), and the distribution and variation of the carbonate properties such as total alkalinity (TA) and surface partial pressure of CO_2 (pCO_2) (Yang et al., 2015; Chen et al., 2016).

Synoptic SSS estimation in the northern GOM has been attempted in several published studies. Using data from SMOS and Aquarius, Fournier et al. (2016) examined the seasonal and interannual variations of SSS in the GOM. However, the study was limited by the coarse spatial resolution (30–100 km) and lack of coverage in coastal waters as a result of sensor limitations. Based on total absorption coefficients at 486 and 551 nm derived from the SNPP-VIIRS (Suomi National Polar-orbiting Partnership satellite with the Visual Infrared Imaging Radiometer Suite) measurements and SSS measurements from several nearshore stations, Vandermeulen et al. (2014) developed a simple SSS model using linear regression between SSS and absorption difference. Due to the dynamics and complexity of the northern GOM, only 65% of the data tested with the model showed a SSS uncertainty of ≤ 2; one possibility for this result is that the relationship between absorption difference and SSS may change in space and time. Indeed, although linear relationships between SSS and a_{CDOM} have been developed on a regional basis (Blough et al., 1993; Ahn et al., 2008; Palacios et al., 2009; Bai et al., 2013), in the northern GOM the SSS-a_{CDOM} relationship appears to be different in several studies (Hu et al., 2003; Del Castillo and Miller, 2008; Lohrenz et al., 2010). Such discrepancies indicate that unlike SSS, CDOM may not follow conservative mixing, and both CDOM production from phytoplankton degradation (Nelson et al., 1998, 2010; Twardowski and Donaghay, 2001; Stedmon and Markager, 2005) and CDOM photochemical bleaching (Chen and Gardner, 2004) may contribute to the variations in the SSS-a_{CDOM} relationship (Del Vecchio and Blough, 2004). Consequently, to date there has been no reliable model to estimate SSS from ocean color measurements in this region.

Extensive SSS data have been collected from the northern GOM by numerous groups and agencies. Acknowledging the limitations of SMOS and Aquarius, lack of reliable ocean color-based SSS models, the unstable SSS-a_{CDOM} relationship in the northern GOM, and high uncertainties in satellite-derived a_{CDOM} (Hu et al., 2003; Le and Hu, 2013; Mannino et al., 2014), the goal of the present study is to address the challenge of mapping SSS from ocean color measurements over the optically complex northern GOM, with the following specific objectives:

1) Develop a relatively robust model to estimate SSS at 1-km resolution from ocean color measurements;
2) Quantify uncertainties in the estimated SSS through extensive evaluations under various oceanographic conditions (e.g., Mississippi-Atchafalaya coastal region, Florida's Big Bend, and Mississippi River plume) and through sensitivity studies;
3) Understand the limitations of this approach in order to determine its applicability to time-series data.

The paper is structured as follows. Field and satellite data are presented first, and optical characteristics of the waters with different SSS ranges are analyzed. Secondly, methods in developing SSS models are briefly reviewed. Finally, in the Results and Discussion sections, the trained SSS model is statistically validated and evaluated under different conditions, with model sensitivities to the model inputs analyzed and model limitations investigated.

2. Data and methods

2.1. Datasets

2.1.1. Field data

To assure enough spatial and temporal coverage under all possible oceanographic conditions and measurement scenarios, we compiled all publically available SSS data collected over the past 20 years in the

Table 1
SSS measurements from different research vessels and buoy platforms in the GOM. These SSS were collected at a depth of ≤ 5 m from all seasons. Only a small portion of these measurements were found to have co-located and concurrent (± 6 h) satellite-derived SST and Rrs data (last column). These SSS data were used to develop the MPNN model. Corresponding cruise tracks are shown in Fig. 1.

Platform (Ship/Buoy)	Data source	Year covered	Range of SSS	Range of SSS with matching satellite data	# of observations	# of observations with matching satellite data
R/V GYRE	TAMU	1997–2000	15.5–36.9	22.2–36.5	77,151	319
R/V Bold	CDIAC	2006–2007	0.2–36.2	22.8–36.5	29,346	60
R/V Cape Hatteras	CDIAC	2009–2010	0.0–37.2	13.6–36.6	26,794	215
R/V Brown	CDIAC	2003,2006–2007, 2009–2010	24.2–36.7	30.4–36.6	26,408	137
M/V Las Cuevas	AOML	2009–2011	6.5–36.8	26.6–36.6	18,649	328
Anonymous Watercraft	FWC	2010–2011	15.0–34.8	32.9	350	1
R/V Falkor	TAMU	2012	35.3–36.9	35.8–36.6	6,947	133
R/V Pelican	CDIAC	2013	0.7–36.4	28.7–29.0	50,703	2
R/V Marcus G. Langseth	LEDO	2013	34.2–36.7	36.3–36.5	2,014	5
R/V WeatherBird II	USF	2011–2013	0.2–38.0	26.2–36.8	56,249	444
R/V Walton Smith	CDIAC	1998–2015	6.0–39.8	29.3–38.0	71,686	194
C/S Explorer of the Seas	CDIAC	2002–2007,2015	33.8–36.6	35.9–36.5	46,833	369
R/V Gordon Gunter	CDIAC	2008–2011,2014–2015	8.6–36.8	28.8–36.6	102,037	1,191
Buoy 42,013 (27.173°N, 82.924°W)	NDBC	2009–2015	20.6–37.9	34.4–36.5	37,063	64
Buoy 42,021 (28.311°N, 83.306°W)	NDBC	2009–2012	28.7–36.6	32.7–35.9	29,286	58
Buoy 42,022 (27.504°N, 83.741°W)	NDBC	2013–2015	28.9–37.3	34.5–36.3	18,826	34
Buoy 42,036 (28.500°N, 84.517°W)	NDBC	2006	35.9–36.2	36.0–36.2	328	3
Buoy crta1 (30.308°N, 88.140°W)	NDBC	2011–2015	0.1–31.9	17.4	77,212	1
Buoy lrkf1 (24.982°N, 80.826°W)	NDBC	2009–2014	6.4–49.4	30.7–35.1	47,589	3
Buoy mbla1 (30.437°N, 88.011°W)	NDBC	2009–2015	0.1–27.6	1.4–24.8	38,469	47
Buoy mlrf1 (25.012°N, 80.376°W)	NDBC	2005–2010	27.5–37.2	33.8	30,359	1
Buoy CoastMS (30°N, 88.6°W)	CDIAC	2009, 2011, 2013–2014	14.0–35.6	22.1–35.6	4,467	31
Total	–	1997–2015	0.0–39.8	1.4–38.0	798,766	3,640

AOML: Atlantic Oceanographic & Meteorological Laboratory; CDIAC: Carbon Dioxide Information Analysis Center; FWC: Florida Fish and Wildlife Conservation Commission; LEDO: Lamont-Doherty Earth Observatory; NDBC: National Data Buoy Center. TAMU: Texas A & M University; USF: University of South Florida.

northern GOM. These include two data types: those collected from synoptic cruise surveys, and those from fixed-location buoys. Tables 1 and 2 present a general description of the data source, data volume, time span, and data range for each dataset. These data cover all seasons. The data in Table 1 were used to develop the SSS model, while the data in Table 2 (independent from those in Table 1) were used to evaluate the SSS model. Collectively these data represent the most complete dataset for the northern GOM.

In Table 1 (model development), the SSS data (collected between 1997 and 2015) ranged between 0.0 and 39.8. Ship-based underway SSS data were obtained from the databases of Carbon Dioxide Information Analysis Center (CDIAC), NOAA Atlantic Oceanographic & Meteorological Laboratory (AOML), Texas A & M University (TAMU), Lamont-Doherty Earth Observatory (LEDO), and University of South Florida (USF). The data were collected by numerous research groups funded by different agencies. For example, between 1997 and 2000, SSS was collected by the Northeastern GOM (NEGOM) program funded by the Bureau of Ocean Energy Management (BOEM, formerly known as Minerals Management Service) and archived at TAMU. Between 2011 and 2013, SSS was collected by the C-IMAGE consortium funded by the GOM Research Initiative, with data archived at USF.

Typically, ship-based SSS data were collected at a depth of ≤ 5 m using a CTD (SBE-21 or SBE-38 or SBE-45, Seabird Inc., USA, YSI 6600) integrated in the shipboard flow-through seawater system, with a measurement interval near 2 min and an accuracy of 0.05. SSS time series from CDIAC and NOAA National Data Buoy Center (NDBC) were collected at a depth of 3 m using a CTD (SBE MicroCAT C-T Recorder, or SBE 37-IM MicroCAT), with a measurement interval of ~ 3 h or ≤ 1 h and an accuracy of 0.02. It is difficult to present each dataset in detailed graphical format, but the full cruise tracks with color-coded SSS values are shown in Fig. 1a, with over 11,000 SSS measurements in each month.

Similar to Table 1, Table 2 lists the various data sources of field SSS measurements that were used for independent model evaluation under differing conditions. Specifically, for a general evaluation of the developed SSS model, SSS data collected at discrete stations were obtained from the NOAA National Centers for Environmental Information (NCEI) and Florida Fish and Wildlife Conservation Commission's (FWC) Fish and Wildlife Research Institute (FWRI). These SSS data were collected in 2010 and 2014, ranging between 3.8 and 37.5. To test the model performance in the Mississippi-Atchafalaya coastal region, underway SSS measurements from two cruises (GM0606 and GM1003) were obtained from CDIAC; these SSS data were collected in June 2006 and March 2010 and ranged between 0.02 and 36.62. To examine the model performance in the Florida's Big Bend region, SSS data collected at discrete stations were obtained from NOAA NCEI and FWC; these data were collected in 2010, 2011 and 2014, ranging between 11.4 and 36.4. To evaluate the model performance in quantifying SSS in the Mississippi river plumes, discrete SSS measurements from USF, and underway SSS from cruise WS15234 from CDIAC, were compiled; these SSS data were collected in Aug. and Sep. 2015, ranging between 29.1 and 36.4. To test the model performance in deriving SSS time-series at fixed locations, SSS time-series data from three buoys ("crta1", "42022", and "CoastMS") were obtained from NDBC and CDIAC. SSS from buoy "crta1" were collected between 2011 and 2015, ranging between 1.0 and 30.1; SSS from buoy "42022" were collected between

Table 2
SSS measurements used to evaluate the MPNN SSS model under different conditions. These SSS were collected at a depth of ≤ 5 m from all seasons. The specific purpose of each dataset is annotated in ***bold italic font***. Only a small portion of these measurements were found to have co-located and concurrent (± 24 h) MODIS SST and Rrs data (last column). Corresponding cruise tracks in each case are shown in Figs. 1–12. Note that the time-series SSS data from buoys "crta1", "42022" and "CoastMS" *shown in italics below* were not used in model development.

Project/cruise_ID[a]	Data source[b]	Date	Data type	Range of SSS	Range of SSS with matching satellite data	# of observations	# of observations with matching satellite data
Purpose	***To conduct a general validation of the MPNN model***						
Deepwater Horizon Support	NCEI	Apr–Oct, 2010	Discrete	3.8–36.7	27.2–36.6	1,279	253
SEAMAP	FWC	Oct, 2014	Discrete	29.1–36.1	34.4–36.1	158	79
SEAMAP	FWC	Jun, 2014	Discrete	24.3–37.5	26.8–37.1	178	80
Total	–	–	–	3.8–37.5	26.8–37.1	1,615	412
Purpose	***To test the model performance in the MARS region***						
GM0606	CDIAC	Jun, 2006	Continuous	0.7–36.2	22.6–36.1	5,938	3,789
GM1003	CDIAC	Mar, 2010	Continuous	0.0–36.6	3.0–36.6	7,811	3,345
Total	–	–	–	0.0–36.6	3.0–36.6	13,749	7,134
Purpose	***To test the model performance in the Mississippi River plumes***						
DEEPEND	USF	Aug, 2015	Discrete	29.1–36.4	31.5–36.3	27	3
WS15234	CDIAC	Sep, 2015	Continuous	32.4–36.0	32.4–35.6	1,609	488
Total	–	–	–	29.1–36.4	31.5–36.3	1,636	491
Purpose	***To test the model performance in the Big Bend region***						
Deepwater horizon support	NCEI	Aug–Sep, 2010	Discrete	32.1–36.1	32.1–36.1	59	26
SEAMAP	FWC	Oct, 2014	Discrete	32.2–35.8	32.2–35.8	37	19
SEAMAP	FWC	Jun, 2014	Discrete	32.1–36.4	34.8–36.4	53	7
Anonymous	FWC	May–Nov, 2010	Discrete	15.1–32.9	20.5–32.9	150	36
Anonymous	FWC	Jan–Nov, 2011	Discrete	24.6–34.8	25.8–34.8	188	106
Anonymous	FWC	Jun, 2014	Discrete	11.4–29.7	20.2–28.1	215	11
Total	–	–	–	11.4–36.4	20.5–36.4	702	205
Purpose	***To test the model performance at fixed locations***						
Buoy 42,022 (27.504°N, 83.741°W)	*NDBC*	*2013–2015*	*Continuous*	*31.7–36.5*	*33.5–36.5*	*493*	*156*
Buoy crta1 (30.308°N, 88.140°W)	*NDBC*	*2011–2015*	*Continuous*	*1.0–30.1*	*2.7–27.6*	*1,661*	*65*
Buoy CoastMS (30°N, 88.6°W)	*CDIAC*	*2009, 2011, 2013–2014*	*Continuous*	*15.7–35.6*	*15.9–35.6*	*567*	*146*
Total	–	–	–	*1.0–36.5*	*2.7–36.5*	*2,721*	*367*

[a] DEEPEND: Deep-Pelagic Nekton Dynamics of the Gulf of Mexico; SEAMAP: Southeast Area Monitoring and Assessment Program.
[b] NCEI: National Centers for Environmental Information.

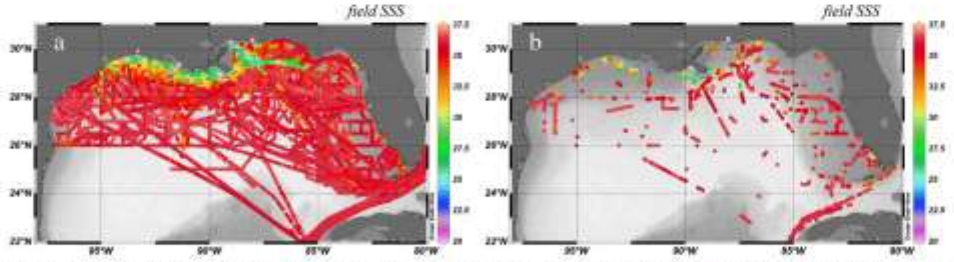

Fig. 1. Spatial distributions of the field-measured SSS in the GOM along the cruise tracks. (a) Cruise tracks from all data described in Table 1; (b) Cruise tracks from the same data but with co-located and concurrent (± 6 h) satellite Rrs and SST. (For interpretation of colors in this figure, the reader is referred to the web version of this article.)

2013 and 2015, ranging between 31.7 and 36.5; SSS from buoy "CoastMS" were collected in 2009, 2011, and 2013–2014, ranging between 15.7 and 35.6. These buoy-measured SSS data represent independent data to evaluate the algorithm performance, as 99.9% of them were excluded in the model development. Furthermore, daily means of these continuous SSS data were used for statistical analysis (see Section 3.5 and Table 2). The spatial distributions of these SSS data are shown in each case in Section 3.

2.1.2. Satellite data

The satellite data used in this study were downloaded from the NASA Goddard Space Flight Center (GSFC) (http://oceancolor.gsfc.nasa.gov/). Daily standard NASA Level-2 ocean color data products (reprocessing version R2014.0) with spatial resolution of ~1 km were derived from the Moderate Resolution Imaging Spectroradiometer (MODIS) on the Aqua satellite and Sea-Viewing Wide Field-of-View Sensor (SeaWiFS) on the SeaStar satellite. MODIS data included SST and Rrs in 5 spectral bands (412, 443, 488, 547, 667 nm) between July 2002 and December 2015, and SeaWiFS data included Rrs in 5 spectral bands (412, 443, 490, 555, 670 nm) between November 1997 and July 2002. Both SST and Rrs data were used as inputs of the SSS model. SST was used to capture the possible contrast in temperature between river

and oceanic waters, particularly the upwelling water masses which are represented by lower temperatures (Palacios et al., 2009). The 5 visible spectral bands were selected mainly considering the exponential decay of CDOM absorption from the blue to the red. Rrs(667) from MODIS or Rrs(670) from SeaWiFS has been used as a surrogate for sediment concentration in the water column (Stumpf and Pennock, 1989; Wynne et al., 2005; Barnes et al., 2015), therefore the use of Rrs667 was to help minimize the turbidity effects in SSS-CDOM retrievals through empirical techniques. Note that although MODIS has a 531-nm band and SeaWiFS has a 510-nm band, for cross-sensor consistency they were not used in this study. For the same reason, to assure consistency between MODIS Rrs(547) and SeaWiFS Rrs(555), MODIS Rrs(547) was converted to Rrs(555) nm based on the standard SeaDAS7.0.2 processing procedure using Eqs. (1) and (2). In addition, to test the published regression model, daily standard MODIS Level-1A data (version R2014.0) in Sep. 2014 were downloaded from NASA GSFC and processed to Level 3 using SeaDAS7.0.2 to derive the total absorption coefficients at 488, 547 and 555 nm.

$$Rrs(555) = 10^{(a_1 \times \log_{10}(Rrs(547)) - b_1)},\ Rrs(547) < sw \quad (1)$$

where sw = 0.001723, a_1 = 0.986, and b_1 = 0.081495.

$$Rrs(555) = a_2 \times Rrs(547) - b_2,\ Rrs(547) \geq sw \quad (2)$$

where sw = 0.001723, a_2 = 1.03, and b_2 = 0.000216.

In addition to the satellite ocean color data products, standard NASA Level-3 monthly SSS composites, derived from Aquarius measurements, were also downloaded from the NASA GSFC. These data were used to compare with the corresponding SSS composites estimated from MODIS measurements with the SSS model developed in this study.

2.2. Method

2.2.1. Model selection, and principle and structure of MPNN

Our first attempt to estimate SSS from satellite-derived Rrs was through the SSS-CDOM relationship where CDOM was estimated from satellite-derived Rrs using the Quasi-Analytical Algorithm (Lee et al., 2002). However, the results were unsatisfactory, with virtually no relationship observed between field-measured SSS and satellite-derived CDOM for SSS between 27 and 37 (Supplemental Fig. S1). Therefore, the approach of deriving SSS through explicit use of CDOM was abandoned, but other empirical methods were tested.

In the published literature, statistical approaches such as multivariate linear regression (MLR) and artificial neural network (ANN) were used to develop satellite-based SSS models (Woog et al., 2007; Ahn et al., 2008; Palacios et al., 2009; Marghany et al., 2011; Urquhart et al., 2012; Bai et al., 2013; Geiger et al., 2013; Qing et al., 2013; Vandermeulen et al., 2014). In this study, the commonly used traditional empirical methods (i.e., MLR, multi-variate nonlinear regression (MNR), and principle component analysis (PCA) regression) and machine learning based approaches (i.e., decision tree, random forest, and Support Vector Machine (SVM) regression) were all tested, but all yielded unsatisfactory results (see below). Among the tested approaches was artificial neural network (ANN), which showed better performance than all other approaches. ANN was then selected for the SSS remote sensing model in this study; one distinct advantage of ANN is that it can approximate the nonlinear relationship between observations and targeted variable (SSS), without explicitly knowing their functional dependence (Thiria et al., 1993).

In the past, ANN techniques have been widely used in retrieving AOPs, IOPs, and other parameters such as CHL and total suspended matter (Tanaka et al., 2004; Chauhan et al., 2005; Vilas et al., 2011; Ioannou et al., 2011, 2013; Jamet et al., 2012; Chen et al., 2014, 2015). The type of ANN used in this study is a multilayer perceptron neural network (MPNN) (Bishop, 1995; Gross et al., 1999), which is a feed-forward neural network that consists of one input layer, one or more hidden layers, and one output layer. As shown in Fig. 2, neurons of each

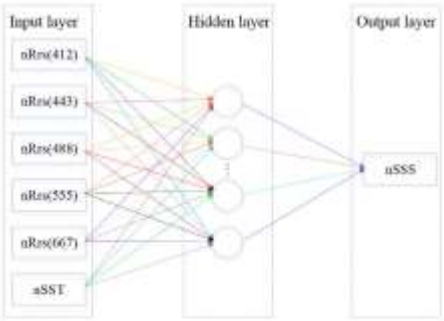

Fig. 2. Architecture of the MPNN, consisting of one input layer, one hidden layer, and one output layer. The cross-layer connections are marked with different colors, indicating different weights and biases. The numbers of neurons in the input and output layers of the MPNN are fixed as specified in the rectangular boxes, and only the number of neurons in the hidden layer was varied to derive the best MPNN frame.

layer are forward connected to the neurons in the adjacent layer, but without any connections to neurons in the preceding layers. Inputs are distributed into the MPNN by the first layer. In the hidden and output layers, each neuron is randomly initialized with two parameters: weight and bias, which are used to transform the input signals by an activation function. Once the number of hidden layers and the number of neurons in each layer are determined, the structure of the MPNN is fixed, and the relations between the inputs and outputs, which depend on the weight and bias values associated with each connection, are also fixed. The values of weights and biases are adjusted through iteration to minimize the sum of the squared errors between the modeled outputs and the real outputs (i.e., the parameters to be retrieved) by a supervised learning technique.

For the MPNN presented in this work, a back-propagation learning technique with a Levenberg-Marquardt optimization and a Bayesian regularization algorithm was implemented in Matlab (R2013a). To transform the input signals in each layer, the classic hyperbolic tangent sigmoid (a = tansig(n)) and linear activation functions (a = purelin (n)) were applied to the hidden and output layers, respectively. The back-propagation learning technique is a backward iterative learning algorithm; it starts at the output layer and ends at the input layer, where the weight and bias of each neuron are updated based on the errors between the current outputs and the actual output values (Hecht-Nielsen, 1989; Goh, 1995). The Levenberg-Marquardt optimization algorithm, also known as the damped least-squares method, is a combination of steepest descent and Gauss-Newton methods. It regulates the network with the probabilistic approach of the Bayes' rule in order to minimize the combination of squared errors and weights, and then determines the correct combination to create a network that can generalize well (Moré, 1978). With Bayesian regularization (Kwok and Yeung, 1996; Burden and Winkler, 2009), the network automatically stops training when reaching a convergence – meaning the sum of squared errors, sum of squared weights, and the effective number of parameters become stable after several iterations. This regularization method is more robust than early stopping techniques (another neural network training technique) because the verification procedure provides an objective criterion for ending the training to avoid over training. The weakness of the early stopping method was also proved in our study as the model showed poor performance (unrealistic SSS retrievals) when applied to satellite images even through the model performance was satisfactory during model training and tuning using discrete data points. The regularization method is also insensitive to the architecture of the network as long as the necessary minimal architecture is provided (Livingstone, 2008). Once the MPNN stops training, the structure of the MPNN will be determined, with the values of

weights and biases finalized.

2.2.2. Data preprocessing of MPNN

Based on the data range of the field SSS measurements in Table 1, both MODIS-derived data products – SST and Rrs (412, 443, 488, 555, 667 nm) and SeaWiFS-derived data products – Rrs (412, 443, 490, 555, 670 nm) were used in the MPNN SSS model development.

To obtain high quality data, concurrent field-measured SSS and satellite-measured SST and Rrs (Table 1) were selected using the following criteria. Considering the diurnal tidal cycle in most regions of the northern GOM, a time window of ± 6 h between field and satellite measurements was used. Various data quality flags (e.g., atmospheric correction failure, stray light, sun glint, etc.) (Barnes and Hu, 2015) were applied to discard all low-quality satellite data, and valid data within a 3 × 3 box centered at the location of each field SSS measurement were extracted and averaged (Bailey and Werdell, 2006) if the number of valid pixels was ≥ 5 and the variance of these valid pixels was ≤ 10%. Such averaged data was used to represent satellite observations over the location. After applying these strict quality controls, and field data binning to match satellite pixel resolution, 3640 conjugate observations of field-measured SSS and satellite data products were determined valid between 1997 and 2015, and available for the MPNN SSS model development (Fig. 1b). Note that for SSS measured between 1997 and 2002, field-measured SST data was used as surrogates of satellite-measured SST due to the lack of SST measurements by SeaWiFS. As demonstrated in the sensitivity analysis in Section 3.6, the MPNN SSS model is insensitive to SST, and this replacement should have little influence in the modeled SSS. In the conjugate dataset, field-measured SSS ranged between 1.4 and 38.0, satellite-measured SST ranged between 9.7 and 33.0 °C, and satellite-measured Rrs covered a wide dynamic range. Detailed statistics of each parameter are described in Table 3.

One advantage of using concurrent satellite SST and Rrs measurements directly to train the MNPP is that uncertainties in these satellite-derived data products will be implicitly included in the empirically-derived weights and biases of the MPNN. When the same data products are used for SSS predictions as those which were used in model development, such uncertainties, to a large extent, should be self-cancelling.

Before the MPNN training, to avoid conditioning problems and to make the MPNN equally sensitive to all inputs and output (Ioannou et al., 2011), both the MPNN inputs (SST and Rrs) and output (SSS) in the conjugate dataset were normalized by subtracting the mean and dividing by the standard deviation (σ) of each parameter using the following equations (Lawrence, 1991):

$$nSST = [(SST - mean(SST))]/\sigma(SST) \quad (3)$$

$$nRrs(\lambda) = [Rrs(\lambda) - mean(Rrs(\lambda))]/\sigma(Rrs(\lambda)) \quad (4)$$

$$nSSS = [SSS - mean(SSS)]/\sigma(SSS) \quad (5)$$

Therefore, the output of the MPNN needs to be denormalized with the mean and standard deviation of SSS using the inversion of Eq. (5).

The normalized conjugate dataset was randomly divided into two parts, with 70% (2548 points) used to train the MPNN, and 30% (1092 points) to test the trained MPNN to confirm the predictive power of the model.

2.2.3. Training of MPNN

Several studies showed that any continuous function can be represented by a MPNN with one hidden layer (Hornik et al., 1989; Aires et al., 2001). Therefore, to train the SSS model using the normalized dataset in Table 1, based on the principle that the number of weights should not be greater than the number of training equations, a group of MPNNs with one hidden layer (Fig. 2) were tested by varying the number of hidden neurons between 1 and 60. In each test, the weights and biases were randomly initialized 10 times to avoid the unfortunate set of initial weights and bias (the case where the MNPP can be trained well but cannot be generalized well when applied to a new dataset or a satellite image). Once the number of hidden neurons was determined, the optimal network structure with finalized coefficients of weights and bias was determined.

In the training phase of the MPNN, different formulas and different combinations of the input variables were thoroughly tested. For example, according to commonly used Rrs formats in CDOM and chlorophyll algorithms (Carder et al., 1999; Hu et al., 2012), Rrs in logarithmic scale, Rrs band ratios (i.e., Rrs(412)/Rrs(555), Rrs(443)/Rrs (555)), and relative band differences were all used as model inputs and tuned following the steps described above. According to Geiger et al. (2013), in the model tuning phase, geological latitude and longitude data were also chosen as the inputs to train the model.

2.2.4. Accuracy assessment

The empirical nature of the MPNN makes it extremely important to understand the model applicability under various oceanographic conditions from different coastal and offshore regions. In this study the model accuracy was evaluated using independent datasets that were not used in model development. These datasets are described in Table 2, representing different scenarios ranging from river plumes and coastal runoff in different regions of the northern GOM. To increase the data volume, the time difference between satellite and field measurements was relaxed to 24 h. In addition, to evaluate model performance, the model-derived SSS was compared with those estimated from the satellite microwave measurements as well as time-series data obtained from marine buoys.

To compare the model-derived SSS and field-measured SSS, and to gauge the performance of the MPNN in the training and various evaluation phases, coefficient of determination (R^2), root mean square error (RMSE), mean bias (MB) and mean ratio (MR) were used, and the same statistics were also applied in the sensitivity analysis below.

2.2.5. Sensitivity to errors in the input variables (SST and Rrs)

The inputs to the MPNN model, namely MODIS-derived SST and Rrs, are not error free. In order to understand the model sensitivity to such input errors, SST and Rrs errors were first simulated using uncertainty values reported in the literature, and then fed to the MPNN model. SSS derived from the same MPNN using error-free inputs and error-added inputs were then compared to determine the model's sensitivity to input errors.

For evaluation of model sensitivity to SST errors, because MODIS SST uncertainties in the GOM are around 0.5–1 °C (Hu et al., 2009), SST

Table 3
Statistics of the conjugate dataset in Table 1 after matching with concurrent satellite SST and Rrs measurements with a time window of ± 6 h (N = 3640). This dataset was used to develop the MPNN SSS model, with 70% used to train the MPNN and the remaining 30% used to test the trained model. Corresponding cruise tracks of this dataset are shown in Fig. 1b.

Variables	Field-measured SSS	Satellite-measured SST (°C)	Rrs412 (sr^{-1})	Rrs443 (sr^{-1})	Rrs488 (sr^{-1})	Rrs555 (sr^{-1})	Rrs667 (sr^{-1})
Maximum	38.0	33.0	0.023055	0.028264	0.037942	0.044670	0.024260
Minimum	1.4	9.7	0.000237	0.000683	0.001256	0.000843	0.000002
Median	35.9	26.4	0.005594	0.005720	0.005183	0.001886	0.000202
Mean	34.6	25.9	0.006003	0.005922	0.005488	0.002942	0.000551

errors of ± 1 °C were added to the SST data in the MPNN model, where the corresponding Rrs values were kept the same.

For evaluation of model sensitivity to Rrs errors, MODIS Rrs errors were simulated using reported MODIS Rrs uncertainty values and spectral dependence of MODIS Rrs errors (Hu et al., 2013). In other words, MODIS Rrs errors are not spectrally independent, but errors in one band, to a large degree, are related to errors in another band, with additional random errors (Fig. 10 of Hu et al., 2013).

The spectrally-dependent and independent Rrs errors were simulated in the following way, following the same approach of Qi et al. (2017):

1) Simulate 5000 Rrs667 errors following a Gaussian distribution with a zero mean and a standard deviation of $5 \times 10^{-5}\ sr^{-1}$ (Hu et al., 2013). This is basically the error distribution determined from MODIS measurements in ocean gyres;
2) Calculate the corresponding spectrally-dependent Rrs errors at 412, 443, 488, and 555 nm using Eqs. (6)–(10) (Hu et al., 2013);
3) Add 5000 spectrally-independent Rrs errors in each band; these errors also follow a Gaussian distribution with zero mean and an assumed standard deviation (Δ). The addition of these errors to those in Step 2 lead to partially spectrally-dependent errors, representing realistic cases from ocean color measurements;
4) Select one Rrs spectrum from the training dataset described in Table 1 (corresponding field-measured SSS = S1), estimate SSS using the MPNN model. Then, add the 5000 erroneous Rrs spectra to the selected Rrs spectrum, one by one, and calculate the corresponding SSS using the same MPNN model (marked as S2 for each of the 5000 input spectra). The SSS errors would be S2-S1 where S2 has 5000 values and S1 is a single value. The standard deviation of the 5000 SSS errors represents the SSS uncertainty due to input Rrs errors;
5) Repeat step 4 for the whole dataset for different S1 values, leading to SSS uncertainties for each S1 due to the same input Rrs errors; and,
6) Bin the S1 values with an interval of 1 in SSS, SSS uncertainties (from the MPNN model) for each bin are calculated as the mean and standard deviation from all standard deviation values within each bin.

$$Rrs547error = 3.830 \times Rrs667error - 0.000041 \quad (6)$$

$$Rrs555error = Rrs547error \quad (7)$$

$$Rrs488error = 2.6635 \times Rrs555error - 0.0002 \quad (8)$$

$$Rrs443error = 0.7322 \times Rrs488error + 0.0001 \quad (9)$$

$$Rrs412error = 0.8154 \times Rrs667error + 0.0003 \quad (10)$$

Note that Eq. (6) was from Hu et al., 2013, Eq. (7) was one assumption made in this study, and Eqs. (8)–(10) were calculated based on Table 3 in Hu et al., 2013, with R^2 of 0.994, 0.996, and 0.241, respectively.

In total, four experiments (Experiments 1, 2, 3 and 4) were conducted based on the steps above. In these experiments, the spectrally-dependent Rrs errors were kept the same, but the spectrally-independent Rrs errors were varied to have their standard deviations (i.e., the Δ term in Step 3 above) of $1.2 \times 10^{-4}\ sr^{-1}$, $2.3 \times 10^{-4}\ sr^{-1}$, and $3.6 \times 10^{-4}\ sr^{-1}$, respectively, in each case.

3. Results

3.1. Optical characteristics of the training dataset

Fig. 3 shows the Rrs spectra of the dataset used for model development (Table 1), which covered a high dynamic range. The Rrs peaks occurred in different bands for different SSS ranges. Specifically, for SSS ≤ 30 (Fig. 3a), Rrs peaks were found in all bands except 412 nm, suggesting significant influence by phytoplankton pigments and/or CDOM as they both strongly absorb light in the blue. For higher SSS (Fig. 3b–d), most spectra showed higher Rrs in the blue than in other wavelengths, indicating clearer waters than the lower-SSS waters. There are some exceptions where the magnitudes of Rrs are high in the green and red wavelengths, indicating waters rich in suspended sediments. From Fig. 3, it is clear that similar spectra shapes may correspond to different SSS values. Such characteristic indicated the complex relationships between SSS and Rrs spectra (or water types), suggesting difficulties in retrieving SSS via traditional inversion algorithms (either empirical or semi-analytical). However, the subtle differences between these spectra formed the basis of using an MPNN approach to address the technical challenge. Furthermore, the full dynamic range in both magnitudes and spectral shapes indicated the comprehensiveness of the dataset, which is important for the MPNN empirical model to work under most, if not all, scenarios because there is no explicit functional relationship between the spectral Rrs and SSS in the model.

3.2. MPNN model training and validation

3.2.1. MPNN model training

Following the procedure described in Section 2.2.3, different formulas and different groups of the input variables were tested. It was found that when SST and spectral Rrs data were used as the model inputs and the number of neurons in the hidden layer was set to 3, the MPNN showed the best performance in terms of RMSE, R^2, MB, and MR when field-measured SSS was used to gauge the model performance. Therefore, this model setting was regarded as the optimal structure of the MPNN. As a reference, Table 4 shows the performance of all tested empirical approaches, including MLR, MNR, PCA, decision tree, random forest, and SVM regression, along with the MPNN. Clearly, the MPNN showed the best performance, and therefore was selected in this study.

As shown in Fig. 4 and Table 5, 70% of the dataset used in the training of the MPNN (Fig. 4a) showed a RMSE of 1.2 (6.9%) and R^2 of 0.86, with MB of − 0.0 and MR of 1.0. The remaining 30% of the dataset used in the testing of the trained MPNN (Fig. 4b) showed a RMSE of 1.2 (1.5%) and R^2 of 0.86, with MB of 0.1 and MR of 1.0. For the entire dataset (Fig. 4c), the testing showed a RMSE of 1.2 (1.0%) and R^2 of 0.86, with MB of 0.0 and MR of 1.0. In addition, the model showed better performance at SSS > 30 than with SSS ≤ 30 in both model training and testing, with RMSE of 1.0 and 3.0, MB of − 0.1 and 1.4, and MR of 1.0 and 1.1 for SSS > 30 and SSS ≤ 30, respectively, in model training, and RMSE of 1.0 and 2.8, MB of − 0.0 and 1.3, and MR of 1.0 and 1.1, respectively, in model testing. The histogram of the residuals in SSS estimation in both model training and testing (Fig. 4d) showed that 78.3% of the residuals were within the RMSE based on the whole dataset (which was 1.2) and 96% of the residuals were within RMSE of 2, indicating great improvement over the published work (Vandemeulen et al., 2014). The near symmetrical distribution around 0.0 indicated minimal mean bias in the modeled SSS. However, the relatively large and positive MB with SSS ≤ 30 indicate overestimation, as the MPNN model is more sensitive to Rrs uncertainties in this salinity range (see Section 3.6).

3.2.2. MPNN model validation

To further validate the developed MPNN SSS model, an independent dataset as described in Table 2 and Fig. 5a was used. Note that this dataset was not used in either the MPNN model training or testing above. The comparison between MODIS-estimated SSS and field-measured SSS in Fig. 5b showed a RMSE of 1.1 (3.4%), MB of 0.0 and MR of 1.0, again with better performance with SSS > 30 (RMSE = 1.0, MB = − 0.1, and MR = 1.0) than with SSS ≤ 30 (RMSE = 3.0, MB = 2.8, and MR = 1.1). Again, similar to the results shown in the model training, relatively large uncertainties occurred for SSS ≤ 30, which was mainly attributed to the relatively high sensitivity of the

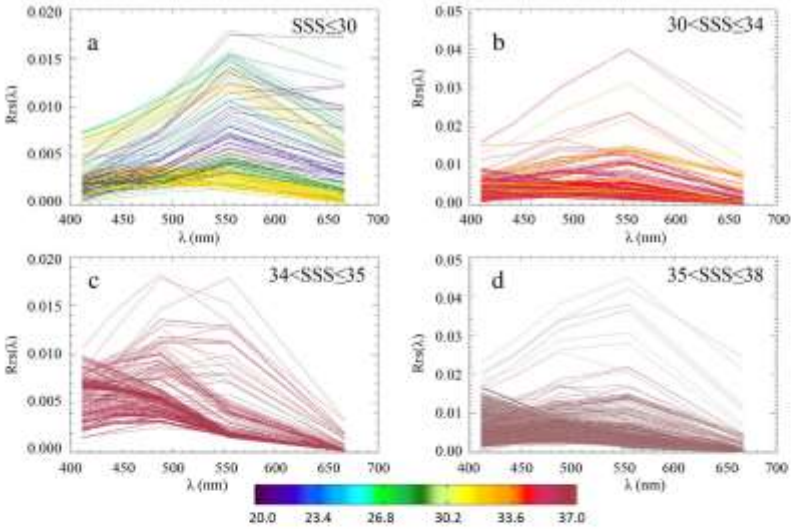

Fig. 3. Spectral characteristics of the dataset described in Table 1 and Fig. 1b for different SSS ranges. These Rrs spectra (units: sr^{-1}), along with SST were used to develop the MPNN SSS model. The spectra cover a wide dynamic range for different optical conditions. (For interpretation of colors in this figure, the reader is referred to the web version of this article.)

MPNN model to Rrs uncertainties in this salinity range (see Section 3.6). The spatial distribution and histogram of the residuals in Fig. 5c & d showed that 78.4% of the residuals were within the RMSE of the developed model and 92.5% were within RMSE of 2. Most of the large residuals (> 2.0 or < − 2.0) were found in the Mississippi river delta where SSS was ≤ 30, and where the positive MB and MR values indicated overestimation.

3.3. Model evaluation for various cases

The scatter plots and statistics of model validation provided overall statistical measures and uncertainties of the MPNN model. To further evaluate the model performance in different regions under different scenarios in the GOM (e.g., Mississippi-Atchafalaya coastal waters, Mississippi River plume, Florida's Big Bend area, etc.), the model was further evaluated with different dataset groups for each case (Table 2, Section 2.1.1). Note that in each case, the field-measured SSS dataset was independent from other cases, and none of these datasets was used in the MPNN training, testing, or validation above.

3.3.1. Mississippi-Atchafalaya coastal waters

Underway SSS measurements from two cruises (GM0606 and GM1003) described in Table 2 were used to evaluate the MPNN model performance in coastal waters off the Mississippi-Atchafalaya region.

The results for cruise GM0606 are shown in Fig. 6. For the whole dataset, the RMSE was 2.4, with MB of 0.4 and MR of 1.0. At SSS > 30, the variation of MODIS-estimated SSS along the cruise track agreed well with the field-measured SSS with RMSE of 1.5, MB of − 0.3, and MR of 1.0. At SSS ≤ 30, the model showed higher uncertainties (RMSE = 4.0, MB = 2.1, and MR = 1.1) especially in three locations (marked as A, B, C in Fig. 6a–c). These locations are in close proximity of the coastline, where the Mississippi-Atchafalaya river flows can change fast (e.g., hours) following tidal mixing. The spatial distribution of the MODIS-estimated SSS along the cruise track in Fig. 6b showed agreement with field-measured SSS (overlaid in Fig. 6d), with low SSS values nearshore and higher SSS values offshore. Furthermore, a 6-day MODIS SSS

Table 4
Model comparison between traditional empirical methods (MLR, MNR, and PCA) and machine-learning based empirical methods (Decision tree, Random Forest, SVM, and MPNN). It is shown that the MPNN model has the optimal performance. The statistics before '/' was derived from model training, and after '/' was from model validation. Note R^2 statistics in our study was based on the calculation of coefficient of determination, therefore negative R^2 could be derived if there were strong bias in the modeled SSS (i.e., Cubic SVM).

Model	Kernel Function	Model Inputs	RMSE	R^2	MB	MR
MLR	–	Rrs Band ratios*	1.8/1.7	0.73/0.73	0.0/0.0	1.0/1.0
MNR	–	Rrs Band ratios and SST	1.5/1.5	0.81/0.79	0.0/0.0	1.0/1.0
PCA Regression	–	Rrs(λ) and SST	2.2/2.2	0.55/0.55	0.0/0.0	1.0/1.0
Decision Tree	Simple Tree	Rrs(λ) and SST	1.5/1.9	0.79/0.66	− 0.0/− 0.0	1.0/1.0
	Medium Tree	Rrs(λ) and SST	1.1/1.8	0.89/0.69	− 0.0/− 0.0	1.0/1.0
	Complex Tree	Rrs(λ) and SST	0.9/1.5	0.93/0.78	0.0/− 0.0	1.0/1.0
Random Forest	Boosted Trees	Rrs(λ) and SST	1.8/2.0	0.71/0.61	− 1.5/− 1.4	1.0/1.0
	Bagged Trees	Rrs(λ) and SST	1.0/1.4	0.91/0.81	0.0/0.0	1.0/1.0
SVM	Linear	Rrs(λ) and SST	2.4/2.6	0.49/0.39	0.4/0.4	1.0/1.0
	Quadratic	Rrs(λ) and SST	1.8/2.0	0.72/0.63	0.2/0.4	1.0/1.0
	Cubic	Rrs(λ) and SST	6.5/17.3	− 2.72/− 26.62	− 2.1/− 1.5	1.0/1.0
	Fine Gaussian	Rrs(λ) and SST	2.3/2.3	0.54/0.52	0.3/0.3	1.0/1.0
	Medium Gaussian	Rrs(λ) and SST	1.7/1.6	0.74/0.75	0.2/0.3	1.0/1.0
	Coarse Gaussian	Rrs(λ) and SST	2.1/2.0	0.61/0.62	0.4/0.4	1.0/1.0
MPNN	*Levenberg-Marquardt optimization and a Bayesian regularization*	Rrs(λ) and SST	1.2/1.2	0.86/0.86	− 0.0/0.1	1.0/1.0

* Rrs Band ratios = [Rrs(667)/Rrs(555), Rrs(667)/Rrs(488),Rrs(667)/Rrs(443)].

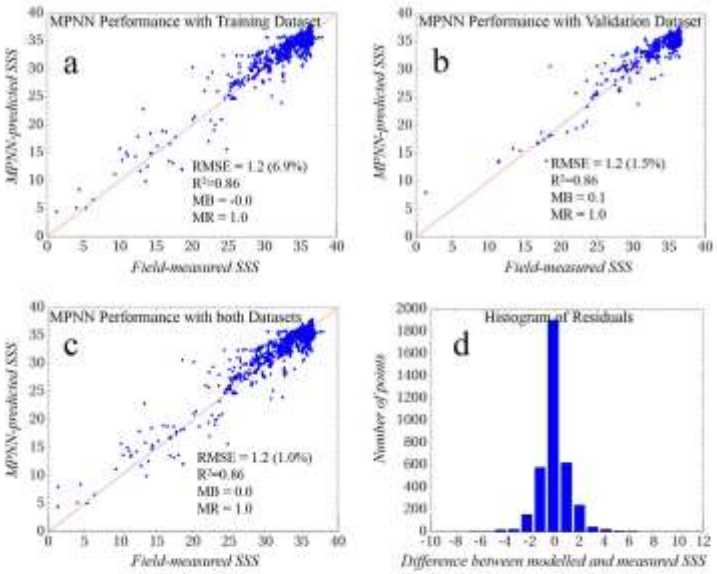

Fig. 4. Performance of the MPNN model in retrieving SSS using the conjugate dataset described in Table 1 and Fig. 1b. (a)–(c) Comparison between MPNN-predicted SSS and field-measured SSS based on the training dataset, testing dataset and the combined (both training and testing) dataset, respectively; (d) histogram of the SSS residuals based on the combined dataset (N = 3640).

composite map (Fig. 6d) covering the cruise period also showed agreement with field-measured SSS (Fig. 6c) although the statistics are slightly worse due to the larger time difference (RMSE = 3.6, MB = −0.3, and MR = 1.0).

Results for the GM1003 cruise are shown in Fig. 7. Similar to those found from the GM0606 cruise, MODIS-estimated SSS mimicked the variation patterns of field-measured SSS, with RMSE of 3.4, MB of 0.0 and MR of 1.0 (Fig. 7a), and the spatial distributions in MODIS-estimated SSS showed lower SSS values in nearshore waters than in offshore waters (Fig. 7b), a result of river discharge and other terrestrial runoff. Also similar to GM0606, better model performance was found for SSS > 30 (RMSE = 1.6, MB = −0.3, and MR = 1.0) than for SSS ≤ 30 (RMSE = 4.7, MB = 0.3, and MR = 1.0). The agreement between MODIS-estimated SSS and field-measured SSS along the cruise track can also be visualized in Fig. 7d. Such an agreement appeared even better when MODIS data along the cruise track was extracted from a 12-day composite map covering the cruise period (Fig. 7c) (RMSE = 3.7, MB = 0.5, and MR = 1.1). Indeed, when the field-measured SSS was color coded in the same way as with the MODIS composite SSS map (Fig. 7d), their agreement in spatial distribution patterns is clearly revealed, both showing lower SSS in nearshore waters than in offshore waters.

In short, in Mississippi-Atchafalaya coastal waters the MPNN SSS model could capture the SSS variations with a reasonable accuracy and quantified uncertainties.

3.3.2. *Mississippi River plume*

To test the model performance in quantifying SSS of river plumes, both discrete and continuous SSS measurements from two experiments were used (Table 2).

The first experiment was in the northern GOM where the Mississippi River plume was found on 14 August 2015 from field measurements. SSS measurements collected between 9 and 21 August 2015 (DEEPEND cruise in Table 2 with cruise track overlaid in Fig. 8b & d) were used to examine the performance of the SSS model, with results shown in Fig. 8a & c. Within a 24-h time window, MODIS-estimated SSS showed agreement with field-measured SSS across the river plume (Fig. 8a), with RMSE of 0.2, MB of 0.2, and MR of 1.0. The corresponding MODIS

Table 5
Performance statistics of the MPNN SSS model during model development (for both model training and testing) and independent model validations under different scenarios using the data described in Tables 1 and 2.

Statistics		RMSE			MB			MR			R^2	# of data points
		SSS ≤ 30	SSS > 30	whole	SSS ≤ 30	SSS > 30	whole	SSS ≤ 30	SSS > 30	whole		
Model development (± 6 h)	Model training	3.0	1.0	1.2	1.4	−0.1	−0.0	1.1	1.0	1.0	0.86	2548
	Model testing	2.8	1.0	1.2	1.3	−0.0	0.1	1.1	1.0	1.0	0.86	1092
	Whole dataset	3.0	1.0	1.2	−0.1	−0.1	0.0	1.1	1.0	1.0	0.86	3640
Independent model validation (± 24 h)												
Northern GOM (A general validation)		3.0	1.0	1.1	2.8	−0.1	0.0	1.1	1.0	1.0	0.70	412
MARS region	GM0606	3.9	1.5	2.4	2.1	−0.3	0.4	1.1	1.0	1.0	0.50	3789
	GM1003	4.7	1.6	3.4	0.3	−0.3	0.0	1.0	1.0	1.0	0.59	3345
River plume	DEEPEND	–	0.2	0.2	–	0.2	0.2	–	1.0	1.0	0.99	3
	WS15234	–	1.0	1.0	–	−0.3	−0.3	–	1.0	1.0	−0.35	488
Big Bend region		2.7	1.7	1.9	−0.7	0.6	0.4	1.0	1.0	1.0	0.62	205
Comparison with Aquarius		–	0.8	0.8	–	0.3	0.3	–	1.0	1.0	0.85	11
Comparison with buoy SSS		4.1	1.3	2.7	2.1	−0.1	0.7	1.1	1.0	1.0	0.86	367

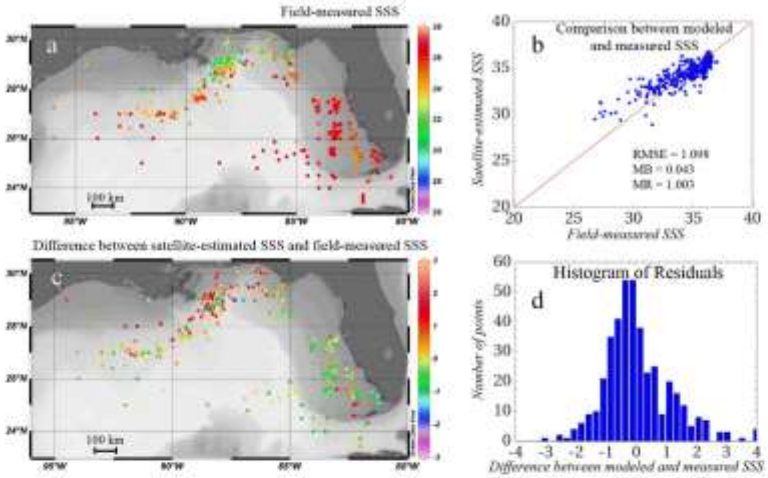

Fig. 5. Performance of the MPNN SSS model from evaluation using an independent dataset in Table 2. Note that this dataset was not used in either model training or model testing as described in Fig. 4. (a) Spatial distributions of the field-measured SSS; (b) comparison between satellite-estimated SSS and field-measured SSS; (c)–(d) spatial distributions and histogram of the SSS residuals, respectively.

SSS map on 14 August 2015 in Fig. 8b clearly showed that the MODIS SSS image not only captured the river plume but also showed high retrieval accuracy for both high-SSS and low-SSS waters. Unfortunately due to cloud cover only one low-SSS data point in the offshore plume was validated (last point in Fig. 8a). To overcome this difficulty, a MODIS SSS composite map for the cruise period (14 days) was generated to examine whether other low-SSS features in the MODIS map could be validated (Fig. 8d). The comparison along the cruise track again showed agreement between MODIS retrievals and field measurements, with a RMSE of 1.3, MB of 0.3 and MR of 1.0. Note that such increased uncertainties (compared to Fig. 8a) are apparently due to the time difference of several days. Even though, the plume feature is well captured by MODIS with moderately accurate SSS retrievals.

The second experiment was from South Florida coastal waters including those around the Florida Strait (Fig. 9) as the Mississippi River plume can reach this region by traveling a distance of > 1000 km (Ortner et al., 1995; Hu et al., 2005). The plume was captured in MODIS imagery between 1 and 4 September 2015 (dark features in Fig. 9c & d) and verified by field data collected during the WS15234 cruise survey. Fig. 9a showed the agreement between concurrent MODIS SSS and field SSS measurements (within ± 24 h) along the cruise track (overlaid in Figs. 9c–e), with RMSE of 1.0, MB of − 0.3, and MR of 1.0. Fig. 9b showed the same comparison but MODIS composite data during the cruise period (4 days) were used, with RMSE of 0.9, MB of − 0.2, and MR of 1.0. In both comparisons, MODIS captured the river plume with relatively low SSS (around 33–34), with uncertainties of < 1.0.

Overall, the two experiments above demonstrated that the SSS model does capture the river plumes well in the GOM, even when the plumes were advected to > 1000 km reaching the Florida Strait. More importantly, MODIS-retrieved SSS in these plumes is relatively accurate with uncertainties < 1.0 for the salinity range of 30–37. Because SSS in offshore plumes is rarely < 30 due to mixing with ocean waters, the SSS model should therefore be regarded as being capable of quantifying SSS in offshore river plumes with known uncertainties.

3.3.3. Florida's Big Bend region

Fig. 10a shows the field-measured SSS in the Big Bend region and in the offshore NEGOM, where the data are described in Table 2. Comparison between concurrent (± 24 h) MODIS-derived SSS and field-measured SSS is shown in Fig. 10b, with a RMSE of 1.9, MB of 0.4 and MR of 1.0. In terms of absolute uncertainties the SSS model showed better performance with SSS > 30 (RMSE = 1.7, MB = 0.6, and MR = 1.0) than with SSS ≤ 30 (RMSE = 2.7, MB = − 0.7, and MR = 1.0). As shown in the enhanced RGB image on 6 June 2014 (Fig. 10c), a wide band of dark feature (near parallel to the coastline) indicated coastal runoff from local rivers and non-point sources. To

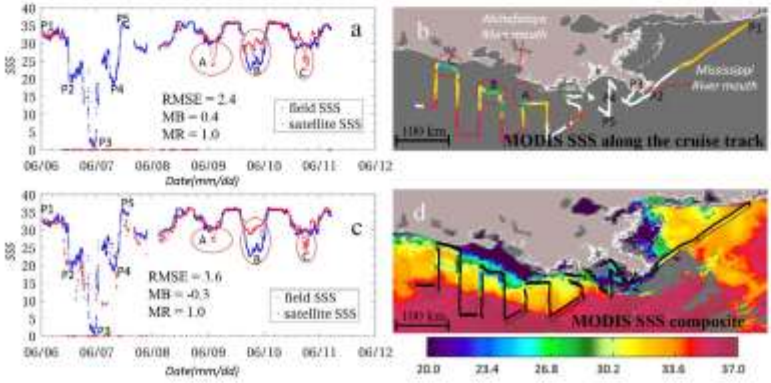

Fig. 6. Performance of the MPNN SSS model in the Mississippi-Atchafalaya coastal region, evaluated with data collected from cruise GM0606 (Table 2). (a) Comparison between field-measured SSS and concurrent (± 24 h) MODIS-derived SSS; (b) spatial distributions of the MODIS-derived SSS along the cruise track in (a). White color indicates no MODIS data; (c) comparison between field-measured SSS and MODIS-derived SSS extracted from the MODIS composite map for the cruise period; (d) MODIS SSS composite map for the cruise period (June 6–11, 2006), with field-measured SSS overlaid and color coded along the cruise track (black). Note that the red dots on the X-axis in (a) and (c) indicate that there are no concurrent MODIS-derived SSS.

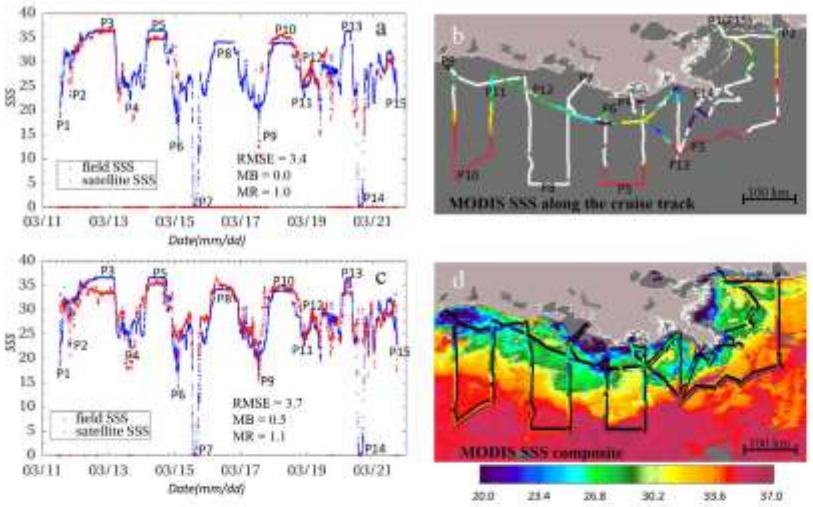

Fig. 7. Same as Fig. 6, but performance of the MPNN SSS model was evaluated with data collected from cruise GM1003 (Table 2). (a) Comparison between field-measured SSS and concurrent (± 24 h) MODIS-derived SSS; (b) spatial distributions of the MODIS-derived SSS along the cruise track in (a). White color indicates no MODIS data; (c) comparison between field-measured SSS and MODIS-derived SSS extracted from the MODIS composite map for the cruise period; and (d) MODIS SSS composite map for the cruise period (March 11–21, 2010), with field-measured SSS overlaid and color coded along the cruise track (black). Note that the red dots on the x-axis in (a) and (c) indicate that there are no concurrent MODIS-derived SSS.

facilitate comparison, field-measured SSS between 6 and 13 June 2014 was color coded and annotated on this image; the corresponding comparison with MODIS is marked as solid circles in Fig. 10b. The comparison showed a RMSE of 1.4, MB of 0.0, and MR of 1.0. The MODIS SSS composite map for this period in Fig. 10d showed low SSS values in the plume region and higher SSS offshore, suggesting that the SSS model worked well in Florida's Big Bend area in revealing not only SSS spatial patterns, but also absolute SSS values.

3.4. Comparison with Aquarius SSS

Aquarius was designed to measure SSS through microwave sensing, with a known uncertainty of < 0.3 (Abe and Ebuchi, 2014). To evaluate the performance of the SSS model developed in this study on a monthly scale, MODIS-estimated SSS and Aquarius-estimated SSS from August 2014 were compared. Fig. 11a & b showed the spatial distributions of MODIS-estimated SSS and Aquarius-estimated SSS. Both captured the offshore river plume, and their spatial patterns appeared to be similar in offshore waters. The striking differences are in their spatial resolutions and coverage. MODIS showed more details in SSS spatial variations because of its much finer resolution (1-km) than Aquarius (1°). Also, due to the coarse resolution, Aquarius simply has no coverage in nearshore waters. In contrast, MODIS showed large near-shore SSS gradients, especially around the Mississippi Delta and Florida's Big Bend. Fig. 11c & d further quantified the comparison between MODIS and Aquarius SSS along two artificial transects (transects 1 and 2 shown

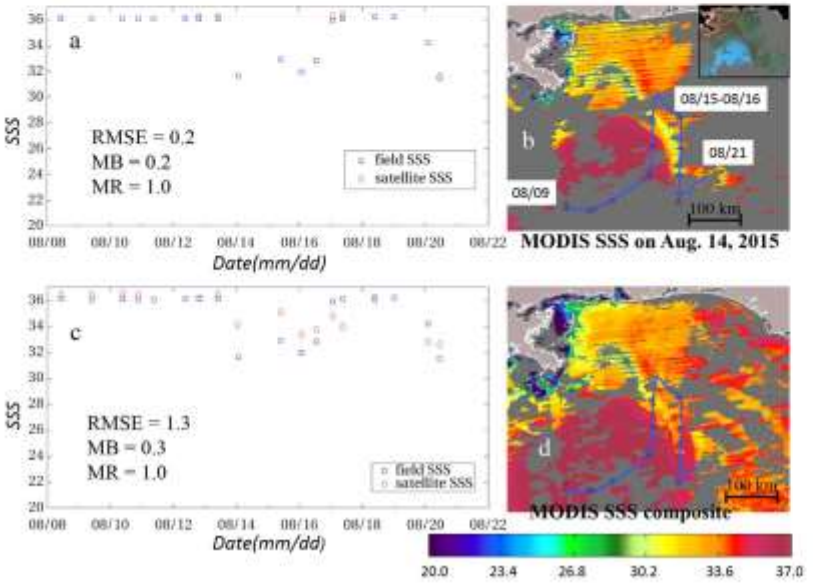

Fig. 8. Performance of the MPNN SSS model in quantifying SSS in the Mississippi River (MR) plume in the northern GOM, evaluated with data collected from the DEEPEND cruise (Table 2). (a) Comparison between field-measured SSS and concurrent (± 24 h) MODIS-derived SSS; (b) MODIS-derived SSS map on 14 August 2015, with the DEEPEND cruise track overlaid and corresponding enhanced RGB (ERGB) image shown in the inset figure. Clearly, the river plume shown in the ERGB image (dark feature) is associated with low SSS; (c) comparison between field-measured SSS and MODIS-derived SSS extracted from the MODIS composite map for the cruise period; (d) MODIS SSS composite map for the cruise period (August 9–21, 2015), with cruise track overlaid.

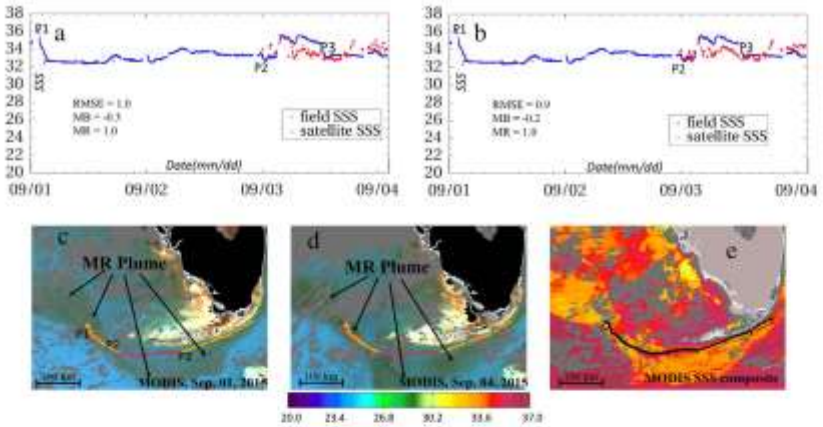

Fig. 9. Performance of the MPNN SSS model in quantifying SSS in river plumes in the Florida Strait, evaluated with data collected from cruise WS15234 (Table 2). (a) Comparison between field-measured SSS and concurrent (± 24 h) MODIS-derived SSS; (b) comparison between field-measured SSS and MODIS-derived SSS extracted from the MODIS composite map for the cruise period; (c)–(d) MODIS ERGB images showing the MR plume (dark feature) in the Florida Strait, with the WS15234 cruise track (color coded by field-measured SSS) overlaid; (e) MODIS SSS composite map for the cruise period (September 1–4, 2015), with cruise tracks overlaid.

in Fig. 11a & b). Clearly, while the SSS magnitudes are similar between the two measurements, MODIS provided more detailed SSS variations along the two offshore transects. When MODIS-estimated SSS along these two transects were averaged over the corresponding Aquarius pixels, the results in Fig. 11e shows agreement between MODIS and Aquarius, with RMSE of 0.8, MB of 0.3 and MR of 1.0.

3.5. Comparison with Buoy-measured SSS

The above evaluations are focused on spatial changes in SSS. To test the model performance in deriving SSS time-series at fixed locations in both nearshore and offshore waters, SSS data collected by several marine buoys (Section 2.1.1, Table 2) were used. The three buoy stations were selected according to their data availability.

During model development, < 0.1% of these buoy data were found to have concurrent (± 6 h) satellite data due to cloud cover, sun glint, and other factors which prevented valid MODIS retrievals. For validation purpose, these 0.1% of data were excluded, but daily means of the buoy data were used to compare with MODIS-derived SSS within ± 1 day. Considering the daily standard deviation of < 1.0 from ~97% of the buoy data, there should be little bias in the derived SSS daily means.

Fig. 12 shows the locations of two nearshore buoys and one offshore buoy, and comparison between MODIS-derived SSS and buoy-measured SSS from 2009 to 2015. Clearly, even for nearshore waters where SSS may approach zero, MODIS-derived SSS showed reasonable agreement with buoy-measured SSS. For the entire range, RMSE in MODIS SSS is 2.7 with a mean ratio of 1.0 (N = 367). However, the errors are not evenly distributed, and tend to show higher uncertainties in the intermediate SSS range (between 12 and 25) than in other SSS ranges. This may be explained by the model sensitivity to input Rrs errors (see section below).

A striking finding is the scarce data from MODIS over the two nearshore locations. Even though the odds of cloud-free conditions are about 30% for the GOM (Hu et al., 2009), valid MODIS data are far < 30% due to sun glint and stray light. This points to the need for correcting these artifacts to recover the low-quality data to make them

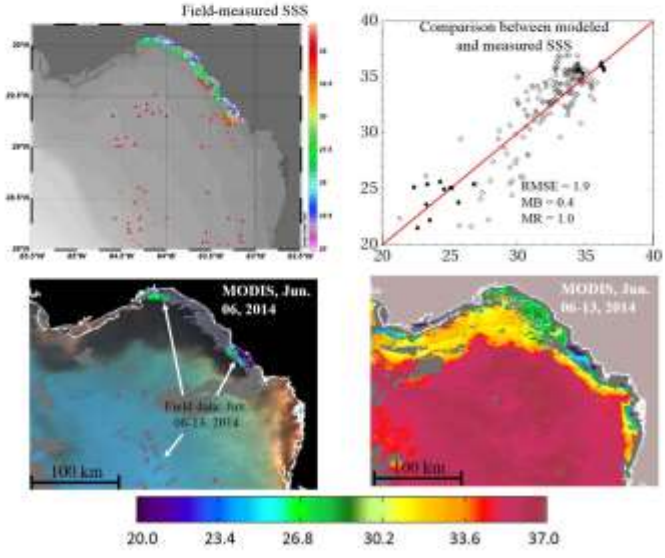

Fig. 10. Performance of the MPNN SSS model in Florida's Big Bend region, evaluated with data collected from several cruise surveys (Table 2). (a) Distributions of the field-measured SSS in the Big Bend region from data collected during 6 cruise surveys between 2010 and 2014 (N = 702); (b) Comparison between field-measured SSS and concurrent (± 24 h) MODIS-derived SSS using data shown in (a) (N = 205 matching pairs). The filled circles represent those shown in (c); (c) ERGB image on 6 June 2014, annotated with color coded field-measured SSS values between 6 and 13 June 2014. These data are shown as filled circles in (b) as long as there is concurrent MODIS-derived SSS; (d) MODIS SSS composite map between 6 and 13 June 2014.

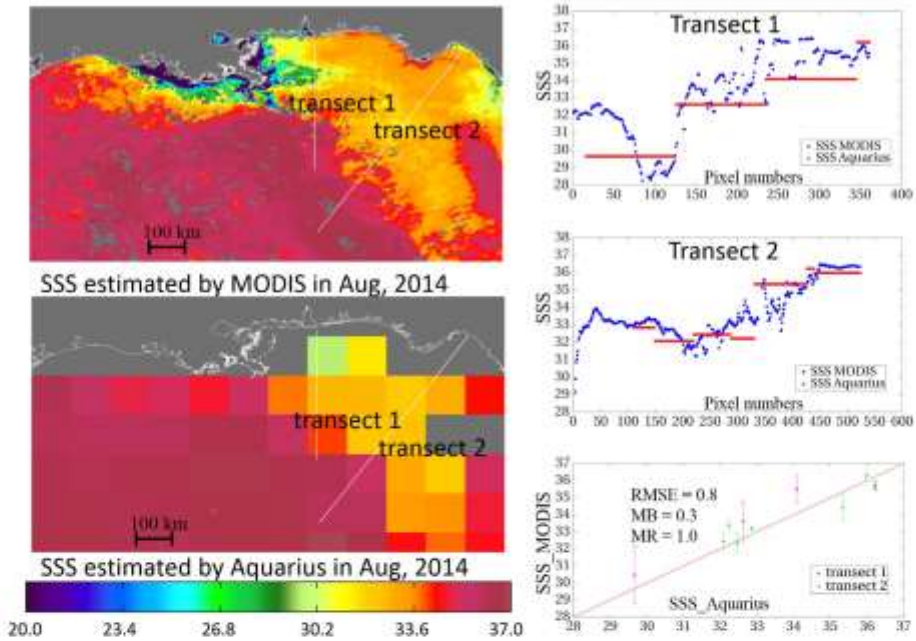

Fig. 11. Comparison between MODIS-derived SSS and Aquarius-derived SSS in August 2014. (a)–(b) SSS images from MODIS and Aquarius, respectively; (c)–(d) Comparisons between MODIS and Aquarius SSS along the two arbitrary transects shown in (a) and (b); (e) Comparison between MODIS and Aquarius SSS for the two transects after averaging MODIS pixels to Aquarius pixel size, with standard deviation shown on the y-axis.

usable for the SSS model.

3.6. Model sensitivity to input SST and Rrs errors

Fig. 13 shows the model sensitivity to input SST errors. Statistically, with +1 °C errors added, the MPNN model showed slight SSS underestimation, with RMSE of 0.3, MB of −0.2, and MB of 1.0. With −1 °C errors added, the MPNN model showed slight overestimation in SSS, with RMSE of 0.3, MB of 0.2 and MR of 1.0. These results suggest that the MNPP SSS model responded to SST errors in a negative way, but in both cases the model was insensitive to SST errors.

Fig. 14 shows the simulated Rrs errors in each experiment. The red lines represent those spectrally-dependent errors (Eqs. (6), (8)–(10)). From Experiment 1 to Experiment 4, with increased spectrally-independent errors, the points become more scattered around the red lines, representing realistic scenarios.

Fig. 15 shows the SSS uncertainties from the MPNN model at each SSS interval (from 1 to 37), corresponding to the input Rrs errors in each experiment. It is interesting to see that the MPNN SSS model was less sensitive to the same input Rrs errors at SSS < 10 and SSS > 23 than at 10 ≤ SSS ≤ 23. The increased uncertainties with decreasing SSS for SSS > 23 are easy to understand because a decrease in SSS is often accompanied by an increase in CDOM and a decrease in Rrs412 and Rrs443 (e.g., Fig. 3), leading to increased *relative* Rrs412 and Rrs443 errors. However, the low SSS uncertainties at SSS < 10 are counterintuitive as the same argument no longer holds true. To investigate the reason, the Rrs spectra for SSS < 10 and 10 ≤ SSS ≤ 23 were compared. Although the values of Rrs412 and Rrs443 at SSS < 10 were lower than those at 10 ≤ SSS ≤ 23, the Rrs spectral shapes at SSS < 10 were much closer to the spectral shapes of the simulated Rrs errors, thus leading to lower SSS uncertainties at SSS < 10.

In general, SSS uncertainties increased with increasing Rrs errors, especially for SSS > 23 (Fig. 15). Because the simulated Rrs errors in Fig. 14 were all larger than those estimated from MODIS measurements (Hu et al., 2013) except for Experiment 1, the SSS uncertainties in Fig. 15 should be regarded as the higher bound of the model sensitivity to input Rrs errors. In Experiment 2 where the spectrally-independent Rrs errors were simulated with a standard deviation of 1.2×10^{-4} sr^{-1}, the resulting SSS uncertainties were < 1.0 at SSS > 30. As SSS of most coast waters in the GOM is > 30, such Rrs error induced SSS uncertainties should have limited effect on the modeled SSS in most regions. Furthermore, because MODIS and SeaWiFS Rrs spectra instead of field-measured Rrs spectra were used in the model development, the uncertainties in MODIS and SeaWiFS Rrs were already taken care of implicitly by the MPNN.

4. Discussion

4.1. Which approach to use?

Regardless of the various approaches published in the literature, because SSS does not have an apparent optical signature in the visible domain, estimating SSS from ocean color measurements is all based on the principle of CDOM-SSS relationship, either explicitly or implicitly. For the former, Hu et al. (2013) clearly showed that CDOM-SSS relationship in the northern GOM varied across different coastal regions, and the test of the CDOM-based approach did not yield any reliable retrievals for the SSS range of 27–37 (see Supplemental Fig. S1). Then, why did the MPNN empirical approach could lead to relatively accurate SSS retrievals without the need of re-tuning of the model across the various sub-regions?

Indeed, although semi-analytical models together with the use of explicit CDOM-SSS relationship have the advantage of better understanding of the various model terms in their physical meanings, in

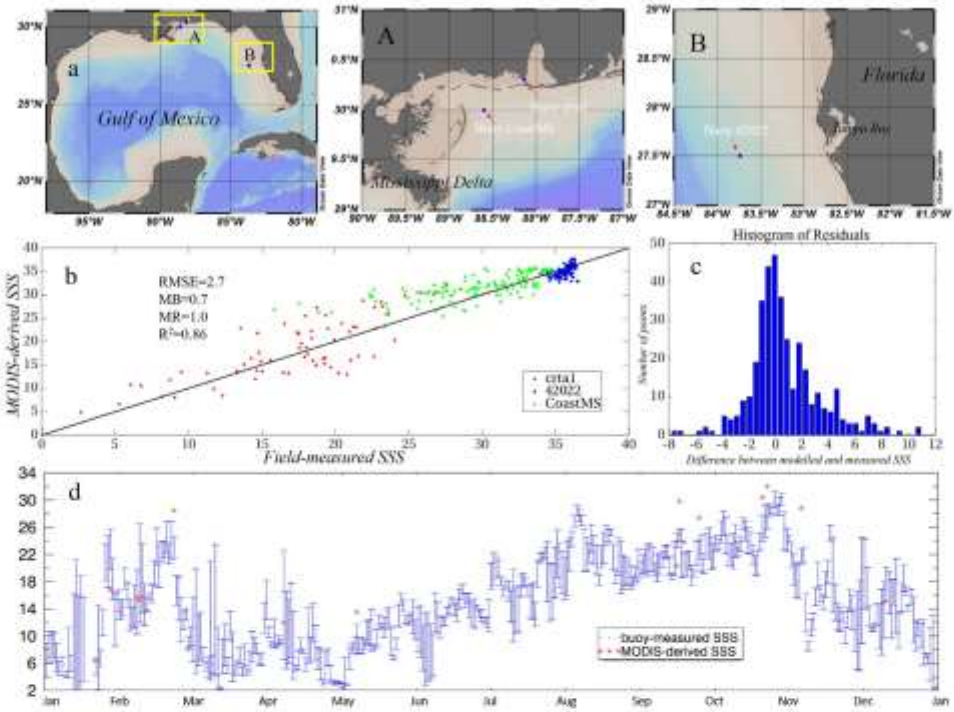

Fig. 12. (a) Locations of the three validation buoys (N = 77,212, 4467, 18,826, for buoy "crta1", "CoastMS" and "42,022", respectively, where N is the original number of the field SSS measurements). (b) Comparison between MODIS-derived SSS and buoy-measured daily mean SSS within ± 1 day between 2009 and 2015 for the three buoys (N = 367). (c) Histogram of residual errors in MODIS-derived SSS. (d) An example of time-series of buoy-derived SSS and MODIS-derived SSS for the "crta1" buoy in 2015 (N = 19 from MODIS). Buoy SSS data is represented by the daily means with standard deviations (vertical bars) plotted. (For interpretation of colors in this figure, the reader is referred to the web version of this article.)

practice they often suffer from uncertainties in the model inputs and from unknown factors (i.e., variable CDOM-salinity relationship across subregions) not accounted for in the models. In contrast, empirical models may deal with all these uncertainties and unknown factors through model tuning of the model forms and empirical coefficients. For example, the impact of turbidity on SSS retrievals is implicitly accounted for through the use of Rrs(667), and the variable CDOM-salinity relationships may be reflected in the Rrs spectral shapes that are also implicitly accounted for through the use of the Rrs in all bands. This has been demonstrated by all empirical models tested in the initial data diagnosis (Table 4). They all showed better performance than the model based on explicit CDOM-salinity relationship. Some of these models (e.g., Random Forest – bagged tree; Decision Tree – complex tree) actually showed only slightly worse performance than the selected MPNN model, suggesting the general feasibility of using empirical models to address complex questions. However, for the same reason why empirical models may work, without explicit understanding of why they work, their application must be restricted only to the environments in which they were trained, and this is exactly why the model was evaluated extensively in different environments.

4.2. Model applicability and limitations

The extensive evaluation results suggest that for the salinity range of ~1 to ~37, the empirical MPNN can estimate SSS with an overall uncertainty of ~1.2. While the uncertainty is higher for intermediate SSS range (10–25) than for other ranges, the relatively small uncertainty for SSS > 30 is particularly useful for monitoring and

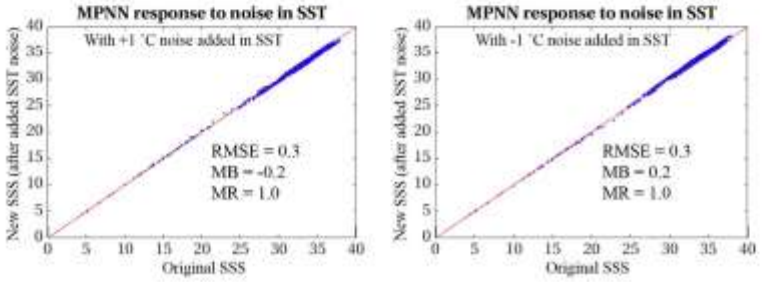

Fig. 13. Sensitivity of the MPNN SSS model to changes in the input SST, based on the dataset used to develop the SSS model in Table 1 and Fig. 1b. Results show that the SSS model is tolerant to at least ± 1 °C noise in the input SST.

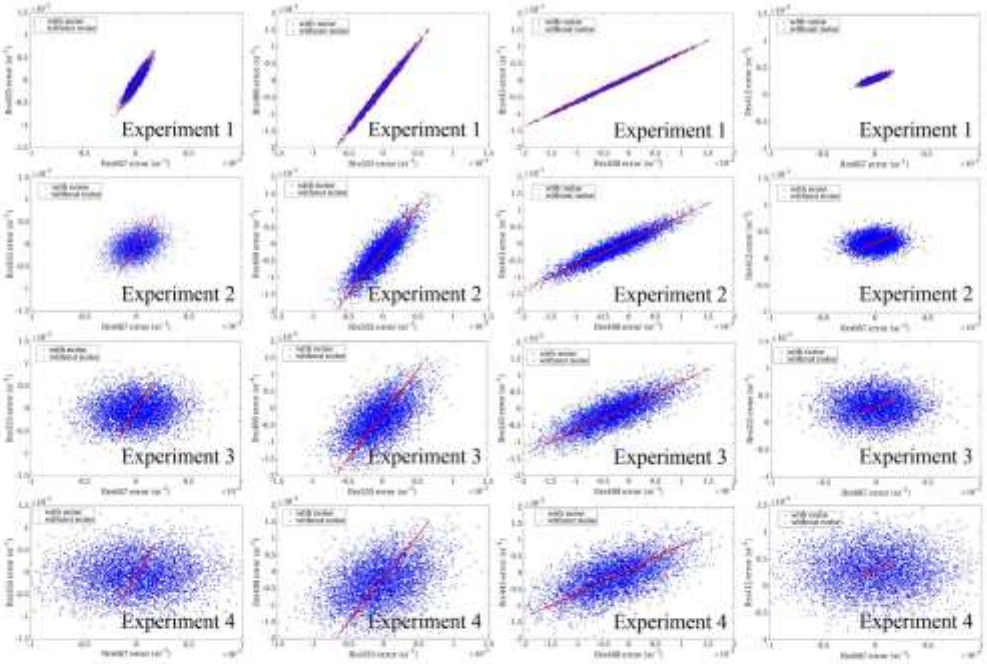

Fig. 14. Simulated Rrs errors in the 4 experiments to test the sensitivity of the MPNN model to input Rrs errors. From Experiment 1 to Experiment 4, Rrs667 errors were assumed to have a normal distribution with standard deviation of 5×10^{-5} sr^{-1} (Hu et al., 2013), and Rrs errors in other bands were calculated using Eqs. (6)–(10) (red line in each panel) superimposed by normally distributed random noise. The standard deviations of the added noises are 2×10^{-5} sr^{-1}, 1.2×10^{-4} sr^{-1}, 2.3×10^{-4} sr^{-1}, and 3.6×10^{-4} sr^{-1}, respectively, in the 4 experiments. In each experiment, the Rrs noises added in each band are completely independent of each other, but with the same standard deviation.

quantifying offshore river plumes and non-point freshwater runoff as SSS in the offshore plumes rarely dropped to < 30 (Hu et al., 2003, 2005). Such ability is particularly useful for studying biogeochemical processes and validating numerical circulation models. For regions with SSS ≤ 30, the uncertainty of SSS estimated by the MPNN model was −3.0. These regions are mostly inshore areas where riverine freshwater mixes with oceanic waters with a high dynamic SSS range. An uncertainty of 3.0 for such highly dynamic low-salinity waters may be acceptable, especially when large salinity anomaly is expected after flooding events. Such ability may help decision-making in aquaculture

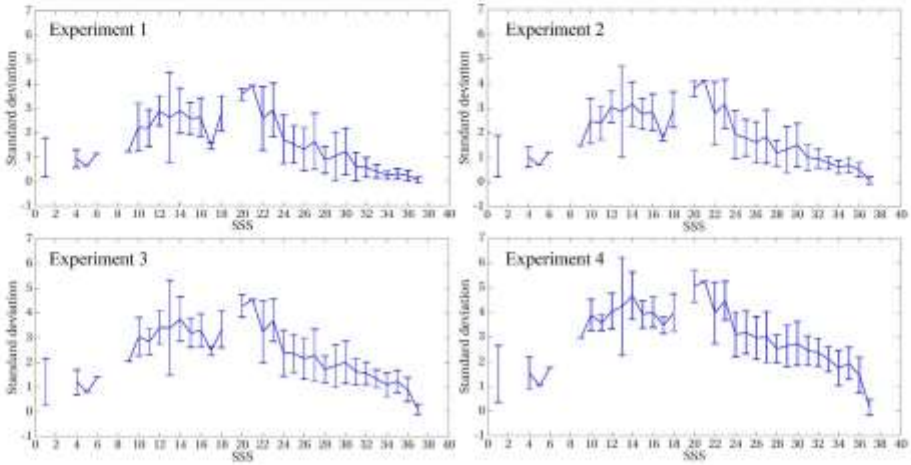

Fig. 15. Sensitivity of the MPNN SSS model to input Rrs errors, based on the simulated Rrs errors in Experiment 1–4 in Fig. 14. In each experiment, each of the 3640 SSS points showed an uncertainty value from the sensitivity experiment, defined as the standard deviation of the 5000 simulated SSS residual errors. These uncertainty values were binned to 1 SSS increment, resulting in mean and standard deviation shown in the y-axis.

management (i.e., oyster farming). Indeed, although empirical in nature, the MPNN model appears to be applicable to most, if not all, coastal waters in northern GOM. This may seem surprising because the CDOM – SSS relationship does vary with region and season (Hu et al., 2003) and therefore, even if error-free CDOM can be derived from MODIS, regional and seasonal CDOM – SSS relationships should still be required for different regions and seasons if a CDOM-explicit model were to be used. One explanation of the robust MPNN performance is that because CDOM is not used explicitly in the MPNN, rather spectral Rrs data with their corresponding SSS were used to train the MPNN, the variable CDOM – SSS relationship was implicitly included in the neurons and empirical coefficients. This is clearly shown in the model evaluation results for the Big Bend region. The region has different CDOM – SSS relationship than from the Mississippi River plume (Hu et al., 2003), yet the same MPNN model worked reasonably well in this region (Fig. 10). One additional advantage of using the MPNN model is that there is no need to assume CDOM is a conservative parameter (Chen and Gardner, 2004), and the complex CDOM-SSS relationship for turbid coastal waters of the northern GOM was addressed implicitly by the MPNN model through the use of the spectral Rrs data. Overall, the evaluation results using ship surveys for nearshore and offshore waters as well as buoy time-series data for nearshore stations suggest the robustness of the model in estimating SSS in coastal waters of the northern GOM.

However, because of its empirical nature, the MPNN model is only applicable to waters that are encompassed by the training datasets. Although we believe that nearly all field-collected SSS data from major cruise surveys in the past 18 years have been used in model training and validation, there is no guarantee that these data covered *all* possible oceanographic conditions. One such exceptional condition is upwelling, which may bring CDOM-rich high-salinity water to the surface, and/or bring nutrients to surface waters which stimulate phytoplankton blooms. Both will result in false underestimation of SSS. However, strong coastal upwelling is rare in the northern GOM (Muller-Karger, 2000), and coastal upwelling on the WFS (Weisberg et al., 2016) only caused slight underestimation in SSS (35.5 in the upwelling zone versus 36.4 in surrounding waters, with underestimation within the model uncertainty). These coastal upwelling events can be identified through the use of SST anomaly imagery. Likewise, offshore upwelling due to deep-water intrusion and/or wind mixing can also be easily recognized and ruled out by examining SST anomalies (Hu et al., 2011). Therefore, these cases are unlikely to cause major problems in model applications. However, to create the best outcomes for the MPNN model, the SST anomaly and bloom data should be used as a selection criterion to mask the MODIS imagery prior to their inclusion in the model. In the future, a scheme to combine the MPNN model results and upwelling index (through either numerical models or SST anomalies) may be implemented for operational use of the model in generating daily SSS imagery from MODIS in near real-time. Such applications may enhance the capacity of the existing Virtual Buoy System (VBS, Hu et al., 2014) in monitoring coastal water quality.

The MPNN model has been thoroughly tested for the northern GOM. One question is whether it can be applied to other coastal regions. While each region may have its unique Rrs – SSS relationship, we believe that the general approach may be applicable as long as sufficient local data have been collected to retrain the model. Indeed, even without such a local tuning, the application of the MPNN model (with its default coefficients) to the East China Sea showed reasonable spatial patterns of low-SSS nearshore waters and higher-SSS offshore waters (see figures in Supplemental materials), which are consistent to those reported in Bai et al. (2013).

Although the MPNN model has been shown applicable to the northern GOM waters with known uncertainties, when applying it to satellite data to derive SSS maps and time series, the limitation is not in the model itself but in scarce MODIS data for nearshore waters. This is clearly shown in Fig. 12d. The scarce MODIS data is due to not only cloud cover but also sun glint, cloud-adjacent stray light, and other factors such as large solar or view angles (Feng and Hu, 2016). Clearly, future effort should also be dedicated to "recover" these low-quality data in order to increase data quantity without sacrificing too much data quality.

Finally, because all empirical ANN models work like a "black-box" and researchers other than the model developers have no way to test them for other regions or other datasets, in this study the MPNN program has been packaged as one executable file for others to test, where a detailed description is also provided in the supplemental materials. It should be straightforward to run the model under a MATLAB environment. Furthermore, although the present MPNN model was developed for MODIS data, it can also be applied to other satellite data with careful attention to the slight difference between their band settings.

5. Conclusion

Accurate estimation of SSS in coastal waters and river plumes of the northern GOM from optical remote sensing has been a challenging task due to non-conservative mixing of CDOM and SSS, variable CDOM-SSS relationship in different regions, and due to high uncertainties in the satellite-derived Rrs and CDOM in turbid and dynamic coastal waters (e.g., Mississippi River delta). In this study, with satellite-estimated Rrs (at 412, 443, 488, 555, and 667 nm) and SST as inputs, a neural network based model (MPNN) has been developed and thoroughly evaluated for coastal waters of the northern GOM and for the offshore Mississippi River plume. The model showed reasonably good performance in the Mississippi-Atchafalaya Coastal region and Florida's Big Bend region, and was capable of detecting and quantifying the offshore Mississippi River plume. However, the operational use of this model in generating daily MODIS SSS maps still requires efforts to rule out some rare cases of coastal upwelling.

Notations

AOML	Atlantic Oceanographic & Meteorological Laboratory
AOPs	Apparent Optical Properties
ANN	Artificial Neural Network
BOEM	Bureau of Ocean Energy Management
CDIAC	Carbon Dioxide Information Analysis Center
CDOM	Colored Dissolved Organic Matter
CHL	Chlorophyll-a Concentration
DEEPEND	Deep-Pelagic Nekton Dynamics of the Gulf of Mexico
FWC	Florida Fish and Wildlife Conservation Commission
FWRI	Fish and Wildlife Research Institute
GOM	Gulf of Mexico
GSFC	Goddard Space Flight Center
IOPs	Inherent Optical Properties
LEDO	Lamont-Doherty Earth Observatory
MARS	Mississippi/Atchafalaya River System
MB	Mean Bias
MLR	Multi-variate Linear Regression
MNR	Multi-variate Nonlinear Regression
MODIS	Moderate Resolution Imaging Spectroradiometer
MPNN	Multilayer Perceptron Neural Network
MR	Mean Ratio
NCEI	National Centers for Environmental Information
NDBC	National Data Buoy Center
NEGOM	Northeastern Gulf of Mexico
PCA	Principle Component Analysis
pCO_2	Partial Pressure of CO_2
R^2	Determination coefficient
RMSE	Root Mean Square Error
Rrs	Remote Sensing Reflectance
SEAMAP	Southeast Area Monitoring and Assessment Program

SeaWiFS	Sea-Viewing Wide Field-of-View Sensor
SMOS	Soil Moisture and Ocean Salinity
SNPP	Suomi National Polar-orbiting Partnership
SST	Sea Surface Temperature
SSS	Sea Surface Salinity
TA	Total Alkalinity
TAMU	Texas A & M University
USF	University of South Florida
VIIRS	Visual Infrared Imaging Radiometer Suite

Acknowledgements

This research was supported by the U.S. NASA Ocean Biology and Bio-geochemistry program (NNX13AD08G, NNX14AL98G, NNX15AB13A) and by a University of South Florida fellowship. The research was also supported by grants from the BP/Gulf of Mexico Research Initiative through the DEEPEND consortium and through a project on river plumes and hydrocarbon transport, with data available in the Gulf of Mexico Research Initiative Information & Data Cooperative (GRIIDC) at https://data.gulfresearchinitiative.org/data/R4.x257.230:0010/. The authors are indebted to all researchers, including those of AOML, CDIAC, FWC, LEDO, NCEI, NDBC, TAMU, and USF, who have collected, quality controlled, and shared all cruise survey data. The authors also thank NASA for providing MODIS, SeaWiFS and Aquarius satellite data. Three anonymous reviewers provided extensive comments to help improve the presentation of this manuscript.

Appendix A. Supplementary data

Supplementary data to this article can be found online at http://dx.doi.org/10.1016/j.rse.2017.09.004.

Reference

Abe, H., Ebuchi, N., 2014. Evaluation of sea-surface salinity observed by Aquarius. J. Geophys. Res. Oceans 119 (11), 8109–8121.

Ahn, Y.H., Shanmugam, P., Moon, J.E., Ryu, J.H., 2008, July. Satellite remote sensing of a low-salinity water plume in the East China Sea. Ann. Geophys. 26 (7), 2019–2035 (Copernicus GmbH).

Aires, F., Prigent, C., Rossow, W.B., Rothstein, M., 2001. A new neural network approach including first guess for retrieval of atmospheric water vapor, cloud liquid water path, surface temperature, and emissivities over land from satellite microwave observations. J. Geophys. Res.: Atmos. 106 (D14), 14887–14907.

Averett, R.C., Leenheer, J.A., McKnight, D.M., Thorn, K.A., 1994. Humic substances in the Suwannee River, Georgia: interactions, properties, and proposed structures (no. 2373). In: USGPO, US Geological Survey, Map Distribution.

Bai, Y., Pan, D., Cai, W.J., He, X., Wang, D., Tao, B., Zhu, Q., 2013. Remote sensing of salinity from satellite-derived CDOM in the Changjiang River dominated East China Sea. J. Geophys. Res. Oceans 118 (1), 227–243.

Bailey, S.W., Werdell, P.J., 2006. A multi-sensor approach for the on-orbit validation of ocean color satellite data products. Remote Sens. Environ. 102 (1), 12–23.

Barnes, B.B., Hu, C., 2015. Cross-sensor continuity of satellite-derived water clarity in the Gulf of Mexico: insights into temporal aliasing and implications for long-term water clarity assessment. IEEE Trans. Geosci. Remote Sens. 53 (4), 1761–1772.

Barnes, B.B., Hu, C., Kovach, C., Silverstein, R.N., 2015. Sediment plumes induced by the Port of Miami dredging: analysis and interpretation using Landsat and MODIS data. Remote Sens. Environ. 170, 328–339. http://dx.doi.org/10.1016/j.rse.2015.09.023.

Bishop, C.M., 1995. Neural Networks for Pattern Recognition. Oxford University Press.

Blough, N.V., Zafiriou, O.C., Bonilla, J., 1993. Optical absorption spectra of waters from the Orinoco River outflow: terrestrial input of colored organic matter to the Caribbean. J. Geophys. Res. Oceans 98 (C2), 2271–2278.

Bowers, D.G., Brett, H.L., 2008. The relationship between CDOM and salinity in estuaries: an analytical and graphical solution. J. Mar. Syst. 73 (1), 1–7.

Burden, F., Winkler, D., 2009. Bayesian regularization of neural networks. In: Artificial Neural Networks: Methods and Applications, pp. 23–42.

Cannizzaro, J.P., Carlson, P.R., Yarbro, L.A., Hu, C., 2013. Optical variability along a river plume gradient: implications for management and remote sensing. Estuar. Coast. Shelf Sci. 131, 149–161.

Carder, K.L., Chen, F.R., Lee, Z.P., Hawes, S.K., Kamykowski, D., 1999. Semianalytic moderate-resolution imaging spectrometer algorithms for chlorophyll a and absorption with bio-optical domains based on nitrate-depletion temperatures. J. Geophys. Res. Oceans 104 (C3), 5403–5421.

Chauhan, P., Nagamani, P.V., Nayak, S., 2005. Artificial neural networks (ANN) based algorithms for chlorophyll estimation in the Arabian Sea. Indian J. Mar. Sci. 34 (4), 368–373.

Chen, R.F., 1999. In situ fluorescence measurements in coastal waters. Org. Geochem. 30 (6), 397–409.

Chen, R.F., Gardner, G.B., 2004. High-resolution measurements of chromophoric dissolved organic matter in the Mississippi and Atchafalaya River plume regions. Mar. Chem. 89 (1), 103–125.

Chen, J., Cui, T., Ishizaka, J., Lin, C., 2014. A neural network model for remote sensing of diffuse attenuation coefficient in global oceanic and coastal waters: exemplifying the applicability of the model to the coastal regions in Eastern China Seas. Remote Sens. Environ. 148, 168–177.

Chen, J., Cui, T., Quan, W., 2015. A neural network-based four-band model for estimating the total absorption coefficients from the global oceanic and coastal waters. J. Geophys. Res. Oceans 120 (1), 36–49.

Chen, S., Hu, C., Byrne, R.H., Robbins, L.L., Yang, B., 2016. Remote estimation of surface pCO_2 on the West Florida Shelf. Cont. Shelf Res. 128, 10–25.

Chester, R., 1990. Marine Geochemistry (698 pp.). Unwin Hyman Ltd, London.

Coble, P., Hu, C., Gould Jr., R.W., Chang, G., Wood, A.M., 2004. Colored dissolved organic matter in the coastal ocean: an optical tool for coastal zone environmental assessment and management. Oceanography 17 (2), 50–59. http://dx.doi.org/10.5670/oceanog.2004.47.

Del Castillo, C.E., Miller, R.L., 2008. On the use of ocean color remote sensing to measure the transport of dissolved organic carbon by the Mississippi River Plume. Remote Sens. Environ. 112 (3), 836–844.

Del Vecchio, R., Blough, N.V., 2004. Spatial and seasonal distribution of chromophoric dissolved organic matter and dissolved organic carbon in the Middle Atlantic Bight. Mar. Chem. 89 (1), 169–187.

Devlin, M.J., Petus, C., Da Silva, E., Tracey, D., Wolff, N.H., Waterhouse, J., Brodie, J., 2015. Water quality and river plume monitoring in the Great Barrier Reef: an overview of methods based on ocean colour satellite data. Remote Sens. 7 (10), 12909–12941.

Feng, L., Hu, C., 2016. Comparison of valid ocean observations between MODIS Terra and Aqua over the global oceans. IEEE Trans. Geosci. Remote Sens. 54 (3), 1575–1585.

Fennel, K., Hetland, R., Feng, Y., DiMarco, S., 2011. A coupled physical-biological model of the Northern Gulf of Mexico shelf: model description, validation and analysis of phytoplankton variability. Biogeosciences 8 (7), 1881–1899.

Font, J., Camps, A., Borges, A., Martín-Neira, M., Boutin, J., Reul, N., Mecklenburg, S., 2010. SMOS: the challenging sea surface salinity measurement from space. Proc. IEEE 98 (5), 649–665.

Fournier, S., Lee, T., Gierach, M.M., 2016. Seasonal and interannual variations of sea surface salinity associated with the Mississippi River plume observed by SMOS and Aquarius. Remote Sens. Environ. 180, 431–439.

Geiger, E.F., Grassi, M.D., Trembanis, A.C., Kohut, J.T., Oliver, M.J., 2013. Satellite-derived coastal ocean and estuarine salinity in the Mid-Atlantic. Cont. Shelf Res. 63, S235–S242.

Goh, A.T.C., 1995. Back-propagation neural networks for modeling complex systems. Artif. Intell. Eng. 9 (3), 143–151.

Gross, L., Thiria, S., Frouin, R., 1999. Applying artificial neural network methodology to ocean color remote sensing. Ecol. Model. 120 (2), 237–246.

Guo, W., Stedmon, C.A., Han, Y., Wu, F., Yu, X., Hu, M., 2007. The conservative and non-conservative behavior of chromophoric dissolved organic matter in Chinese estuarine waters. Mar. Chem. 107 (3), 357–366.

Hecht-Nielsen, Robert, 1989. Theory of the backpropagation neural network. Neural Networks, 1989. In: IJCNN, International Joint Conference on IEEE.

Hong, H., Wu, J., Shang, S., Hu, C., 2005. Absorption and fluorescence of chromophoric dissolved organic matter in the Pearl River Estuary, South China. Mar. Chem. 97 (1), 78–89.

Hurrer-Devine, A.R., Hetland, R.D., MacDonald, D.G., 2015. Mixing and transport in coastal river plumes. Annu. Rev. Fluid Mech. 47, 569–594.

Hornik, K., Stinchcombe, M., White, H., 1989. Multilayer feedforward networks are universal approximators. Neural Netw. 2 (5), 359–366.

Hu, C., Muller-Karger, F.E., Biggs, D.C., Carder, K.L., Nababan, B., Nadeau, D., Vanderbloemen, J., 2003. Comparison of ship and satellite bio-optical measurements on the continental margin of the NE Gulf of Mexico. Int. J. Remote Sens. 24 (13), 2597–2612.

Hu, C., Chen, Z., Clayton, T.D., Swarzenski, P., Brock, J.C., Muller-Karger, F. E., 2004. Assessment of estuarine water-quality indicators using MODIS medium-resolution bands: initial results from Tampa Bay, FL. Remote Sens. Environ. 93 (3), 423–441.

Hu, C., Nelson, J.R., Johns, E., Chen, Z., Weisberg, R.H., Muller-Karger, F.E., 2005. Mississippi River water in the Florida Straits and in the Gulf Stream off Georgia in summer 2004. Geophys. Res. Lett. 32 (14).

Hu, C., Muller-Karger, F., Murch, B., Myhre, D., Taylor, J., Luerssen, R., Hendee, J., 2009. Building an automated integrated observing system to detect sea surface temperature anomaly events in the Florida Keys. IEEE Trans. Geosci. Remote Sens. 47 (6), 1607–1620.

Hu, C., Weisberg, R.H., Liu, Y., Zheng, L., Daly, K.L., English, D.C., Zhao, J., Vargo, G.A., 2011. Did the northeastern Gulf of Mexico become greener after the Deepwater Horizon oil spill? Geophys. Res. Lett. 38 (9).

Hu, C., Lee, Z., Franz, B., 2012. Chlorophyll a algorithms for oligotrophic oceans: a novel approach based on three-band reflectance difference. J. Geophys. Res. 117 (C1). http://dx.doi.org/10.1029/2011jc007395.

Hu, C., Feng, L., Lee, Z., 2013. Uncertainties of SeaWiFS and MODIS remote sensing reflectance: implications from clear water measurements. Remote Sens. Environ. 133, 168–182.

Hu, C., Barnes, B.B., Murch, B., Carlson, P., 2014. Satellite-based virtual buoy system (VBS) to monitor coastal water quality. Opt. Eng. 53 (5), 051402. http://dx.doi.org/10.1117/1.OE.53.5.051402.

Ioannou, I., Gilerson, A., Gross, B., Moshary, F., Ahmed, S., 2011. Neural network approach to retrieve the inherent optical properties of the ocean from observations of MODIS. Appl. Opt. 50 (19), 3168–3186.
Ioannou, I., Gilerson, A., Gross, B., Moshary, F., Ahmed, S., 2013. Deriving ocean color products using neural networks. Remote Sens. Environ. 134, 78–91.
Jamet, C., Loisel, H., Dessailly, D., 2012. Retrieval of the spectral diffuse attenuation coefficient Kd (λ) in open and coastal ocean waters using a neural network inversion. J. Geophys. Res. Oceans 117 (C10).
Johnson, D.R., Miller, J., Schofield, O., 2003. Dynamics and optics of the Hudson River outflow plume. J. Geophys. Res. Oceans 108 (C10).
Kerr, Y.H., Waldteufel, P., Wigneron, J.P., Delwart, S., Cabot, F.O., Boutin, J., Juglea, S.E., 2010. The SMOS mission: new tool for monitoring key elements ofthe global water cycle. Proc. IEEE 98 (5), 666–687.
Kobinsky, C.J., Hildebrand, P., LeVine, D., Pellerano, F., Chao, Y., Wilson, W., Lagerloef, G., 2003. Sea surface salinity from space: science goals and measurement approach. Radio Sci. 38 (4).
Kwok, T.Y., Yeung, D.Y., 1996. Bayesian regularization in constructive neural networks. In: Artificial Neural Networks, ICANN 96. Springer, Berlin Heidelberg, pp. 557–562.
Lagerloef, G., Colomb, F.R., Le Vine, D., Wentz, F., Yueh, S., Ruf, C., Feldman, G., 2008. The Aquarius/SAC-D mission: designed to meet the salinity remote-sensing challenge. Oceanography 21 (1), 68–81.
Lawrence, J., 1991. Data preparation for a neural network. AI Expert. 6 (11), 34–41.
Le, C., Hu, C., 2013. A hybrid approach to estimate chromophoric dissolved organic matter in turbid estuaries from satellite measurements: a case study for Tampa Bay. Opt. Express 21 (16), 18849–18871.
Le, C., Lehrter, J.C., Hu, C., Obenour, D.R., 2016. Satellite-based empirical models linking river plume dynamics with hypoxic area and volume. Geophys. Res. Lett. 43, 2693–2699. http://dx.doi.org/10.1002/2015GL067521.
Lee, Z., Carder, K.L., Arnone, R.A., 2002. Deriving inherent optical properties from water color: a multiband quasi-analytical algorithm for optically deep waters. Appl. Opt. 41 (27), 5755–5772.
Livingstone, D.J., 2008. Artificial Neural Networks: Methods and Applications (Methods in Molecular Biology). Humana Press.
Lohrenz, S.E., Cai, W.J., Chen, F., Chen, X., Tuel, M., 2010. Seasonal variability in air-sea fluxes of CO_2 in a river-influenced coastal margin. J. Geophys. Res. Oceans 115 (C10).
Mannino, A., Novak, M.G., Hooker, S.B., Hyde, K., Aurin, D., 2014. Algorithm development and validation of CDOM properties for estuarine and continental shelf waters along the northeastern US coast. Remote Sens. Environ. 152, 576–602.
Marghany, M., Hashim, M., 2011, July. Retrieving seasonal sea surface salinity from MODIS satellite data using a Box-Jenkins algorithm. In: Geoscience and Remote Sensing Symposium (IGARSS), 2011 IEEE International. IEEE, pp. 2017–2020.
Mattraw, H.C., Elder, J.F., 1984. Nutrient and Detritus Transport in the Apalachicola River, Florida (No. 2196-C). USGPO.
Milliman, J.D., Meade, R.H., 1983. World-wide delivery of river sediment to the oceans. J. Geol. 91 (1), 1–21.
Moré, J.J., 1978. The Levenberg-Marquardt algorithm: implementation and theory. In: Numerical Analysis. Springer, Berlin Heidelberg, pp. 105–116.
Muller-Karger, F.E., 2000. The spring 1998 Northeastern Gulf of Mexico (NEGOM) cold water event: remote sensing evidence for upwelling and for eastward advection of Mississippi Water. In: Gulf of Mexico Science. 1. pp. 55–67.
Murrell, M.C., Stanley, R.S., Lores, E.M., DiDonato, G.T., Smith, L.M., Flemer, D.A., 2002. Evidence that phosphorus limits phytoplankton growth in a Gulf of Mexico estuary: Pensacola Bay, Florida, USA. Bull. Mar. Sci. 70 (1), 155–167.
Nelson, N.B., Siegel, D.A., Michaels, A.F., 1998. Seasonal dynamics of colored dissolved material in the Sargasso Sea. Deep-Sea Res. I Oceanogr. Res. Pap. 45 (6), 931–957.
Nelson, N.B., Siegel, D.A., Carlson, C.A., Swan, C., Smethie, W.M., Khatiwala, S., 2007. Hydrography of chromophoric dissolved organic matter in the North Atlantic. Deep-Sea Res. I Oceanogr. Res. Pap. 54 (5), 710–731.
Nelson, N.B., Siegel, D.A., Carlson, C.A., Swan, C.M., 2010. Tracing global biogeochemical cycles and meridional overturning circulation using chromophoric dissolved organic matter. Geophys. Res. Lett. 37 (3).
O'Connor, B.S., Muller-Karger, F.E., Nero, R.W., Hu, C., Peebles, E.B., 2016. The role of Mississippi River discharge in offshore phytoplankton blooming in the northeastern Gulf of Mexico during August 2010. Remote Sens. Environ. 173, 133–144.
Ortner, P.B., Lee, T.N., Milne, P.J., Zika, R.G., Clarke, M.E., Podesta, G.P., Swart, P.B., Tester, P.A., Atkinson, L.P., Johnson, W.R., 1995. Mississippi River flood waters that reached the Gulf Stream. J. Geophys. Res. Oceans 100 (C7), 13595–13601.
Palacios, S.L., Peterson, T.D., Kudela, R.M., 2009. Development of synthetic salinity from remote sensing for the Columbia River plume. J. Geophys. Res. Oceans 114 (C2).
Qi, L., Lee, Z., Hu, C., Wang, M., 2017. Requirement of minimal signal-to-noise ratios of ocean color sensors and uncertainties of ocean color products. J. Geophys. Res. Oceans 122, 2595–2611. http://dx.doi.org/10.1002/2016JC012558.
Qing, S., Zhang, J., Cui, T., Bao, Y., 2013. Retrieval of sea surface salinity with MERIS and MODIS data in the Bohai Sea. Remote Sens. Environ. 136, 117–125.
Rabalais, N.N., Turner, R.E., Justic, D., Dortch, Q., Wiseman, W.J., Gupta, B.K.S., 1996. Nutrient changes in the Mississippi River and system responses on the adjacent continental shelf. Estuaries 19 (2), 386–407.
Rabalais, N.N., Turner, R.E., Wiseman Jr., W.J., 2002. Gulf of Mexico hypoxia, AKA "the dead zone". Annu. Rev. Ecol. Syst. 235–263.
Siddorn, J.R., Bowers, D.G., Hogarne, A.M., 2001. Detecting the Zambezi River plume using observed optical properties. Mar. Pollut. Bull. 42 (10), 942–950.
Stedmon, C.A., Markager, S., 2005. Tracing the production and degradation of autochthonous fractions of dissolved organic matter by fluorescence analysis. Limnol. Oceanogr. 50 (5), 1415–1426.
Stumpf, R.P., Pennock, J.R., 1989. Calibration of a general optical equation for remote sensing of suspended sediments in a moderately turbid estuary. J. Geophys. Res. 94 (C10), 14363–14371.
Tanaka, A., Kishino, M., Doerffer, R., Schiller, H., Oishi, T., Kubota, T., 2004. Development of a neural network algorithm for retrieving concentrations of chlorophyll, suspended matter and yellow substance from radiance data of the ocean color and temperature scanner. J. Oceanogr. 60 (3), 519–530.
Thiria, S., Mejia, C., Badran, F., Crepon, M., 1993. A neural network approach for modeling nonlinear transfer functions: application for wind retrieval from spaceborne scatterometer data. Journal of Geophysical Research: Oceans 98 (C12), 22827–22841.
Twardowski, M.S., Donaghay, P.L., 2001. Separating in situ and terrigenous sources of absorption by dissolved materials in coastal waters. J. Geophys. Res. Oceans 106 (C2), 2545–2560.
U.S. Army Corps of Engineers, 2008. The Atchafalaya Basin Project, Report, New Orleans, La. Available at: http://www.mvn.usace.army.mil/pao/ben/AtchafalayaBasinProject.pdf.
Urquhart, E.A., Zaitchik, B.F., Hoffman, M.J., Guikema, S.D., Geiger, E.F., 2012. Remotely sensed estimates of surface salinity in the Chesapeake Bay: a statistical approach. Remote Sens. Environ. 123, 522–531.
Vandermeulen, R.A., Arnone, R., Ladner, S., Martinolich, P., 2014, May. Estimating sea surface salinity in coastal waters of the Gulf of Mexico using visible channels on SNPP-VIIRS. In: Proc. SPIE 9111, Ocean Sensing and Monitoring VI, pp. 911109. http://dx.doi.org/10.1117/12.2053417. (2014/05/23).
Vilas, L.G., Spyrakos, E., Palenzuela, J.M.T., 2011. Neural network estimation of chlorophyll a from MERIS full resolution data for the coastal waters of Galician rias (NW Spain). Remote Sens. Environ. 115 (2), 524–535.
Vodacek, A., Blough, N.V., DeGrandpre, M.D., Peltzer, E.T., Nelson, R.K., 1997. Seasonal variation of CDOM and DOC in the Middle Atlantic Bight: terrestrial inputs and photooxidation. Limnol. Oceanogr. 42 (4), 674–686.
Weisberg, R.H., Zheng, L., Liu, Y., Lembke, C., Lenes, J.M., Walsh, J.J., 2014. Why no red tide was observed on the West Florida Continental Shelf in 2010. Harmful Algae 38, 119–126.
Weisberg, R.H., Zheng, L., Liu, Y., Corcoran, A.A., Lembke, C., Hu, C., Lenes, J.M., Walsh, J.J., 2016. Karenia brevis blooms on the West Florida Shelf: a comparative study of the robust 2012 bloom and the nearly null 2013 event. Cont. Shelf Res. 120, 106–121.
Wiseman, Wm.J., Rabalais, N.N., Turner, R.E., Dinnel, S.P., Mac Naughton, A., 1997. Seasonal and interannual variability within the Louisiana coastal current: stratification and hypoxia. J. Mar. Syst. 12 (1–4), 237–248. http://dx.doi.org/10.1016/S0924-7963(96)00100-5.
Wong, M.S., Lee, K.H., Kim, Y.J., Nichol, J.E., Li, Z., Emerson, N., 2007. Modeling of suspended solids and sea surface salinity in Hong Kong using Aqua/MODIS satellite images. Kor. Can. J. Remote. Sens. 23 (3), 161–169.
Wynne, Timothy T., et al., 2005. Detecting Karenia brevis blooms and algal resuspension in the western Gulf of Mexico with satellite ocean color imagery. Harmful Algae 4, 992–1003.
Xue, Z., He, R., Fennel, K., Cai, W.J., Lohrenz, S., Hopkinson, C., 2013. Modeling ocean circulation and biogeochemical variability in the Gulf of Mexico. Biogeosciences 10 (11), 7219–7234.
Yang, B., Byrne, R.H., Wanninkhof, R., 2015. Subannual variability of total alkalinity distributions in the northeastern Gulf of Mexico. J. Geophys. Res. Oceans 120 (5), 3805–3816.
Zhao, J., Temimi, M., Ghedira, H., 2017. Remotely sensed sea surface salinity in the hyper-saline Arabian Gulf: application to landsat 8 OLI data. Estuar. Coast. Shelf Sci. http://dx.doi.org/10.1016/j.ecss.2017.01.008.

APPENDIX D:

A MACHINE LEARNING APPROACH TO ESTIMATE SURFACE OCEAN *P*CO_2 FROM SATELLITE MEASUREMENTS

Chen, S., Hu, C., Wanninkhof, R., Cai, W. J., and Barbero, L. A machine learning approach to estimate surface ocean *p*CO_2 from satellite measurements (*submitted*).

A machine learning approach to estimate surface ocean pCO_2 from satellite measurements

Shuangling Chen[1], Chuanmin Hu[1*], Brian B. Barnes[1], Rik Wanninkhof[2], Wei-Jun Cai[3], Leticia Barbero[2]

[1] College of Marine Science, University of South Florida, 140 7th Avenue, South, St. Petersburg, Florida, USA 33701

[2] NOAA's Atlantic Oceanographic and Meteorological Laboratory, 4301 Rickenbacker Causeway, Miami, FL 33149

[3] College of Earth, Ocean, & Environment, University of Delaware, 111 Robinson Hall, Newark, Delaware, USA 19716

Abstract

Surface partial pressure of CO_2 (pCO_2) is a critical parameter in the quantification of air-sea CO_2 flux, which further plays an important role in quantifying the global carbon budget and understanding ocean acidification. Yet, the remote estimation of pCO_2 in coastal waters (under influences of multiple processes) has been difficult due to complex relationships between environmental variables and surface pCO_2. To date there is no unified model to remotely estimate surface pCO_2 in oceanic regions that are dominate by different oceanic processes. In our study area, the Gulf of Mexico (GOM), this challenge is addressed through the evaluation of different approaches, including multi-linear regression (MLR), multi-nonlinear regression (MNR), principle component regression (PCR), decision tree, supporting vector machines (SVMs), multilayer perceptron neural network (MPNN), and random forest based regression ensemble

* Corresponding author. Email: huc@usf.edu

(RFRE). After modeling, validation, and extensive tests under different scenarios, the RFRE model proved to be the best approach. The RFRE model was trained using data comprised of extensive pCO_2 datasets (collected over 16 years by many groups) and MODIS (Moderate Resolution Imaging Spectroradiometer) estimated sea surface temperature (SST), sea surface salinity (SSS), surface chlorophyll concentration (Chl), and diffuse attenuation of downwelling irradiance (Kd). This RFRE-based pCO_2 model allows for the estimation of surface pCO_2 from satellites with a spatial resolution of ~1 km. It showed an overall performance of a root mean square error (RMSE) of 9.1 μatm, with a coefficient of determination (R^2) of 0.95, a mean bias (MB) of -0.03 μatm, a mean ratio (MR) of 1.00, a unbiased percentage difference (UPD) of 0.07%, and a mean ratio difference (MRD) of 0.12% for pCO_2 ranging between 145 and 550 μatm. The model, with its original parameterization, has been tested with independent datasets collected over the entire GOM, with satisfactory performance in each case. The sensitivity of the RFRE-based pCO_2 model to input errors of each environmental variable was also thoroughly examined. The results showed that all induced uncertainties were close to, or within, the uncertainty of the model itself with slightly higher sensitivity to SST and SSS than to Chl and Kd. The extensive validation, evaluation, and sensitivity analysis indicate the robustness of the RFRE model in estimating surface pCO_2 in most, if not all, GOM waters. The RFRE model approach was applied to the Gulf of Maine (a contrasting oceanic region to GOM), with local model training. The results showed significant improvement over other models suggesting that the RFRE may serve as a robust approach for other regions once sufficient field-measured pCO_2 data are available for model training.

Keywords: surface pCO_2, SST, SSS, Chlorophyll, Kd, satellite remote sensing, Gulf of Mexico

1. Introduction

Since the industrial revolution, the continuous consumption of fossil fuels has increased atmospheric CO_2 by ~40% (Sabine et al., 2004; Solomon et al., 2007). Correspondingly, the oceanic uptake of CO_2 has resulted in a ~30% increase in ocean acidity and ~0.1 (pH units) decrease of pH (Orr et al., 2005; Doney et al., 2009; Sun et al., 2012; Pachauri and Meyer 2014). These changes in the ocean have led to a decrease in marine biota and a degradation of marine ecosystems (Widdicombe and Spicer 2008; Doney, 2010; Dickinson et al., 2012). Therefore, understanding oceanic uptake of anthropogenic CO_2 and its changing rate are pressing concerns of the research community. However, due to the dynamics of the partial pressure of surface water CO_2 (pCO_2), large uncertainties still exist in the quantification of regional air-sea CO_2 flux (Takahashi et al., 2002, 2009, 2014; Sarma, 2003; Borges et al., 2005; Hofmann et al., 2011; Sarma et al., 2012; Chen et al., 2013; Wanninkhof et al., 2013a). Therefore, accurate and synoptic knowledge of surface oceanic pCO_2 is critical to studying the ocean's role in global carbon cycling within a changing world.

Satellite remote sensing, with its advantages of spatial and temporal resolution and coverage, has become an important tool for synoptic estimation of oceanic surface pCO_2. In principle, surface pCO_2 is mainly controlled by four interrelated processes – a thermodynamic process, biological activities, physical mixing, and the air-sea CO_2 exchange (Fennel et al., 2008; Ikawa et al., 2013; Xue et al. 2016). These four processes are closely related to satellite-derived environmental variables such as sea surface temperature (SST, ^{o}C), sea surface salinity (SSS, dimensionless), surface chlorophyll-a concentration (Chl, mg m^{-3}), diffuse attenuation of downwelling irradiance (Kd, m^{-1}), as well as other variables such as wind speed (m s^{-1}) and mixed layer depth (MLD, m) (i.e., Bai et al., 2015; Marrec et al., 2015; Moussa et al., 2016; Chen et al., 2016 & 2017; Lohrenz et al., 2018, etc.). Specifically, the thermodynamic quantities, solubility of CO_2 and the

dissociation constants of the carbonate system are mainly controlled by SST and SSS (Weiss, 1974; Millero et al., 2006). SST and SSS can also be good tracers of water masses (i.e., freshwater inputs, upwelled waters) that have distinct carbonate characteristics such as total alkalinity (TA) and dissolved inorganic carbon (DIC) (Lee et al., 2006; Yang et al., 2015). Because of the consumption and production of CO_2 in the biological processes of photosynthesis and respiration, and the depletion of TA and DIC in a 2 to 1 ratio in biological calcification (i.e., Reynaud et al., 2003; Salisbury et al., 2008; Fay & McKinley, 2017), the biological effects on surface pCO_2 can be implicitly interpreted from optical parameters such as Chl and Kd. Ocean mixing (both horizontal and vertical) is closely related to MLD as well as SST and SSS; and, the influence of air-sea CO_2 exchange on surface pCO_2 can be deduced from wind speed (Bates et al., 1998; Bates and Merlivat, 2001; Turk et al., 2013). However, in a specific oceanic system, only one or two processes (and thus their corresponding environmental variables), may dominantly control the changes of surface pCO_2 (Bai et al., 2015).

Using the environmental variables mentioned above, several satellite-based surface pCO_2 models have been proposed and developed in the published literature for different oceanic regions (both open and coastal ocean waters). Of these, remote estimation of surface pCO_2 in the open ocean is relative mature due to less variability in the open ocean's environmental conditions than those in coastal oceans. Both traditional empirical regressions (i.e., multi-linear regression (MLR), multi-nonlinear regression (MNR)) (e.g., Stephens et al., 1995; Sarma, 2003; Ono et al., 2004; Olsen et al., 2004; Rangama et al., 2005; Sarma et al., 2006; Jamet et al., 2007; Chen et al., 2011) and machine-learning based regressions (i.e., multilayer perceptron neural network (MPNN), self-organizing maps (SOMs)) (e.g., Telszewski et al., 2009; Friedrich and Oschlies, 2009; Nakaoka et al., 2013; Moussa et al., 2016; Landshützer et al. 2014) have been used to model surface pCO_2 for

open-ocean waters, with a root mean square error (RMSE) of < 17 μatm in most cases. For coastal oceans, due to their complexity and dynamics in the biogeochemical and physical processes, satellite mapping of surface pCO_2 is still a challenging task. Specifically, in addition to MLR, MNR, and SOMs (e.g., Lefèvre et al., 2002; Chierici et al., 2009; Zhu et al., 2009; Shadwick et al., 2010; Borges et al., 2010; Jo et al., 2012; Tao et al., 2012; Signorini et al., 2013; Marrec et al., 2014; Parard et al., 2014; Marrec et al., 2015; Chen et al., 2016), other empirical approaches such as principle component regression (PCR) (Lohrenz & Cai, 2006; Lohrenz et al., 2010) and regression tree (Lohrenz et al., 2018), and semi-analytical approaches (Hale et al., 2012; Bai et al., 2015; Chen et al., 2017) have been proposed for different coastal regions dominated by a single oceanic process (river-dominated, upwelling-dominated, or ocean current-dominated). For these complex regions, RMSE in the satellite-derived pCO_2 from these approaches is generally much higher than for open-ocean waters, and it can reach 88.6 μatm.

Despite these extensive efforts in establishing the various approaches or models, several problems still exist in the current satellite mapping of surface pCO_2. First, most approaches mentioned above are investigated in only one oceanic region, often dominated by a single major oceanic process. Although Signorini et al. (2013) proposed a MLR approach for the entire U. S. East Coast, in which the East Coast was actually divided into different sub-regions through SOMs and the MLR pCO_2 model was parameterized for each sub-region with RMSE of 22.4 ~ 36.9 μatm. Similarly, Hales et al. (2012) developed a semi-analytical approach for the entire U. S. West Coast, but the West Coast was divided into different sub-regions through SOMs, each with a unique pCO_2 model parameterization for each sub-region. The resulted RMSE varied between 6.6 and 65.0 μatm. Because such models are developed and parameterized for specific regions, any proposed models to estimate pCO_2 for a certain ocean region may have poor applicability in other regions even after

local parameterization. In other words, at present there is no unified approach, let alone unified model to remotely estimate surface pCO_2 for large ocean regions dependent on differing oceanic processes such as Gulf of Mexico (GOM). The semi-analytical approach proposed by Bai et al. (2015) showed potential to work for any oceanic waters, yet in practice it is difficult or even impossible to separate and quantify the effects of each oceanic process (i.e., horizontal mixing, vertical mixing, biological activities, air-sea CO_2 exchange) on surface pCO_2 with high accuracy (i.e., RMSE < 10 μatm). Further, in Bai's study, the semi-analytical approach was implemented for the East China Sea, but tested solely with summertime data. Chen et al. (2017) adopted Bai's approach to the northern GOM with localized parameterization, and similarly, using summertime data. Chen et al. (2017) found that the semi-analytical approach was not as good as an empirical approach in terms of model uncertainties and the model's capability in estimating pCO_2 under different oceanic conditions (i.e., coastal upwelling).

Therefore, the objective of this work was to develop an empirical approach with general applicability to estimate surface pCO_2 from satellites for large oceanic regions encompassing multiple processes, with improved model performance over those published in the literature. The ultimate goal is to extend this approach to all regional oceans around the globe. Below we present such a machine-learning based approach, namely a random forest based regression ensemble (RFRE). The RFRE approach was selected over many other approaches after extensive testing (see Section 2.3.1 for details about performance of each tested approach). Using this approach, a pCO_2 model with low uncertainties was developed for the entire GOM, a semi-enclosed subtropical sea that encompasses many different oceanic processes (see Section 2.1 for details about the selection of this study region). To show the general applicability of this approach, the RFRE was also tested over high-latitude waters in the Gulf of Maine (G. Maine), which showed improved performance

over other published approaches and therefore great potential for general applications in other oceanic regions.

This paper is arranged as follows. First, the study region is briefly introduced to justify the selection, followed by description of the satellite and field data used. Then, methods in data preprocessing, model development, accuracy assessment, model sensitivities to the errors of satellite variables are described. Results of the monthly pCO_2 climatologic maps and time series of surface pCO_2 are presented. Finally, the environmental variables used to model surface pCO_2 and to trace its interannual variabilities, the general application of the approach to other oceanic regions, as well as its advantages and limitations, are discussed.

2. Data and methods

2.1. Study region

The region of GOM, bounded by 18 ~ 31° N and -98 ~ -79° W, was selected to test the RFRE approach for three reasons. First, neither regional satellite-based pCO_2 models, nor a unified pCO_2 approach or model, is available for the entire GOM. Most of the sub-regional studies (Lohrenz & Cai, 2006; Lohrenz et al., 2010; Chen at al., 2016 & 2017; Lohrenz et al., 2018) are focused on the West Florida Shelf (WFS) and the northern GOM waters, where large uncertainties exist in the satellite-derived pCO_2 (i.e., variable RMSE of 12.0 ~ 50.2 μatm). Second, due to lack of synoptic and frequent mapping of surface pCO_2 over the entire GOM, it is still unclear whether the GOM serves as a CO_2 source or sink, as shown by the discrepancies in the published studies (Takahashi et al., 2009; Coble et al., 2010; Robbins et al., 2014; Xue et al., 2014). Third, as a semi-enclosed subtropical ocean, the GOM covers multiple regions with different dominating processes (i.e., freshwater inputs from Mississippi and Atchafalaya River System (MARS), Loop Current, oceanic

currents, mesoscale ocean circulation, occasional coastal upwelling) which control surface pCO_2. Therefore, if a RFRE-based unified pCO_2 model can be developed in this challenging environment, it may suggest that the application of the RFRE approach to other oceanic regions may deliver good results.

2.2. Data source

2.2.1. Field data

Over the past 16 years, there have been more than 220 cruise surveys that collected underway pCO_2 data from the GOM waters during different seasons. We compiled all the publicly available flow-through pCO_2 data measured in the GOM, as well as pCO_2 data collected from a fixed-location buoy in the Mississippi River delta. The data used for model development and independent validation are presented in Tables 1 and 2, respectively, with a general description of the data source, data volume, time span and data range for each dataset. Collectively these data represent the most complete pCO_2 dataset for the GOM.

Table 1. Underway and buoy pCO_2 measurements from different platforms in the GOM. These surface pCO_2 data were collected at a depth of ≤ 5m over all seasons. Only a small portion of these measurements were found to have co-located and contemporaneous (± 6h) satellite derived Chl, Kd, SSS and SST data (last column). These surface pCO_2 data encompass typical variation range in surface pCO_2 in most of the GOM waters, and these data were used to develop an optimal satellite pCO_2 model for the GOM through thorough tests of different empirical approaches. The corresponding spatial distributions of the surface pCO_2 data are shown in Fig. 1.

Platform (Vessel/Buoy)	Data Source	Year covered	pCO_2 range (µatm)	pCO_2 range (µatm)*	# of data	# of data*
Buoy CoastMS (30°N, 88.6°W)	NCEI/NODC	2009-2014	72.10-464.50	251.20-468.73	5,132	47
R/V Cape Hatteras	NCEI/NODC	2009-2010	102.73-1708.85	145.32-437.27	26,794	748

C/S Explorer of the Seas	NCEI/NODC	2002-2015	332.76-432.64	338.68-410.96	46,833	5,066
R/V Pelican	NCEI/NODC	2013	223.05-1836.05	382.19-387.84	47,275	9
R/V Gordon Gunter	AOML	2008-2016	68.66-1484.22	195.29-538.39	202,718	7,679
M/V Las Cuevas	AOML	2009-2012	199.08-528.60	273.87-486.89	30,859	1,238
R/V Marcus G. Langseth	NCEI/NODC	2013	304.55-536.31	350.93-370.05	2,014	98
R/V Pelican	UD	2004-2006	181.29-1668.42	364.40-439.07	9,998	27
R/V Brown	NCEI/NODC	2003-2012	192.74-502.54	206.01-443.71	35,622	828
R/V Falkor	TAMU	2012	370.00-452.20	371.1-419.2	6,938	207
R/V Bold	NCEI/NODC	2006-2007	84.04-2083.60	198.90-448.55	36,045	295
F. G. Walton Smith	NCEI/NODC	2011-2015	85.83-2773.92	280.13-552.42	100,007	1,309
Total		2002-2016	72.10-2773.92	145.32-552.42	550,235	17,551

* Data statistics after matching with contemporaneous (±6h) satellite data.

In Table 1 (data used for model development), the pCO_2 data (collected between 2002 and 2016) ranged between 72.10 and 2773.92 µatm. These *in situ* pCO_2 field data were obtained from the databases of NOAA National Centers for Environmental Information (NCEI) (formerly the National Oceanographic Data Center (NODC) (https://www.nodc.noaa.gov/ocads/) (Sutton et al., 2012; Wang & Huang, 2014(a-c); Millero et al., 2016(a-d); Salisbury et al., 2016; Takahashi et al., 2016a; Wanninkhof et al., 2011(a-f), 2013(b-g), & 2016d), NOAA Atlantic Oceanographic and Meteorological Laboratory (AOML) (http://www.aoml.noaa.gov/ocd/ocdweb/occ.html) (Wanninkhof et al., 2014(a-b), 2016(a-c, e-g)), University of Delaware (UD), and Texas A&M University (TAMU). The corresponding spatial distribution of these pCO_2 data is shown in Fig. 1a, with over 550,000 pCO_2 measurements in total.

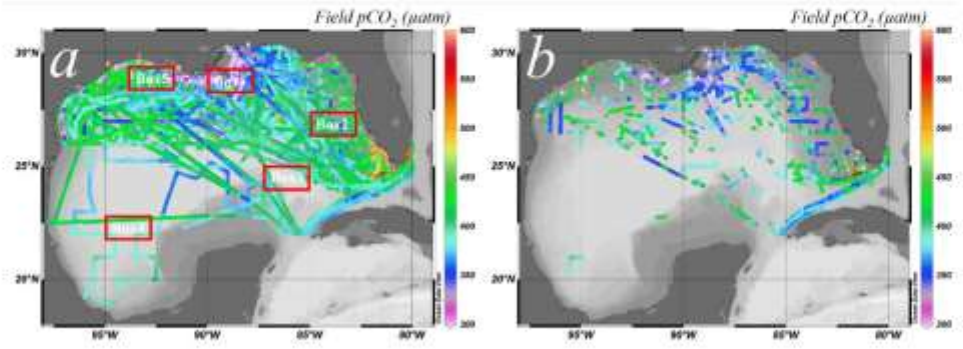

Fig. 1. Spatial distributions of the surface pCO_2 measurements in the GOM along the cruise tracks. (a) Cruise tracks from all data described in Table 1 (N=550,235); (b) Cruise tracks from the same data but with co-located and contemporaneous (± 6h) satellite Chl, Kd, SSS and SST (N=17,551) data. Five sub-regions, each about 220 km by 110 km, are selected to examine the interannual monthly time series of surface pCO_2. Box 1 is near the Mississippi River delta, Box 2 is on the West Florida Shelf, Box 3 is near the Loop Current, Box 4 is in the western GOM open waters, and Box 5 presents the "dead zone" along the Louisiana coast.

Typically, the ship-based surface pCO_2 data were collected at a depth of 5 m using a combination of a gas equilibrator and a non-dispersive, infrared analyzer Li-COR™ (model 6251, or 6262, or 7000 or 840A) integrated in the shipboard flow-through seawater system, with a measurement interval of 2 or 3 min and an accuracy of 2 µatm (or better). The buoy-based pCO_2 data were collected at a depth of < 1 m using a Li-COR™ model 820 with a sampling frequency of every 3h and an accuracy of 2 µatm. The details of data collection, processing, and quality control can be found in Feely et al. (1998), Sabine (2005), Pierrot et al. (2009), and Huang et al. (2015).

Table 2. Underway pCO_2 measurements used for independent validation of the developed pCO_2 model. These surface pCO_2 measurements were collected from different cruises (N=10) by the

research vessel of R/V Gordon Gunter. None of these datasets was used in the pCO_2 model training and they were not included in Table 1. See section 3.2 and supplemental file for the spatial distribution of each cruise dataset.

Cruise ID	Data Source	Date	pCO_2 range (µatm)	pCO_2 range (µatm)*	# of data	# of data*
GU0902_leg1	AOML	Apr. 2009	354.33 - 412.10	358.33 - 393.64	4,027	976
GU0902_leg2	AOML	Apr. and May 2009	359.38 - 391.76	373.57 - 388.30	7,234	771
GU1606_Leg1	AOML	Sep. 2016	157.42 - 484.47	247.10 - 448.21	5,626	1,051
GU1609_Leg2	AOML	Nov. 2016	330.39 - 412.19	330.39 - 390.02	5,000	723
GU1701_Transit_Leg	AOML	May, 2017	326.46 - 399.13	326.46 - 396.70	1,231	429
GU1703_Leg1	AOML	Jul. 2017	253.30 - 443.21	372.99 - 443.21	7,285	1,157
GU1703_Leg2	AOML	Jul.22 - Aug.05, 2017	129.73 - 453.17	253.46 - 437.58	7,288	725
GU1704_Leg2	AOML	Sep. 2017	283.31 - 511.31	311.02 - 428.80	6,308	1,548
GU1705_Transit_Leg	AOML	Oct. 2017	383.59 - 408.43	384.26 - 405.31	1,323	253
GU1706_Transit_Leg	AOML	Nov. 2017	327.26 - 403.66	327.26 - 384.01	1,352	639

*Data statistics after matching with contemporaneous (±24h) satellite data.

Similar to Table 1, Table 2 lists data from ten flow-through pCO_2 cruise surveys that were used for independent model evaluation under different conditions. These cruises were conducted on the NOAA research vessel – R/V Gordon Gunter, and the pCO_2 data were obtained from the NOAA AOML databases (Wanninkhof et al., 2014b & 2016f; Sullivan et al., 2017). Specifically, pCO_2 data collected in Apr. and May 2009 (GU0902_leg1 and GU0902_leg2) were from the southern and western GOM waters, ranging between 354.33 and 412.10 µatm; data collected in Sep. and Nov. 2016 (GU1606_Leg1 and GU1609_Leg2) and Sep. 2017 (GU1704_Leg2) were from the northern and western GOM waters, ranging between 157.42 and 511.31 µatm; data collected in Jul. and Aug. 2017 (GU1703_Leg2) focused on the northern GOM waters, ranging between 129.73 and 453.17 µatm; and, data collected in May, Jul., Oct., and Nov. 2017 (GU1701_Transit_Leg, GU1703_Leg1, GU1705_Transit_Leg, and GU1706_Transit_Leg) focused on the northern and eastern GOM, with a pCO_2 range of 253.30 – 443.21 µatm. Note that all these cruise data in Table 2 represent independent datasets for evaluating the pCO_2 model performance as 99% of them were

excluded in the model development. The spatial distributions of these pCO_2 datasets are shown in Section 3.2 and in the supplemental materials.

2.2.2. Satellite data

NASA standard daily Level-2 data products (version R2014.0) covering the GOM for the period of Jul. 2002 – Dec. 2017 with a spatial resolution of ~1 km were downloaded from the NASA Goddard Space Flight Center (GSFC) (https://oceancolor.gsfc.nasa.gov/). These Level-2 data products were derived from measurements by the Moderate Resolution Imaging Spectroradiometer (MODIS) on the Aqua satellite, and they included Chl, SST, and spectral remote sensing reflectance (Rrs, sr^{-1}) in 7 bands between 412 and 678 nm. The spectral Rrs data were used to calculate the diffuse attenuation coefficient at 488 nm (Kd, m^{-1}) using the semi-analytical algorithm developed by Lee et al. (2005), and to calculate SSS using an empirical approach recently developed by Chen & Hu (2017). The Kd product is often called Kd_Lee but for brevity it is simply called Kd in this study. The MODIS-derived environmental variables including Chl, Kd, SST, and SSS were used as inputs of the surface pCO_2 model. Specifically, SST was used to capture the thermodynamic effects, SSS was used to monitor the freshwater characteristics of multiple river inputs, and Chl and Kd were used to quantify (implicitly) the effects of biological activities on surface pCO_2.

2.3. Methods

2.3.1. Data preprocessing

Time and location data from the *in situ* pCO_2 measurements were used to identify the co-located and contemporaneous MODIS-derived data products (Chl, Kd, SST, and SSS) between July 2002 and December 2017. These data were used in the RFRE pCO_2 model development.

To obtain high-quality data, co-located and contemporaneous field-measured pCO_2 and MODIS-derived Chl, Kd, SST and SSS were selected using the following criteria. Considering the tidal cycle characteristics (i.e., diurnal) in most regions of the GOM, a time window of ± 6h between field and MODIS measurements was used. Low-quality satellite data under various non-optimal conditions (e.g., atmospheric correction failure, cloud, stray light, sun glint, etc.) were excluded using the NASA standard quality control criteria (Patt et al., 2003; Barnes and Hu, 2015). Valid satellite data within a 3×3 km box centered on the location of each *in situ* field pCO_2 measurement were extracted and averaged (Bailey and Werdell, 2006). Only if the number of valid pixels in the 3×3 km box was ≥ 5 and its variance was ≤ 10% the extracted data were used together with the field measurement in the model development. After applying these quality control screenings, 17,551 conjugate observations of field-measured pCO_2 and satellite data products between 2002 and 2016 were determined to be valid and available for the RFRE pCO_2 model development (Fig. 1b). In this conjugated dataset, both the responsive variable (surface pCO_2) and predictive variables (SST, SSS, Chl, and Kd) show a typical variation of each, although some extremely low and high field pCO_2 measurements in the nearshore waters (Fig. 1a) were excluded due to lack of valid contemporaneous satellite observations. Specifically, in the model development, field-measured pCO_2 ranged between 145.32 and 552.42 μatm, MODIS Chl ranged between 0.03 and 53.96 mg m^{-3}, MODIS Kd ranged between 0.019 and 1.373 m^{-1}, MODIS SST ranged between 13.48 and 33.28 °C, and MODIS SSS ranged between 10.90 and 38.34.

The selection of the predictive variables (i.e., SST, SSS, Chl and Kd) was based on our previous studies in the northern GOM and eastern GOM (Chen et al., 2016 & 2017). In Chen et al. (2016), various experiments were conducted to examine the relationship between surface pCO_2 and different environmental variables (i.e., SST, SSS, Chl, Kd, colored dissolved organic matter

(CDOM)) in different forms (i.e., linear scale or $\log_{10}$ scale). From these experiments, $\log_{10}$(Chl), $\log_{10}$(Kd), and SST were proven to be the most effective variables in estimating surface pCO_2 in WFS waters. The study in Chen et al. (2017) found that in addition to SST, $\log_{10}$(Chl), and $\log_{10}$(Kd), SSS was also a critical parameter in estimating surface pCO_2 in the northern GOM. This is because of the large freshwater inputs with distinct carbonate characteristics from the MARS. In addition, in both studies (and in many other studies), Julian day (Jday, or day of year) normalized sinusoidally was used as a "tuning" parameter to emphasize the seasonal cycle of surface pCO_2 (Friedrich and Oschlies, 2009; Lefèvre et al., 2005; Signorini et al., 2013; Chen et al., 2016 & 2017). Therefore, to estimate the surface pCO_2 for the entire GOM, all the four environmental variables (SST, SSS, Chl, and Kd) as well as Jday should be included in the RFRE pCO_2 model.

One advantage of using contemporaneous satellite-derived data (SST, SSS, Chl, Kd, and Jday) instead of *in situ* data to train the RFRE pCO_2 model, is that uncertainties in the satellite-derived data will be implicitly included in the empirically-derived weights of the RFRE (i.e., model coefficients). Then, when the same data products are used for surface pCO_2 predictions, such uncertainties in the satellite-derived data, to a large extent, should be cancelled.

2.3.2. Model selection, and principle and training of RFRE

In the published literature, both empirical and semi-analytical approaches were used to develop satellite-based surface pCO_2 models (see Section 1). The study in Chen et al. (2017) showed that although semi-analytical approaches had the advantages of explaining oceanic processes explicitly, their performance for northern GOM were not as good as those of empirical approaches. Therefore, in this study, the commonly used traditional empirical approaches (i.e., MLR, MNR, and PCR) and machine-learning based empirical approaches (i.e., MPNN, regression tree, regression ensembles, and SVMs) were all tested using the same training dataset (Table 1 & Fig. 1b) and the

same input variables. Among these trialed approaches, RFRE showed the best performance over all others (Eq. 1), and thus, RFRE was selected to develop the satellite-based pCO_2 model in this study (see Section 3.1 for detailed model comparison results). One distinct advantage of the machine-learning based RFRE approach is that it can approximate the nonlinear relationship between predictive variables and targeted variable (i.e., surface pCO_2) without explicitly knowing their functional dependence.

$$pCO_2 = f(\text{input variables}) = f_{RFRE}(SST, SSS, \log_{10}(Chl), \log_{10}(Kd), \cos(Jday/365)) \quad (1)$$

RFRE is one type of ensemble learning which combines many weighted regression trees to implement the random forest algorithm (Breiman, 2001) in Matlab (R2017a). Individual regression trees tend to overfit, and the RFRE takes the advantage of each regression tree via bootstrap aggregation (or bagging) to reduce model overfitting and to improve model generalization (Breiman, 1996; James et al., 2013). In model training, regression trees in the ensemble grow independently on a drawn bootstrap replica of the training dataset. In other words, each regression tree can select a random subset of predictors to use at each decision split and can involve many splits in the random forest algorithm. This way, correlations among the developed regression trees are greatly reduced, resulting in improved independency among the regression trees. In addition, this subsampling allows an out-of-bag estimate of the predictive performance by evaluating the predictions on those observations which were not used in the bootstrap sample. In this study, the regression ensemble function "fitrensemble" in Matlab (R2017a) was used to develop the relationship between surface pCO_2 and environmental variables. There are two important parameters to define this RFRE model structure: the minimum leaf size and number of learning cycles (i.e., the number of regression trees). Leaf size refers to the number of data samples used in each node of a regression tree, and the minimum leaf size, thus determines the splits and depth of

a regression tree. The number of regression learning cycles determines the number of regression trees to be included in the RFRE. By trial and error, the minimum leaf size and the number of learning cycles of the RFRE were optimized to 8 and 30, respectively. With these settings, the prediction accuracy of the RFRE model became stable, and the RFRE model were developed to predict surface pCO_2.

2.3.3. Accuracy assessment

Two types of model evaluation were used to quantify the performance of the RFRE model in estimating surface pCO_2 in the GOM.

First, in the model development phase, the modeled pCO_2 were compared with the *in situ* field pCO_2 in both model training and cross-validation. A 10-fold cross validation was used during this phase, where the training dataset was randomly partitioned into 10 equal-size subsamples. Of these 10 subsamples, 9 subsamples were used to train the model, and the remaining subsample was retained to test the model. The cross-validation process was repeated 10 times, with each of the 10 subsamples used exactly once as the validation dataset. The advantage of such a validation method is that all observations are used in both model training and model validation to include all the scenarios in the training dataset, and each observation is used for validation only once. Standard statistical measures, including root mean square error (RMSE, both absolute and relative), coefficient of determination (R^2), mean bias (MB), mean ratio (MR), unbiased percent difference (UPD), and mean relative difference (MRD) (Barnes & Hu, 2015), were used to quantify the accuracy of the RFRE-estimated pCO_2.

Second, for the developed RFRE pCO_2 model, extensive independent validation was conducted using the ten cruise datasets listed in Table 2. In each cruise-based independent validation,

satellite-derived surface pCO_2 along the cruise track from contemporaneous (± 24h) daily pCO_2 maps and from the pCO_2 composites of the cruise period were compared with the field-measured pCO_2, respectively. The 24h criteria was set based on the assumption that surface pCO_2 would not show significant variation (i.e., < 5 μatm) within 24h. In each comparison, statistics of RMSE, R^2, MB, MR, UPD, and MRD were calculated. Also, the field-measured surface pCO_2 data along the cruise track were color-coded (in the same way as the satellite pCO_2 map) and overlaid onto the pCO_2 composite to visually examine the consistency between the field-measured pCO_2 and the satellite-derived pCO_2.

2.3.4. Model sensitivity to errors in the input variables

The satellite input variables to the RFRE pCO_2 model (SST, SSS, Chl, and Kd) have inherent uncertainties. In order to understand the sensitivity of the RFRE model to such input errors, the uncertainties of each MODIS-derived variable were fed into the RFRE model. Surface pCO_2 derived from the same RFRE using error-free inputs and error-added inputs were then compared to determine the model's sensitivity to input errors of each variable.

Errors in each of the satellite-derived environmental variables were quantified based on the published literature. Specifically, satellite SST has an uncertainty of ≤ 1 °C (Hu et al., 2009), SSS has an uncertainty of ≤ 1 for SSS > 30 (Chen & Hu, 2017), Chl shows an uncertainty of 5%–30% (Gregg and Casey, 2004; Bailey and Werdell, 2006; Melin et al., 2007) and 12–24% in waters of > 5m bottom depth (Cannizzaro et al., 2013), and Kd has an uncertainty of ~13% (Zhao et al., 2013). To be consistent with the published studies (i.e., Chen et al., 2016; Lohrenz et al., 2018), errors of ± 1 °C, ± 1, ± 20%, ± 20% were added in the MODIS-derived SST, SSS, Chl, and Kd, respectively, to understand the error propagation to the satellite-derived pCO_2.

3. Results

3.1. Model performance

Using the same training dataset (Table 1 and Fig. 1b), all the empirical approaches described in Section 2.3.2, including MLR, MNR, PCR, regression tree, regression ensembles, SVMs, and MPNN were trialed with the same model inputs of SST, SSS, Chl, and Kd (Eq. 1) (see Section 2.3.1 for the selection of these variables). Table 3 shows the model results of each approach. Clearly the RFRE showed the best performance. However, the three regression trees (simple tree, medium tree, and complex tree) and the MPNN (red in Table 3) also tended to be good models with only slightly worse performance (i.e., RMSE < 20 µatm), thus these models together with the RFRE were selected as potentially good models. To confirm whether the RFRE model is indeed the best one, based on the cruise dataset of GU1703_Leg2, independent validation was done for each of the potentially good models selected in Table 3. The cruise GU1703_Leg2 was used mainly because the pCO_2 data were collected around the Mississippi River delta, which was the most dynamic region in the GOM. Table 4 shows the comparison of these potentially good models. The RFRE did show the best performance over others. Validation using several other cruise datasets in Table 2 also showed that the RFRE had better performance than others, and the RFRE was therefore selected in this study.

Table 3. Model comparison of different empirical approaches including traditional empirical approaches (MLR, MNR, and PCR) and machine-learning based empirical approaches (regression tree, regression ensemble, SVMs, and MPNN). The non-shaded statistics were derived from model training, and the shaded statistics were derived from model validation. Models with an RMSE < 20 µatm are shown in red and these models were further compared through an independent validation (see text). The random forest based regression ensemble (RFRE) model is highlighted

in bold to contrast it as the best-performance model. All these models were developed using the same dataset (see Table 1) and the same input variables. Each of them was optimized in the tests, with the best results shown here. For models trained with regression tree, ensemble of regression trees, SVMs, a 10-fold cross validation was implemented.

Approach	Algorithm/Kernel function	RMSE (μatm)	R^2	MB (μatm)	MR	UPD (%)	MRD (%)	N
MLR	–	26.55 (8.56%)	0.53	0.00	1.00	4.83	-0.63	8,776
		26.51 (8.58%)	0.54	-0.01	1.00	4.83	-0.64	8,775
MNR	–	25.10 (7.66%)	0.58	0.00	1.01	4.32	-0.54	8,776
		24.70 (7.59%)	0.60	0.00	1.01	4.30	-0.53	8,775
PCR	–	26.73 (8.68%)	0.53	-0.00	1.01	4.89	-0.64	8,776
		26.72 (8.71%)	0.53	0.01	1.01	4.90	-0.65	8,775
Regression tree	Simple tree	14.71 (4.52%)	0.86	-0.00	1.00	0.10	0.20	17,551
		16.14 (4.94%)	0.83	-0.05	1.00	0.09	0.21	17,551
	Medium tree	8.80 (2.61%)	0.95	0.00	1.00	0.03	0.07	17,551
		11.79 (3.57%)	0.91	0.02	1.00	0.05	0.11	17,551
	Complex tree	4.97 (1.53%)	0.98	0.00	1.00	0.01	0.02	17,551
		9.34 (2.82%)	*0.94*	*-0.04*	*1.00*	*0.00*	*0.04*	*17,551*
Ensemble of regression trees	Boosted trees	*24.27 (6.35%)*	*0.61*	*-15.88*	*0.96*	*-4.10*	*-3.89*	*17,551*
		24.66 (6.44%)	*0.60*	*-15.86*	*0.96*	*-4.09*	*-3.88*	*17,551*
	Random forest (bagged trees)	**6.68 (2.04%)**	**0.97**	**-0.03**	**1.00**	**0.06**	**0.08**	**17,551**
		9.09 (2.79%)	**0.95**	**-0.03**	**1.00**	**0.07**	**0.12**	**17,551**
SVM	Linear	27.94 (9.73%)	0.48	0.41	1.01	0.45	0.85	17,551
		27.96 (9.74%)	0.48	0.49	1.01	0.46	0.87	17,551
	Quadratic	24.46 (7.20%)	0.60	-1.18	1.00	-0.20	0.10	17,551
		24.57 (7.23%)	0.60	-1.18	1.00	-0.20	0.10	17,551
	Cubic	27.58 (8.20%)	0.50	-11.34	0.97	-2.85	-2.54	17,551
		32.30 (9.73%)	0.31	-5.36	0.99	-1.48	-1.04	17,551
	Fine Gaussian	9.06 (2.91%)	0.95	-0.02	1.00	0.07	0.11	17,551
		10.87 (3.56%)	0.92	-0.04	1.00	0.08	0.14	17,551
	Medium Gaussian	19.23 (5.69%)	0.76	-1.07	1.00	-0.13	0.02	17,551
		19.81 (5.86%)	0.74	-1.03	1.00	-0.12	0.04	17,551
	Coarse Gaussian	23.29 (6.98%)	0.64	-1.24	1.00	-0.11	0.12	17,551
		23.40 (7.05%)	0.64	-1.41	1.00	-0.15	0.08	17,551
MPNN	Levenberg-Marquardt and Bayesian	11.16 (3.20%)	0.92	-0.00	1.00	0.05	0.10	11,701
		11.98 (3.50%)	0.90	0.13	1.00	0.08	0.14	5,850

Table 4. Model results comparison with RMSE < 20 μatm in Table 3 (red font) based on independent validation using the underway pCO_2 data collected on cruise "GU1703_Leg2" (see Table 2). This cruise data was used primary because it was collected around the Mississippi River delta, the most dynamic region in the GOM. The random forest based regression ensemble (RFRE) model is highlighted in red to contrast it as the best model performance. The RFRE model also showed better performance than others when evaluated using other datasets listed in Table 2. Note

that the difference in the number of data matchups (N) of each approach is due to the requirement of the spatial homogeneity in the matchup selection criteria (see Section 2.3.1).

Approach	Algorithm/Kernel function	RMSE (µatm)	MB (µatm)	MR	UPD (%)	MRD (%)	N
Regression tree	Simple tree	53.80 (14.57%)	-28.15	0.92	-8.79	-7.57	706
	Medium tree	56.53 (15.47%)	-33.89	0.91	-10.50	-9.12	718
	Complex tree	54.24 (14.75%)	-33.10	0.91	-10.04	-8.80	717
Ensemble of regression trees	Random forest (bagged trees)	18.88 (5.53%)	-1.22	1.00	-0.16	-0.01	725
SVM	Fine Gaussian	29.29 (8.27%)	-10.45	0.98	-2.28	-1.95	726
MPNN	Levenberg-Marquardt and Bayesian	37.07 (11.49%)	7.12	1.03	2.10	2.67	717

Fig. 2 shows the performance of the RFRE model in both model training and cross-validation, color coded by data density (the number of data points in each pCO_2 interval of 2 µatm). Clearly, most of the data pairs of field pCO_2 and modeled pCO_2 follow closely along the 1:1 line without apparent outliers (see the red and green color). Statistically, during the model training, the RFRE-modeled pCO_2 showed good agreement with the field-measured pCO_2 with a RMSE of 6.68 µatm (2.04%), R^2 of 0.97, MB of -0.03 µatm, MR of 1.00, UPD of 0.06%, and MRD of 0.08%. Similar statistics were also found in the 10-fold cross validation (RMSE = 9.09 µatm (2.79%), R^2 = 0.95, MB = -0.03 µatm, MR = 1.00, UPD = 0.07%, MRD = 0.12%).

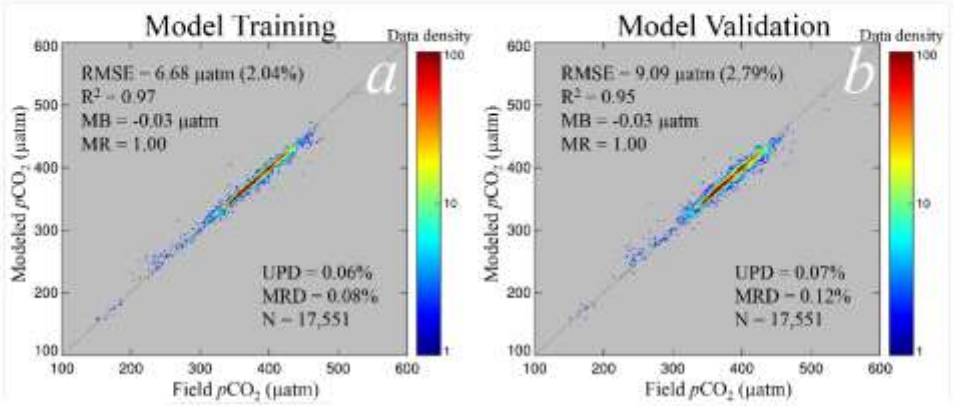

Fig. 2. RFRE model performance in estimating surface pCO_2 in the GOM in both (a) model training, and (b) model validation, using the conjugate dataset described in Table 1 and Fig. 1b. The data pairs are color coded by data density, which represents the number of data points at each pCO_2 interval of 2 µatm.

3.2. Independent validation under different scenarios

To conduct independent model validation, in addition to the cross-validation in the model development, the developed RFRE pCO_2 model was further examined to quantify its predictability in estimating surface pCO_2 from satellites under different scenarios in the GOM, using 10 cruise datasets collected over the GOM in different months (Table 2). For each cruise, the field-measured surface pCO_2 dataset was independent from other cruises, and none of these 10 cruise datasets were used in the model training above.

Fig. 3 shows the results based on the underway pCO_2 data collected from cruise GU1703_Leg2 between July 22 and August 05, 2017. This cruise mainly covered the Mississippi Delta and its offshore area (Fig.3a). The field-measured pCO_2 showed dynamic variation with very low pCO_2 values around the Mississippi river mouth and in the river plume, and relatively high pCO_2 in the

offshore waters. Fig. 3b shows the comparison between field-measured pCO_2 and contemporaneous satellite-derived pCO_2. Clearly, the spatial and temporal variations of the field-measured pCO_2 along the cruise track were well captured in the contemporaneous satellite-derived pCO_2, with a RMSE of 18.88 µatm (5.53%), MB of -1.22 µatm, MR of 1.00, UPD of -0.16%, and MRD of -0.01%. Furthermore, a 15-day MODIS pCO_2 composite map (Fig. 3a) covering the cruise period also showed agreement with the field-measured pCO_2 with low pCO_2 values nearshore and high pCO_2 values offshore, although the statistics is a bit worse due to the larger time difference (RMSE = 37.65 µatm (16.13%), MB= -1.22 µatm, MR = 1.01, UPD = 0.31%, and MRD = 1.31%, N = 5,331).

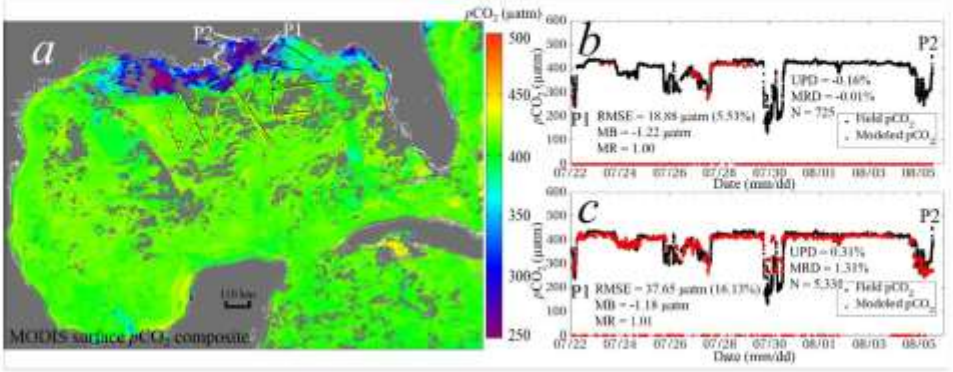

Fig. 3. RFRE surface pCO_2 model performance in the Mississippi River delta and offshore regions, evaluated with underway pCO_2 data collected from cruise GU1703_Leg2 (Table 2). The underway data was not used in the model training. (a) MODIS surface pCO_2 composite map for the cruise period (Jul. 22–Aug. 05, 2017), with field-measured pCO_2 along the cruise track overlaid and color coded in the same way as the MODIS image; (b) Comparison between field-measured pCO_2 and contemporaneous (± 24h) MODIS-derived pCO_2; (c) Comparison between field-measured pCO_2 and MODIS-derived pCO_2 extracted from the MODIS composite map for the cruise period (a).

The red dots with values of 0 on the X-axis in (b) and (c) indicate that there are no contemporaneous MODIS-derived pCO_2 due to various non-optimal satellite observing conditions, and 'P1' and 'P2' in each panel represent the start and end of the cruise, respectively.

Fig. 4 is the validation result based on one cruise dataset (GU1606_Leg1) collected in the northwestern GOM as well as the Mississippi delta between September 03 and 15, 2016. Although there were no strong river discharges during this cruise period, low field-measured pCO_2 values were found in the nearshore region along the Louisiana and Texas coast with distinct increases towards offshore waters (Fig. 4a). Similar to those found from cruise GU1703_Leg2 in Fig. 3, MODIS-estimated surface pCO_2 mimicked the variation patterns of the field-measured pCO_2 (Fig. 4b), with RMSE of 26.10 µatm (7.57%), MB of -6.44 µatm, MR of 0.99, UPD of -1.36% and MRD of -1.10%. This agreement was also evident in the comparison between field-measured pCO_2 and satellite-derived pCO_2 extracted from a 13-day composite map covering the cruise period (Fig. 4a & 4c), with lower pCO_2 in nearshore waters than in offshore waters.

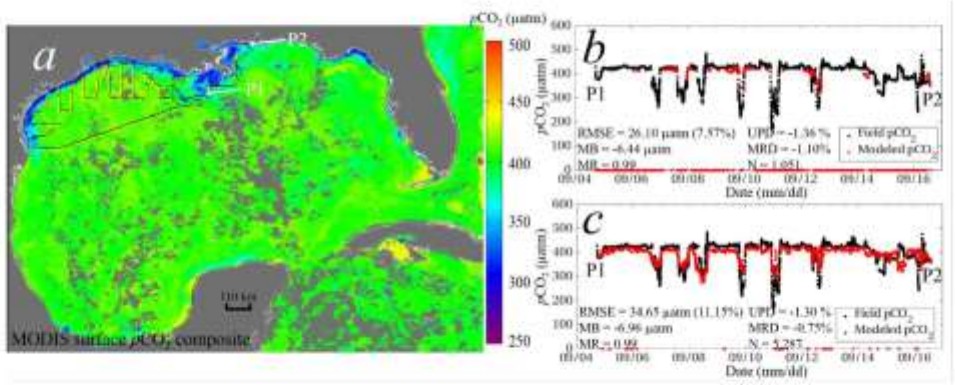

Fig. 4. Same as Fig. 3, but the RFRE surface pCO_2 model performance was evaluated along the Louisiana and Texas coast with underway pCO_2 data collected from cruise GU1606_Leg1 (Table

2). The underway data was not used in the model training. (a) MODIS surface pCO_2 composite map for the cruise period (Sep. 03–15, 2016), with field-measured pCO_2 overlaid and color coded along the cruise track; (b) Comparison between field-measured pCO_2 and contemporaneous (± 24h) MODIS-derived pCO_2; (c) Comparison between field-measured pCO_2 and MODIS-derived pCO_2 extracted from the MODIS composite map for the cruise period (a). The red dots with values of 0 on the X-axis in (b) and (c) indicate that there are no contemporaneous MODIS-derived pCO_2 due to various non-optimal satellite observing conditions, and 'P1' and 'P2' in each panel represent the start and end of the cruise, respectively.

In addition to cruise GU1606_Leg1, two other cruises (GU1704_Leg2 and GU1609_Leg2, see supplemental file) also covered a similar region (i.e., northwestern GOM and the Mississippi delta). In Fig. S1a, surface pCO_2 was measured on cruise GU1704_Leg2 in late September (17-31) 2017, with cruise track almost exactly the same as cruise GU1606_Leg1 (Fig. 4). Similar to cruise GU1606_Leg1, the spatial variation in surface pCO_2 showed the same pattern with low pCO_2 values inshore and high values offshore, but with less spatial contrast in surface pCO_2 possibly due to reduced river discharge and land runoff. Again, agreement with similar statistics were found between the field-measured pCO_2 and the satellite-derived pCO_2 extracted either from the contemporaneous (± 24h) pCO_2 maps or from the 14-day pCO_2 composite covering the cruise period. Different from cruise GU1606_Leg1 and GU1704_Leg2, results in Fig. S2 were based on a winter cruise (GU1609_Leg2) between November 03 and 14, 2016, which collected surface pCO_2 from the Mississippi delta and offshore waters in the northwestern GOM. The surface pCO_2 in winter showed lower values than in summer, with much reduced spatial variation along the cruise track. The comparison along the cruise track also showed agreement between MODIS retrievals and field measurements with similar statistics.

Fig. 5 is the results based on flow-through pCO_2 data collected from cruise GU1703_Leg1 in the eastern GOM waters between July 02 and 17, 2017. Field-measured pCO_2 from this cruise showed large difference between the southern and northern GOM waters (Fig. 5a). In the southern waters, surface pCO_2 was around 420 µatm with little spatial variation, while in the northern part, under the influence of the Mississippi River discharge, low surface pCO_2 with dynamic variation (250-380 µatm) was found. Additionally, this cruise also captured the low pCO_2 (~380 µatm) characteristics of the Mississippi river plume relative to the surrounding waters. Statistically, the contemporaneous (±24h) satellite-derived pCO_2 agreed with the field-measured pCO_2 with RMSE of 21.90 µatm (5.40%), MB of -12.96 µatm, MR of 0.97, UPD of -3.31%, and MRD of -3.15% (Fig. 5b). Similar model performance was also found in the comparison between field-measured pCO_2 and satellite-derived pCO_2 from the 16-day pCO_2 composite map of the cruise period (RMSE = 20.62 µatm (5.13%), MB = -12.66 µatm, MR = 0.97, UPD = -3.06%, and MRD = -2.92%, Fig. 5c). Specifically, the low pCO_2 values and their dynamic variation in the northern coastal waters of the GOM and the low pCO_2 features in the river plume (which were not captured (or not captured completely) in Fig. 5b due to the lack of contemporaneous (±24h) satellite measurements, were well revealed in Fig. 5a & 5c. Satellite-derived surface pCO_2 in both Figs. 5b & 5c showed underestimation as compared to the field-measured pCO_2, and this could be caused by the time difference between field and satellite measurements. As mentioned in Section 2.3.3, the 24h time window was selected by assuming insignificant surface pCO_2 variations within the time window. However, in reality, waters in the river-dominated coastal region and along the edge of the river plume could vary in finer timescale (i.e., < 24h), in which case the satellite-derived pCO_2 did not correspond to the same water masses as measured in the field.

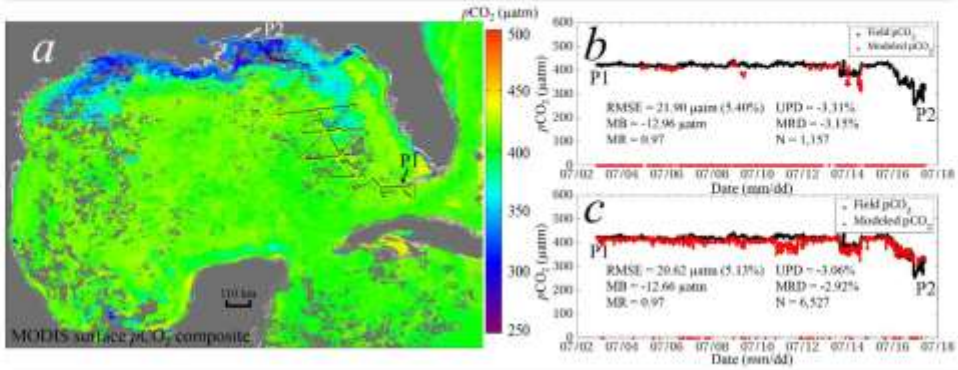

Fig. 5. RFRE surface pCO_2 model performance in the eastern GOM, evaluated with underway pCO_2 data collected from cruise GU1703_Leg1 (Table 2). The underway data was not used in the model training. (a) MODIS surface pCO_2 composite map for the cruise period (Jul. 02–17, 2017), with field-measured pCO_2 overlaid and color coded along the cruise track; (b) Comparison between field-measured pCO_2 and contemporaneous (± 24h) MODIS-derived pCO_2; (c) Comparison between field-measured pCO_2 and MODIS-derived pCO_2 extracted from the MODIS composite map for the cruise period (a). The red dots with values of 0 on the X-axis in (b) and (c) indicate that there are no contemporaneous MODIS-derived pCO_2 due to various non-optimal satellite observing conditions, and 'P1' and 'P2' in each panel represent the start and end of the cruise, respectively.

In addition to cruise GU1703_Leg1, three other cruises (GU1701_Transit_Leg, GU1705_Transit_Leg, and GU1706_Transit_Leg) in Table 2 also collected flow-through pCO_2 from the eastern GOM. These data were collected in different months which represented different seasonal characteristics of surface pCO_2 in the GOM. The results, based on each of these three cruise datasets, are shown in Figs. S3-S5, respectively. In Fig. S3, cruise GU1701_Transit_Leg was conducted between May 05 and 08, 2017. In contrast to cruise GU1703_Leg1 data in Fig. 5,

there was no obvious Mississippi River plume during this cruise. Surface pCO_2 showed lower but similar spatial variation from the southern to northern GOM waters, and such spatial variations were well captured in both the contemporaneous satellite-derived pCO_2 (RMSE = 10.78 µatm (3.04%), MB = 4.97 µatm, MR = 1.01, UPD = 1.39%, and MRD = 1.43%) and the satellite pCO_2 composite map covering the cruise period along the cruise track (RMSE = 10.20 µatm (2.81%), MB = 2.91 µatm, MR = 1.01, UPD = 0.81%, and MRD = 0.85%). The cruise surveys used in Figs. S4 & S5 followed almost the same cruise tracks as shown in Fig. S3; one collected pCO_2 in October 2017 (Fig. S4) and the other in November 2017 (Fig. S5). Again, there was no significant Mississippi River plume and little spatial variation in the field-measured pCO_2 during these two cruise periods. In both cases, the satellite-derived pCO_2 (both contemporaneous, (± 24h) satellite pCO_2, and pCO_2 from satellite composite of the cruise period) showed high consistency with the field-measured pCO_2, with similar statistics as shown in Fig. S3.

Results in Fig. 6 are based on flow-through pCO_2 data collected from cruise GU0902_leg2 between April 21 and May 06, 2009. This cruise covered the western GOM, mainly the southwestern and the northern offshore waters. From the spatial distribution of surface pCO_2 along the cruise track (Fig. 6a) and its time series distribution (black dots in Figs. 6b & 6c), surface pCO_2 did not show much spatial variation (360~400 µatm). For the contemporaneous (± 24h) satellite-derived pCO_2, it showed almost perfect agreement with the field-measured pCO_2 with a RMSE of 4.39 µatm (1.14%), MB of -0.80 µatm and MR of 1.00, UPD of -0.21% and MRD of -0.21%. Similar statistics were also derived for pCO_2 extracted from satellite pCO_2 composite map covering the cruise period.

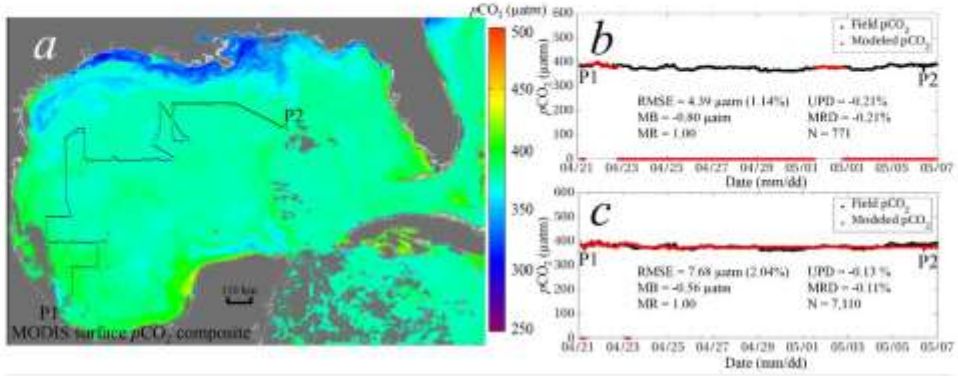

Fig. 6. RFRE pCO_2 model performance in quantifying surface pCO_2 in the southern GOM, evaluated with underway pCO_2 data collected from cruise GU0902_leg2 (Table 2). The underway data was not used for model training. (a) MODIS surface pCO_2 composite map for the cruise period (Apr. 21–May 06, 2009), with field-measured pCO_2 overlaid and color coded along the cruise track; (b) Comparison between field-measured pCO_2 and contemporaneous (± 24h) MODIS-derived pCO_2; (c) Comparison between field-measured pCO_2 and MODIS-derived pCO_2 extracted from the MODIS composite map for the cruise period (a). The red dots with values of 0 on the X-axis in (b) and (c) indicate that there are no contemporaneous MODIS-derived pCO_2 due to various non-optimal satellite observing conditions, and 'P1' and 'P2' in each panel represent the start and end of the cruise, respectively.

Similar to GU0902_leg2 in Fig. 6, cruise GU0902_leg1 covered the other part of the western GOM between Apr. 7 and 16, 2009, with surface pCO_2 between ~350 µatm and ~410 µatm. The validation results from cruise GU0902_leg1 are shown in Fig. S6. The spatial and temporal variations in surface pCO_2 were well captured in both the contemporaneous satellite-derived pCO_2 (RMSE = 8.89 µatm (2.31%), MB = -4.42 µatm, MR = 0.99, UPD = -1.17%, and MRD = -1.15%)

and the satellite-derived pCO_2 composite covering the cruise period (RMSE = 13.31 µatm (3.39%), MB = -6.63 µatm, MR = 0.98, UPD = -1.74%, and MRD = -1.68%).

3.3. Model sensitivity

Fig. 7 shows the sensitivity of the RFRE pCO_2 model to the input errors of each satellite variable (SST, SSS, Chl, and Kd). A visual interpretation of Fig. 7 indicates that the model is more sensitive to input errors in SST and SSS than in Chl and Kd, and the errors introduced in each case were close to or within the uncertainties of the model itself.

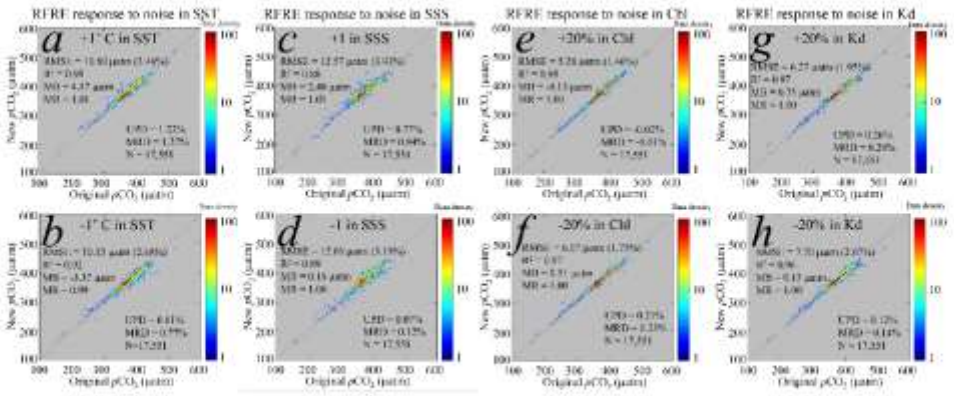

Fig. 7. RFRE pCO_2 model sensitivity to changes in the input SST, SSS, Chl, and Kd, based on the dataset used to develop the pCO_2 model in Table 1 and Fig. 1b. The data pairs are color coded by data density, which represents the number of data points at each pCO_2 interval of 2 µatm. Results show that the pCO_2 model is tolerant to at least ± 1 ˚C noise in the input SST, ± 1 noise in the input SSS, ± 20% noise in the input Chl, and ± 20% noise in the input Kd, and the pCO_2 model is more tolerant to noise in Chl and Kd than in SST and SSS.

Statistically, with +1 ˚C errors added (Fig. 7a), the RFRE model showed slight overestimation, with RMSE of 10.80 µatm (3.46%), R^2 of 0.91, MB of 2.17 µatm, MR of 1.01, UPD of 1.22% and

MRD of 1.27%. With -1 ˚C errors added (Fig. 7a), the RFRE model showed slight underestimation in surface pCO_2, with RMSE of 10.13 µatm (2.68%), R^2 of 0.92, MB of 0.99, UPD of 0.81%, and MRD of 0.77%. These results suggest that the RFRE pCO_2 model responded to SST errors in a positive way (an increase in SST would lead to an increase in surface pCO_2, and vice versa), but in both cases the model was insensitive to SST errors considering the model uncertainties described in Section 3.1.

The sensitivity of the RFRE model to SSS was similar to SST, and in both cases of +1 and -1 errors added into SSS, the response of the RFRE did not show great difference comparing to the originally-modeled surface pCO_2. Specifically, with +1 errors added in SSS, the RFRE model showed slight overestimation in surface pCO_2 (RMSE = 12.57 µatm (3.93%), R^2 = 0.88, MB = 2.40 µatm, MR = 1.01, UPD = 0.77%, MRD = 0.84%). With -1 errors added into SSS, the RFRE model still showed little overestimation (RMSE = 12.06 µatm (3.19%), R^2 = 0.89, MB = 0.18 µatm, MR = 1.00, UPD = 0.07%, MRD = 0.12%). However, clearly for pCO_2 > 450 µatm, the newly-predicted pCO_2 was obviously underestimated.

Unlike SST and SSS, the RFRE pCO_2 model showed little sensitivity to Chl, and the uncertainties introduced in the estimated pCO_2 by adding ± 20% errors in Chl was < 7 µatm (Figs. 7e & 7f). Specifically, with 20% errors added, the newly-predicted pCO_2 was slightly underestimated (RMSE = 5.28 µatm (1.46%), R^2 = 0.98, MB = -0.13 µatm, MR = 1.00, UPD = -0.02%, and MRD = -0.01 %). With -20% errors added, the newly-predicted pCO_2 was slightly overestimated (RMSE = 6.07 µatm (1.75%), R^2 = 0.97, MB = 0.51 µatm, MR = 1.00, UPD = 0.21%, and MRD = 0.23%).

Similar to Chl, the RFRE model also showed little sensitivity to Kd. In both cases of +20% and -20% errors added in Kd, the newly-predicted pCO_2 did not show much difference from the originally-predicted pCO_2. With +20% errors added in Kd, the model showed a RMSE of 6.27

μatm (1.95%), R^2 of 0.97, MB of 0.75 μatm, MR of 1.00, UPD of 0.26%, and MRD of 0.28%. With -20% errors added in Kd, the model showed similar statistics (RMSE = 7.70 μatm (2.07%), R^2 = 0.96, MB = 0.15 μatm, MR = 1.00, UPD = 0.12%, and MRD = 0.14%).

Overall, the RFRE pCO_2 model did not show high sensitivity to the errors in each input satellite variable including SST, SSS, Chl, and Kd. With errors added in each variable, the uncertainties induced in the new-predicted pCO_2 were all close to or within the uncertainties of the model itself. Since satellite data of each variable were used directly in the model development, such uncertainties were implicitly included in the developed model, and these uncertainties would be cancelled to a large extent when applying the RFRE model to the same satellite data products. The insensitivities of the RFRE pCO_2 model to Chl and Kd are further discussed in Section 4.1.

3.4. Seasonal and interannual variations of surface pCO_2

Fig. 8 shows the monthly climatological maps of surface pCO_2 of the GOM based on the MODIS data between July 2002 and December 2017. Fig. 9 shows the area-averaged monthly time series of surface pCO_2 in the GOM. Fig. 10 shows the interannual variations of surface pCO_2 monthly anomalies (i.e., monthly mean minus monthly climatology) in the study period. Generally, on seasonal timescale, distinct seasonal pCO_2 patterns can be seen in both Fig. 8 and Fig. 9, with high pCO_2 in summer and lower pCO_2 in winter; on decadal timescale, there is small interannual variability (e.g., within ±10 μatm) in surface pCO_2 over the GOM except in the northern coastal waters (e.g., Box 1, Box 5, where anomalies are within ±30 μatm).

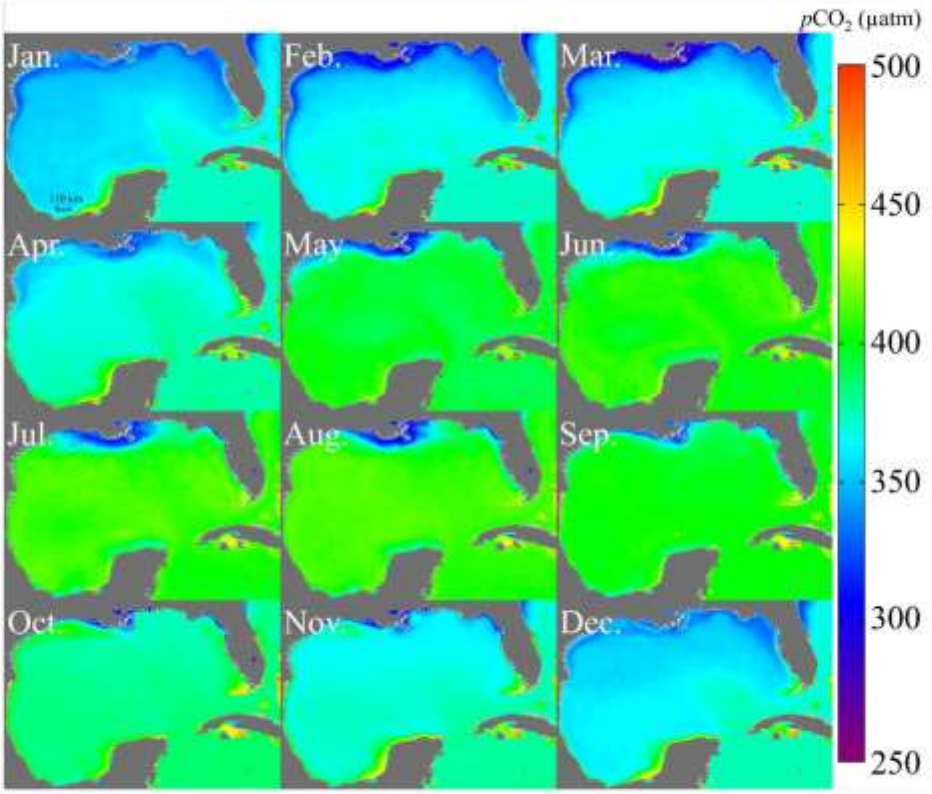

Fig. 8. Monthly climatology of surface pCO_2 in the GOM, derived from MODIS using the RFRE pCO_2 model for the period between July 2002 and December 2017. These maps are valid only for the GOM waters as described in Fig. 1.

In terms of spatial distribution, surface pCO_2 (Fig. 8) was characterized by relatively low pCO_2 values (300-350 µatm) along the northern GOM coasts (especially the Louisiana coast) accompanied with low SSS in most months. This result is quite different from the results shown in Xue et al. (2013), which found relatively high pCO_2 values ($\geq$ 500 µatm) in the Louisiana coastal waters. The difference between the findings of this study and those of Xue et al. (2013) is possibly

due to their overestimation in surface pCO_2 on the Louisiana shelf. In Lohrenz et al. (2018), similar low surface pCO_2 was also found in this area, but with relatively higher model uncertainties (RMSE > 30 μatm). Indeed, from the spatial distribution of field-measured pCO_2 data of the GOM shown in Fig. 1a, low surface pCO_2 values (< 350 μatm) were found along the Louisiana coast all the year round. There were some extremely high pCO_2 (> 1000 μatm) values collected in the very nearshore regions, but these high pCO_2 values were located in the estuaries. Due to the sharp changes in water properties (i.e., SST, SSS, TA, and DIC), there was a sharp decrease in surface pCO_2 from estuaries to the adjacent coastal waters. Additionally, fewer low pCO_2 waters were found between September and November due to the low river discharge (~5,000-10,000 m^3/sec) during this period. On the WFS, surface pCO_2 showed little spatial variation in each month, with low surface pCO_2 (~350 μatm) in winter and high pCO_2 (~400 μatm) in summer. This result agreed well with the results shown in Chen et al. (2016), except that relatively high pCO_2 (500-550 μatm) was estimated along the nearshore waters of Florida between May and August in Chen et al. (2016) but not here. In fact, water properties on the WFS are mainly controlled by oceanic currents and winds (e.g., wind-driven coastal currents, Loop Current) with winter conditions favoring upwelling (Liu & Weisberg, 2005 & 2012). The spatial distribution of field-measured pCO_2 on the WFS in Fig. 1a also showed little spatial gradient from inshore to offshore waters. Due to the high temperature of the Loop Current, relatively high pCO_2 was found in these waters during wintertime. In winter and early spring, the southern GOM showed relatively higher pCO_2 values than the northern GOM, mainly due to its lower latitude (thus relatively higher SST). Between May and October, the GOM waters become near isothermal with little spatial gradient in SST, and the surface pCO_2 in the GOM-wide regions (except the northern coastal regions) showed almost homogeneous distribution with slight spatial variation in each month.

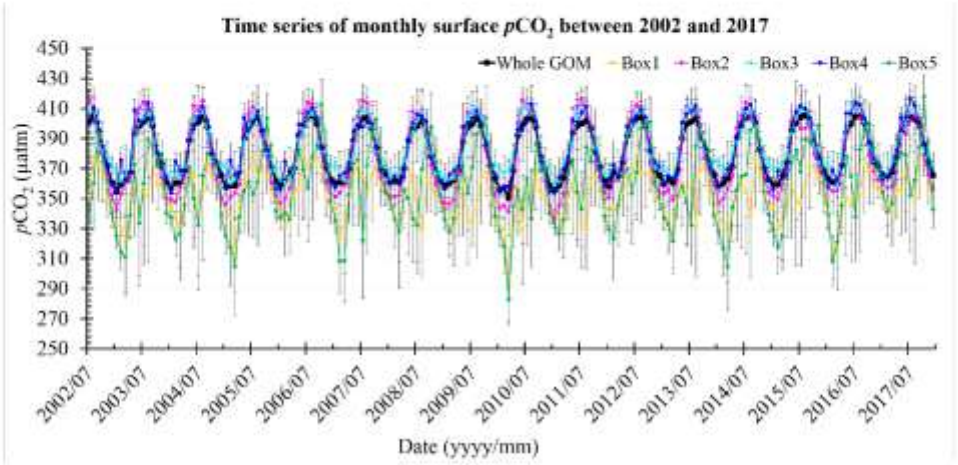

Fig. 9. Monthly surface pCO_2 time series in the whole GOM and in the five sub-regions annotated in Fig. 1a. Errorbars in each time series plot represent the standard deviations of the monthly mean of surface pCO_2 in each region. Box 1 is near the Mississippi River delta, Box 2 is on the West Florida Shelf, Box 3 is near the Loop Current, Box 4 is in the western GOM open waters, and Box 5 presents the "dead zone" along the Louisiana coast.

In terms of seasonal variations, monthly time series of surface pCO_2 based on pCO_2 maps between July 2002 and December 2017 of the entire GOM (black line in Fig. 9) showed high pCO_2 values (~405 µatm) in summer and low pCO_2 (~355 µatm) in winter with a standard deviation of ~ ± 17 µatm on average. Xue et al. (2013) also found comparable seasonal variation in the Gulf-wide averaged pCO_2, but with a relatively higher standard deviation (≥ 50 µatm). Similarly, in Fig 9, pCO_2 in the selected sub-regions of Box 2, Box 3, and Box 4, representing the WFS, Loop Current and southwestern GOM, respectively, also showed similar temporal variation patterns although with some differences in magnitude. For example, pCO_2 in the sub-region of Loop Current waters (Box 3), was relatively higher than pCO_2 in the sub-regions of WFS and southwestern GOM in

winter. Such difference is mainly caused by the warmer characteristics (thus higher SST) of the Loop Current. The seasonal variation of the pCO_2 time series in the northern GOM was quite different from that of the regions mentioned above. In the Mississippi River delta represented by Box 1, pCO_2 showed lower values (~290-380 μatm, ± 23 μatm) than most GOM waters (Fig. 8) in all seasons. In addition to the general variation patterns of high to low from summer to winter, finer time scale variations were found in summertime, with a pCO_2 decrease in July or August in most of the years. This decrease in surface pCO_2 was mainly attributed to the phytoplankton blooms, induced by the nutrient-rich freshwater inputs through the MARS river discharge in the spring (April to June). The depletion of nutrients restricted the continuous biological uptake of surface water CO_2 and kept the surface pCO_2 from decreasing further (Huang et al., 2012 & 2015; Guo et al., 2012). The resulted richness in oxygen and organic matter promoted the growth of bacteria, which decomposed the organic matters (either from terrestrial river runoff or generated from biological activities) in the water column and released CO_2 back to seawater (Gardner et al., 1994; Cai et al., 2011; Cai, 2011). Therefore, surface pCO_2 tended to increase in late summer and fall, and then decreased as the water became colder. Similar to the case shown in the Mississippi delta, the representative sub-region of the Louisiana coast (Box 5) showed a similar variation pattern in surface pCO_2 but with larger seasonal magnitude (~280-420 μatm, ± 17 μatm). The region is the famous "dead zone" in the GOM (Keul et al., 2010). In summertime, the eutrophication and excessive utilization of oxygen cause hypoxia in this area (Rabalais et al., 2002; Laurent et al., 2017), thus more CO_2 is released back to the seawater and, therefore, surface pCO_2 tends to be higher as compared to the Mississippi delta. The finer time scale variation in surface pCO_2 on the Louisiana Shelf (demonstrated by the two sub-regions around the Mississippi river delta (Box 1) and the Hypoxia zone off the Louisiana coast (Box 5)), was also found by Lohrenz

et al. (2018) but with higher standard deviation and variation, but was not found by Xue et al. (2013).

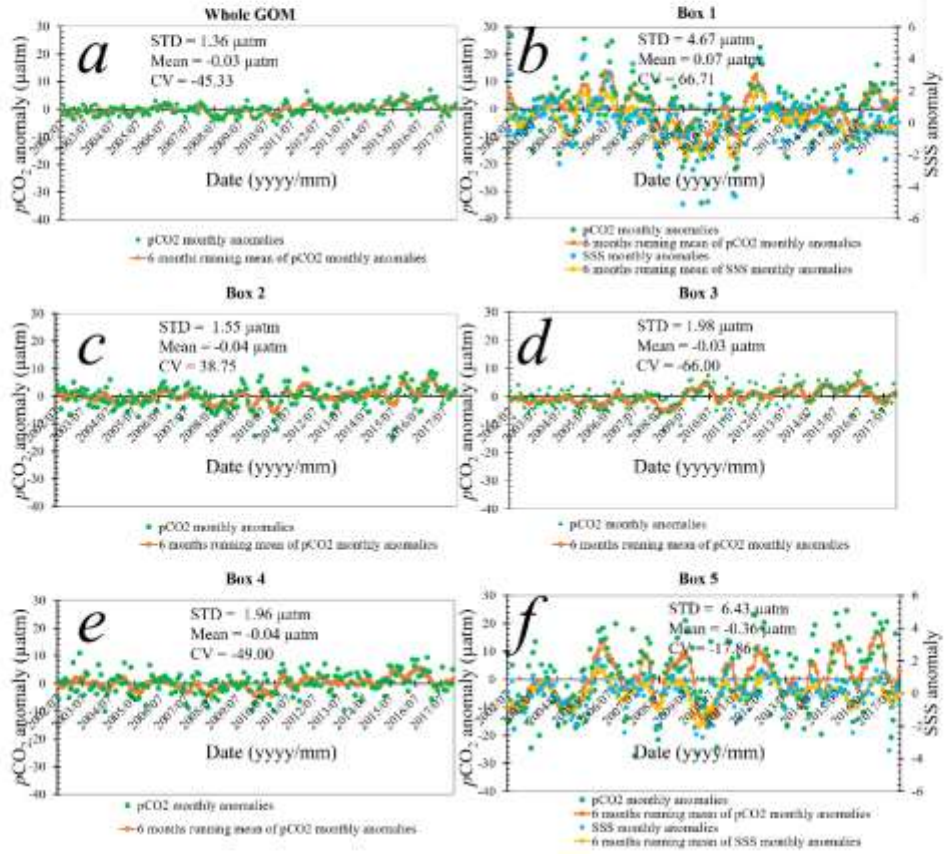

Fig. 10. Interannual variability of the modeled pCO_2 in the entire GOM (a) and the five sub-regions (b-f) over the study period of 2002-2017. Monthly pCO_2 anomalies on the Y-axis in each panel were derived by subtracting the monthly climatology from the monthly mean. In panels b & f, a secondary Y-axis of SSS was added to show the corresponding interannual SSS anomalies in the sub-regions of Mississippi delta (Box 1) and "dead zone" (Box 5). Box 1 is near the Mississippi

River delta, Box 2 is on the West Florida Shelf, Box 3 is near the Loop Current, Box 4 is in the western GOM open waters, and Box 5 presents the "dead zone" along the Louisiana coast.

In terms of interannual variation, overall, there is indistinguishable decadal trend in the monthly pCO_2 anomalies (Fig. 10). Over the river-dominated coastal region in the northern GOM, surface pCO_2 showed relatively larger interannual variability than in other GOM waters. Over the entire GOM (Fig. 10a), the interannual monthly pCO_2 anomalies showed little variation of within ± 5 µatm, with negative (positive) values in most months before (after) the year of 2012. In the Mississippi delta (Box 1) and "dead zone" area (Box 5), due to the complexity and dynamics of the biogeochemical processes in these regions, pCO_2 showed larger anomalies between -30 and 30 µatm. For these two regions, it is found that the anomalies in SSS showed similar variation to surface pCO_2 variation, indicating that SSS may control the interannual variations of surface pCO_2 in these regions. Different from the northern coastal waters, pCO_2 in other GOM waters (WFS, Loop Current, Southwestern GOM waters) represented by Boxes 2 – 4 (Figs. 10c-10e) showed similar but slightly larger anomalies (within ± 10 µatm) comparing to that of the entire GOM (Fig. 10a). Similar to the interannual variations of pCO_2 over the entire GOM in Fig. 10a, in these regions, the anomalies in surface pCO_2 tended to be positive (close and above zero) over the years since 2012, while the increasing trend is still indistinguishable considering the overall variations of the pCO_2 anomalies in the study period. Generally, surface pCO_2 in the GOM tended to increase but the increasing trend is not well captured in our data. In addition, the decadal variation here could be part of the long-term trend (≥30 years), or part of the decadal timescale fluctuation (Thomas et al., 2008; Gruber, 2009; Mckinley et al., 2011; Fay & Mckinley, 2013). Yet it is impossible to differentiate these two scenarios using our data. In the study of Landschützer et al. (2013), both positive and negative trends were found in surface pCO_2 of the GOM over the period

of 1998-2007, leading to no apparent overall trend over the entire GOM. We also examined the interannual variations of the four satellite-derived environmental variables (SST, SSS, Chl, and Kd), and found no decadal trend. Because these variables were used to model surface pCO_2, it is no surprise to see indistinguishable decadal trend in the modeled surface pCO_2 over the GOM.

4. Discussion

4.1. Which environmental variables to use in the RFRE

In this study, we used four environmental variables, including SST, SSS, Chl, and Kd, to model surface pCO_2 in the GOM. These variables were selected based on our previous studies and other studies in the published literature. In Chen et al. (2016 &2017), all these variables were proven to be important and efficient in modeling surface pCO_2 in the GOM, although other empirical approaches other than the RFRE were used. Indeed, SST and SSS are commonly used to capture the effects of thermodynamics and ocean mixing, and Chl and Kd are used to implicitly quantify the biological effect on surface pCO_2. Because there is no known function between each predictive variable and surface pCO_2, a machining-learning based RFRE approach was used to model the unknown complex relationships between these predictive variables and surface pCO_2. The RFRE approach was selected after extensive comparison with other empirical approaches. The RFRE-based pCO_2 model, after modeling training using extensive datasets, showed excellent performance in estimating surface pCO_2 with little uncertainties (RMSE < 10 μatm) for a large dynamic range.

In section 3.3, a model sensitivity analysis showed that the response of the RFRE model to the added errors in each model input variable was close to or within the model uncertainties, with relatively higher sensitivity to SST and SSS than to Chl and Kd. These results suggest that the

model is insensitive to small errors (+-20%) in the satellite data products. Such insensitivity may raise the question of whether true changes in surface pCO_2 can be captured by the model. For example, while an increasing rate of 1.5 µatm per year has been reported in atmospheric pCO_2 (Landschützer et al., 2013), the model did not show any long-term trend in surface pCO_2. Then two fundamental questions arise: 1) because the model showed little sensitivity to small errors in Chl and Kd, why are they still used in the RFRE model? 2) Can the model capture the long-term trend of surface pCO_2 in response to increased atmospheric pCO_2?

Indeed, although the RFRE model is insensitive to small errors in the input Chl and Kd, it does not mean that Chl and Kd are not important in modeling surface pCO_2 for two reasons. One, both Chl and Kd were scaled logarithmically before being used in the model in order to account for their log-normality in their large-scale distributions (Campbell, 1995). Then, their dynamic ranges were "dampened" after log transformation, and same occurred with the input errors. For example a 20% error is transformed to an error of 0.08 (=log(1.2)). In comparison, the variations of Chl and Kd in $\log_{10}$ scale (and their errors) were much smaller than those in SST (13.48~33.28 °C, with 1 °C error) and SSS (10.90~38.34, with 1.0 error). This explains why the RFRE model was more sensitive to SST and SSS changes than to Chl and Kd changes. On the other hand, both Chl and Kd carry information (implicitly) of biological activities, thus cannot be ignored in the model. In fact, Chl and Kd showed strong negative correlations (Figs. 11a & 11b) to surface pCO_2 in the northern GOM. In coastal waters, surface pCO_2 showed strong correlation with Chl, Kd, and SSS (Fig. 10a, 10b, & 10d), indicating that the biological activities and freshwater inputs are the dominant factors in controlling surface pCO_2 in these waters. On the other hand, in the GOM oligotrophic waters and coastal areas with little freshwater inputs, SST appeared to be the dominant

factor in controlling surface pCO_2 (Fig. 10c). Therefore, it is necessary to include all four environmental variables in the RFRE pCO_2 model.

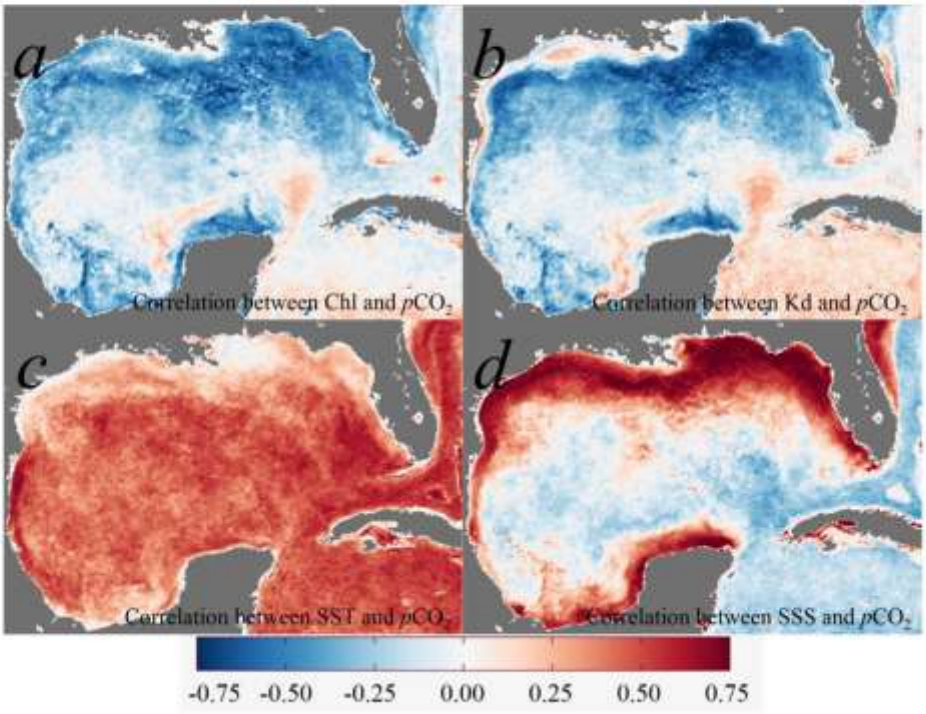

Fig. 11. Maps of correlation coefficients at 1-km resolution between Chl (a), Kd (b), SST (c), SSS (d), and surface pCO_2, respectively. These correlations were derived from the interannual monthly anomalies.

Then, because atmospheric pCO_2 was not used in the model explicitly, if changes in atmospheric pCO_2 cannot be captured implicitly in one or more of the four variables (SST, SSS, Chl, and Kd), it would be impossible for the RFRE pCO_2 model to capture the changes in the atmospheric pCO_2 (~ 1.5 μatm per year, Landschützer et al. 2013), mainly caused by the human activities (e.g., fossil

fuel burning). It is therefore desirable to include atmospheric pCO_2 in future modeling efforts in order to better detecting decadal trends in surface pCO_2 under anthropogenic forcing. Nevertheless, the work here introduces an empirical pCO_2 approach that is applicable to a large oceanic region (e.g., GOM) with different dominant oceanic processes, making it possible to better understand the spatial and seasonal variations in surface pCO_2 of the entire GOM, as compared to ship-based measurements.

4.2. Implication for general applications over other regions

The results shown in Section 3 demonstrate that the RFRE-based pCO_2 model developed for the entire GOM can be well applied to different regions of the GOM. This is true in both river-dominated and current-dominated regions, both with low uncertainties (RMSE < 10 µatm). One question is whether this RFRE approach (not the model itself) can be applied to other oceanic regions. To examine its general applicability to other oceanic waters, we tested this RFRE approach on the G. Maine which was selected for two main reasons: First, the G. Maine shows great contrast to GOM with relatively small riverine discharge (i.e., <1000 m^3/sec from the largest river – Saint John River) but strong semi-diurnal tidal mixing, as well as wide-open interactions with the North Atlantic waters (i.e., Gulf Stream, Labrador Current). Second, it is located at a relatively high latitude (41.7~46 °N, 71~64 °W), and rapid warming is found with an increasing rate of 0.23 °C per year in SST since 2004 (Pershing et al., 2015). In addition to the resulting ecological impact (i.e., decrease in fisheries), this warming would have direct impact on air-sea CO_2 flux and long-term carbon cycling. However, the published study of satellite mapping of surface pCO_2 over this region shows very large uncertainties (i.e. RMSE ~ 35 µatm) (Signorini et al., 2013). Therefore, it would be significant if the RFRE approach could work in the G. Maine with a much lower uncertainty.

Surface pCO_2 data collected in the G. Maine between 2002 and 2016 (Fig. 12a) were compiled from the global surface pCO_2 database (LDEO) (version 2015, Takahashi et al., 2016b) and matched with the MODIS data products (including SST, Chl, and Kd) using the criteria described in Section 2.2.1. Here a time window of ± 3h was used to account for the semi-diurnal tidal characteristics in the G. Maine. The conjugate pCO_2 dataset (Fig. 12b) showed dynamic variation range in each variable (field-measured pCO_2: 202~558 µatm; satellite SST: 1.6~25 °C; field-measured SSS: 25~34 (note there is no satellite SSS available for the G. Maine at 1 km resolution); satellite Chl: 0.26~19.9 mg m^{-3}; and satellite Kd: 0.05~0.68 m^{-1}).

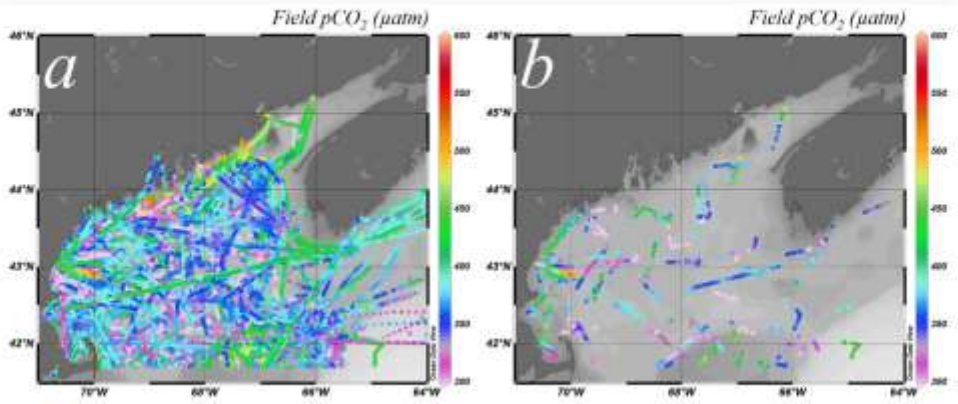

Fig. 12. Spatial distributions of the surface pCO_2 measurements in the Gulf of Maine along the cruise tracks. (a) Cruise tracks from all data between 2002 and 2016 in all seasons (N=482,584); (b) Cruise tracks from the same data but with co-located and contemporaneous (± 3h) satellite Chl, Kd and SST (N=4,559).

Before locally tuning a RFRE pCO_2 model for the G. Maine, we first tested the locally parameterized MLR model proposed by Signorini et al. (2013) for the G. Maine. Similar to its original results, the model was found to yield a RMSE of ~42 µatm. Then we tested the RFRE

model (Fig. 2), which was parameterized for the GOM, to the G. Maine. Poor model performance was obtained (RMSE = 89.6 µatm), suggesting that the effects of the input variables to surface pCO_2 may work differently in the G. Maine than from the GOM. Because the RFRE-based pCO_2 model is empirical and is locally-trained, it can only be applied to similar environments. Whereas the GOM-trained RFRE model uses satellite SSS as an input to account for the effect of freshwater mixing, in the G. Maine, because there is no relevant satellite SSS available at 1 km spatial resolution, it is not practical to include SSS as a predictor. Furthermore, considering the relatively small river discharge in this area and the poor correlation (R~0.07) between SSS and surface pCO_2, SSS may not necessarily be an effective predictor in surface pCO_2 in the G. Maine. Therefore, in the G. Maine, the only satellite variables used as predictive variables to model surface pCO_2 were SST, Chl, and Kd as well as Julian day. Similar to the GOM, using the same training dataset (Fig. 10b) and same input variables (SST, Chl, Kd, and Julian day), all the empirical approaches described in Section 2.3.2 were also tested in the G. Maine. The RFRE approach proved to have the best model performance in the G. Maine as well.

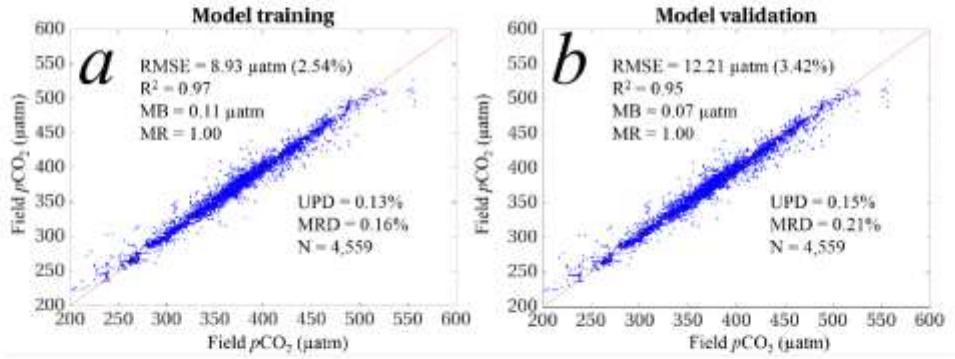

Fig. 13. RFRE model performance in estimating surface pCO_2 in the Gulf of Maine in both model training (a) and model validation (b) using the conjugate dataset described in Fig. 10b.

Fig. 13 shows the performance of the locally tuned RFRE in the G. Maine. In the model training, satellite-derived pCO_2 showed good agreement with the field-measured pCO_2 with a RMSE of 8.93 µatm (2.54%), R^2 of 0.97, MB of 0.11 µatm, MR of 1.00, UPD of 0.13%, and MRD of 0.16%. In the 10-fold cross validation, similar statistics were also derived (see Fig. 13b). We further validated this locally parameterized RFRE model in the G. Maine using several independent datasets, and similar results were found as in the validation shown in Section 3.2. These results demonstrated the feasibility of the RFRE approach in the G. Maine once local parameterization was achieved. As an example, Fig. 14 shows the monthly pCO_2 maps in the G. Maine in 2013. Comparing to the GOM, distinct and opposite seasonality with high pCO_2 in winter and lower pCO_2 in summer is shown for the G. Maine, indicating different driving mechanisms of surface pCO_2 in these two contrasting oceanic regions. In the G. Maine, strong vertical mixing during wintertime brings large amounts of DIC to the surface. Although large amounts of nutrients are also brought to the surface, due to low SST and poor light availability, there is no strong biological uptake of CO_2. In the summertime, more light is available, with warming of surface waters, biological activities (i.e., algal blooms) become active and the corresponding uptake of CO_2 begins to draw the surface pCO_2 down.

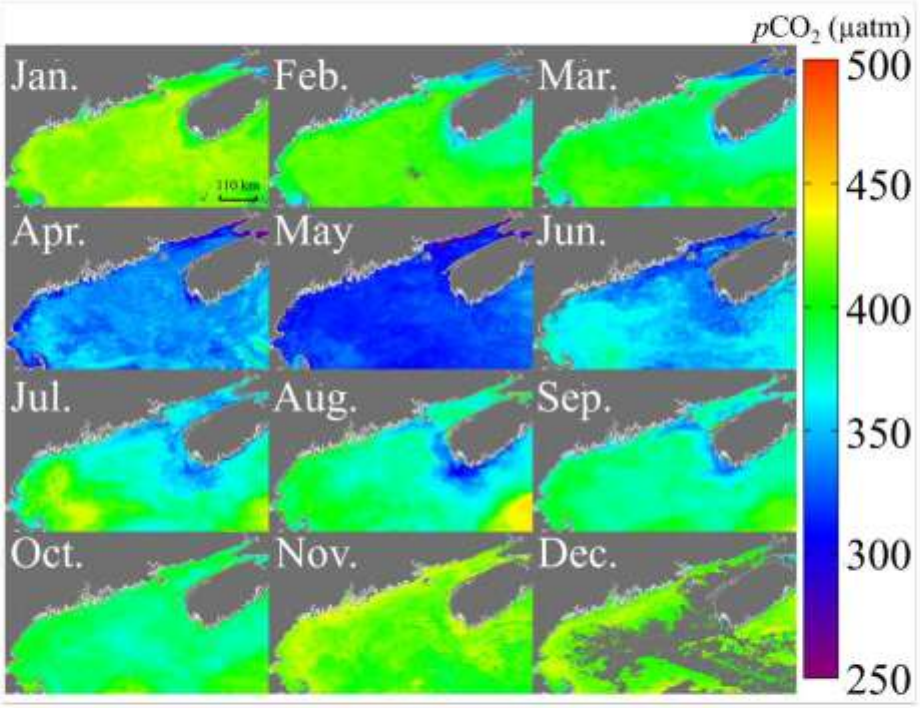

Fig. 14. Monthly surface pCO_2 of 2013 in the Gulf of Maine (latitude: 41.7~46.0˚ N, longitude: -71.0 ~ -64˚ W), derived from MODIS using the RFRE pCO_2 model. Large data gaps in the pCO_2 map of Dec. 2013 were mainly caused by various non-optimal satellite observing conditions (i.e., cloud, stray light).

In short, although the RFRE-based model (with model parameterization developed for the GOM) could not be directly applied to the G. Maine, the RFRE approach can still be applied to the G. Maine with localized parametrization. The resulting model performance appears to exhibit significant improvement over those published in the literature. This result strongly suggests the potential of the RFRE approach in regional applications around the globe.

4.3. Advantages and limitations of the RFRE

The extensive evaluation results in Section 3.2 suggest that for surface pCO_2 of 145~550 μatm in the GOM, the empirical RFRE model can estimate surface pCO_2 with an overall uncertainty of < 10 μatm. Comparing to other empirical approaches (either traditional or machine-learning based) tested in this study, the RFRE approach shows great advantages in estimating surface pCO_2 in different environments of the GOM. Specifically, the northern GOM waters, with large amounts of freshwater inputs from the MARS, have distinct and different carbonate properties than other GOM waters. Most of the empirical approaches showed poor performance when applied to the entire GOM, possibly due to their poor local parameterization in dealing with disparate water masses. In contrast, the RFRE approach presented in this study appears to work well in all these different-processes-dominated regions of the GOM. Consequently, a GOM-wide RFRE pCO_2 model is generalized, with the variable relationships between predictors and response variables implicitly included in the empirical coefficients (i.e., weights of each regression tree). In addition, the weak response of the RFRE pCO_2 model to errors in each of the satellite variables (i.e., RMSE ≤ 12 μatm, see sensitivity analysis in Section 3.3) shows the model's tolerance to input errors in the satellite variables. Furthermore, a test of the RFRE approach in the G. Maine (after local parameterization) also shows better performance and significant improvement over other empirical approaches, including the approaches tested in this study and those in the published literature. In contrast, the GOM-parameterized RFRE model performs poorly in the G. Maine without local parameterization; this indicates the intrinsic empirical nature of the RFRE approach. Overall, the RFRE approach shows great advantages over other empirical approaches in satellite mapping of surface pCO_2 in the two contrasting ocean regions of the GOM and the G. Maine. The flexibility of the RFRE model in dealing with these two different oceanic processes indicates its likely

potential to serve as a robust approach in estimating surface pCO_2 from satellites for other ocean regions.

Although the RFRE-based pCO_2 model has shown to be applicable to most GOM waters with relatively low uncertainties, due to its empirical nature, it is unknown whether it works for waters with surface pCO_2 outside the 145~550 µatm range. This limitation is caused by the scarcity of valid MODIS data outside this range, although this range should represent the surface pCO_2 levels of most GOM waters (Fig. 1a). Furthermore, even within this range, for empirical approaches the model's satisfactory performance does not necessarily indicate that the model is applicable in all types of waters driven by different processes. However, because of the extensive dataset used to train the model and another extensive dataset used to validate the model, the typical concern of lack of data with empirical approaches may be eliminated. Indeed, the data used in training the model consisted of > 220 cruise surveys in the past 16 years covering all seasons and water types in the GOM, thus representing the most complete pCO_2 dataset for the GOM. Likewise, the validation results from another similar comprehensive dataset, under different scenarios in the GOM, suggest that the RFRE model should be able to estimate surface pCO_2 for most, if not all, GOM waters. Similar conclusions may be drawn for the G. Maine, where most of the pCO_2 collected between 2002 and 2016 were used to train and validate the RFRE model. Because only a small amount of data were available in winter, the model performance for the G. Maine requires further evaluation more wintertime field data become available. Likewise, pCO_2 in the GOM can certainly be > 550 µatm or < 145 µatm (Fig. 1a) along the northern coasts and in the Florida Bay, yet these data were not included in the model training due to the unavailability of contemporaneous satellite data after quality control and application of the matchup criteria (see Section 2.2.1). However, these extreme pCO_2 values only appeared in some of the very nearshore waters, and in

practice these waters should be masked to avoid misinterpretation of the model results. In fact, most of these waters have no satellite data retrievals due to various reasons (e.g., atmospheric correction failure, straylight, land contamination, etc.), thus having little effect on the model results.

In addition to the model applicability range, due to its empirical nature and its machine-learning based technique, the RFRE approach works like a "black box" without explicit understanding of the driving mechanisms between the input and output variables. Unlike the semi-analytical approaches (i.e., Bai et al., 2015; Chen et al., 2017) which separate and explicitly quantify the contributions of different processes to the overall surface pCO_2 (i.e., river-ocean mixing, biological activities, etc.), the RFRE approach quantifies all of them together. As a result, it is difficult to explain clearly how each process affects the variation of surface pCO_2. On the other hand, because different oceanic processes may not be independent from each other and they may collectively drive the surface pCO_2, it may be advantageous to treat all input variables as a whole in order to achieve a better model accuracy. Indeed, the comparison between empirical and semi-analytical approaches in Chen et al. (2017) did show that the empirical approach could produce better estimates of surface pCO_2 than the semi-analytical approach under different conditions.

Finally and most importantly, the satisfactory performance of the RFRE approach in the two contrasting regions, the GOM and the G. Maine, indicates that the RFRE approach could serve as a robust empirical approach for other ocean regions once local parameterization is obtained. Indeed, a preliminary test indicated that if the training datasets of the GOM and the G. Maine were merged together, an RFRE model with the same parameterization for both regions could yield similar model performance statistics as those from the two separate models (Figs. 2 &11). This additional test strongly suggests that the RFRE approach offers great potential for estimating surface pCO_2 in different ocean regions.

5. Conclusion

Accurate estimation of surface ocean pCO_2 from satellite remote sensing has been a challenging task due to the different regional processes that dominate pCO_2. Such processes are difficult to model with mechanistic approaches, and also difficult to model with traditional empirical approaches because the predictor-response relationship can vary substantially across adjacent sub-regions and because high uncertainties may exist in the satellite-derived intermediate data products (SSS, Chl and Kd) in turbid and dynamic coastal waters. In this study, with satellite-derived SST, SSS, Chl, and Kd as inputs, a random forest based regression ensemble (RFRE) approach has been developed and thoroughly evaluated for a large, semi-enclosed sea - the Gulf of Mexico. The RFRE-based model showed good performance with an overall uncertainty of < 10 μatm and higher uncertainty in the northern GOM than in the southern GOM due to the complexity and dynamics of the Mississippi-Atchafalaya River system. This is the first time that a unified empirical pCO_2 model has been demonstrated to show consistent performance across many different water types in the entire GOM. The RFRE approach used to test the G. of Maine indicates great potential for the RFRE to be a robust approach for regional pCO_2 modeling in regional studies as long as sufficient *in situ* field data are available for model training. Finally, future research needs to be focused on improving the capability of the satellite-based RFRE pCO_2 model in tracing decadal and long-term scale variations in surface pCO_2 under anthropogenic forcing.

Acknowledgements

This research was supported by a University of South Florida student fellowship and the U.S. NASA Ocean Biology and Biogeochemistry program (NNX14AL98G, NNX17AH03G). The authors are indebted to all researchers, including those of NOAA AOML, NOAA NCEI, Weijun Cai (UD), and Xinping Hu (TAMU), who have collected, processed, quality controlled, and shared

all the cruise survey data. These data played an essential role in calibrating and validating the empirical pCO_2 algorithm in this work. The authors also thank NASA for providing MODIS satellite data.

Notations

AOML Atlantic Oceanographic and Meteorological Laboratory

CDOM Colored dissolved organic matter

Chl Surface water chlorophyll-a concentration, in mg m^{-3}

DIC Dissolved inorganic carbon, in µmol kg^{-1}

Kd Diffuse attenuation coefficient of downwelling irradiance, in m^{-1}

G. Maine Gulf of Maine

GOM Gulf of Mexico

GSFC Goddard Space Flight Center

Jday Julian day

LDEO Global surface pCO_2 database collated by T. Takahashi of the Lamont-Doherty Earth Observatory of Columbia University

MARS Mississippi and Atchafalaya River system

MB Mean bias

MLD Mixed layer depth

MLR Multi-linear regression

MNR	Multi-nonlinear regression
MODIS/Aqua	Moderate Resolution Imaging Spectroradiometer on Aqua satellite
MPNN	Multilayer Perceptron Neural Network
MR	Mean ratio
MRD	Mean relative difference
NCEI	National Centers for Environmental Information
NODC	National Oceanographic Data Center
pCO_2	Partial pressure of surface water CO_2, in µatm
PCR	Principle component regression
R^2	Coefficient of determination
RFRE	Random Forest based Regression Ensemble, a machine learning technique
RMSE	Root mean square error
SOMs	Self-organizing maps
SSS	Sea surface salinity
SST	Sea surface temperature, in ˚C
SVMs	Supporting vector machines
TA	Total alkalinity, unit: µmol kg^{-1}
TAMU	Texas A&M University

UD	University of Delaware
UPD	Unbiased percent difference
WFS	West Florida Shelf

Reference

Bai, Y., Cai, W. J., He, X., Zhai, W., Pan, D., Dai, M., & Yu, P. (2015). A mechanistic semi-analytical method for remotely sensing sea surface pCO_2 in river-dominated coastal oceans: A case study from the East China Sea. Journal of Geophysical Research: Oceans, 120(3), 2331-2349. https://doi.org/10.1002/2014JC010632.

Bailey, S. W., & Werdell, P. J. (2006). A multi-sensor approach for the on-orbit validation of ocean color satellite data products. Remote Sensing of Environment, 102(1-2), 12-23. https://doi.org/10.1016/j.rse.2006.01.015.

Barnes, B. B., & Hu, C. (2015). Cross-sensor continuity of satellite-derived water clarity in the Gulf of Mexico: Insights into temporal aliasing and implications for long-term water clarity assessment. IEEE Transactions on Geoscience and Remote Sensing, 53(4), 1761-1772.

Bates, N. R., Knap, A. H., & Michaels, A. F. (1998). Contribution of hurricanes to local and global estimates of air–sea exchange of CO_2. Nature, 395(6697), 58-61.

Bates, N. R., & Merlivat, L. (2001). The influence of short‐term wind variability on air‐sea CO_2 exchange. Geophysical Research Letters, 28(17), 3281-3284.

Borges, A. V., Delille, B., & Frankignoulle, M. (2005). Budgeting sinks and sources of CO_2 in the coastal ocean: Diversity of ecosystems counts. Geophysical research letters, 32(14), L14601.

Borges, A., Ruddick, K., Lacroix, G., Nechad, B., Astoreca, R., Rousseau, V., & Harlay, J. (2010). Estimating pCO_2 from remote sensing in the Belgian coastal zone. ESA Special Publication SP-686.

Breiman, L. (1996). Bagging predictors, Machine Learning. Springer, 24(2), 123-140. https://doi.org/10.1007/BF00058655.

Breiman, L. (2001). Random forests, Machine learning. Springer, 45(1), 5-32. https://doi.org/10.1023/A:1010933404324.

Cai, W.-J., Hu, X., Huang, W.-J., Murrell, M. C., Lehrter, J. C., Lohrenz, S. E., Chou, W.-C., Zhai, W., Hollibaugh, J.T.,Wang, Y., Zhao, P., Guo, X., Gundersen, K., Dai, M., and Gong, G.-C. (2011). Acidification of subsurface coastal waters enhanced by eutrophication. Nature Geosci. 4: 766–770.

Cannizzaro, J. P., Hu, C., Carder, K. L., Kelble, C. R., Melo, N., Johns, E. M., Vargo, G.A., & Heil, C. A. (2013). On the accuracy of SeaWiFS ocean color data products on the West Florida Shelf. Journal of Coastal Research, 29(6), 1257-1272.

Chen, C. T., Huang, T. H., Chen, Y. C., Bai, Y., He, X., & Kang, Y. (2013). Air-sea exchanges of CO_2 in the world's coastal seas. Biogeosciences, 10(10), 6509–6544.

Chen, L., Xu, S., Gao, Z., Chen, H., Zhang, Y., Zhan, J., & Li, W. (2011). Estimation of monthly air-sea CO_2 flux in the southern Atlantic and Indian Ocean using in-situ and remotely sensed data. Remote sensing of environment, 115(8), 1935-1941.

Chen, S., Hu, C., Byrne, R. H., Robbins, L. L., & Yang, B. (2016). Remote estimation of surface pCO_2 on the West Florida Shelf. Continental Shelf Research, 128, 10-25. https://doi.org/10.1016/j.csr.2016.09.004.

Chen, S., Hu, C., Cai, W. J., & Yang, B. (2017). Estimating surface pCO_2 in the northern Gulf of Mexico: Which remote sensing model to use? Continental Shelf Research, 151, 94-110. https://doi.org/10.1016/j.csr.2017.10.013.

Chen, S., & Hu, C. (2017). Estimating sea surface salinity in the northern Gulf of Mexico from satellite ocean color measurements. Remote Sensing of Environment, 201, 115-132. https://doi.org/10.1016/j.rse.2017.09.004

Chierici, M., Olsen, A., Johannessen, T., Trinañes, J., & Wanninkhof, R. (2009). Algorithms to estimate the carbon dioxide uptake in the northern North Atlantic using shipboard observations, satellite and ocean analysis data. Deep Sea Research Part II: Topical Studies in Oceanography, 56(8-10), 630-639. https://doi.org/10.1016/j.dsr2.2008.12.014.

Coble, P. G., Robbins, L. L., Daly, K. L, Cai, W. J., Fennel, K., & Lohrenz S. E. (2010). A Preliminary Carbon Budget for the Gulf of Mexico. Fall 2010 issue of the OCB newsletter.

Dickinson, G. H., Ivanina, A. V., Matoo, O. B., Portner, H. O., Lannig, G., Bock, C., Beniash, E. & Sokolova, I. M. (2012). Interactive effects of salinity and elevated CO_2 levels on juvenile eastern oysters, Crassostrea virginica. Journal of Experimental Biology, 215(1), 29-43.

Doney, S. C., Balch, W. M., Fabry, V. J., & Feely, R. A. (2009). Ocean acidification: a critical emerging problem for the ocean sciences. Oceanography, 22(4), 16-25. https://doi.org/10.5670/oceanog.2009.93.

Doney, S.C., 2010. The Growing Human Footprint on Coastal and Open-Ocean Biogeochemistry. Science, 328(5985): 1512-1516. doi: 10.1126/science.1185198.

Fay, A. R. and McKinley, G. A., (2013). Global trends in surface ocean pCO_2 from *in situ* data, Global Biogeochem. Cy. 27, 1–17, doi:10.1002/gbc.20051.

Fay, A. R., & McKinley, G. A. (2017). Correlations of surface ocean pCO_2 to satellite chlorophyll on monthly to interannual timescales. Global Biogeochemical Cycles, 31(3), 436-455. https://doi.org/10.1002/2016GB005563.

Feely, R. A., Wanninkhof, R., Milburn, H. B., Cosca, C. E., Stapp, M., & Murphy, P. P. (1998). A new automated underway system for making high precision pCO_2 measurements onboard research ships. Analytica Chimica Acta, 377(2-3), 185-191.

Fennel, K., Wilkin, J., Previdi, M., & Najjar, R. (2008). Denitrification effects on air‐sea CO_2 flux in the coastal ocean: Simulations for the northwest North Atlantic. Geophysical Research Letters, 35(24), L24608. doi: 10.1029/2008GL036147.

Friedrich, T., & Oschlies, A. (2009). Neural network‐based estimates of North Atlantic surface pCO_2 from satellite data: A methodological study. Journal of Geophysical Research: Oceans, 114(C3), C03020. https://doi.org/10.1029/2007JC004646.

Gardner, W. S., Cotner, J. B., Eadie, B. J., Cavaletto, J. F., Benner, R., & Chin-Leo, G. (1994). Mineralization of organic material and bacterial dynamics in Mississippi River plume water. Estuaries, 17(4), 816-828.

Gregg, W. W., & Casey, N. W. (2004). Global and regional evaluation of the SeaWiFS chlorophyll data set. Remote Sensing of Environment, 93(4), 463-479.

Gruber, N., (2009). Fickle trends in the ocean, Nature, 458, 155–156.

Guo, X., Cai, W. J., Huang, W. J., Wang, Y., Chen, F., Murrell, M. C., Lohrenz, S. E., Jiang, L. Q., Dai, M., Hartmann, J., Lin, Q., & Culp, R. (2012). Carbon dynamics and community production in the Mississippi River plume. Limnology and Oceanography, 57(1), 1-17.

Hales, B., Strutton, P. G., Saraceno, M., Letelier, R., Takahashi, T., Feely, R., Sabine, C., & Chavez, F. (2012). Satellite-based prediction of pCO_2 in coastal waters of the eastern North Pacific. Progress in Oceanography, 103, 1-15. https://doi.org/10.1016/j.pocean.2012.03.001.

Hofmann, E. E., Cahill, B., Fennel, K., Friedrichs, M. A., Hyde, K., Lee, C., Mannino, A., Najjar, R. G., O'Reilly, J. E., Wilkin, J., & Xue, J. (2010). Modeling the dynamics of continental shelf carbon. Annual Review of Marine Science, 3, 93-122. doi: 10.1146/annurev-marine-120709-142740.

Hu, C., Muller-Karger, F., Murch, B., Myhre, D., Taylor, J., Luerssen, R., Moses, C., Zhang, C., Gramer, L., & Hendee, J. (2009). Building an Automated Integrated Observing System to Detect Sea Surface Temperature Anomaly Events in the Florida Keys. IEEE Transactions on Geoscience and Remote Sensing, 47(7), 2071-2084.

Huang, W.-J., W.-J. Cai, R. T. Powell, S. E. Lohrenz, Y. Wang, L. Q. Jiang, and C. S. Hopkinson (2012). The stoichiometry of inorganic carbon and nutrient removal in the Mississippi River plume and adjacent continental shelf. Biogeosciences, 9(7), 2781–2792.

Huang, W. J., Cai, W. J., Wang, Y., Lohrenz, S. E., & Murrell, M. C. (2015). The carbon dioxide system on the Mississippi River-dominated continental shelf in the northern Gulf of Mexico: 1. Distribution and air-sea CO_2 flux. Journal of Geophysical Research: Oceans, 120(3), 1429-1445. https://doi.org/10.1002/2014JC010498.

Ikawa, H., Faloona, I., Kochendorfer, J., Paw, U., & Oechel, W. C. (2013). Air–sea exchange of CO2 at a Northern California coastal site along the California Current upwelling system. Biogeosciences, 10(7), 4419-4432. doi: 10.5194/bg-10-4419-2013.

James, G., Witten, D., Hastie, T., & Tibshirani, R. (2013). Tree-Based Methods, An introduction to statistical learning. Springer. 112, 303-328.

Jamet, C., Moulin, C., & Lefèvre, N. (2007). Estimation of the oceanic pCO_2 in the North Atlantic from VOS lines in-situ measurements: parameters needed to generate seasonally mean maps. Annales Geophysicae, European Geosciences Union. 25(11), 2247-2257.

Jo, Y. H., Dai, M., Zhai, W., Yan, X. H., & Shang, S. (2012). On the variations of sea surface pCO_2 in the northern South China Sea: A remote sensing based neural network approach. Journal of Geophysical Research: Oceans, 117(C8), C08022. https://doi.org/10.1029/2011JC007745.

Keul, N., Morse, J. W., Wanninkhof, R., Gledhill, D. K., & Bianchi, T. S. (2010). Carbonate chemistry dynamics of surface waters in the northern Gulf of Mexico. Aquatic geochemistry, 16(3), 337-351.

Landschützer, P., Gruber, N., Bakker, D. C. E., Schuster, U., Nakaoka, S., Payne, M. R., ... & Zeng, J. (2013). A neural network-based estimate of the seasonal to inter-annual variability of the Atlantic Ocean carbon sink. Biogeosciences, 10(11), 7793-7815.

Laurent, A., Fennel, K., Cai, W. J., Huang, W. J., Barbero, L., & Wanninkhof, R. (2017). Eutrophication‐induced acidification of coastal waters in the northern Gulf of Mexico: Insights into origin and processes from a coupled physical‐biogeochemical model. Geophysical Research Letters, 44(2), 946-956.

Lee, K., Tong, L. T., Millero, F. J., Sabine, C. L., Dickson, A. G., Goyet, C., Park, G. H., Wanninkhof, R., Richard A., & Key, R. M. (2006). Global relationships of total alkalinity

with salinity and temperature in surface waters of the world's oceans. Geophysical Research Letters, 33(19), L19605. https://doi.org/10.1029/2006GL027207.

Lee, Z. P., Darecki, M., Carder, K. L., Davis, C. O., Stramski, D., & Rhea, W. J. (2005). Diffuse attenuation coefficient of downwelling irradiance: An evaluation of remote sensing methods. Journal of Geophysical Research: Oceans, 110(C2), C02016. https://doi.org/10.1029/2004JC002573.

Lefèvre, N., Aiken, J., Rutllant, J., Daneri, G., Lavender, S., & Smyth, T. (2002). Observations of pCO_2 in the coastal upwelling off Chile: Spatial and temporal extrapolation using satellite data. Journal of Geophysical Research: Oceans, 107(C6), 3055. doi: 10.1029/2000JC000395.

Lefèvre, N., Watson, A. J., & Watson, A. R. (2005). A comparison of multiple regression and neural network techniques for mapping *in situ* pCO_2 data. Tellus B, 57(5), 375-384.

Liu, Y., & Weisberg, R. H. (2005). Patterns of ocean current variability on the West Florida Shelf using the self‐organizing map. Journal of Geophysical Research: Oceans, 110(C6), C06003.

Liu, Y., & Weisberg, R. H. (2012). Seasonal variability on the West Florida shelf. Progress in Oceanography, 104, 80-98.

Lohrenz, S. E., & Cai, W. J. (2006). Satellite ocean color assessment of air‐sea fluxes of CO_2 in a river‐dominated coastal margin. Geophysical Research Letters, 33(1), L01601. doi: 10.1029/2005GL023942.

Lohrenz, S. E., Cai, W. J., Chen, F., Chen, X., & Tuel, M. (2010). Seasonal variability in air-sea fluxes of CO_2 in a river-influenced coastal margin. Journal of Geophysical Research: Oceans, 115(C10), C10034. doi: 10.1029/2009JC005608.

Lohrenz, S. E., Cai, W. J., Chakraborty, S., Huang, W. J., Guo, X., He, R., Xue Z., Fennel K., Howden S., & Tian, H. (2018). Satellite estimation of coastal pCO_2 and air-sea flux of carbon dioxide in the northern Gulf of Mexico. Remote Sensing of Environment, 207, 71-83. https://doi.org/10.1016/j.rse.2017.12.039.

Marrec, P., Cariou, T., Macé, É., Morin, P., Salt, L. A., Vernet, M., Taylor, B., Paxman, K., & Bozec, Y. (2015). Dynamics of air-sea CO_2 fluxes in the northwestern European shelf based on voluntary observing ship and satellite observations. Biogeosciences, 12(18), 5371-5391.

McKinley, G. A., Fay, A. R., Takahashi, T., and Metzl, N., (2011). Convergence of atmospheric and North Atlantic carbon dioxide trends on multidecadal timescales, Nat. Geosci., 4, 606–610, doi: 10.1038/NGEO1193.

Mélin, F., Zibordi, G., & Berthon, J. F. (2007). Assessment of satellite ocean color products at a coastal site. Remote Sensing of Environment, 110(2), 192-215.

Millero, F. J., Graham, T. B., Huang, F., Bustos-Serrano, H., & Pierrot, D. (2006). Dissociation constants of carbonic acid in seawater as a function of salinity and temperature. Marine Chemistry, 100(1-2), 80-94.

Millero, F.; R. Wanninkhof; R. Woosley (2016). Partial pressure (or fugacity) of carbon dioxide, salinity and other variables collected from Surface underway observations using Carbon dioxide (CO_2) gas analyzer, Shower head chamber equilibrator for autonomous carbon

dioxide (CO_2) measurement and other instruments from F.G. Walton Smith in the Coastal Waters of Florida, Florida Keys National Marine Sanctuary and others from 2011-10-20 to 2011-12-16 (NCEI Accession 0157433). Version 1.1. NOAA National Centers for Environmental Information. Dataset. doi:10.3334/CDIAC/OTG.COAST_WALTON_SMITH_2011.

Millero, F.; R. Wanninkhof; R. Woosley (2016a). Partial pressure (or fugacity) of carbon dioxide, salinity and other variables collected from Surface underway observations using Carbon dioxide (CO_2) gas analyzer, Shower head chamber equilibrator for autonomous carbon dioxide (CO_2) measurement and other instruments from F.G. Walton Smith in the Caribbean Sea, Coastal Waters of Florida and others from 2012-02-27 to 2012-09-25 (NCEI Accession 0157425). Version 1.1. NOAA National Centers for Environmental Information. Dataset. doi:10.3334/CDIAC/OTG.COAST_WALTON_SMITH_2012.

Millero, F.; R. Wanninkhof; R. Woosley (2016b). Partial pressure (or fugacity) of carbon dioxide, salinity and other variables collected from Surface underway observations using Carbon dioxide (CO_2) gas analyzer, Shower head chamber equilibrator for autonomous carbon dioxide (CO_2) measurement and other instruments from F.G. Walton Smith in the Coastal Waters of Florida, Coastal Waters of Louisiana and others from 2013-03-31 to 2013-12-21 (NCEI Accession 0157431). Version 1.1. NOAA National Centers for Environmental Information. Dataset. doi:10.3334/CDIAC/OTG.COAST_WALTON_SMITH_2013.

Millero, F.; R. Wanninkhof; R. Woosley (2016c). Partial pressure (or fugacity) of carbon dioxide, salinity and other variables collected from Surface underway observations using Carbon dioxide (CO_2) gas analyzer, Shower head chamber equilibrator for autonomous carbon dioxide (CO_2) measurement and other instruments from F.G. Walton Smith in the Coastal

Waters of Florida, Coastal Waters of Louisiana and others from 2014-04-22 to 2014-12-05 (NCEI Accession 0157432). Version 1.1. NOAA National Centers for Environmental Information. Dataset. doi:10.3334/CDIAC/OTG.COAST_WALTON_SMITH_2014.

Millero, F.; R. Wanninkhof; R. Woosley (2016d). Partial pressure (or fugacity) of carbon dioxide, salinity and other variables collected from Surface underway observations using Carbon dioxide (CO_2) gas analyzer, Shower head chamber equilibrator for autonomous carbon dioxide (CO_2) measurement and other instruments from F.G. Walton Smith in the Coastal Waters of Florida, Florida Keys National Marine Sanctuary and others from 2015-01-12 to 2015-11-20 (NCEI Accession 0157434). Version 1.1. NOAA National Centers for Environmental Information. Dataset. doi:10.3334/CDIAC/OTG.COAST_WALTON_SMITH_2015.

Moussa, H., Benallal, M. A., Goyet, C., & Lefèvre, N. (2016). Satellite-derived CO_2 fugacity in surface seawater of the tropical Atlantic Ocean using a feedforward neural network. International Journal of Remote Sensing, 37(3), 580-598.

Nakaoka, S., Telszewski, M., Nojiri, Y., Yasunaka, S., Miyazaki, C., Mukai, H., & Usui, N. (2013). Estimating temporal and spatial variation of ocean surface pCO_2 in the North Pacific using a self-organizing map neural network technique. Biogeosciences, 10(9), 6093-6106.

Olsen, A., Triñanes, J. A., & Wanninkhof, R. (2004). Sea–air flux of CO2 in the Caribbean Sea estimated using *in situ* and remote sensing data. Remote Sensing of Environment, 89(3), 309-325.

Ono, T., Saino, T., Kurita, N., & Sasaki, K. (2004). Basin-scale extrapolation of shipboard pCO_2 data by using satellite SST and Chl a. International Journal of Remote Sensing, 25(19), 3803-3815.

Orr, J. C., Fabry, V. J., Aumont, O., Bopp, L., Doney, S. C., Feely, R. A., Gnanadesikan A., Gruber N., Ishida A., Joos F., Key R. M., Lindsay K., Maier-Reimer E., Matear R., Monfray P., Mouchet A., Najjar R. G., Plattner G.-K., Rodgers K. B., Sabine C. L., Sarmiento J. L., Schlitzer R., Slater R. D., Totterdell I.J., Weirig M.-F., Yamanaka Y. & Yool A. (2005). Anthropogenic ocean acidification over the twenty-first century and its impact on calcifying organisms. Nature, 437(7059): 681-686.

Pachauri, R. K., & Meyer, L. A. (2014). Climate Change 2014: Synthesis Report. IPCC, Geneva, Switzerland, 151.

Parard, G., Charantonis, A. A., & Rutgerson, A. (2014). Remote sensing algorithm for sea surface CO_2 in the Baltic Sea. Biogeosci. Discuss, 11, 12255-12294.

Patt, F. S., et al., "Algorithm updates for the fourth SeaWiFS data reprocessing, NASA tech memo 2003-206892, volume 22," in SeaWiFS Post-launch Technical Report Series, S. B. Hooker and E. R. Firestone, Eds. Greenbelt, MD, USA: National Aeronautics and Space Administration (NASA), 2003.

Pershing, A. J., Alexander, M. A., Hernandez, C. M., Kerr, L. A., Le Bris, A., Mills, K. E., Nye, J. A., Record, N. R., Scannell, H. A., Scott, J. D., Sherwood, G. D., & Thomas., A. C. (2015). Slow adaptation in the face of rapid warming leads to collapse of the Gulf of Maine cod fishery. Science, 350(6262), 809-812.

Pierrot, D., Neill, C., Sullivan, K., Castle, R., Wanninkhof, R., Lüger, H., Johannessen, T., Olsen, A., Feely, R.A., & Cosca, C. E. (2009). Recommendations for autonomous underway pCO_2 measuring systems and data-reduction routines. Deep Sea Research Part II: Topical Studies in Oceanography, 56(8-10), 512-522.

Rabalais, N. N., Turner, R. E., & Wiseman Jr, W. J. (2002). Gulf of Mexico hypoxia, A.K.A. "The dead zone". Annual Review of ecology and Systematics, 33(1), 235-263.

Rangama, Y., Boutin, J., Etcheto, J., Merlivat, L., Takahashi, T., Delille, B., Frankignoulle, M., & Bakker, D. C. (2005). Variability of the net air–sea CO_2 flux inferred from shipboard and satellite measurements in the Southern Ocean south of Tasmania and New Zealand. Journal of Geophysical Research: Oceans, 110(C9), C09005. doi: 10.1029/2004JC002619.

Reynaud, S., Leclercq, N., Romaine-Lioud, S., Ferrier-Pages, C., Jaubert, J., & Gattuso, J. P. (2003). Interacting effects of CO_2 partial pressure and temperature on photosynthesis and calcification in a scleractinian coral. Global Change Biology, 9(11), 1660-1668.

Robbins, L. L., Wanninkhof, R., Barbero, L., Hu, X., Mitra, S., Yvon-Lewis, S., Cai, W. J., Huang, W. J., & Ryerson, T. (2014). Air-Sea Exchange. In: Benway, H.M., Coble, P.G. (Editors), 2014, Report of the U.S, Gulf of Mexico Carbon Cycle Synthesis Workshop, March 27-28, 2013, Ocean Carbon and Biogeochemistry Program and North American Carbon Program, pp. 17- 23. http://www.us-ocb.org/publications/GMx_report_FINAL.pdf

Sabine, C. L., Feely, R. A., Gruber, N., Key, R. M., Lee, K., Bullister, J. L., Wanninkhof, R., Wong, C. S., Wallace, D. W. R., Tilbrook, B., Millero, F. J., Peng, T., Kozyr, A., Ono, T., & Millero, F. J. (2004). The oceanic sink for anthropogenic CO_2. Science, 305(5682), 367-371.

Sabine, C. 2005. High-resolution ocean and atmosphere pCO_2 time-series measurements. The State of the Ocean and the Ocean Observing System for Climate, Annual Report, Fiscal Year 2004, NOAA/OGP/Office of Climate Observation, Section 3.32a:246-253.

Salisbury, J. E., Vandemark, D., Hunt, C. W., Campbell, J. W., McGillis, W. R., & McDowell, W. H. (2008). Seasonal observations of surface waters in two Gulf of Maine estuary-plume systems: Relationships between watershed attributes, optical measurements and surface pCO_2. Estuarine, Coastal and Shelf Science, 77(2), 245-252.

Salisbury, J.; C. Hunt; A. Mannino (2016). Partial pressure (or fugacity) of carbon dioxide, dissolved inorganic carbon, pH, alkalinity, temperature, salinity and other variables collected from Surface underway, discrete sample and profile observations using Alkalinity titrator, CTD and other instruments from PELICAN in the Coastal Waters of Louisiana, Coastal Waters of Texas and Gulf of Mexico from 2013-09-09 to 2013-09-22 (NCEI Accession 0157461). Version 1.1. NOAA National Centers for Environmental Information. Dataset.

Sarma, V. V. S. S. (2003). Monthly variability in surface pCO_2 and net air-sea CO_2 flux in the Arabian Sea, Journal of Geophysical Research, 108(C8): 3255, doi:10.1029/2001JC001062.

Sarma, V. V. S. S., Saino, T., Sasaoka, K., Nojiri, Y., Ono, T., Ishii, M., Inoue, H. Y., & Matsumoto, K. (2006). Basin-scale pCO_2 distribution using satellite sea surface temperature, Chl a, and climatological salinity in the North Pacific in spring and summer. Global biogeochemical cycles, 20(3), GB3005. doi: 10.1029/2005GB002594.

Sarma, V. V. S. S., Krishna, M. S., Rao, V. D., Viswanadham, R., Kumar, N. A., Kumari, T. R., Gawade, L., Ghatkar, S., & Tari, A. (2012). Sources and sinks of CO_2 in the west coast of Bay of Bengal. Tellus B: Chemical and Physical Meteorology, 64(1), 10961.

Shadwick, E. H., Thomas, H., Comeau, A., Craig, S. E., Hunt, C. W., & Salisbury, J. E. (2010). Air-Sea CO_2 fluxes on the Scotian Shelf: seasonal to multi-annual variability. Biogeosciences, 7(11), 3851-3867.

Signorini, S. R., Mannino, A., Najjar, R. G., Friedrichs, M. A., Cai, W. J., Salisbury, J., Wang, Z. A., Thomas, H., & Shadwick, E. (2013). Surface ocean pCO_2 seasonality and sea-air CO_2 flux estimates for the North American east coast. Journal of Geophysical Research: Oceans, 118(10), 5439-5460.

Solomon, S., Qin, D., Manning, M., Chen, Z., Marquis, M., Averyt, K. B., Tignor, M., & Miller, H. L. (2007). Climate change 2007: the physical science basis. Contribution of Working Group I to the Fourth Assessment Report of the Intergovernmental Panel on Climate Change, Cambridge Univ. Press, New York.

Stephens, M. P., Samuels, G., Olson, D. B., Fine, R. A., & Takahashi, T. (1995). Sea‐air flux of CO_2 in the North Pacific using shipboard and satellite data. Journal of Geophysical Research: Oceans, 100(C7), 13571-13583.

Sullivan, K.; US DOC/NOAA/OAR > Atlantic Oceanographic and Meteorological Laboratory (2017). Partial pressure (or fugacity) of carbon dioxide, temperature, salinity and other variables collected from the coastal surface underway observations using carbon dioxide gas analyzer, shower head equilibrator and other instruments from NOAA Ship Gordon Gunter in the North Atlantic Ocean, US North-East coast and Gulf of Mexico during 2017. http://www.aoml.noaa.gov/ocd/ocdweb/gunter/gunter_introduction.html.

Sun, Q., Tang, D., & Wang, S. (2012). Remote-sensing observations relevant to ocean acidification. International journal of remote sensing, 33(23), 7542-7558.

Sutton, A., C. Sabine, S. Howden, S. Musielewicz, S. Maenner, C. Dietrich, R. Bott, J. Osborne (2012). High-resolution ocean and atmosphere pCO_2 time-series measurements from mooring CoastalMS_88W_30N in the Coastal Waters of Louisiana and Gulf of Mexico from 2009-05-12 to 2015-03-30 (NODC Accession 0100068). Version 5.5. National Oceanographic Data Center, NOAA. Dataset. doi:10.3334/CDIAC/OTG.TSM_COASTALMS_88W_30N.

Takahashi, T., Sutherland, S. C., Sweeney, C., Poisson, A., Metzl, N., Tilbrook, B., Bates, N., Wanninkhof, R., Feely, R. A., Sabine, C., Olafsson, J. & Nojiri Y. (2002). Global sea–air CO_2 flux based on climatological surface ocean pCO_2, and seasonal biological and temperature effects. Deep Sea Research Part II: Topical Studies in Oceanography, 49(9-10), 1601-1622.

Takahashi, T., Sutherland, S. C., Wanninkhof, R., Sweeney, C., Feely, R. A., Chipman, D. W., Hales, B., Friederich, G., Chavez, F., Chris, S., Watson, A. J., Bakker, D., Schuster, U., Metzl, N., Yoshikawa-Inoue, H., Ishii, M., Midorikawa, T., Nojiri, Y., Arne, K., Tobias, S., Hoppeman, M., Olafsson, J., Arnarson, T. S., Tilbrook, B., Johannessen, T., Olsen, A., Bellerby, R., Wong, C. S., Delille, B., Bates, N. R., & Baar, H. (2009). Climatological mean and decadal change in surface ocean pCO_2, and net sea–air CO_2 flux over the global oceans. Deep Sea Research Part II: Topical Studies in Oceanography, 56(8-10), 554-577.

Takahashi, T., Sutherland, S. C., Chipman, D. W., Goddard, J. G., Ho, C., Newberger, T., Sweeney C., & Munro, D. R. (2014). Climatological distributions of pH, pCO_2, total CO_2, alkalinity, and $CaCO_3$ saturation in the global surface ocean, and temporal changes at selected locations. Marine Chemistry, 164, 95-125.

Takahashi, T.; C. Sweeney; S. C. Sutherland (2016a). Partial pressure (or fugacity) of carbon dioxide, salinity and other variables collected from Surface underway observations using Carbon dioxide (CO_2) gas analyzer, Shower head chamber equilibrator for autonomous carbon dioxide (CO_2) measurement and other instruments from Marcus G. Langseth in the Caribbean Sea, Cordell Bank National Marine Sanctuary and others from 2013-02-28 to 2013-06-25 (NCEI Accession 0144355). Version 2.2. NOAA National Centers for Environmental Information. Dataset. doi:10.3334/CDIAC/OTG.VOS_MG_LANGSETH_LINES_2013.

Takahashi, T., S. C. Sutherland and A. Kozyr., (2016b). Global Ocean Surface Water Partial Pressure of CO_2 Database: Measurements Performed During 1957-2015 (Version 2015). ORNL/CDIAC-161, NDP-088(V2015). Carbon Dioxide Information Analysis Center, Oak Ridge National Laboratory, U.S. Department of Energy, Oak Ridge, Tennessee, doi: 10.3334/CDIAC/OTG.NDP088(V2015).

Tao, Z., Qin, B., Li, Z., & Yang, X. (2012). Satellite observations of the partial pressure of carbon dioxide in the surface water of the Huanghai Sea and the Bohai Sea. Acta Oceanologica Sinica, 31(3), 67-73.

Telszewski, M., Chazottes, A., Schuster, U., Watson, A. J., Moulin, C., Bakker, D. C. E., Gonzalez-Davila, M., Johannessen, T., Kortzinger, A., Luger, H., Olsen, A., Omar, A., Padin, X. A., Rıos, A. F., Steinhoff, T., Santana-Casiano, M., Wallace, D. W. R., & Wanninkhof, R. (2009). Estimating the monthly pCO_2 distribution in the North Atlantic using a self-organizing neural network. Biogeosciences, 6, 1405-1421. https://doi.org/10.5194/bg-6-1405-2009.

Thomas, H., Prowe, F. A. E., Lima, I. D., Doney, S. C.,Wanninkhof, R., Greatbatch, R. J., Schuster, U., and Corbière, A., (2008). Changes in the North Atlantic Oscillation influence CO_2 uptake in the North Atlantic over the past 2 decades, Global Biogeochem. Cy. 22(4), GB4027, doi: 10.1029/2007GB003167.

Turk, D., Book, J. W., & McGillis, W. R. (2013). pCO_2 and CO_2 exchange during high bora winds in the Northern Adriatic. Journal of Marine Systems, 117-118, 65-71. https://doi.org/10.1016/j.jmarsys.2013.02.010.

Wang, Y., Huang, J. (2014a). Partial pressure (or fugacity) of carbon dioxide, salinity and other variables collected from Surface underway observations using Carbon dioxide (CO_2) gas analyzer, Shower head chamber equilibrator for autonomous carbon dioxide (CO_2) measurement and other instruments from the USS BOLD in the Gulf of Mexico from 2006-06-06 to 2006-09-11 (NODC Accession 0117493). Version 1.1. National Oceanographic Data Center, NOAA. Dataset. doi:10.3334/CDIAC/OTG.UG_GOM_UW_2006.

Wang, Y., Huang, J. (2014b). Partial pressure (or fugacity) of carbon dioxide, salinity and SEA SURFACE TEMPERATURE collected from Surface underway observations using Carbon dioxide (CO_2) gas analyzer, Shower head chamber equilibrator for autonomous carbon dioxide (CO_2) measurement and other instruments from the USS BOLD in the Gulf of Mexico from 2007-05-02 to 2007-08-24 (NODC Accession 0117500). Version 1.1. National Oceanographic Data Center, NOAA. Dataset. doi:10.3334/CDIAC/OTG.UG_GOM_UW_2007.

Wang, Y., Huang, J. (2014c). Partial pressure (or fugacity) of carbon dioxide, salinity and other variables collected from underway - surface observations using Carbon dioxide (CO_2) gas

analyzer, Shower head chamber equilibrator for autonomous carbon dioxide (CO_2) measurement and other instruments from the CAPE HATTERAS in the Gulf of Mexico from 2009-01-09 to 2010-03-21 (NODC Accession 0115765). Version 1.1. National Oceanographic Data Center, NOAA. Dataset. doi:10.3334/CDIAC/OTG.CAPE_HATTERAS_GM.

Wanninkhof, R.; R. D. Castle; J. Shannahoff (2011a). Partial pressure (or fugacity) of carbon dioxide, salinity and other variables collected from Surface underway observations using Barometric pressure sensor, Carbon dioxide (CO_2) gas analyzer and other instruments from NOAA Ship RONALD H. BROWN in the Caribbean Sea, Coastal Waters of Florida and others from 2003-02-06 to 2003-11-21 (NODC Accession 0081017). Version 3.3. National Oceanographic Data Center, NOAA. Dataset. doi:10.3334/CDIAC/OTG.VOS_RB_2003.

Wanninkhof, R., B. Huss, R. Castle (2011b). Partial pressure (or fugacity) of carbon dioxide, salinity and other variables collected from underway - surface observations using Barometric pressure sensor, Carbon dioxide (CO_2) gas analyzer and other instruments from the EXPLORER OF THE SEAS in the Caribbean Sea, Gulf of Mexico and North Atlantic Ocean from 2003-02-08 to 2004-01-03 (NODC Accession 0081032). Version 3.3. National Oceanographic Data Center, NOAA. Dataset. doi:10.3334/CDIAC/OTG.VOS_EXP2003.

Wanninkhof, R., B. Huss, R. Castle (2011c). Partial pressure (or fugacity) of carbon dioxide, salinity and other variables collected from underway - surface observations using Barometric pressure sensor, Carbon dioxide (CO_2) gas analyzer and other instruments from the EXPLORER OF THE SEAS in the Caribbean Sea, Gulf of Mexico and North Atlantic Ocean from 2004-01-03 to 2005-01-02 (NODC Accession 0081033). Version 3.3. National Oceanographic Data Center, NOAA. Dataset. doi:10.3334/CDIAC/OTG.VOS_EXP2004.

Wanninkhof, R.; R. D. Castle; J. Shannahoff (2011d). Partial pressure (or fugacity) of carbon dioxide, salinity and other variables collected from Surface underway observations using Barometric pressure sensor, Carbon dioxide (CO_2) gas analyzer and other instruments from NOAA Ship RONALD H. BROWN in the Caribbean Sea, Coastal Waters of Florida and others from 2006-02-16 to 2006-12-02 (NODC Accession 0081021). Version 3.3. National Oceanographic Data Center, NOAA. Dataset. doi:10.3334/CDIAC/OTG.VOS_RB_2006.

Wanninkhof, R., B. Huss, R. Castle (2011e). Partial pressure (or fugacity) of carbon dioxide, salinity and other variables collected from underway - surface observations using Barometric pressure sensor, Carbon dioxide (CO_2) gas analyzer and other instruments from the EXPLORER OF THE SEAS in the Bay of Fundy, Caribbean Sea and others from 2006-12-31 to 2007-12-01 (NODC Accession 0081035). Version 3.3. National Oceanographic Data Center, NOAA. Dataset. doi:10.3334/CDIAC/OTG.VOS_EXP2007.

Wanninkhof, R.; R. D. Castle; J. Shannahoff (2011f). Underway pCO_2 and other measurements aboard NOAA Ship Ronald H. Brown during the 2007 cruises (NODC Accession 0081023). Version 4.4. National Oceanographic Data Center, NOAA. Dataset. doi:10.3334/CDIAC/OTG.VOS_RB_2007.

Wanninkhof, R., Park, G. H., Takahashi, T., Sweeney, C., Feely, R. A., Nojiri, Y., Gruber, N., Doney, S. C., McKinley, G. A., Lenton, A., Le Quere, C., Heinze, C., Schwinger, J., Graven, H., & Khatiwala, S. (2013a). Global ocean carbon uptake: magnitude, variability and trends.

Wanninkhof, R.; B. Huss; R. Castle (2013b). Partial pressure (or fugacity) of carbon dioxide, salinity and other variables collected from underway - surface observations using Carbon

dioxide (CO_2) gas analyzer, Shower head chamber equilibrator for autonomous carbon dioxide (CO_2) measurement and other instruments from the EXPLORER OF THE SEAS in the Caribbean Sea, Gulf of Mexico and North Atlantic Ocean from 2002-03-02 to 2002-12-28 (NODC Accession 0108131). Version 1.1. National Oceanographic Data Center, NOAA. Dataset. doi:10.3334/CDIAC/OTG.VOS_EXP2002.

Wanninkhof, R.; B. Huss; R. Castle (2013c). Partial pressure (or fugacity) of carbon dioxide, salinity and other variables collected from underway - surface observations using Barometric pressure sensor, Carbon dioxide (CO_2) gas analyzer and other instruments from the EXPLORER OF THE SEAS in the Caribbean Sea, Gulf of Mexico and North Atlantic Ocean from 2005-01-02 to 2005-12-18 (NODC Accession 0109924). Version 1.1. National Oceanographic Data Center, NOAA. Dataset. doi:10.3334/CDIAC/OTG.VOS_EXP2005.

Wanninkhof, R.; B. Huss; R. Castle (2013d). Partial pressure (or fugacity) of carbon dioxide, salinity and other variables collected from underway - surface observations using Barometric pressure sensor, Carbon dioxide (CO_2) gas analyzer and other instruments from the EXPLORER OF THE SEAS in the Caribbean Sea, Gulf of Mexico and others from 2006-01-15 to 2006-12-24 (NODC Accession 0109925). Version 1.1. National Oceanographic Data Center, NOAA. Dataset. doi:10.3334/CDIAC/OTG.VOS_EXP2006.

Wanninkhof, R.; R. D. Castle; J. Shannahoff (2013e). Partial pressure (or fugacity) of carbon dioxide, salinity and other variables collected from underway - surface observations using Carbon dioxide (CO_2) gas analyzer, Shower head chamber equilibrator for autonomous carbon dioxide (CO_2) measurement and other instruments from NOAA Ship RONALD H. BROWN in the Caribbean Sea, Gulf of Mexico and others from 2009-04-17 to 2009-10-

18 (NODC Accession 0109931). Version 1.1. National Oceanographic Data Center, NOAA. Dataset. doi:10.3334/CDIAC/OTG.VOS_RB_2009

Wanninkhof, R.; R. D. Castle; J. Shannahoff (2013f). Partial pressure (or fugacity) of carbon dioxide, salinity and other variables collected from underway - surface observations using Carbon dioxide (CO_2) gas analyzer, Shower head chamber equilibrator for autonomous carbon dioxide (CO_2) measurement and other instruments from NOAA Ship RONALD H. BROWN in the Gulf of Guinea, Gulf of Mexico, North Atlantic Ocean and South Atlantic Ocean from 2010-03-08 to 2010-12-20 (NODC Accession 0108093). Version 2.2. National Oceanographic Data Center, NOAA. Dataset. doi:10.3334/CDIAC/OTG.VOS_RB_2010

Wanninkhof, R.; R. D. Castle; J. Shannahoff (2013g). Partial pressure (or fugacity) of carbon dioxide, salinity and other variables collected from Surface underway observations using Carbon dioxide (CO_2) gas analyzer, Shower head chamber equilibrator for autonomous carbon dioxide (CO_2) measurement and other instruments from NOAA Ship RONALD H. BROWN in the Coastal Waters of Florida, Florida Keys National Marine Sanctuary and others from 2012-02-15 to 2012-08-27 (NODC Accession 0109926). Version 2.2. National Oceanographic Data Center, NOAA. Dataset. doi:10.3334/CDIAC/OTG.VOS_RB_2012

Wanninkhof, R.; D. Pierrot; K. Sullivan; B. Huss (2014a). Partial pressure (or fugacity) of carbon dioxide, salinity and other variables collected from Surface underway observations using Carbon dioxide (CO_2) gas analyzer, Shower head chamber equilibrator for autonomous carbon dioxide (CO_2) measurement and other instruments from NOAA Ship GORDON GUNTER in the Gulf of Mexico from 2008-04-03 to 2008-11-20. Gordon Gunter website: http://www.aoml.noaa.gov/ocd/ocdweb/gunter/gunter_introduction.html.

Wanninkhof, R.; K. Sullivan; D. Pierrot (2016g). Partial pressure (or fugacity) of carbon dioxide, temperature, salinity and other variables collected from surface underway observations using carbon dioxide gas analyzer, shower head equilibrator and other instruments from M/V Las Cuevas cruises in the Gulf of Mexico and Caribbean Sea from 2009 to 2012. Las Cuevas website: http://www.aoml.noaa.gov/ocd/gcc/lascuevas_introduction.php.

Weiss, R. F. (1974). Carbon dioxide in water and seawater: the solubility of a non-ideal gas, Marine chemistry, 2(3), 203-215. https://doi.org/10.1016/0304-4203(74)90015-2.

Widdicombe, S., & Spicer, J. I. (2008). Predicting the impact of ocean acidification on benthic biodiversity: what can animal physiology tell us? Journal of Experimental Marine Biology and Ecology, 366(1-2), 187-197. https://doi.org/10.1016/j.jembe.2008.07.024.

Xue, L., Cai, W. J., Hu, X., Sabine, C., Jones, S., Sutton, A. J., Jiang, L. Q., & Reimer, J. J. (2016). Sea surface carbon dioxide at the Georgia time series site (2006–2007): Air–sea flux and controlling processes. Progress in Oceanography, 140, 14-26. https://doi.org/10.1016/j.pocean.2015.09.008.

Xue, Z., He, R., Fennel, K., Cai, W. J., Lohrenz, S., Huang, W., & Tian, H. (2014). Modeling pCO_2 variability in the Gulf of Mexico, Biogeosciences Discussions, 11(8): 12673-12695. doi: 10.5194/bgd-11-12673-2014.

Yang, B., Byrne, R. H., & Wanninkhof, R. (2015). Subannual variability of total alkalinity distributions in the northeastern Gulf of Mexico. Journal of Geophysical Research: Oceans, 120(5), 3805-3816.

Zhao, J., Barnes, B., Melo, N., English, D., Lapointe, B., Muller-Karger, F., Schaeffer B., & Hu, C. (2013). Assessment of satellite-derived diffuse attenuation coefficients and euphotic

APPENDIX E:

DOMINANT CONTROLS OF SURFACE OCEAN *P*CO2 IN COASTAL OCEANS: ANALYSIS OF *IN SITU* TIME SERIES DATA

Chen, S., and Hu, C. Dominant controls of surface water pCO_2 in different coastal environments (*prepared*).

Dominant controls of surface water pCO_2 in different coastal environments

Shuangling Chen[1], Chuanmin Hu[1*]

[1] College of Marine Science, University of South Florida, 140 7th Avenue, South, St. Petersburg, Florida, USA 33701

Abstract

Atmospheric pCO_2 has been increasing significantly since global industrialization. Satellite observing systems and new algorithms allow for synoptic estimation of surface pCO_2, which has great advantages in quantifying the air-sea CO_2 flux and understanding ocean acidification. However, most published satellite pCO_2 remote sensing algorithms are quite limited in capturing the interannual variabilities in surface pCO_2 especially in the coastal ocean environments. To improve the capabilities of satellite remote sensing in monitoring surface pCO_2 in such environments, the driving mechanisms of surface pCO_2 over seasonal and interannual time scales need to be well understood. As such, a time series of *in situ* pCO_2 data, and other environmental variables from field or satellite measurements along the coasts of the United States of America and its territories at different latitudes were analyzed by separating the effects of temperature and non-temperature on surface pCO_2. On seasonal time scales, surface pCO_2 tended to be dominated by the temperature effect (pCO_2_T) through sea surface temperature (SST) and wind speed (with exceptions in special environments such as river-dominated) in tropical and subtropical oceanic waters, and tended to be driven by the non-temperature effect (pCO_2_nonT) in temperate zone. On interannual time scales, both atmospheric pCO_2 and surface pCO_2 showed significant increasing trends over short time scales (i.e., < 10 years). In contrast to the seasonal driving mechanisms in

* Corresponding author: huc@usf.edu

surface pCO_2, the interannual variabilities of surface pCO_2 was mainly controlled the non-temperature effect (through air-sea CO_2 exchange via atmospheric pCO_2) in tropical and subtropical waters but by the temperature effect (warming effect of SST) in temperate regions. It was the first time that the driving mechanisms of surface pCO_2 in various coastal ocean environments over both seasonal and interannual time scales were thoroughly examined. This study suggests that, to better capture the seasonal and interannual signals in surface pCO_2 from satellites, atmospheric pCO_2 needs to be considered in the surface pCO_2 remote sensing algorithms. The non-temperature effect on surface pCO_2 especially the biological effects (e.g., algal blooms) need to be further investigated in the future.

Keywords: surface pCO_2, sea surface temperature, Chlorophyll, driving mechanisms, remote sensing

1. Introduction

Since global industrialization, fossil fuel burning and land use change (e.g., deforestation) have projected large amounts of carbon into the atmosphere. Based on the most recent report, in the past decade (2007-2016), there were ~10.7 ±1.2 Gg C yr^{-1} anthropogenic carbon released into the atmosphere, with 4.7 ± 0.1 Gg C yr^{-1} remaining in the atmosphere, 2.4 ± 0.5 Gg C yr^{-1} absorbed by the ocean, and the rest being taken up by the terrestrial biosphere (Le Quéré et al., 2018). As a result, global warming, carbon cycling, and ocean acidification are rapidly becoming pressing concerns for the environmental research community. To better understand the carbon cycling and ocean acidification processes in the rapidly changing world, surface partial pressure of CO_2 (pCO_2) is one of the key parameters to measure and study. Studies show that surface pCO_2 has been increasing with an average rate of ~1.5-1.9 µatm yr^{-1} and variable rates between 1.2 ± 0.5 and 2.1 ± 0.5 µatm yr^{-1} in different ocean basins (Takahashi et al., 2009; 2014). However, these rates are

for the open ocean waters, which is mainly controlled by the large-scale ocean circulations. Yet, little is known about the interannual variabilities of surface pCO_2 in coastal oceans, due to the scarcities of field data measurements and the dynamic and complex biogeochemical and physical processes in coastal regions.

Although the coastal ocean only represents ~7% of the global oceanic area, it accounts for ~50% of the world's net primary production (Muller-Karger et al., 2005). However, due to the inadequate knowledge of CO_2 uptake or release from various ecosystems (i.e., estuaries, salt marshes, coral reefs, and upwelling shelves) in the coastal margins, coastal oceans are still the most controversial regions in balancing the global budget of CO_2 (Chen et al., 2003). For example, Borges (2005) found the coastal oceans behave as a CO_2 sink at high, subtropical, and tropical latitudes, and a CO_2 source at temperate latitudes, while Cai et al. (2006) suggested that the continental shelves serve as a CO_2 sink at middle and high latitudes, and a source of CO_2 at low latitudes. Most of the uncertainties in the quantification of air-sea CO_2 fluxes in the coastal oceans come from the large variations of surface pCO_2 and its lack of spatial and temporal coverages from field data measurements.

In contrast to field data measurements, several recent studies proved the capabilities and advantages of using ocean color satellite remote sensing in monitoring surface pCO_2 in coastal oceans (e.g., Lohrenz and Cai, 2006; Lohrenz et al., 2010 and 2018; Hales et al., 2012; Signorini et al., 2013; Bai et al., 2015). However, two major problems exist in these published pCO_2 remote sensing algorithms. First, large uncertainties exist in most of these satellite-derived surface pCO_2 (i.e., Root Mean Square Error (RMSE) $\geq$ 20 µatm). These large uncertainties are mainly caused by the insufficiency of the defined regression formula in modeling the complex and unknown relationships between surface pCO_2 and related environmental variables. Using multi-variate

second order polynomial regression fit, Chen et al. (2016 and 2017) improved the accuracy in the satellite-derived surface pCO_2 with reduced RMSE of < 12 μatm, but the algorithms were only locally tuned for the West Florida Shelf and northern Gulf of Mexico (GOM), respectively. Second, most of the published pCO_2 remote sensing algorithms were applied for the seasonal variations in surface pCO_2, while few of them were attempted to monitor the interannual changes in surface pCO_2. Recently, Chen et al. (under review) did such analysis for the entire GOM using an unified pCO_2 remote sensing algorithm and found that surface pCO_2 anomalies in the GOM tended to be positive (by ~ 5 μatm) after 2012. This increase in surface pCO_2 is quite smaller comparing to the increasing rate in atmospheric pCO_2. To further verify this result and to increase the capabilities of satellite remote sensing in monitoring surface pCO_2 under anthropogenic forcing, the driving mechanisms in surface pCO_2 over interannual time scales need to be investigated and well understood.

In the open ocean waters, the dominant controls of surface pCO_2 were attempted in several studies on seasonal time scales (Takahashi et al., 2002; Bennington et al., 2009; Fay and McKinley, 2013 and 2017). Specifically, Takahashi et al. (2002) proposed a computational method to decompose the seasonal variation of surface pCO_2 into two parts: one is caused by the temperature effect (pCO_2_T), and the other is caused by the non-temperature effect (pCO_2_nonT). The temperature effect on surface pCO_2 is computed by perturbing the mean annual surface pCO_2 with the difference between the mean and the observed sea surface temperature (SST, ˚C) using Eq. 1, based on the isochemical seawater experiments ($\frac{\partial lnpCO_2}{\partial SST} = 0.0423^o\ C^{-1}$) in Takahashi et al. (1993). That's, a parcel of seawater with an annual mean pCO_2 value was subjected to seasonal temperature changes under isochemical conditions, to determine if changes in the seasonal SST (alone) would change the surface pCO_2. Eq. 2 is the quantification of the non-temperature effect

on surface pCO_2 (pCO_2_nonT), in which the temperature effect is removed from the observed surface pCO_2 by normalizing the observed pCO_2 to a constant annual mean SST. Changes in pCO_2 from this component primarily come from change in total dissolved inorganic carbon (DIC, μmol/kg) and total alkalinity (TA, μmol/kg), and it includes the net consumption of CO_2 by phytoplankton, net TA change due to calcification and nitrate utilization, air-sea exchange of CO_2, and variation of DIC and TA by vertical mixing of subsurface waters or horizontal mixing of different water masses. In the open ocean, the non-temperature effect mainly refers to the net biological effect. Using this method, Takahashi et al. (2002) found that, the seasonal amplitude of surface pCO_2 in high latitudes ($\geq 40^{\circ}$ poleward) and equatorial zones was dominated by the biology effect (which refers to the non-temperature effect, more exactly), and dominated by the temperature effect in the subtropical regions. Similar findings were also shown in Fay & McKinley (2017).

In contrast to the open ocean, because of the dynamic and complex biogeochemical and physical processes in coastal oceans, the driving mechanisms of surface pCO_2 over seasonal time scales could be different from the open oceans even at similar latitudes. However, such knowledge is quite limited in current studies. This study will fill in this research gap towards a better understanding of the driving mechanisms in the seasonal and interannual variations of surface pCO_2, meanwhile it will also facilitate the future development of surface pCO_2 remote sensing algorithms.

$$pCO_2\_T = pCO_{2(annual\ mean)} \times exp[0.0423(SST_{obs}-SST_{mean})] \quad (1)$$

$$pCO_2\_nonT = pCO_{2obs} \times exp[0.0423(SST_{mean}-SST_{obs})] \quad (2)$$

Great efforts have been made to observe surface pCO_2 in the coastal ocean via the global time series observation system (NOAA Pacific Marine Environmental Laboratory (PMEL) moored pCO_2 systems) in the past decade to document the temporal changes in oceanic carbon, although the observing network is still in its infancy. To address the questions described above and to improve the quantification of surface pCO_2 from ocean color remote sensing, the objectives of this study include: 1) Investigate the seasonal and interannual variations of surface pCO_2 in the coastal ocean environments in tropical and subtropical and temperate zones; 2) Quantify the effects of temperature and non-temperature components (pCO_2_T and pCO_2_nonT) on surface pCO_2 and analyze the dominant controls of surface pCO_2 at different latitudes over seasonal and interannual time scales; and 3) Examine the correlations between environmental variables and surface pCO_2 components.

2. Data and methods

2.1. Data

2.1.1. *In situ* data time series

Table 1 provides a summary of the time series observations from buoy systems compiled for this study. The corresponding geolocations of these buoys are shown in Fig. 1. These time series data were collected by the NOAA PMEL carbon program (https://www.pmel.noaa.gov/co2/story/Buoys+and+Autonomous+Systems), and obtained from the NOAA National Centers for Environmental information (NCEI) (https://www.nodc.noaa.gov/ocads/oceans/Moorings/) (Sabine et al., 2010; Cross et al., 2014(a-c); Sutton et al., 2010, 2011, 2013(a-d), 2014(a-b), and 2015). Basically, to assure sufficient temporal coverage, only those buoys that have at least two years' data collection were selected. As a result,

ten buoys (C1-C10, where "C" represents Coastal Ocean) data collected along the coasts of the United States of America and its territories were finally processed. These buoys covered various coastal ocean ecosystems different latitudes. Generally, buoys C1-C5 are located in the tropical and subtropical zones, and buoys C6-C10 are located in the temperate zone. Specifically, buoy C1 and C2 were in coral reef environments, with buoy C1 deployed on the southwestern coast of Puerto Rico and C2 positioned in the Cheeca Rocks, an inshore patch reef within the Florida Keys National Marine Sanctuary; buoy C3 was located in the nearshore region of the Louisiana Shelf, which was greatly affected by the Mississippi River discharge (river discharge rate of ~17,000 m^3 s^{-1}) and river plume with a sea surface salinity (SSS) range of 14.00-35.64, and buoy C6 was deployed in the southwestern coast of the Gulf of Maine at a higher latitude than buoy C3, and it was also affected by river discharge but at a greatly reduced magnitude (river discharge rate of ~0.27 m^3 s^{-1}) with a SSS range of 22.56-33.38 and by strong tidal currents (~2 m s^{-1}); buoy C4 was located in the Gray's Reef National Marine Sanctuary in the subtropical coastal ocean waters at a slightly higher latitude of 31.399 °N than buoy C3, and it represents a general coastal ocean environments (e.g., without coral reef and river discharges); Buoys of C5 and C7 were placed in the coastal upwelling zones at different latitudes; and buoys of C8-C10 were located in the Gulf of Alaska ecosystem, which is seasonally affected by the ice-melt freshwater inputs. In addition, three open ocean buoys (O1-O3, where "O" represents Open Ocean) located in the oligotrophic waters of Atlantic and Pacific were also selected because of their sufficient temporal coverage. Buoys O1 and O2 are in the tropical and subtropical zones, and O3 is in the temperate zone. These three open ocean buoys were mainly used as references for the analysis of the buoy time series data (i.e., buoys C1-C10) in the coastal ocean.

For each of the buoys, both atmospheric and surface pCO_2 were measured with a non-dispersive, infrared analyzer Li-COR™ (model LI-820) (Sabine, 2005; Sutton et al., 2014c). The Li-COR™ data had an accuracy of 2 µatm (or better) and a sampling frequency of every 3 h. Surface pCO_2 data were collected at a water depth of < 1 m, and atmospheric pCO_2 data were collected at 1.2 m above the sea surface. The details of data collection, processing, and quality control can be found in Sabine (2005) and Sutton et al. (2014c). In addition, SST and sea surface salinity (SSS) data were obtained using a CTD (SBE37, MicroCAT C-T Recorder) integrated in the autonomous CO_2 mooring system.

2.2. Satellite data

For each buoy listed in Table 1, a spatial area of 110km (N to S) by 110 km (W to E) covering the buoy location was defined. Correspondingly, standard daily Level-2 ocean color data products at spatial resolution of 1-km (Version R2018.0) from Moderate Resolution Imaging Spectroradiometer (MODIS) Aqua covering the defined area for the time domain of the buoy data (Table 1) were downloaded from NASA Goddard Space Flight Center (http://oceancolor.gsfc.nasa.gov/). These Level-2 data products included ocean color data such as Chlorophyll-a concentration (Chl, mg m^{-3}) and spectral remote sensing reflectance (Rrs, sr^{-1}) at visible bands between 412 and 678 nm. The spectral Rrs data were used to calculate the diffuse attenuation coefficient of downwelling irradiance at 488 nm (K_d, m^{-1}) using the semi-analytical algorithm developed by Lee et al. (2005).

In addition to ocean color data products, global daily wind data products at 10m above the sea surface between 2005 and 2017 were obtained from the NOAA National Centers for Environmental Prediction (NCEP) reanalysis dataset. This reanalysis dataset is a joint product from the NCEP and the National Center for Atmospheric Research (NCAR) with a spatial

resolution of 2.5 degree. These wind data products are wind vectors (in *u* (W to E) and *v* (S to N) directions), and daily wind speed were calculated from the *u* and *v* vectors and then interpolated to the same spatial resolution (i.e., 1-km) as the ocean color data.

2.2. Methods

2.2.1. Data preprocessing

Time and location data from the *in situ* pCO_2 measurements were used to identify the co-located and contemporaneous Chl, K_d, and wind speed data for each of the buoys listed in Table 1. These data, together with the *in situ* time series of SST, SSS, and atmospheric pCO_2, were used as ancillary data for the investigation of the seasonal and interannual variation of surface pCO_2.

To obtain high-quality data, contemporaneous field-measured pCO_2 and MODIS-derived Chl and K_d for each buoy were selected using the following criteria. A time window of ± 6h between field and MODIS measurements was used. Low-quality MODIS data under various non-optimal observing conditions (e.g., atmospheric correction failure, cloud, stray light, sun glint, etc.) were excluded using the NASA standard quality control criteria (Patt et al., 2003; Barnes and Hu, 2015). Valid satellite data within a 3×3 km box centered on the location of each buoy were extracted and averaged (Bailey and Werdell, 2006). To assure the satellite data quality, only if the number of valid pixels in the 3×3 km box was ≥ 5 and its variance was ≤ 10%, the extracted data were used.

Similar to the extraction of Chl and K_d, the wind speed data were also matched for each buoy. Since there was no detailed hour and minute stamps of the daily wind speed data products, valid wind speed data within a 3×3 km box centered on the location of each buoy were extracted and averaged for any daily wind speed data, as long as there was *in situ* pCO_2 measurements on that

day. Again, to assure the matchup data quality, the extracted data were used only if the number of valid pixels in the 3×3 km box was ≥ 5 and its variance was ≤ 10%.

2.2.2. Decomposition of surface pCO_2

Basically, Eqs. 1 and 2 were used to decompose the temperature effect (pCO_2_T) and non-temperature effect (pCO_2_nonT) on surface pCO_2. The pCO_2_T component is derived by disturbing the annual mean of surface pCO_2 with seasonal SST relative to the annual mean SST. The pCO_2_nonT component is calculated by normalizing the observed pCO_2 to a constant annual mean SST, in which the temperature effect was removed from the observed pCO_2.

Therefore, to apply these two equations (Eqs. 1 and 2), two terms are needed: the annual mean of surface pCO_2 and SST. To calculate these two terms for each of the buoys listed in Table 1, all the available *in situ* data in the time domain (from multiple years) of each buoy were used. Specifically, for each buoy, first, the monthly means of surface pCO_2 and SST in each year were calculated from the *in situ* daily measurements; second, the derived monthly means of each year were used to calculate the monthly climatology (i.e., the average of the multi-year monthly means) of surface pCO_2 and SST; and finally, based on the monthly climatology of surface pCO_2 and SST, the annual mean surface pCO_2 and SST were derived. Here, it should be clarified that, the monthly climatology of surface pCO_2 and SST does not mean the real monthly climatology (i.e., over ≥ 30 years), in fact, they are the multi-year average of the monthly means in each year.

With the derived annual mean of surface pCO_2 and SST for each buoy, Eqs. 1 and 2 were applied to the *in situ* data to derive the two components of surface pCO_2: pCO_2_T and pCO_2_nonT. Following the steps described above, the monthly mean of these pCO_2 components in each year,

and their monthly climatology (i.e., multi-year based monthly averages) were also derived for subsequent data analyses.

2.2.3. Statistical analyses

To quantify the seasonal magnitudes of surface pCO_2 and its pCO_2 components, their seasonal maximum and minimum were derived first. Then the seasonal magnitude of surface pCO_2 was computed using Eq. 3, and this seasonal magnitude represents the net seasonal variation of *in situ* surface pCO_2. The seasonal magnitudes of the pCO_2_T and pCO_2_nonT components were also computed similarly using Eqs. 4 and 5, respectively.

$$\Delta pCO_2 = max(pCO_2) - min(pCO_2) \quad (3)$$

$$\Delta pCO_{2\_T} = max(pCO_{2\_T}) - min(pCO_{2\_T}) \quad (4)$$

$$\Delta pCO_{2\_nonT} = max(pCO_{2\_nonT}) - min(pCO_{2\_nonT}) \quad (5)$$

The relative importance (*RI*) of the temperature and non-temperature effects was quantified by normalizing the difference of seasonal magnitudes between pCO_2_T and pCO_2_nonT with the seasonal magnitude of surface pCO_2 based on Eq. 6.

$$RI = (\Delta pCO_{2\_T} - \Delta pCO_{2\_nonT})/\Delta pCO_2 \quad (6)$$

RI is an indictor to tell briefly about which effect dominates the seasonal variations of surface pCO_2. Generally, if *RI* is positive, it means the effect of temperature changes on surface pCO_2 exceeds the effect of the non-temperature (i.e., changes in TA and DIC), suggesting that the temperature effect is a dominant driver of seasonal surface pCO_2, and vice versa. Besides, if *RI* is more close to 1 (-1) at one station comparing to other stations, it means the temperature (non-temperature) effect plays a more important role in modulating the seasonal changes of surface

pCO_2 at that station. In contrast, if *RI* is close to 0, it would suggest that these two compete processes (temperature and non-temperature effects) plays comparable but opposite roles in varying seasonal surface pCO_2, thus they cancel with each other to a large extent.

To further understand the seasonal variations of surface pCO_2 and its driving environmental factors, the correlations between surface pCO_2 (as well as pCO_2_T and pCO_2_nonT) and the environmental variables (i.e., SST, SSS, Chl, K_d, and wind speed) were investigated. The correlations were quantified by Pearson correlation coefficient (*R*) based on the time series data of the monthly anomalies, which were derived by removing the climatological seasonality from the interannual monthly mean. Only if the *p* value was < 0.05, the correlation *R* was considered as a significant correlation.

In addition to the analysis of dominant drivers (i.e., temperature or non-temperature effect) and the corresponding dominant environmental variables in the seasonal variations of surface pCO_2 in different coastal ocean systems, to further understand the driving mechanisms in surface pCO_2 on interannual time scales, the interannual trends (if there is any) over short term time scales (i.e., <10 years) in surface pCO_2, as well as atmospheric pCO_2 and environmental variables (i.e., SST, SSS, Chl, K_d, and wind speed) in these coastal ocean environments were also examined at a confidence level of $\geq 95\%$, based on the their time series data of interannual monthly anomalies.

3. Results

3.1. Seasonal variations of surface pCO_2 and its components

Following the steps described in Section 2.2, the seasonal variations of surface pCO_2 and its components (pCO_2_T and pCO_2_nonT) for each buoy (Table 1) were derived (Figs. 2 and 3), and their seasonal amplitudes were quantified (Table 2). Generally, it was found that, the temperature

effect and non-temperature effect are in opposite phases with 6 months difference. Surface pCO_2 was dominated by the temperature effect in the tropical and subtropical zones, and was dominated by the non-temperature effect in the temperate zone. There are a few exceptions in some special ocean environments (e.g., coral reefs, river-dominated, upwelling-dominated), where surface pCO_2 showed irregular seasonality and both temperature and non-temperature effects play comparable roles in modulating seasonal changes of surface pCO_2.

3.1.1. Tropical and subtropical zones

Fig. 2 shows the seasonal variations of surface pCO_2 and its components (pCO_2_T and pCO_2_nonT) of the buoys located in tropical and subtropical zones. From tropical to subtropical regions, surface pCO_2 showed stronger seasonal signals with high values in summer and low in winter. The seasonality of surface pCO_2 showed variable patterns in coastal oceans because of the particular biogeochemical and physical processes at each station.

In open ocean waters (Fig. 2 and Table 2), surface pCO_2 in the tropical zone (represented by buoy O1 at 22.670 °N) showed very small seasonal variation with an amplitude of 22.22 μatm, corresponding to small changes in seasonal SST (23.7 – 26.5 °C). Similarly, both the temperature and non-temperature components also showed very small seasonal changes with an amplitude of 44.48 μatm and 23.29 μatm, respectively. The seasonal variations of surface pCO_2 mainly follows with the temperature effect (pCO_2_T) with a relative importance factor *RI* of 0.95, suggesting the dominant controls of temperature effect on seasonal surface pCO_2. In the subtropical zone (represented by buoy O2 at 31.780 °N), surface pCO_2 also showed similar but stronger seasonality (seasonal amplitude = 90.68 μatm) comparing to buoy O1, with a *RI* factor of 0.78. That's, the seasonal warming effect also dominates the seasonal variations of surface pCO_2 in the subtropical open ocean waters. At both stations, the non-temperature effect (pCO_2_nonT) is about 6 months

out of phase relative to temperature effect (pCO_2_T). Although this competing non-temperature effect is not a dominant control of the seasonal pCO_2, clearly it does play a role in modulating the overall seasonal changes in surface pCO_2 with a reduced seasonal amplitude than without this effect. These results are consistent with the findings in previous studies (Takahashi et al., 2002; Ullman et al., 2009; Fay and McKinley, 2017).

Comparing to open ocean waters, surface pCO_2 in coastal oceans varied quite differently even at similar latitudes or in the same kind of coastal ecosystems (Fig. 2 and Table 2). But generally, similar to those found in the open ocean waters, pCO_2_T and pCO_2_nonT are ~6 months out of phase, and surface pCO_2 is also primarily dominated by pCO_2_T in coastal regions except for special coastal environments (e.g., coral reefs, river-dominated, upwelling-dominated). For example, station C4 is located in a common coastal environment (i.e., with little river inputs, without upwelling, no coral reefs). As a result, surface pCO_2 at station C4 followed closely with pCO_2_T in phase with high pCO_2 in winter and low in summer, indicating that surface pCO_2 is mainly controlled by SST over seasonal time scales. In fact, the overall seasonal variations of surface pCO_2 and its components at buoy C4 is quite similar to those of buoy O2 in the subtropical open ocean waters with the same relative importance factor *RI* of 0.78. The major difference between the two is that, surface pCO_2 at buoy C4 had a larger seasonal amplitude (154.37 μatm at C4 *vs.* 90.68 μatm at O2) because of the active oceanic process in coastal oceans.

In the coral reef coastal environments (represented by buoy C1 and C2), surface pCO_2 could show quite different seasonal variations from that in tropical and subtropical oceanic waters. It is found that, surface pCO_2 was mainly dominated by pCO_2_T at site C1 (in tropical zone), while it was mainly dominated by pCO_2_nonT at site C2 (in subtropical zone). Specifically, at site C1, surface pCO_2 had a seasonal amplitude of 60.26 μatm, and a relative importance factor *RI* of 0.63. The

overall seasonal changes of surface pCO_2 was closely in phase with the pCO_2_T, suggesting the dominant controls of the temperature effect in affecting seasonal surface pCO_2. This result is consistent with the published studies for the same coral reef environment (Gray et al., 2012). In contrast, at site C2, the seasonal variation of surface pCO_2 follows the change of pCO_2_nonT closely, with a larger seasonal amplitude of 227.94 μatm than that at buoy C1 and a negative relative importance factor *RI* of -0.53. That's, instead of being dominated by pCO_2_T, the seasonal variation of surface pCO_2 at site C2 is mainly controlled by the non-temperature effect.

In the river-dominated coastal environment (represented by buoy C3), Surface pCO_2 showed irregular and complex seasonal variations as expected. From January to September, surface pCO_2 tended to be dominated by pCO_2_nonT, and October and December, it tended to be mainly affected by pCO_2_T. The two competing effects of pCO_2_T and pCO_2_nonT resulted in a seasonal amplitude of surface pCO_2 of 114.88 μatm in this coastal environment. The relative importance factor *RI* was -0.05, suggesting that the temperature and non-temperature effects played comparable roles in affecting the overall seasonality of surface pCO_2.

In the coastal upwelling ecosystem (represented by buoy C5), Surface pCO_2 varies from high to low from spring to fall, and this variation was coupled in phase with the pCO_2_nonT with the relative importance factor *RI* of -0.90, suggesting the non-temperature effect was the major control of the seasonal surface pCO_2.

3.1.2. Temperate zone

Fig. 3 is the seasonal variations of surface pCO_2 and its components (pCO_2_T and pCO_2_nonT) of the buoys in temperate zones. Similar to the findings in tropical and subtropical zones, the temperature effect and non-temperature were also ~6 months out of phase with each other,

suggesting their competing roles in varying seasonal surface pCO_2. However, in contrast to the results in tropical and subtropical zones, the seasonality of surface pCO_2 was found to be dominated by the non-temperature effect in the temperate zone with a few exceptions in special ocean environments where surface pCO_2 showed irregular seasonal patterns.

In the open ocean waters (represented by buoy O3, Fig. 3 and Table 2), surface pCO_2 did not show clear seasonality from winter to summer (e.g., no obvious sinusoidal variation patterns). As to its pCO_2 components, both pCO_2_T and pCO_2_nonT showed strong and comparable seasonal amplitudes (seasonal amplitude of pCO_2_T = 127.21 μatm, and seasonal amplitude of pCO_2_nonT = 125.71 μatm) but in the opposite phase. Most likely, the two competing effects partially cancel with each other to a large extent on seasonal scales, thus leading to little seasonal changes in surface pCO_2. In this oceanic environment, both the temperature and non-temperature effects play important roles in affecting surface pCO_2, with a relative importance factor *RI* of 0.07. Based on the pCO_2 data collected from the Weather Station "P" (50° N, 145° W, which is ~23 km from buoy O3) in 1972-1975 by Wong and Chan (1991), Takahashi et al. (2002) also found similar seasonal variation patterns in surface pCO_2 and its components, but with some difference in the seasonal amplitude of surface pCO_2 (i.e., surface pCO_2 amplitude = 20 μatm in this study, and surface pCO_2 amplitude = 50 μatm in Takahashi et al. (2002)). Since the statistics in Takahashi et al. (2002) was based on data collected in 1972-1975, and the present study is based on data collected in 2007-2015, the ocean environment could have changed within > 30 years with the increase of anthropogenic atmospheric pCO_2.

In the coastal ocean waters (Fig. 3 and Table 2), surface pCO_2 showed low values in spring and summer and high values in winter time at most stations, with some difference in the seasonal patterns from station to station. Specifically, in the river-dominated region at buoy C6, although

surface pCO_2 reached a minimum in spring and a maximum in winter, similar to the surface pCO_2 at buoy C3 (around the Mississippi delta), it showed some finer irregular seasonal patterns (e.g., a sub-maximum in August). In details, surface pCO_2 was in phase with pCO_2_T between April and August, while it was in couple with the variation of pCO_2_nonT in other months. These two competing effects of pCO_2_T and pCO_2_nonT resulted in a seasonal amplitude of surface pCO_2 138.22 μatm and a relative importance factor *RI* of 0.29, suggesting that the temperature effect plays a relatively more dominant role in controlling the seasonal variation of surface pCO_2 than at station C3 (where *RI* = -0.05). This is reasonable because the river discharge at this station was way-less than that at station C3 (i.e., 17,000 $m^3 s^{-1}$ *vs.* 0.27 $m^3 s^{-1}$).

In the coastal upwelling ecosystem, similar to the pCO_2 in the subtropical upwelling system at site C5, surface pCO_2 at site C7 also followed closely with the pCO_2_nonT in phase, with a relative important factor *RI* of -0.76, suggesting the non-temperature effect is the major control of the seasonal surface pCO_2. However, the seasonal variation patterns of surface pCO_2 is quite different from that at C5. Here at C7, surface pCO_2 reached a minimum in summer and maximum in winter. The different seasonal variation patterns of surface pCO_2 in these two upwelling systems were mainly attributed to the difference of the balance between the biological uptake of CO_2 and upwelling enrichment of CO2, and was discussed in Section 4.1.

In the coastal regions with seasonal ice melting, represented by buoy C8-C10 in the Gulf of Alaska ecosystems, it was found that surface pCO_2 showed strong seasonal amplitude of 309.81 μatm, 279.42 μatm, and 168.28 μatm, at station C8, C9, and C10, respectively. The seasonal pCO_2 varies in couple with pCO_2_nonT closely in phase, which suggests the dominant control of the non-temperature effect over the temperature effect in surface pCO_2 over seasonal time scales in these coastal environments. This result is quite different from the findings in the temperate open ocean

waters (represented by buoy O3), where the two competing effects both dominated the seasonal variations of surface pCO_2, leading to little seasonality in surface pCO_2. With the increase of latitude from buoy C8 to buoy C10, the relative importance of the non-temperature effect seems to increase with the relative important factor *RI* of -0.77, -0.80, and -0.84, for buoy C8, C9, and C10, respectively.

3.2. Interannual variations of surface pCO_2

In addition to the seasonal variabilities, we also examined the interannual variabilities of surface pCO_2 as well as atmospheric pCO_2 for each buoy in Table 1, with results shown in Figs. 4 and 5, and Table 3. The interannual variabilities of the surface pCO_2 components (pCO_2 _T and pCO_2 _nonT) were also quantified to help find the dominant controls of the interannual changes in surface pCO_2. Due to the data limitation, the interannual trends analyzed here mainly refers to the short-term (3-10 years) trend, which may differ from the long-term (i.e., > 30 years) trend signals. In general, both atmospheric pCO_2 and surface pCO_2 and its components showed interannual variation trends in most sites (with exceptions in some special environments) selected in this study. It was found that, the interannual variabilities in surface pCO_2 was mainly dominated by the non-temperature effect in tropical and subtropical zones, and was mainly controlled by the temperature effect in the temperate zone.

3.2.1. Tropical and subtropical zones

Fig. 4 is the interannual variations of surface pCO_2 and atmospheric pCO_2 of the buoys located in tropical and subtropical zones. Generally, atmospheric pCO_2 showed significant increasing rates (i.e., 1.20~3.60 μatm yr^{-1} at $p < 0.05$) in all buoy stations. However, the corresponding surface pCO_2 showed variable interannual signals in different ocean environments.

In the open ocean waters from tropical (represented by buoy O1) to subtropical zone (represented by buoy O2) (Fig. 4 and Table 3), atmospheric pCO_2 showed clear interannual increase with a rate of 1.20 μatm yr^{-1} and 1.94 μatm yr^{-1} (at $p < 0.05$) over a short-term time scale of 2007-2015 and 2005-2007 at buoy O1 and O2, respectively. Correspondingly, surface pCO_2 also showed significant interannual increase with a rate of 2.77 μatm yr^{-1} and 5.76 μatm yr^{-1} (at $p < 0.05$). It is found that, the increase in surface pCO_2 was mainly resulted from the increase of the pCO_2_nonT (i.e., the interannual trend of pCO_2_nonT is greater than that of pCO_2_T, see Table 3). However, we did not find any strong and significant interannual trend in SST, SSS, and wind speed. While considering the significance of the stable increase of the interannual atmospheric pCO_2, we believe that the dominant control of the non-temperature effect in the interannual trend of surface pCO_2 is most likely attributed to continuous sink of CO_2 from air to the surface ocean waters over interannual time scales under anthropogenic forcing. On the other hand, although the increase rate of surface pCO_2 in subtropical zone is statistically over doubled than that in tropical zone, the interannual trend of surface pCO_2 in subtropical zone was only based on 3 years' data (i.e., 2005-2007). More data over longer time series are needed to verify this finding (see discussion in Section 4.2).

In the coastal ocean waters at different latitudes (buoy C1-C5 in Fig. 4 and Table 3), atmospheric pCO_2 all showed clear interannual trend at an increasing rate of 1.69-3.60 μatm yr^{-1} (at $p < 0.05$) over a short-term scale (3-10 years). However, the interannual surface pCO_2 varied from region to region. Nevertheless, In the coastal environment without coral reefs and river discharges (represented by site C4), surface pCO_2 did show significant interannual trend at an increasing rate of 2.97 μatm yr^{-1} (at $p < 0.05$), and most of this interannual variability came from the pCO_2_nonT component (i.e., the interannual trend of pCO_2_nonT = 3.44 μatm yr^{-1}, and the interannual trend

of pCO_2_T = -0.97 µatm yr^{-1}, see Table 3), suggesting that the non-temperature effect is the dominant control of surface pCO_2 over interannual time scale. Interestingly, the surface pCO_2 actually showed two interannual signals with a clear increase before 2012 (i.e., 2006-2012) and a clear decrease after 2012 (2012-2015). Yet more data are needed to further verify this phenomenon (See discussion in Section 4.2).

In the coral reef environments (represented by buoy C1 in tropical zone and C2 in subtropical zone), surface pCO_2 and its components did not show any significant trend over years of 2009-2015 in the tropical zone. While in the subtropical zone, surface pCO_2 showed a significant increasing trend of 11.44 µatm yr^{-1} (at $p < 0.05$) over the period of 2010-2015. This interannual variabilities were found to be mainly dominated by the non-temperature effect pCO_2_nonT (see Table 3).

In the river-dominated coastal environment (represented by buoy C3), no significant trend were found in surface pCO_2 as well as its temperature and non-temperature components (i.e., pCO_2_T and pCO_2_nonT). In fact, there is only a few months' data available over the period of 2009-2014. Therefore, the results derived here may not be representative for the real situation, and more data are needed for further examination (see discussion in Section 4.2).

In the coastal upwelling environment (represented by buoy C5), surface pCO_2 showed large interannual variability mostly within ± 50 µatm but without clear interannual trend over the period of 2010-2015. However, significant and comparable interannual trends were found in both pCO_2_T (rate = 8.17 µatm yr^{-1}) and pCO_2_nonT (rate = -8.13 µatm yr^{-1}) in opposite directions. Thus it seems these two competing effects canceled with each other to a large extent over interannual time scales, resulting in little interannual variabilities in surface pCO_2. It is noticed that surface pCO_2 seems to show an increase in the period of 201-2012 and a decrease over the years

of 2012-2013, but the data was very noisy and more data over longer time series are required to further analysis (see discussion in Section 4.2).

3.2.2. Temperate zone

Fig. 5 is the interannual variations of surface pCO_2 and atmospheric pCO_2 of the buoys located in temperate zone. Again, atmospheric pCO_2 were found to be increasing with significant increasing rates (i.e., 1.20~3.60 μatm yr^{-1} at $p < 0.05$) in all buoy stations, and the corresponding surface pCO_2 also showed significant increase except a few special ocean environments.

In the open ocean waters (represented by buoy O3, Fig. 5 and Table 3), surface pCO_2 showed slight but insignificant increasing trend (0.57 μatm yr^{-1}). However, the two competing components of pCO_2 _T and pCO_2 _nonT did show significant but opposite trends with a rate of 5.38 μatm yr^{-1} and -4.60 μatm yr^{-1}, respectively. Thus it seems that these two competing components canceled with each other to a large extent, leading to little interannual trend in surface pCO_2, and statistically the slight interannual increase was mainly attributed to the temperature effect.

In the river-dominated coastal environment (represented by buoy C6, Fig. 5 and Table 3), similar to the results found in subtropical zone (i.e., C3), there was no significant trends shown in surface pCO_2 as well as its temperature and non-temperature components (pCO_2 _T and pCO_2 _nonT). However, different from buoy C3, here the statistics were based on data collected from each month over 9 years (i.e., 2006-2014), so there should not be large uncertainties in the derived surface pCO_2 anomalies. Considering the dynamics of river discharges to such coastal ocean environment, it seems that, the interannual variabilities of surface pCO_2 in this coastal environment was mainly driven by the river discharges, despite of the anthropogenic forcing of the pCO_2 increase in the atmosphere.

In the coastal upwelling environment (represented by buoy C7, Fig. 5 and Table 3), in contrast to the phenomenon at buoy C5, surface pCO_2 here showed a significant decrease with a rate of -5.69 μatm yr^{-1} over the years of 2006-2015, despite of the interannual increase in atmospheric pCO_2. Meanwhile, both pCO_2_T and pCO_2_nonT showed significant trends with an increase rate of 2.32 μatm yr^{-1} and a decrease rate of -7.98 μatm yr^{-1}, respectively, suggesting that the non-temperature effect is the dominant control of surface pCO_2 on interannual time scales.

In the coastal regions with seasonal ice melting (represented by buoy C8-C10, Fig. 5 and Table 3), surface pCO_2 all showed significant increasing trends at variable rates of 24.97 μatm yr^{-1}, 10.68 μatm yr^{-1}, and 5.37 μatm yr^{-1}, at sites C8, C9, and C10, respectively. At site C8, the statistics was based on data in 2013-2016, it is found that, both pCO_2 _T and pCO_2 _nonT showed positive interannual increase with a rate of 6.54 μatm yr^{-1}, and 15.56 μatm yr^{-1}, respectively, but the increase of pCO_2 _nonT was insignificant (i.e., $p > 0.05$). Therefore, the extremely high increasing trend in surface pCO_2 at site C8 is skeptical. Considering the significance of the interannual increase of pCO_2_T, we believe the increase in surface pCO_2 was mainly controlled by the temperature effect (see discussion in Section 4.2). Similarly, it was found that the significant interannual increases of surface pCO_2 at sites C9 and C10 were mainly attributed to the significant increase in pCO_2_T, suggesting the dominant control of the temperature effect in the interannual surface pCO_2 in these coastal ocean environments (see discussion in Section 4.2).

4. Discussion

4.1. Driving mechanisms in seasonal surface pCO_2

As shown in Section 3.1, over seasonal time scales, surface pCO_2 was found to be mainly driven by the temperature effect in tropical and subtropical zones and was mainly controlled by the non-

temperature effect in the temperate zone with exceptions in a few special environments (e.g., coral reefs, river-dominated, upwelling-dominated). It was easy to understand the temperature effect was mainly related to SST and environmental variables that are closely related to SST such as wind speed. While for the non-temperature effect, it is not clear that which environmental variable is important in modulating this effect.

In fact, the non-temperature effect is the overall effect of biological activities (e.g., net CO_2 utilization, net TA change due to carbonate production and nitrate utilization), ocean mixing between different water masses that are characterized by different carbonate properties (i.e., changes in DIC and TA), and air-sea CO_2 fluxes. Yet it is very difficult to separate and quantify each of these non-temperature effect because of the interactions among them. Therefore, to help better understand the dominant environmental variables in affecting the non-temperature effect on surface pCO_2 over seasonal time scales and to improve the accuracy of satellite remote sensing of surface pCO_2, various environmental variables were used as proxies of different biogeochemical and physical processes in affecting surface pCO_2. Specifically, optical parameters such as Chl and K_d are used as proxies of the biological productivities, atmospheric pCO_2 and wind speed are used to approximate the effect of the air-sea CO_2 exchange, SST, SSS, and wind speed are used as to indicate the effect of ocean mixing. The correlations between these environmental variables and surface pCO_2 as well as its components (pCO_2_T and pCO_2_nonT) were analyzed in details (Table 4).

In the tropical and subtropical ocean waters, surface pCO_2 was mainly dominated by the temperature component pCO_2_T (i.e., buoy O1-O2, C1, and C4, see Section 3.1.1), and strong correlations (i.e., $R > 0.9$) between pCO_2_T and SST were found with consistence (Table 4). Correspondingly, wind speed also showed significant negative correlations with pCO_2_T in these

ocean environments, suggesting wind-driven ocean mixing plays a role in modulating pCO_2_T and thus surface pco2. It should be clarified that, the dominant control of temperature effect does mean the unimportance of the non-temperature effect. In fact, both effects are important in modulating the overall seasonal variation of surface pCO_2. In these ocean environments, significant correlations were found between pCO_2_nonT and atmospheric pCO_2, suggesting the contribution of the air-sea CO_2 fluxes to the seasonal variations of pCO_2_nonT, and thus surface pCO_2.

In the temperate ocean waters, surface pCO_2 was mainly driven by the non-temperature effect pCO_2_nonT (i.e., buoy C7-C10, see Section 3.1.2). However, the non-temperature effect refers to different oceanic processes in different ocean environments. For example, the non-temperature effect mainly refers to upwelling at station C7, while it mainly refers to the seasonal ice-melting and mixing between the freshwater and oceanic waters at stations C8-C10. Specifically, for the buoys (i.e., C8-C10) located in the Gulf of Alaska which is affected by seasonal ice-melting, SSS can be < 20 (see Table 1). However, we did not find any significant correlations between pCO_2_nonT and SSS except at station C9 (R = -0.43). Because of the cold water characteristic of the ice-melting freshwater, we did find significant negative correlations found between pCO_2_nonT and SST. In the open ocean waters (represented by buoy O3), both pCO_2_T and pCO_2_nonT play comparable but competing roles in modulating seasonal surface pCO_2 (see Section 3.1.2). For this ocean environment, pCO_2_nonT showed strong correlations with SST, SSS, and wind speed, with R of -0.88, 0.66, and 0.31, respectively, suggesting the effect of ocean mixing on the non-temperature effect of surface pCO_2. In addition, pCO_2_nonT also showed significant correlations with atmospheric pCO_2, thus the air-sea CO_2 fluxes also contributed to the seasonal variations of pCO_2_nonT and thus surface pCO_2. On the other hand, SST, SSS and wind speed also showed strong correlations with pCO_2_T but in the opposite directions as with pCO_2_nonT,

with R of 0.99, -0.67, and -0.28, indicating the effect of ocean mixing as well as thermodynamics on the temperature effect of surface pCO_2.

However, as shown in Section 3.1.1, there are a few special coastal ocean environments are found to have irregular seasonal signals in surface pCO_2. In the coral reef environment at buoy C2, the non-temperature effect (pCO_2_nonT) dominated the seasonal surface pCO_2 (RI = -0.53). As a result, pCO_2_nonT showed a significant negative correlation (R = -0.31) with SSS and significant positive correlation (R = 0.16) with wind speed (Table 4), suggesting that the effect of ocean mixing on the carbonate properties (e.g., TA and DIC). Meanwhile, atmospheric pCO_2 also showed a significant positive correlation (R = 0.37) with pCO_2_nonT, indicating the contribution of air-sea CO_2 fluxes to the non-temperature pCO_2 component (pCO_2_nonT). In fact, this effect is also visible in Fig. 2 for station C2, where the seasonal pCO_2_nonT co-varies with the seasonal atmospheric pCO_2 to some extent.

In the river-dominated regions in both subtropical zone (C3) and temperate zone (C6), surface pCO_2 was found to be dominant by the temperature effect in summertime and by the non-temperature effect in other seasons. However, there is some difference between the two, as C3 is affected by large river discharges (i.e., 17,000 $m^3 s^{-1}$) while C6 is affected by small river discharge (i.e., ~0.27 $m^3 s^{-1}$) but strong tidal mixing (i.e, ~ 2 m s^{-1}). Both freshwater inputs and strong ocean mixing would affect the non-temperature pCO_2 component (pCO_2_nonT), as these two processes would bring DIC and nutrient enriched waters to the ocean surface. Indeed, as a good indicator of these processes, SSS showed significant positive correlations (R = 0.42 at C3, and R = 0.23 at C6) with pCO_2_nonT at both stations. Meanwhile, significant correlations were also found between the biological proxies (i.e., Chl and K_d) and pCO_2_nonT at site C6 (Table 4), suggesting the biological uptake of CO_2 also has an effect on the non-temperature pCO_2 component. However,

negative but insignificant correlations were found between biological proxies and pCO_2_nonT at site C3. Considering the data quantity (N = 19) used in the correlation statistics, more data are needed for further verification. On the other hand, the mixing between freshwater and open ocean waters and the tidal mixing typically would bring colder waters to the ocean surface, and this would also affect the surface ocean temperature. As a result, strong negative correlations (R = -0.92 at C3, and R = -0.61 at C6) were found between pCO_2_nonT and SST at both river-dominated regions.

In the upwelling-dominated regions in both subtropical zone (i.e., C5) and temperate zone (i.e., C7), surface pCO_2 was found to be dominant by the non-temperature effect (see Section 3.1). However, the seasonal patterns are quite different between the two regions, as surface pCO_2 varied from high to low from spring to fall at C5, but from high to low from winter to summer at C7 (see Figs. 2 and 3). Upwelling along the U.S. western coast in spring and summer brings lots of CO_2 and nutrient enriched waters to the surface of these oceanic systems (e.g., Renault et al., 2016), which would enhance the growth of phytoplankton. It's found that the intensities of the biological uptake of nutrient and CO_2 is much stronger at station C7 (i.e, peak Chl > 5 mg m^{-3}) than at station C5 (i.e., peak Chl < 2.5 mg m^{-3}) especially in spring. Thus, the competing processes of addition of CO_2 through upwelling and the biological drawdown of CO_2 via phytoplankton uptake finally leads to a net pCO_2 increase in spring at station C5. However, we did not find any significant correlations between the biological proxies (i.e., Chl and K_d) and pCO_2_nonT. Considering the large uncertainties (~30%) in the satellite derived Chl and K_d, the signal to noise ratio could be very low after removing the seasonality in these parameters, making it difficult to detect the correlations between these parameters with pCO_2_nonT. On the other hand, the upwelling waters

are typically characterized as cold water, correspondingly, strong negative correlations were found between pCO_2_nonT and SST (R = -0.70 at C5 and R = -0.57 at C7, at $p < 0.05$).

4.2. Driving mechanisms in interannual surface pCO_2

To further examine the dominant controls of surface pCO_2 over interannual time scales, the interannual variations of the environmental variables (e.g., SST, SSS, and wind speed, atmospheric pCO_2) for each buoy in Table 1 were also processed and analyzed (Table 3). Specifically, SST is used as a proxy of the temperature effect (pCO_2_T), and SSS, wind speed, and atmospheric pCO_2 were used as proxies of the non-temperature effect (pCO_2_nonT). It should be clarified that Chl and K_d were not used in this analysis mainly because of the data scarcities and large uncertainties of these data in the study period of each buoy.

In the tropical and subtropical zones, the interannual surface pCO_2 was found to be mainly dominated by the non-temperature effect with exceptions in special ocean environments (e.g., river-dominated, upwelling-dominated) (see Section 3.2). However, the interannual anomalies of SSS and Wind speed did not show clear signals in most stations, suggesting that there was little change in the physical ocean environments (e.g., ocean mixing). In contrast, the atmospheric pCO_2 all showed clear interannual increase for all the buoys located in the tropical and subtropical zones. Therefore, it is most likely that, the dominant control of non-temperature effect on the interannual increase of surface pCO_2 was mainly caused by the interannual changes in the air-sea CO_2 flux. The air-sea CO_2 flux mainly depends on the CO_2 gas solubility which is related to SST, the gas transfer velocity which is related to wind speed, and the relative difference between the atmospheric pCO_2 and surface pCO_2 (e.g., Borges et al., 2005; Takahashi et al., 2009; Wanninkhof et al., 2013). Since there is little changes in both SST and wind speed (buoys O1-O2 and C1-C5, see Table 3), it is most likely that the interannual increase in surface pCO_2 was mainly driven by

the atmospheric pCO_2. Yet, it still could be possible that Chl and K_d may have some interannual signals that dominates the non-temperature effect on surface pCO_2. However, a recent study by Chen et al. (prepared) did not find any interannual trend in both Chl and K_d in the different regions of the Gulf of Mexico. Further studies need to be conducted for a clear interpretation of this non-temperature effect.

In the temperate zone, surface pCO_2 was found to be mainly controlled by the temperature effect over interannual time scales with some exceptions in special ocean environments (e.g., river-dominated, upwelling-dominated) (see Section 3.2). Interestingly, although SST did not show clear interannual patterns in tropical and subtropical zones, it did show significant interannual trends with variable increasing rates between 0.17 and 0.65 $^{\circ}C\ yr^{-1}$ in the temperate zone. This finding confirmed the dominant warming effects on surface pCO_2 over short-term interannual time scales in the temperate zone, despite of the leading control of the non-temperature effect on the seasonal changes of surface pCO_2 in this region.

In the river-dominated regions (represented by buoy C3 and C6), surface pCO_2 did not show clear and significant interannual trends as presented in Figs. 4 and 5. At station C3, SSS showed a significant decrease with a rate of -0.46 yr^{-1} over the period of 2009-2014, while at station C6, SSS showed a significant but slight increase with a rate of 0.09 yr^{-1} over the period of 2006-2014. Therefore, it seems the insignificant increase (decrease) trend in surface pCO_2 at station C3 (C6) was mainly caused by interannual decrease (increase) in SSS. Still, further investigation is needed with more *in situ* time series data available.

In the upwelling-dominated regions (represented by buoy C5 and C7), surface pCO_2 showed decrease over interannual time scales at both C5 (-0.28 µatm yr^{-1}, at $p > 0.05$) and C7 (-5.69 28 µatm yr^{-1}, at $p < 0.05$). At both stations, SST and SSS showed significant interannual trends, while

no significant interannual signal was found in the wind speed. It is suspected that, the strong biological uptake of CO_2 with the sufficient supply of nutrients from upwelling may exceed the enrichment of CO_2 from subsurface over interannual time scales, and the difference between the two is getting stronger over years. Still, more ancillary data over long time series are required to further investigation.

4.3. Implication and future improvements

Based on the buoy data time series located in various oceanic ecosystems, the seasonal and interannual variations of surface pCO_2 were investigated in this study. We found that, over seasonal time scales, surface pCO_2 was mostly driven by the temperature effect in tropical and subtropical zones and was mainly dominated by the non-temperature effect in temperate zones; and over interannual time scales, surface pCO_2 was mainly controlled by the non-temperature effect in the tropical and subtropical zones and was mainly driven by the temperature effect in the temperate zone. Specifically, for the non-temperature effect either over seasonal or interannual time scales, the effects of ocean mixing and air-sea CO_2 fluxes are expressed well by the environmental proxies (e.g., SST, SSS, and wind speed). It is found that, atmospheric pCO_2 is an important parameter in driving both seasonal and interannual surface pCO_2 at most buoy stations in this study. However, this factor was not included in most of the published surface pCO_2 satellite remote sensing algorithms. Thus it should be why these developed pCO_2 remote sensing algorithms are most limited in capturing the interannual variabilities in surface pCO_2.

Although the general seasonal and interannual variations patterns in surface pCO_2 and its dominant controls of the temperature or non-temperature effects as well as the dominant environmental variables were found, future improvements are still needed to increase the accuracy of satellite mapping of surface pCO_2.

Specifically, in the coastal oceans, the biological activities are known to be active and it is thought to be an important process in modulating surface pCO_2 (Norman et al., 2013; Ikawa et al., 2013; Huang et al., 2015). However, due to the data insufficiencies of both the field and concurrent satellite measurements, no significant correlations were found between surface pCO_2 and the satellite-based optical parameters (i.e., Chl, K_d) for most coastal ocean buoys. It is possible that the biological proxies may vary on different time scales from that of the surface pCO_2. This is not an unreasonable possibility, considering the complexities of the biological processes (i.e., photosynthesis, respiration, and calcification) in modulating surface pCO_2. In the future, instead of using limited satellite-based Chl and K_d data, *in situ* time series of the biological proxies (i.e., dissolved oxygen, apparent oxygen utilization, nutrients, Chl fluorescence, and K_d) should be measured together with surface pCO_2 for a better understanding of the biological role in changing surface pCO_2. More importantly, the algal bloom effect on surface pCO_2 needs to be thoroughly investigated by examining the pCO_2 variations before, during, and after an algal bloom.

In terms of interannual variations of surface pCO_2, the current analyses were based on 3-10 years of time series data, therefore, the derived short-term interannual variabilities may not be representative of a long-term (i.e., > 30 years) trend. Besides, the analyses were based on data collected over different time periods. From Figs. 4 and 5, it seems the interannual variation rate of surface pCO_2 changes over different study periods. For example, at station C4, the surface pCO_2 seems to be increasing between 2006 and 2012 but seems to be decreasing between 2012 and 2015. Therefore, to better quantify the interannual variabilities in surface pCO_2, more time series data are needed. Furthermore, it is found that non-temperature effect (pCO_2_nonT) dominates the interannual changes of surface pCO_2 in most cases, with a much higher rate than the increase of atmospheric pCO_2. To further differentiate the effects of air-sea CO_2 change, biological effects,

and vertical mixing, and quantify the role of each process in the interannual variations of surface pCO_2, long term field-measured biological data (i.e., oxygen, nutrients, Chl, and K_d) and physical data (i.e., mixed layer depth, and wind speed) are needed.

Last, but not least, for similar types of coastal environments (i.e., coral reef, river-dominated, and upwelling) the dominant control of surface pCO_2 varies, due to the different environmental characteristics (e.g., the strength of river discharges and tidal mixing) in each system at different latitudes. To further interpret the difference in surface pCO_2 in the same type of coastal environment, more ancillary data are also needed to better characterize the carbonate process in each coastal ecosystem.

5. Conclusion

Using both *in situ* time series data and satellite data at different latitudes along the coasts of the U. S. and its territories, the dominant controls and driving mechanisms of surface pCO_2 on seasonal and short-term interannual time scales were quantified and analyzed. The temperature (non-temperature) effect was found to be dominant in modulating the seasonal pCO_2 variations in the tropical and subtropical zones (temperate zone) and the interannual pCO_2 variations in the temperate zone (tropical and subtropical zones), with exceptions in a few special coastal ocean environments (e.g., coral reefs, river-dominated, upwelling-dominated). The study also suggests future directions in the development of surface pCO_2 satellite remote sensing algorithms. For example, atmospheric pCO_2 should be used in the surface pCO_2 remote sensing algorithms to better capture the interannual variabilities in surface pCO_2. Meanwhile, to further examine the driving mechanisms of surface pCO_2 on different time scales, more data (e.g., Chl) collected over longer time series are required for future investigation.

Acknowledgements

This research was supported by a University of South Florida student fellowship. The authors are indebted to all researchers, including those of NOAA NCEI, who have collected, processed, quality controlled, and shared all the cruise survey data. These data played an essential role in this work. The authors also thank NASA for providing MODIS ocean color data, NCEP for providing the wind speed data.

Reference

Bai, Y., Cai, W. J., He, X., Zhai, W., Pan, D., Dai, M., and Yu, P. (2015). A mechanistic semi-analytical method for remotely sensing sea surface pCO_2 in river-dominated coastal oceans: A case study from the East China Sea. Journal of Geophysical Research: Oceans, 120(3), 2331-2349. https://doi.org/10.1002/2014JC010632.

Bailey, S. W., and Werdell, P. J. (2006). A multi-sensor approach for the on-orbit validation of ocean color satellite data products. Remote Sensing of Environment, 102(1-2), 12-23. https://doi.org/10.1016/j.rse.2006.01.015.

Barnes, B. B., and Hu, C. (2015). Cross-sensor continuity of satellite-derived water clarity in the Gulf of Mexico: Insights into temporal aliasing and implications for long-term water clarity assessment. IEEE Transactions on Geoscience and Remote Sensing, 53(4), 1761-1772.

Bennington, V., McKinley, G. A., Dutkiewicz, S., and Ullman, D. (2009). What does chlorophyll variability tell us about export and air-sea CO_2 flux variability in the North Atlantic? Global Biogeochemical Cycles, 23(3).

Borges, A. V. (2005). Do we have enough pieces of the jigsaw to integrate CO_2 fluxes in the coastal ocean? Estuaries, 28(1), 3-27.

Borges, A. V., Delille, B., & Frankignoulle, M. (2005). Budgeting sinks and sources of CO_2 in the coastal ocean: Diversity of ecosystems counts. Geophysical research letters, 32(14).

Cai, W. J., Dai, M., and Wang, Y. (2006). Air-sea exchange of carbon dioxide in ocean margins: A province-based synthesis. Geophysical Research Letters, 33(12).

Chen, C.-T. A., et al. (2003), Continental margin exchanges, in Ocean Biogeochemistry: The Role of the Ocean Carbon Cycle in Global Change, edited by M. J. R. Fasham, pp. 53-98, Springer, New York.

Chen, S., Hu, C., Byrne, R. H., Robbins, L. L., & Yang, B. (2016). Remote estimation of surface pCO_2 on the West Florida Shelf. Continental Shelf Research, 128, 10-25. https://doi.org/10.1016/j.csr.2016.09.004.

Chen, S., Hu, C., Cai, W. J., & Yang, B. (2017). Estimating surface pCO_2 in the northern Gulf of Mexico: Which remote sensing model to use? Continental Shelf Research, 151, 94-110. https://doi.org/10.1016/j.csr.2017.10.013.

Chen, S., C. Hu, B. B. Barnes, R. Wanninkhof, W. J. Cai, and L. Barbero. A machine learning approach to estimate surface ocean pCO_2 from satellite measurements, Remote Sensing of Environment (under review).

Cross, J., J. Mathis, N. Monacci, S. Musielewicz, S. Maenner, and J. Osborne (2014a). High-resolution ocean and atmosphere pCO_2 time-series measurements from mooring GAKOA_149W_60N.

http://cdiac.esd.ornl.gov/ftp/oceans/Moorings/GAKOA_149W_60N/. Carbon Dioxide Information Analysis Center, Oak Ridge National Laboratory, US Department of Energy, Oak Ridge, Tennessee. doi: 10.3334/CDIAC/OTG.TSM_GAKOA_149W_60N.

Cross, J., J. Mathis, N. Monacci, S. Musielewicz, S. Maenner, and J. Osborne (2014b). High-resolution ocean and atmosphere pCO_2 time-series measurements from mooring Kodiak_152W_57N. http://cdiac.ornl.gov/ftp/oceans/Moorings/Kodiak_152W_57N/. Carbon Dioxide Information Analysis Center, Oak Ridge National Laboratory, US Department of Energy, Oak Ridge, Tennessee. doi: 10.3334/CDIAC/OTG.TSM_KODIAK_152W_57N.

Cross, J., J. Mathis, N. Monacci, S. Musielewicz, S. Maenner, and J. Osborne (2014c). High-resolution ocean and atmosphere pCO_2 time-series measurements from mooring Southeast_AK_56N_134W. http://cdiac.ess-dive.lbl.gov/ftp/oceans/Moorings/Southeast_AK_56N_134W/. Carbon Dioxide Information Analysis Center, Oak Ridge National Laboratory, US Department of Energy, Oak Ridge, Tennessee. doi: 10.3334/CDIAC/OTG.TSM_Southeast_AK_56N_134W

Fay, A. R., & McKinley, G. A. (2013). Global trends in surface ocean pCO_2 from in situ data. Global Biogeochemical Cycles, 27(2), 541-557.

Fay, A. R., and McKinley, G. A. (2017). Correlations of surface ocean pCO_2 to satellite chlorophyll on monthly to interannual timescales. Global Biogeochemical Cycles, 31(3), 436-455.

Hales, B., Strutton, P. G., Saraceno, M., Letelier, R., Takahashi, T., Feely, R., Sabine, C., and Chavez, F. (2012). Satellite-based prediction of pCO_2 in coastal waters of the eastern North Pacific. Progress in Oceanography, 103, 1-15.

Huang, W. J., Cai, W. J., Wang, Y., Lohrenz, S. E., and Murrell, M. C. (2015). The carbon dioxide system on the M ississippi R iver ‐ dominated continental shelf in the northern Gulf of Mexico: 1. Distribution and air-sea CO_2 flux. Journal of Geophysical Research: Oceans, 120(3), 1429-1445.

Ikawa, H., Faloona, I., Kochendorfer, J., Paw, U., and Oechel, W. C. (2013). Air–sea exchange of CO_2 at a Northern California coastal site along the California Current upwelling system. Biogeosciences, 10(7), 4419-4432.

Lee, Z. P., Darecki, M., Carder, K. L., Davis, C. O., Stramski, D., and Rhea, W. J. (2005). Diffuse attenuation coefficient of downwelling irradiance: An evaluation of remote sensing methods. Journal of Geophysical Research: Oceans, 110(C2), C02016. https://doi.org/10.1029/2004JC002573.

Le Quéré, C., Andrew, R. M., Canadell, J. G., Sitch, S., Korsbakken, J. I., ... Global Carbon Budget 2016, Earth Syst. Sci. Data, 8, 605-649, https://doi.org/10.5194/essd-8-605-2016, 2016.

Lohrenz, S. E., and Cai, W. J. (2006). Satellite ocean color assessment of air-sea fluxes of CO_2 in a river-dominated coastal margin. Geophysical Research Letters, 33(1), L01601. doi: 10.1029/2005GL023942.

Lohrenz, S. E., Cai, W. J., Chen, F., Chen, X., and Tuel, M. (2010). Seasonal variability in air-sea fluxes of CO_2 in a river-influenced coastal margin. Journal of Geophysical Research: Oceans, 115(C10), C10034. doi: 10.1029/2009JC005608.

Lohrenz, S. E., Cai, W. J., Chakraborty, S., Huang, W. J., Guo, X., He, R., Xue Z., Fennel K., Howden S., and Tian, H. (2018). Satellite estimation of coastal pCO_2 and air-sea flux of carbon dioxide in the northern Gulf of Mexico. Remote Sensing of Environment, 207, 71-83. https://doi.org/10.1016/j.rse.2017.12.039.

Muller-Karger, F. E., Varela, R., Thunell, R., Luerssen, R., Hu, C., and Walsh, J. J. (2005). The importance of continental margins in the global carbon cycle. Geophysical research letters, 32(1): L01602, doi: 10.1029/2004GL021346.

Norman, M., Parampil, S. R., Rutgersson, A., and Sahlée, E. (2013). Influence of coastal upwelling on the air–sea gas exchange of CO_2 in a Baltic Sea Basin. Tellus B: Chemical and Physical Meteorology, 65(1), 21831.

Patt, F. S., et al., "Algorithm updates for the fourth SeaWiFS data reprocessing, NASA tech memo 2003-206892, volume 22," in SeaWiFS Post-launch Technical Report Series, S. B. Hooker and E. R. Firestone, Eds. Greenbelt, MD, USA: National Aeronautics and Space Administration (NASA), 2003.

Randerson, J. T., Thompson, M. V., Conway, T. J., Fung, I. Y., and Field, C. B. (1997). The contribution of terrestrial sources and sinks to trends in the seasonal cycle of atmospheric carbon dioxide. Global Biogeochemical Cycles, 11(4), 535-560.

Renault, L., Deutsch, C., McWilliams, J. C., Frenzel, H., Liang, J. H., and Colas, F. (2016). Partial decoupling of primary productivity from upwelling in the California Current system. Nature Geoscience, 9(7), 505.

Sabine, C. (2005). High-resolution ocean and atmosphere pCO_2 time-series measurements. The State of the Ocean and the Ocean Observing System for Climate, Annual Report, Fiscal Year 2004, NOAA/OGP/Office of Climate Observation, Section 3.32a, 246–253.

Sabine, C., N. Bates, S. Maenner, R. Bott, and A. Sutton (2010). High-resolution ocean and atmosphere pCO_2 time-series measurements from mooring BTM_64W_32N. http://cdiac.ess-dive.lbl.gov/ftp/oceans/Moorings/BTM_64W_32N/. Carbon Dioxide Information Analysis Center, Oak Ridge National Laboratory, US Department of Energy, Oak Ridge, Tennessee. doi: 10.3334/CDIAC/otg.TSM_BTM_64W_32N.

Signorini, S. R., Mannino, A., Najjar, R. G., Friedrichs, M. A., Cai, W. J., Salisbury, J., Wang, Z. A., Thomas, H., and Shadwick, E. (2013). Surface ocean pCO_2 seasonality and sea-air CO_2 flux estimates for the North American east coast. Journal of Geophysical Research: Oceans, 118(10), 5439-5460.

Sutton, A., C. Sabine, C. Dietrich, S. Maenner, S. Musielewicz, R. Bott, and J. Osborne (2010). High-resolution ocean and atmosphere pCO_2 time-series measurements from mooring WHOTS_158W_23N. http://cdiac.ess-dive.lbl.gov/ftp/oceans/Moorings/WHOTS_158W_23N/. Carbon Dioxide Information Analysis Center, Oak Ridge National Laboratory, US Department of Energy, Oak Ridge, Tennessee. doi: 10.3334/CDIAC/OTG.TSM_WHOTS

Sutton, A., C. Sabine, W.-J. Cai, S. Noakes, S. Musielewicz, S. Maenner, C. Dietrich, R. Bott, and J. Osborne (2011). High-resolution ocean and atmosphere pCO_2 time-series measurements from mooring GraysRf_81W_31N. http://cdiac.esd.ornl.gov/ftp/oceans/Moorings/GraysRf_81W_31N/. Carbon Dioxide

Information Analysis Center, Oak Ridge National Laboratory, US Department of Energy, Oak Ridge, Tennessee. doi: 10.3334/CDIAC/OTG.TSM_GRAYSRF_81W_31N.

Sutton, A., C. Sabine, U. Send, M. Ohman, S. Musielewicz, S. Maenner, C. Dietrich, R. Bott, and J. Osborne (2013a). High-resolution ocean and atmosphere pCO_2 time-series measurements from mooring CCE2_121W_34N. http://cdiac.esd.ornl.gov/ftp/oceans/Moorings/CCE2_121W_34N/. Carbon Dioxide Information Analysis Center, Oak Ridge National Laboratory, US Department of Energy, Oak Ridge, Tennessee. doi: 10.3334/CDIAC/OTG.TSM_CCE2_121W_34N.

Sutton, A., C. Sabine, D. Manzello, S. Musielewicz, S. Maenner, C. Dietrich, R. Bott, and J. Osborne (2013b). High-resolution ocean and atmosphere pCO_2 time-series measurements from mooring Cheeca_80W_25N. http://cdiac.ess-dive.lbl.gov/ftp/oceans/Moorings/Cheeca_80W_25N/. Carbon Dioxide Information Analysis Center, Oak Ridge National Laboratory, US Department of Energy, Oak Ridge, Tennessee. doi: 10.3334/CDIAC/OTG.CHEECA_80W_25N.

Sutton, A., C. Sabine, J. Salisbury, D. Vandemark, S. Musielewicz, S. Maenner, C. Dietrich, R. Bott, and J. Osborne (2013c). High-resolution ocean and atmosphere pCO_2 time-series measurements from mooring NH_70W_43N. http://cdiac.esd.ornl.gov/ftp/oceans/Moorings/NH_70W_43N/. Carbon Dioxide Information Analysis Center, Oak Ridge National Laboratory, US Department of Energy, Oak Ridge, Tennessee. doi: 10.3334/CDIAC/OTG.TSM_NH_70W_43N.

Sutton, A., C. Sabine, S. Musielewicz, S. Maenner, C. Dietrich, R. Bott, and J. Osborne (2013d). High-resolution ocean and atmosphere pCO_2 time-series measurements from mooring

WA_125W_47N. http://cdiac.ess-dive.lbl.gov/ftp/oceans/Moorings/WA_125W_47N/. Carbon Dioxide Information Analysis Center, Oak Ridge National Laboratory, US Department of Energy, Oak Ridge, Tennessee. doi: 10.3334/CDIAC/OTG.TSM_WA_125W_47N.

Sutton, A., C. Sabine, S. Howden, S. Musielewicz, S. Maenner, C. Dietrich, R. Bott, and J. Osborne (2014a). High-resolution ocean and atmosphere pCO_2 time-series measurements from mooring CoastalMS_88W_30N. http://cdiac.ess-dive.lbl.gov/ftp/oceans/Moorings/CoastalMS_88W_30N/. Carbon Dioxide Information Analysis Center, Oak Ridge National Laboratory, US Department of Energy, Oak Ridge, Tennessee.doi: 10.3334/CDIAC/OTG.TSM_COASTALMS_88W_30N.

Sutton, A., C. Sabine, J. Morell, S. Musielewicz, S. Maenner, C. Dietrich, R. Bott, and J. Osborne (2014b). High-resolution ocean and atmosphere pCO_2 time-series measurements from mooring La_Parguera_67W_18N. http://cdiac.esd.ornl.gov/ftp/oceans/Moorings/La_Parguera_67W_18N/. Carbon Dioxide Information Analysis Center, Oak Ridge National Laboratory, US Department of Energy, Oak Ridge, Tennessee. doi: 10.3334/CDIAC/OTG.TSM_La_Parguera_67W_18N.

Sutton, A. J., Sabine, C. L., Maenner-Jones, S., Lawrence-Slavas, N., Meinig, C., Feely, R. A., Mathis, J. T., Musielewicz, S., Bott, R., McLain, P. D., Fought, H. J., and Kozyr, A. (2014c). A high-frequency atmospheric and seawater pCO_2 data set from 14 open-ocean sites using a moored autonomous system. Earth System Science Data, 6(2), 353-366.

Sutton, A., C. Sabine, S. Maenner, S. Musielewicz, R. Bott, and J. Osborne (2015). High-resolution ocean and atmosphere pCO_2 time-series measurements from mooring Papa_145W_50N.

Takahashi, T., Olafsson, J., Goddard, J. G., Chipman, D. W., and Sutherland, S. C. (1993). Seasonal variation of CO_2 and nutrients in the high-latitude surface oceans: A comparative study. Global Biogeochemical Cycles, 7(4), 843-878.

Takahashi, T., Sutherland, S. C., Sweeney, C., Poisson, A., Metzl, N., Tilbrook, B., ... and Olafsson, J. (2002). Global sea–air CO_2 flux based on climatological surface ocean pCO_2, and seasonal biological and temperature effects. Deep Sea Research Part II: Topical Studies in Oceanography, 49(9-10), 1601-1622.

Takahashi, T., Sutherland, S. C., Wanninkhof, R., Sweeney, C., Feely, R. A., Chipman, D. W., ... and Watson, A. (2009). Climatological mean and decadal change in surface ocean pCO_2, and net sea–air CO_2 flux over the global oceans. Deep Sea Research Part II: Topical Studies in Oceanography, 56(8-10), 554-577.

Takahashi, T., Sutherland, S. C., Chipman, D. W., Goddard, J. G., Ho, C., Newberger, T., ... and Munro, D. R. (2014). Climatological distributions of pH, pCO_2, total CO_2, alkalinity, and $CaCO_3$ saturation in the global surface ocean, and temporal changes at selected locations. Marine Chemistry, 164, 95-125.

Tucker, C. J., Fung, I. Y., Keeling, C. D., and Gammon, R. H. (1986). Relationship between atmospheric CO_2 variations and a satellite-derived vegetation index. Nature, 319(6050), 195.

Ullman, D. J., McKinley, G. A., Bennington, V., and Dutkiewicz, S. (2009). Trends in the North Atlantic carbon sink: 1992–2006. Global Biogeochemical Cycles, 23(4).

Wanninkhof, R., Park, G. H., Takahashi, T., Sweeney, C., Feely, R. A., Nojiri, Y., ... & Le Quere, C. (2013). Global ocean carbon uptake: magnitude, variability and trends.

Wanninkhof, R., Park, G.-H., Takahashi, T., Sweeney, C., Feely, R., Nojiri, Y., Gruber, N., Doney, S. C., McKinley, G. A., Lenton, A., Le Quéré, C., Heinze, C., Schwinger, J., Graven, H., and Khatiwala, S. (2013). Global ocean carbon uptake: magnitude, variability and trends, Biogeosciences, 10, 1983-2000, doi: 10.5194/bg-10-1983-2013.

Wong, C. S., & Chan, Y. H. (1991). Temporal variations in the partial pressure and flux of CO_2 at ocean station P in the subarctic northeast Pacific Ocean. Tellus B, 43(2), 206-223.

Table 1. Summary of *in situ* time series data compiled for this study (from low latitude to high latitudes in sequence). Buoys of O1-O2 and C1-C5 are located in the tropical and subtropical zones (i.e., latitude within 0~35°N, shaded in blue), and buoys of O3 and C6-C10 are located in the temperate zone (i.e., latitude within 35~66.5°N, shaded in green). Note that "O" represents Open Ocean, and "C" represents Coastal Ocean. See Fig. 1 for the location of each buoy.

Buoy	Geolocation	Period	SST	SSS	Atmospheric pCO_2	Surface pCO_2	Number of data
C1	17.954°N, 67.051°W	2009-2015	25.92-31.71	31.73-36.57	357.4-427.4	317.9-538.4	16,454
O1	22.670°N, 157.970°W	2007-2015	22.90-29.20	34.03-35.57	364.9-393.1	343.1-436.7	17,201
C2	24.898°N, 80.618°W	2010-2015	16.75-33.13	32.45-38.82	364.0-413.3	182.4-736.8	10,760
C3	30.000°N, 88.600°W	2009-2014	12.46-32.42	14.00-35.64	350.7-430.0	72.1-607.5	5,622
C4	31.399°N, 80.868°W	2006-2015	9.84-30.99	29.20-36.80	352.6-436.3	268.2-619.8	15,663
O2	31.780°N, 64.200°W	2005-2007	18.81-28.74	35.44-36.88	357.1-387.4	317.0-447.2	5,116
C5	34.320°N, 120.810°W	2010-2015	9.93-20.90	31.09 -33.92	366.3-433.2	220.4-806.3	13,223
C6	43.024°N, 70.543°W	2006-2014	0.85-22.32	22.56-33.38	353.0-462.6	194.4-696.2	17,611
C7	47.340°N, 124.750°W	2006-2015	6.17-18.06	23.85-32.95	364.1-452.9	112.9-557.3	15,025
O3	50.120°N, 144.830°W	2007-2015	4.55-16.23	32.12-32.76	357.1-406.6	340.1-466.6	16,826
C8	56.273°N, 134.657°W	2013-2016	3.48-13.59	24.83-31.99	374.2-435.9	113.4-679.1	7,424
C9	57.697°N, 152.315°W	2013-2015	2.73-14.71	17.52-32.42	367.3-437.5	138.5-586.4	8,270
C10	59.911°N, 149.348°W	2011-2017	3.06-18.78	17.25-33.03	359.3-419.6	124.6-487.4	12,291

Table 2. Seasonal amplitudes of atmospheric pCO_2, surface pCO_2 and its components (pCO_2_T and pCO_2_nonT), and the relative importance (Eq. 6) of the temperature and non-temperature effects in affecting surface pCO_2 at each buoy location (Table 1, from low latitude to high latitudes in sequence). Note that statistics of the buoys located in the tropical and subtropical zones and temperate zone are shaded in blue and green, respectively.

Buoy	Seasonal amplitude (μatm)				Relative importance (*RI*) of pCO_2_T and pCO_2_nonT (Eq. 6)
	Surface pCO_2	Atmospheric pCO_2	pCO_2_T	pCO_2_nonT	
C1	60.26	9.67	58.59	20.69	0.63
O1	22.22	12.61	44.48	23.29	0.95
C2	227.94	15.08	137.08	255.18	-0.53
C3	114.88	30.23	195.26	201.27	-0.05
C4	154.37	23.19	270.45	149.75	0.78
O2	90.68	15.05	128.59	57.47	0.78
C5	95.82	16.58	67.32	153.90	-0.90
C6	138.22	17.55	247.55	207.53	0.29
C7	123.22	19.75	69.54	162.79	-0.76
O3	20.81	16.18	127.21	125.71	0.07
C8	309.81	12.06	98.08	336.52	-0.77
C9	279.42	17.24	114.92	337.60	-0.80
C10	168.28	18.21	131.35	273.00	-0.84

Table 3. Interannual variabilities (i.e., interannual trend) of the atmospheric pCO_2, surface pCO_2 and its components (pCO_2_T and pCO_2_nonT), and the corresponding environmental variables based on the buoy time series data in Table 1 and Fig. 1 (from low latitude to high latitudes in sequence). Statistics of the buoys located in the tropical and subtropical zones and temperate zone are shaded in blue and green, respectively. Note that values in brackets are the corresponding R^2 of each statistic of the interannual trend, and statistics are highlighted in blue if the corresponding p value is < 0.05.

Buoy	Interannual trend							Period	N
	Surface pCO_2 (μatm/yr)	Atmospheric pCO_2 (μatm/yr)	pCO_2_T (μatm/yr)	pCO_2_nonT (μatm/yr)	SST (°C/yr)	SSS	Wind speed (m s^{-1}/yr)		
C1	-0.02 (0.00)	1.69 (0.74)	-0.32 (0.01)	0.29 (0.01)	-0.02 (0.01)	0.01 (0.01)	0.08 (0.06)	2009-2015	79
O1	2.77 (0.67)	1.20 (0.76)	0.87 (0.11)	1.93 (0.42)	0.05 (0.12)	0.01 (0.07)	-0.10 (0.08)	2007-2015	76
C2	11.44 (0.26)	2.40 (0.67)	2.57 (0.21)	9.91 (0.21)	0.14 (0.05)	-0.00 (0.00)	-0.02 (0.00)	2010-2015	48
C3	2.03 (0.01)	2.19 (0.72)	-3.65 (0.16)	7.19 (0.07)	-0.32 (0.19)	-0.46 (0.27)	0.02 (0.00)	2009-2014	24
C4	2.97 (0.09)	1.99 (0.86)	-0.97 (0.04)	3.44 (0.11)	-0.05 (0.03)	-0.04 (0.04)	0.01 (0.00)	2006-2015	75
O2	5.76 (0.43)	1.94 (0.59)	1.34 (0.02)	4.56 (0.25)	0.09 (0.02)	-0.06 (0.18)	-0.66 (0.27)	2005-2007	25
C5	-0.28 (0.00)	3.60 (0.72)	8.17 (0.47)	-8.13 (0.11)	0.48 (0.47)	0.09 (0.40)	-0.07 (0.07)	2010-2015	62
C6	-0.13 (0.00)	2.33 (0.86)	0.87 (0.03)	-0.90 (0.01)	0.05 (0.02)	0.09 (0.22)	0.02 (0.00)	2006-2014	87
C7	-5.69 (0.32)	1.75 (0.80)	2.32 (0.25)	-7.98 (0.44)	0.17 (0.25)	-0.06 (0.14)	-0.03 (0.05)	2006-2015	70
O3	0.57 (0.02)	2.16 (0.83)	5.38 (0.50)	-4.60 (0.27)	0.33 (0.51)	-0.01 (0.09)	-0.06 (0.02)	2007-2015	76
C8	24.97 (0.21)	1.22 (0.34)	6.54 (0.28)	15.56 (0.08)	0.36 (0.30)	0.13 (0.11)	0.21 (0.14)	2013-2016	33
C9	10.68 (0.22)	1.42 (0.28)	10.05 (0.70)	1.00 (0.00)	0.65 (0.72)	-0.14 (0.15)	0.20 (0.07)	2013-2015	38
C10	5.37 (0.23)	2.55 (0.72)	4.55 (0.57)	0.67 (0.00)	0.34 (0.55)	-0.09 (0.04)	-0.04 (0.01)	2011-2017	55

Table 4. Correlations (Pearson correlation coefficient – *R*) between surface pCO_2 as well as its components (pCO_2_T and pCO_2_nonT) and different environmental variables (i.e., SST, SSS, atmospheric pCO_2, Chl and K_d in $\log_{10}$ scale, and wind speed) for all the buoys listed in Table 1 from low latitude to high latitude in sequence. Statistics of the buoys located in the tropical and subtropical zones and temperate zone are shaded in blue and green, respectively. Note that the value of *R* is highlighted in blue if the corresponding *p* value is < 0.05.

Buoy	Variables	SST	SSS	Atmospheric pCO_2	Chl	K_d	Wind speed
C1	Surface pCO_2	0.44	0.30	-0.10	NaN	NaN	-0.25
	pCO_2_T	1.00	-0.10	-0.29	NaN	NaN	-0.54
	pCO_2_nonT	-0.32	0.38	0.12	NaN	NaN	0.17
	N	79	79	79	0	0	79
O1	Surface pCO_2	0.54	0.10	0.69	-0.04	-0.08	-0.35
	pCO_2_T	1.00	-0.06	0.07	0.13	-0.03	-0.34
	pCO_2_nonT	-0.23	0.17	0.72	-0.15	-0.06	-0.10
	N	76	76	76	63	63	76
C2	Surface pCO_2	0.41	-0.27	0.25	NaN	NaN	0.01
	pCO_2_T	0.99	0.08	-0.10	NaN	NaN	-0.32
	pCO_2_nonT	-0.05	-0.31	0.37	NaN	NaN	0.16
	N	48	48	48	0	0	48
C3	Surface pCO_2	-0.74	0.53	0.20	-0.20	-0.26	0.38
	pCO_2_T	0.99	-0.22	-0.57	0.35	0.49	-0.32
	pCO_2_nonT	-0.92	0.42	0.41	-0.29	-0.44	0.39
	N	24	24	24	19	19	20
C4	Surface pCO_2	-0.00	0.04	0.37	-0.29	-0.30	0.11
	pCO_2_T	0.97	0.22	-0.35	-0.05	-0.06	-0.49
	pCO_2_nonT	-0.49	-0.07	0.47	-0.16	-0.17	0.31
	N	75	75	75	73	73	75
O2	Surface pCO_2	0.51	-0.21	0.47	-0.31	-0.28	-0.51
	pCO_2_T	1.00	-0.28	0.00	-0.21	-0.18	-0.38
	pCO_2_nonT	-0.52	0.09	0.45	-0.07	-0.07	-0.09
	N	25	25	25	20	20	25
C5	Surface pCO_2	-0.31	0.38	0.14	-0.04	-0.24	0.19
	pCO_2_T	1.00	0.15	0.39	-0.38	-0.37	-0.20
	pCO_2_nonT	-0.70	0.22	-0.08	0.14	-0.01	0.24
	N	62	62	62	60	61	62
C6	Surface pCO_2	-0.16	0.21	0.02	-0.24	-0.39	-0.03
	pCO_2_T	0.98	-0.14	0.14	0.07	0.03	-0.12
	pCO_2_nonT	-0.61	0.23	-0.03	-0.27	-0.38	0.01
	N	87	87	87	81	82	87
C7	Surface pCO_2	-0.25	0.47	-0.58	-0.12	-0.23	0.52
	pCO_2_T	1.00	-0.32	0.31	-0.16	-0.14	-0.07
	pCO_2_nonT	-0.57	0.50	-0.61	-0.05	-0.17	0.47
	N	70	70	70	59	61	70
O3	Surface pCO_2	-0.14	0.25	0.30	-0.22	-0.26	0.09
	pCO_2_T	0.99	-0.67	0.58	-0.12	0.09	-0.28
	pCO_2_nonT	-0.88	0.66	-0.32	-0.06	-0.23	0.31
	N	76	76	76	28	28	76
C8	Surface pCO_2	-0.11	0.15	0.27	NaN	NaN	0.31
	pCO_2_T	1.00	0.21	0.55	NaN	NaN	0.05
	pCO_2_nonT	-0.35	-0.01	0.14	NaN	NaN	0.27
	N	33	33	33	0	0	33
C9	Surface pCO_2	0.35	-0.23	0.21	-0.13	-0.25	0.29
	pCO_2_T	0.99	-0.43	0.56	0.05	-0.50	-0.00
	pCO_2_nonT	-0.14	0.05	-0.01	-0.13	-0.08	0.29

	N	38	38	38	12	15	38
C10	Surface pCO_2	0.28	-0.04	0.46	NaN	NaN	0.03
	pCO_2_T	0.99	-0.20	0.66	NaN	NaN	0.05
	pCO_2_nonT	-0.27	0.07	0.11	NaN	NaN	0.00
	N	55	55	55	0	0	55

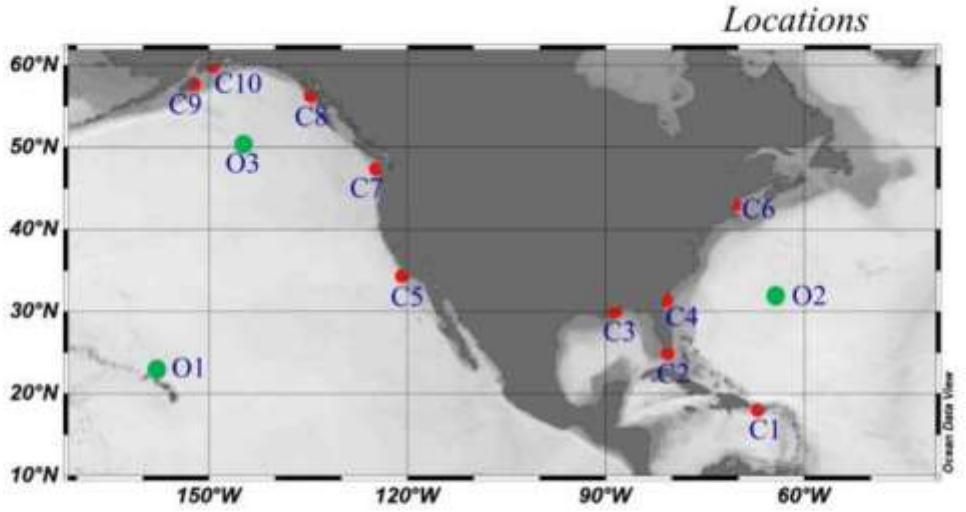

Fig. 1. Spatial distributions of the buoys listed in Table 1. Buoys of O1-O2 and C1-C5 are located in the tropical and subtropical zones (i.e., latitude within 0~35 °N), and buoys of O3 and C6-C10 are located in the temperate zone (i.e., latitude within 35~66.5 °N). Note that "O" represents Open Ocean, and "C" represents Coastal Ocean. See Table 1 for detailed description of the data collected from each buoy.

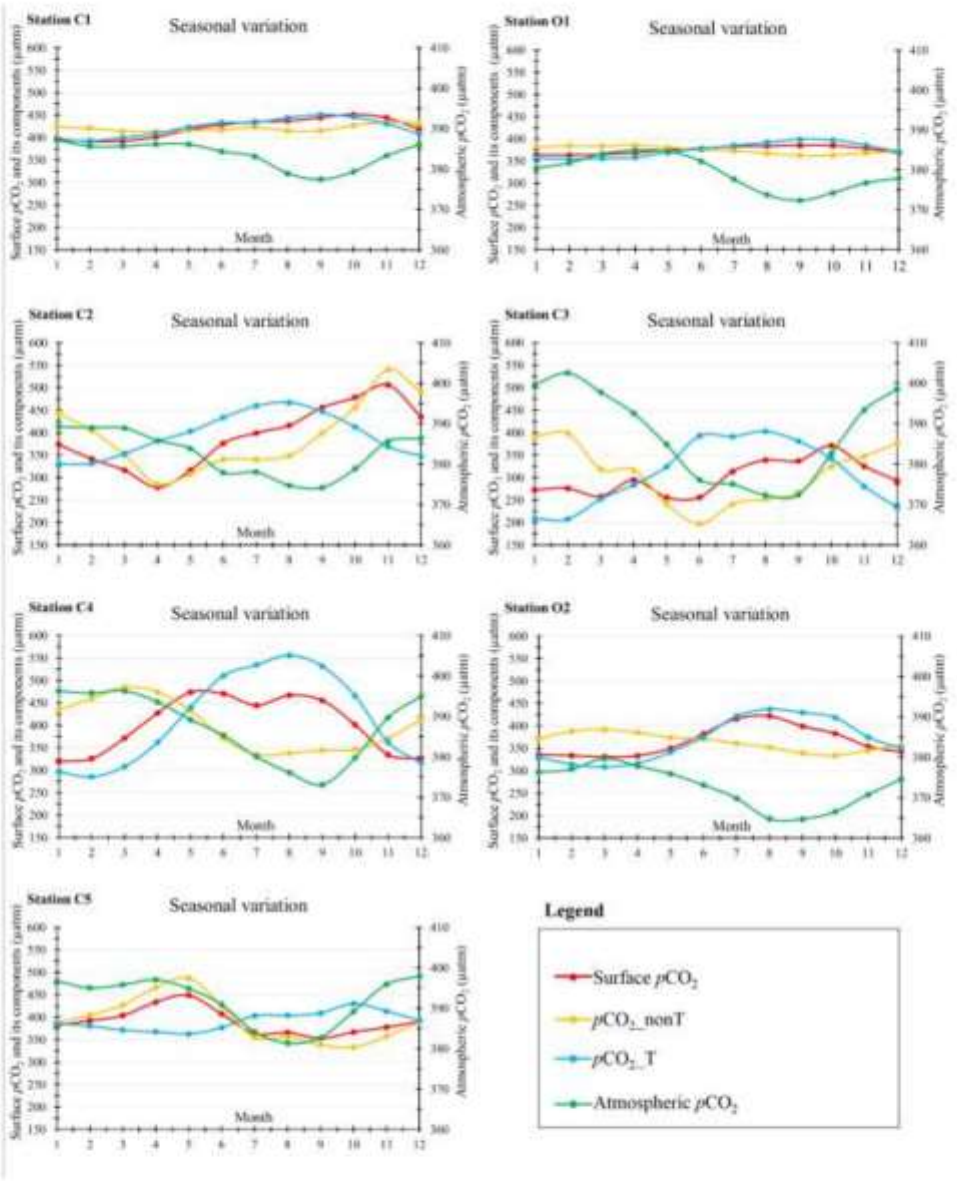
Station C1
Seasonal variation
Station O1
Seasonal variation
Station C2
Seasonal variation
Station C3
Seasonal variation
Station C4
Seasonal variation
Station O2
Seasonal variation
Station C5
Seasonal variation
Month
Legend
Surface pCO_2
pCO_2_nonT
pCO_2_T
Atmospheric pCO_2

Fig. 2. Seasonal variations of atmospheric pCO_2, surface pCO_2 and its components (pCO_2_T and pCO_2_nonT) of the buoys located in the tropical and subtropical zones (see Table 1 and Fig. 1) from low latitude to high latitude in sequence. See Table 2 for detailed statistics.

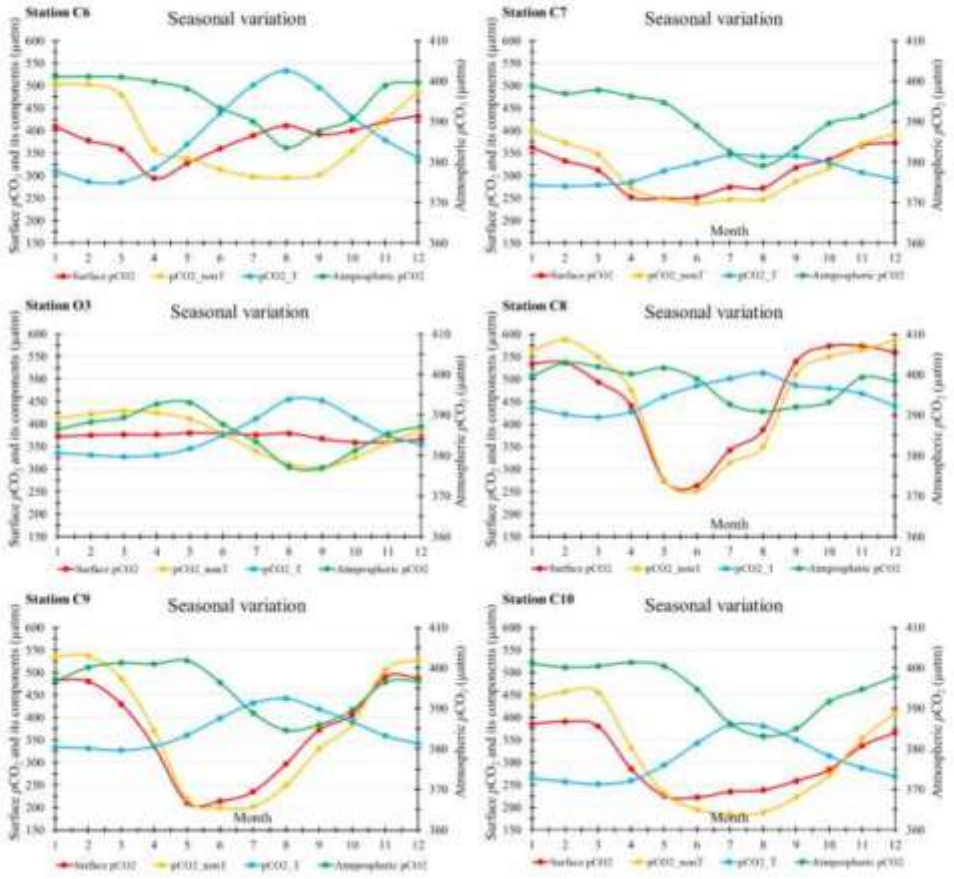

Fig. 3. Same as Fig. 2, here are the seasonal variations of atmospheric pCO_2, surface pCO_2 and its components (pCO_2_T and pCO_2_nonT) of the buoys located in the temperate zone (see Table 1 and Fig. 1) from low latitude to high latitude in sequence. See Table 2 for detailed statistics.

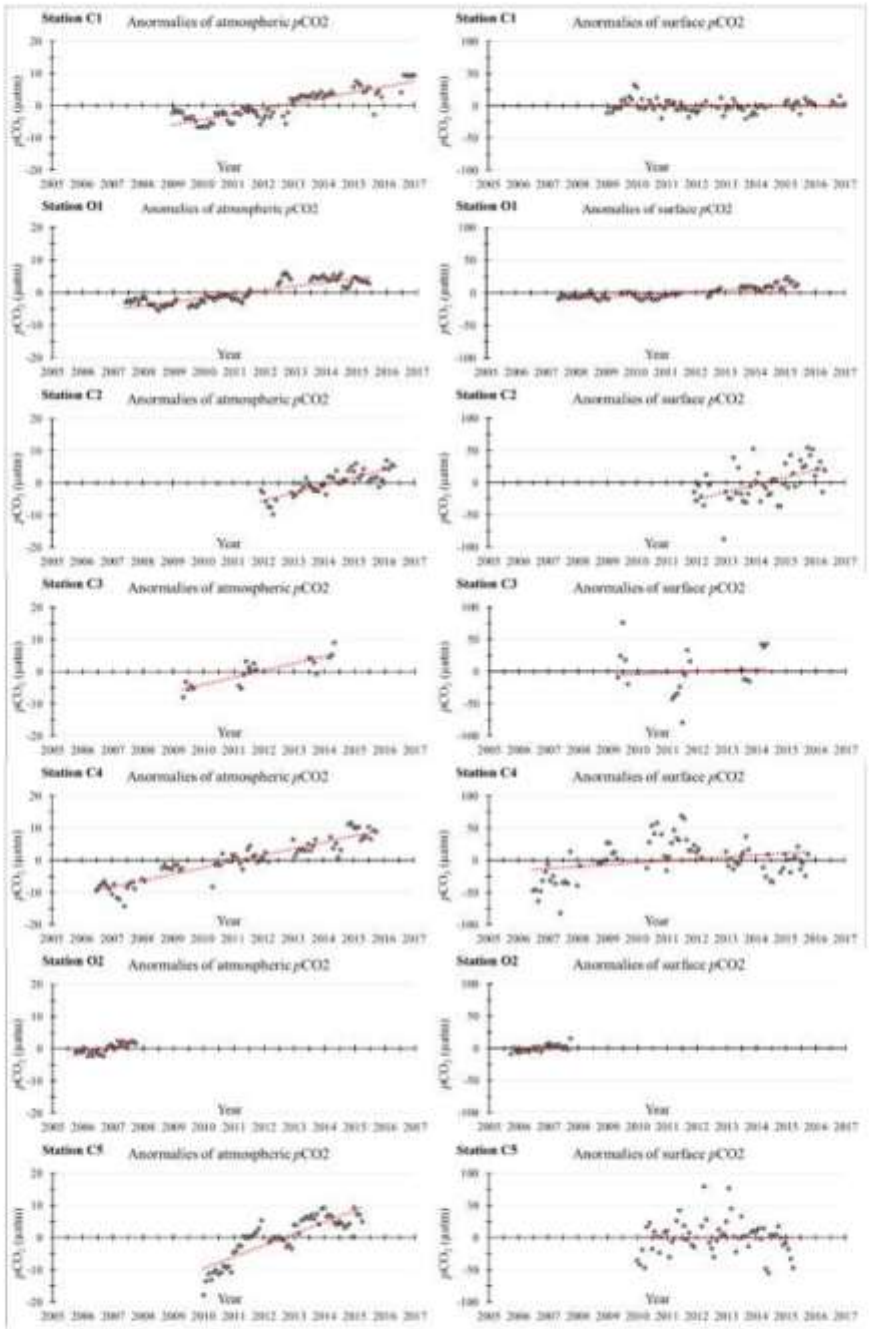
Station C1
Anomalies of atmospheric pCO2
Station C1
Anomalies of surface pCO2
Station O1
Anomalies of atmospheric pCO2
Station O1
Anomalies of surface pCO2
Station C2
Anomalies of atmospheric pCO2
Station C2
Anomalies of surface pCO2
Station C3
Anomalies of atmospheric pCO2
Station C3
Anomalies of surface pCO2
Station C4
Anomalies of atmospheric pCO2
Station C4
Anomalies of surface pCO2
Station O2
Anomalies of atmospheric pCO2
Station O2
Anomalies of surface pCO2
Station C5
Anomalies of atmospheric pCO2
Station C5
Anomalies of surface pCO2
Year

51

Fig. 4. Interannual variabilities of atmospheric pCO_2 and surface pCO_2 of the buoys located in the tropical and subtropical zones (see Table 1 and Fig. 1) from low latitude to high latitude in sequence. The overlaid dashed red line is the interannual variation trend. See Table 3 for detailed statistics.

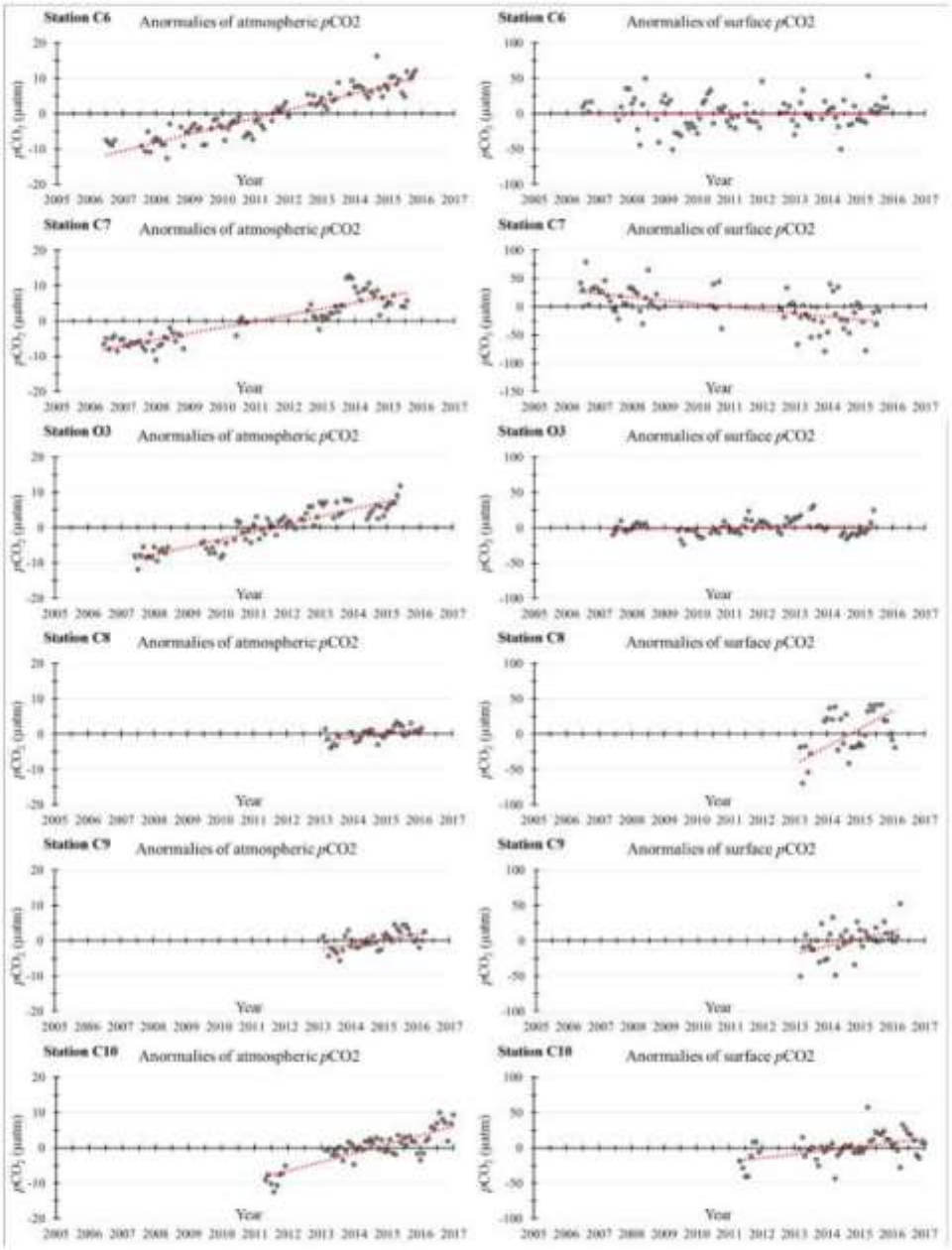
Station C6
Anomalies of atmospheric pCO2
Anomalies of surface pCO2
Station C7
Station O3
Station C8
Station C9
Station C10
Year

Fig. 5. Same as Fig. 4, here are the interannual variabilities of the atmospheric pCO_2 and surface pCO_2 of the buoys located in the temperate zone (see Table 1 and Fig. 1) from low latitude to high latitude in sequence. The overlaid dashed red line is the interannual variation trend. See Table 3 for detailed statistics.

APPENDIX F:

AUTHOR CONTRIBUTIONS AND COPYRIGHT CLEARANCES

1. Author Contributions

Appendix A: Remote estimation of surface pCO_2 on the West Florida Shelf

S. Chen developed the research approach, processed the data, conducted the analyses, and wrote the manuscript.

C. Hu assisted in developing the research approach, acquired funding for the research, and reviewed drafts of the manuscript.

R. H. Byrne analyzed data and reviewed drafts of the manuscript.

L. L. Robbins provided and analyzed data, and reviewed drafts of the manuscript.

B. Yang analyzed data and reviewed the manuscript.

Appendix B: Estimating surface pCO_2 in the northern Gulf of Mexico: Which remote sensing model to use?

S. Chen developed the research approach, processed the data, conducted the analyses, and wrote the manuscript.

C. Hu assisted in developing the approach, acquired funding for the research, and reviewed drafts of the manuscript.

W. J. Cai analyzed the data and reviewed drafts of the manuscript.

B. Yang reviewed drafts of the manuscript.

Appendix C: Estimating sea surface salinity in the northern Gulf of Mexico from satellite ocean color measurements

S. Chen developed approach, processed data, conducted analyses and wrote manuscript

C. Hu developed approach, acquired funding, and reviewed manuscript

Appendix D: A machine learning approach to estimate surface ocean pCO_2 from satellite measurements

S. Chen developed approach, processed data, conducted analyses and wrote manuscript

C. Hu developed approach, acquired funding, and reviewed manuscript

R. Wanninkhof provided data and reviewed manuscript

W. J. Cai provided data and reviewed manuscript

L. Barbero provided data and reviewed manuscript

2. Copyright Clearances

Appendix A:

Appendix B:

Appendix C:

APPENDIX G:

PUBLICATIONS (PUBLISHED AND SUBMITTED)

Chen, S., and C. Hu (2014). In search of oil seeps in the Cariaco basin using MODIS and MERIS medium-resolution data. Remote Sensing Letters. 5(5): 442-450.

Hu, C., **S. Chen**, M. Wang, B. Murch, and J. Taylor (2015). Detecting surface oil slicks using VIIRS nighttime imagery under moon glint: a case study in the Gulf of Mexico. Remote Sensing Letters, 6:295-301.

Chen, S., C. Hu, R. H. Byrne, L. L. Robbins, and B. Yang (2016). Remote estimation of surface pCO_2 on the West Florida Shelf. Continental Shelf Research, 128, 10-25.

Chen, S., Hu, C., Cai, W. J., and Yang, B. (2017a). Estimating surface pCO_2 in the northern Gulf of Mexico: Which remote sensing model to use? Continental Shelf Research, 151, 94-110.

Chen, S., and C. Hu (2017b). Estimating sea surface salinity in the northern Gulf of Mexico from satellite ocean color measurements. Remote Sensing of Environment, 201, 115-132.

Chen, S., C. Hu, B. B. Barnes, Y. Xie, G. Lin, and Z. Qiu. Improving ocean color data coverage through machine learning. Remote Sensing of Environment (*submitted*).

Chen, S., C. Hu, B. B. Barnes, R. Wanninkhof, W. J. Cai, and L. Barbero. A machine learning approach to estimate surface ocean pCO_2 from satellite measurements. Remote Sensing of Environment (*submitted*).